

EFFECT OF LOAD PATTERN AND HISTORY ON PERFORMANCE OF REINFORCED  
CONCRETE COLUMNS

by

FATEMEH SHIRMOHAMMADI

BS, Isfahan University of Technology, 2007  
MS, Isfahan University of Technology, 2010

AN ABSTRACT OF A DISSERTATION

submitted in partial fulfillment of the requirements for the degree

DOCTOR OF PHILOSOPHY

Department of Civil Engineering  
College of Engineering

KANSAS STATE UNIVERSITY  
Manhattan, Kansas

2015

## **Abstract**

Accurate and realistic assessment of the performance of columns in general, and those in critical locations that may cause progressive failure of the entire structure, in particular, is significantly important. This performance is affected by the load history, pattern, and intensity. Current design code does not consider the effect of load pattern on the load and displacement capacity of columns. A primary research sponsored by Kansas Department of Transportation (KDOT) was conducted as the initial step of the present study (No. K-TRAN: KSU-11-5). The main goals of the KDOT project were: (1) investigation of new KDOT requirements in terms of the column design procedure and detailing and their consistency with AASHTO provisions; (2) verification of the KDOT assumptions for the plastic hinge regions for columns and bridge piers, (3) provide assessment of the load capacity of the existing columns and bridge piers in the light of the new specifications and using the new load demand as in the new provisions; and finally recommendations for columns and bridge piers that do not meet the new requirements. A conclusion was drawn that there is a need for conducting more studies on the realistic performance of Reinforced Concrete (RC) sections and columns. The studies should have included performance of RC members under various loading scenarios, assessment of columns capacity considering confinement effect provided by lateral reinforcement, and investigation on performance of various monotonic and cyclic material models applied to simulate the realistic performance.

In the study reported here, monotonic material models, cyclic rules, and plastic hinge models have been utilized in a fiber-based analytical procedure, and validated against experimental data to simulate behavior of RC section under various loading scenarios. Comparison of the analytical predictions and experimental data, through moment–curvature and

force–deflection analyses, confirmed the accuracy and validity of the analytical algorithm and models. The performance of RC columns under various axial and lateral loading patterns was assessed in terms of flexural strength and energy dissipation.

FRP application to enhance ductility, flexural strength, and shear capacity of existing deficient concrete structures has increased during the last two decades. Therefore, various aspects of FRP-confined concrete members, specifically monotonic and cyclic behavior of concrete members confined and reinforced by FRP, have been studied in many research programs, suggesting various monotonic models for concrete confined by only FRP. Exploration of existing model performances for predicting the behavior of several tested specimens shows a need for improvement of existing algorithms. The model proposed in the current study is a step in this direction. FRP wrapping is typically used to confine existing concrete members containing conventional lateral steel reinforcement (tie/spiral). The confining effect of lateral steel reinforcement in analytical studies has been uniquely considered in various models. Most models consider confinement due to FRP and ignore the effect of conventional lateral steel reinforcement. Exploration of existing model performances for predicting the behavior of several tested specimens confined by both FRP and lateral steel shows a need for improvement of existing algorithms. A model was proposed in this study which is a step in this direction. Performance of the proposed model and four other representative models from literature was compared to experimental data from four independent databases.

In order to fulfill the need for a simple, yet accurate analytical tool for performance assessment of RC columns, a computer program was developed that uses relatively simple analytical methods and material models to accurately predict the performance of RC structures under various loading conditions, including cyclic lateral displacement under a non-

proportionally variable axial load (Esmaeily and Xiao 2005, Esmaeily and Peterman 2007). However, it was limited to circular, rectangular, and hollow circular/rectangular sections and uniaxial lateral curvature or displacement.

In this regards, a computer program was developed which is the next generation of the aforesaid program with additional functionality and options. Triangulation of the section allows opportunity for cross-sectional geometry. Biaxial lateral curvature/displacement/force combined with any sequence of axial load provides opportunity to analyze the performance of a reinforced concrete column under any load and displacement path. Use of unconventional reinforcement, such as FRP, in lateral as well as longitudinal direction is another feature of this application.

EFFECT OF LOAD PATTERN AND HISTORY ON PERFORMANCE OF REINFORCED  
CONCRETE COLUMNS

by

FATEMEH SHIRMOHAMMADI

BS, Isfahan University of Technology, 2007  
MS, Isfahan University of Technology, 2010

A DISSERTATION

submitted in partial fulfillment of the requirements for the degree

DOCTOR OF PHILOSOPHY

Department of Civil Engineering  
College of Engineering

KANSAS STATE UNIVERSITY  
Manhattan, Kansas

2015

Approved by:

Major Professor  
Prof. Asad Esmaeily

# **Copyright**

FATEMEH SHIRMOHAMMADI

2015

## **Abstract**

Accurate and realistic assessment of the performance of columns in general, and those in critical locations that may cause progressive failure of the entire structure, in particular, is significantly important. This performance is affected by the load history, pattern, and intensity. Current design code does not consider the effect of load pattern on the load and displacement capacity of columns. A primary research sponsored by Kansas Department of Transportation (KDOT) was conducted as the initial step of the present study (No. K-TRAN: KSU-11-5). The main goals of the KDOT project were: (1) investigation of new KDOT requirements in terms of the column design procedure and detailing and their consistency with AASHTO provisions; (2) verification of the KDOT assumptions for the plastic hinge regions for columns and bridge piers, (3) provide assessment of the load capacity of the existing columns and bridge piers in the light of the new specifications and using the new load demand as in the new provisions; and finally recommendations for columns and bridge piers that do not meet the new requirements. A conclusion was drawn that there is a need for conducting more studies on the realistic performance of Reinforced Concrete (RC) sections and columns. The studies should have included performance of RC members under various loading scenarios, assessment of columns capacity considering confinement effect provided by lateral reinforcement, and investigation on performance of various monotonic and cyclic material models applied to simulate the realistic performance.

In the study reported here, monotonic material models, cyclic rules, and plastic hinge models have been utilized in a fiber-based analytical procedure, and validated against experimental data to simulate behavior of RC section under various loading scenarios. Comparison of the analytical predictions and experimental data, through moment–curvature and

force–deflection analyses, confirmed the accuracy and validity of the analytical algorithm and models. The performance of RC columns under various axial and lateral loading patterns was assessed in terms of flexural strength and energy dissipation.

FRP application to enhance ductility, flexural strength, and shear capacity of existing deficient concrete structures has increased during the last two decades. Therefore, various aspects of FRP-confined concrete members, specifically monotonic and cyclic behavior of concrete members confined and reinforced by FRP, have been studied in many research programs, suggesting various monotonic models for concrete confined by only FRP. Exploration of existing model performances for predicting the behavior of several tested specimens shows a need for improvement of existing algorithms. The model proposed in the current study is a step in this direction. FRP wrapping is typically used to confine existing concrete members containing conventional lateral steel reinforcement (tie/spiral). The confining effect of lateral steel reinforcement in analytical studies has been uniquely considered in various models. Most models consider confinement due to FRP and ignore the effect of conventional lateral steel reinforcement. Exploration of existing model performances for predicting the behavior of several tested specimens confined by both FRP and lateral steel shows a need for improvement of existing algorithms. A model was proposed in this study which is a step in this direction. Performance of the proposed model and four other representative models from literature was compared to experimental data from four independent databases.

In order to fulfill the need for a simple, yet accurate analytical tool for performance assessment of RC columns, a computer program was developed that uses relatively simple analytical methods and material models to accurately predict the performance of RC structures under various loading conditions, including cyclic lateral displacement under a non-



proportionally variable axial load (Esmaily and Xiao 2005, Esmaily and Peterman 2007). However, it was limited to circular, rectangular, and hollow circular/rectangular sections and uniaxial lateral curvature or displacement.

In this regards, a computer program was developed which is the next generation of the aforesaid program with additional functionality and options. Triangulation of the section allows opportunity for cross-sectional geometry. Biaxial lateral curvature/displacement/force combined with any sequence of axial load provides opportunity to analyze the performance of a reinforced concrete column under any load and displacement path. Use of unconventional reinforcement, such as FRP, in lateral as well as longitudinal direction is another feature of this application.

# Table of Contents

List of Figures .....	xiii
List of Tables .....	xx
Acknowledgements .....	xxi
Dedication .....	xxii
Chapter 1 - Introduction .....	1
1-1 Introduction .....	1
1-2 Objectives .....	4
1-3 Scopes .....	5
Chapter 2 - Literature Review .....	7
2-1 Introduction .....	7
2-2 Effect of Lateral Displacement/Loading Pattern on Performance of RC Members .....	7
2-2-1 Kim and Lee (2000) .....	7
2-2-2 Sfakianakis (2002) .....	8
2-2-3 Qiu et al. (2002) .....	9
2-2-4 Lejano (2007) .....	9
2-2-5 Charalampakis and Koumousis (2008) .....	10
2-2-6 Papanikolaou (2012) .....	11
2-2-7 Rodrigues et al. (2012) .....	11
2-2-8 Rodrigues et al. (2013) .....	13
2-2-9 Dutta and Kunnath (2013) .....	13
2-2-10 Bouchaboub and Samai (2013) .....	14
2-3 Effect of Axial Loading Pattern on Performance of RC Members .....	14
2-3-1 Saadeghvaziri and Foutch (1990) .....	15
2-3-2 Saadeghvaziri and Foutch (1991) .....	15
2-3-3 Papazoglou and Elnashai (1996) .....	16
2-3-4 Saadeghvaziri (1997) .....	17
2-3-5 Collier and Elnashai (2001) .....	18
2-3-6 Esmaily and Xiao (2004) .....	20
2-3-7 Esmaily and Xiao (2005) .....	21

2-3-8 Kim et al. (2011) .....	21
2-3-9 Lee and Mosalam (2013).....	22
2-3-10 Mwafy (2012).....	23
2-4 Material and Plastic Hinge Models .....	24
2-4-1 Monotonic Material Model .....	24
2-4-2 Cyclic Material Models.....	65
2-4-3 Plastic Hinge Models .....	85
Chapter 3 - Analytical Models and Algorithm .....	115
3-1 Introduction .....	115
3-1 Applied Analytical Method and Assumptions.....	117
3-2 Cross Section .....	119
3-3 Material Properties .....	121
3-4 Material Models.....	121
3-4-1 Monotonic Material Models.....	121
3-4-1 Cyclic Material Models.....	126
3-5 Analysis .....	129
3-5-1 Moment-Curvature Analysis.....	132
3-5-2 Force-Deflection Analysis.....	134
3-5-3 Axial Force-Bending Moment Interaction Curves.....	138
3-6 Validation Examples.....	141
3-6-1 Moment-Curvature Analysis .....	142
3-6-2 Force-Deflection Analysis.....	145
3-6-3 Axial Force-Bending Moment Interaction Curves.....	149
3-7 Developing New Model for Circular Concrete Column Confined by FRP and Conventional Lateral Steel.....	152
3-7-1 Proposed Stress-Strain Curve.....	154
3-7-2 Peak Stress and Strain in Confined Concrete.....	157
3-7-3 Validation .....	160
3-8 Summary.....	175
Chapter 4 - Parametric Study on Load History and Pattern.....	178
4-1 Introduction .....	178

4-2 Effect of Lateral Displacement/Loading Pattern on Performance of RC Members.....	178
4-2-1 Analytical Model.....	178
4-2-2 Validation of Analytical Model.....	183
4-2-3 Vital Consideration of Biaxial Analysis.....	192
4-3 Effect of Axial Loading Pattern on Performance of RC Members .....	209
4-3-1 Analytical Model.....	209
4-3-2 Validation of Analytical Model.....	209
4-3-3 Vital Consideration of Axial Force Variation .....	214
4-3-4 Results and Discussion.....	217
4-4 Summary.....	225
Chapter 5 - Conclusions and Recommendations .....	228
5-1 Summary.....	228
5-2 Conclusion .....	229
5-3 Recommendations .....	230
References .....	232
Appendix A - Developed Computer Application Help File .....	243

## List of Figures

Figure 2-1	Vertical-to-horizontal earthquake GPA ratio (Elanashi and Papazoglou, 1997) .....	19
Figure 2-2	Typical monotonic curve of mild steel in tension .....	26
Figure 2-3	Multilinear models: (a) bilinear or elastic-perfectly plastic model and (b) quad linear model.....	26
Figure 2-4	Monotonic stress-strain model for steel proposed by Menegotto-Pinto (1973).....	27
Figure 2-5	Proposed stress-strain model for reinforcing steel by Mander et al. (1984) .....	28
Figure 2-6	Esmaeily-Xiao (2005) monotonic stress-strain model curve of steel .....	31
Figure 2-7	Proposed stress-strain model for FRP-confined concrete (Lam and Teng (2003)) ...	43
Figure 2-8	Unification of column shapes (Wei and Wu (2012)).....	52
Figure 2-9	Monotonic stress-strain model proposed by Lee et al. for FRP steel spiral-confined concrete.....	62
Figure 2-10	Esmaeily and Xiao's cyclic model.....	70
Figure 2-11	Linear cyclic model.....	71
Figure 2-12	Park et al. model for hysteretic behavior of concrete.....	72
Figure 2-13	Kuramoto and Kabeyasawa model for hysteretic behavior of concrete .....	72
Figure 2-14	Mander et al. (1984) model for hysteretic behavior of concrete.....	73
Figure 2-15	Esmaeily-Xiao hysteretic model for concrete, descending branch .....	74
Figure 2-16	Esmaeily-Xiao hysteretic model for concrete, ascending branch .....	75
Figure 2-17	Schematic of FRP-confined envelope curve .....	81
Figure 2-18	Schematic of FRP-confined concrete cyclic model .....	83
Figure 2-19	Determination of plastic hinge length based on bending moment diagrams .....	93
Figure 2-20	Frame loading.....	96
Figure 2-21	Assumption of curvature distribution along column height.....	111
Figure 3-1	Main window of the developed window-based computer application.....	117
Figure 3-2	Composite section .....	120
Figure 3-3	Example of "custom model" for plain or confined concrete.....	123
Figure 3-4	Implemented steel stress-strain models in computer application: (a) elastic-perfectly plastic model, (b) Mander et al. model (1984), (c) Esmaeily-Xiao model (2005), and (d) Menegotto-Pinto model (1973).....	125

Figure 3-5	Implemented confined concrete cyclic models: (a) Esmaily-Xiao model, (b) linear model.....	128
Figure 3-6	Implemented steel cyclic models: (a) Esmaily-Xiao model, (b) Menegotto-Pinto model.....	129
Figure 3-7	Calculation of fiber's strain under biaxial bending.....	130
Figure 3-8	Displacement-controlled code-based moment-curvature curve.....	132
Figure 3-9	Force-controlled code-based moment-curvature curve.....	133
Figure 3-10	Curvature distributing along column height as assumed in (a) Priestley and Park and Priestley and Park revised by Xiao's methods, (b) Esmaily's first method, and (c) Esmaily's second method.....	134
Figure 3-11	Force-deflection analysis flowchart .....	137
Figure 3-12	Curvature change in Method 1 .....	139
Figure 3-13	Curvature change in Method 2.....	139
Figure 3-14	(a) Sinusoidal and (b) triangular axial force loading pattern .....	141
Figure 3-15	Geometry and reinforcement of the specimen TP-36; (a) elevation, (b) cross section .....	142
Figure 3-16	Comparison of analytical and experimental moment-curvature response curves for the hollow square cross section (TP-36).....	144
Figure 3-17	Oval cross section (TP-9).....	145
Figure 3-18	Comparison of analytical and experimental force-deflection response curves for oval section .....	146
Figure 3-19	Comparison of analytical force-deflection with experimental data for specimen PB12-N15 in (a) x-, and (b) y-direction under expanding square path .....	147
Figure 3-20	Comparison of analytical force-deflection with experimental data for specimens PB12-N16 .....	147
Figure 3-21	Failure curves for square section.....	149
Figure 3-22	Failure-surface of square section .....	150
Figure 3-23	ACI Axial force-bending moment interaction surface.....	151
Figure 3-24	ACI Axial force-bending moment interaction surface.....	151
Figure 3-25	Confining mechanism for concrete confined by FRP and lateral steel.....	159

Figure 3-26 Relationship between (a) second and (b) third term of confinement effectiveness and experimental ultimate stress.....	159
Figure 3-27 Relationship between (a) second, and (b) third term of confinement effectiveness and experimental ultimate strain.....	160
Figure 3-28 Proposed stress-strain curve for confined concrete by FRP and lateral steel .....	160
Figure 3-29 Comparison of confinement models to experimental stress-strain of S2F2 (monotonic concentric).....	161
Figure 3-30 Comparison of confinement models to experimental stress-strain of S2F3 (monotonic concentric).....	162
Figure 3-31 Comparison of confinement models to experimental stress-strain of S4F2 (monotonic concentric).....	163
Figure 3-32 Comparison of confinement models to experimental stress-strain of A3NP2C (monotonic concentric).....	164
Figure 3-33 Comparison of confinement models to experimental stress-strain of U25-2 (monotonic concentric).....	164
Figure 3-34 Predicted versus experimental ultimate strength.....	165
Figure 3-35 Predicted versus experimental ultimate strain.....	165
Figure 3-36 Fiber representation of circular section.....	167
Figure 3-37 Menegotto-Pinto monotonic and cyclic model .....	168
Figure 3-38 Analytical stress-strain of (a) TP-22 (with one layer of CFRP) and (b) TP-23 specimen (with two layers of CFRP) (monotonic concentric).....	170
Figure 3-39 Moment-curvature analysis for TP-22 (with one layer of CFRP) using (a) Lee, (b) Kawashima, (c) Youssef, (d) Samaan, and (e) proposed model for confined concrete.....	171
Figure 3-40 Moment-curvature analysis for TP-23 (with two layers of CFRP) using (a) Lee, (b) Kawashima, (c) Youssef, (d) Samaan, and (e) proposed model for confined concrete.....	172
Figure 3-41 Moment-curvature envelope of (a) specimen TP-22 (with one layer of CFRP) and (b) specimen TP-23 (with two layers of CFRP) .....	174
Figure 4-1 Fiber representation of a square cross section.....	179
Figure 4-2 Monotonic and hysteretic stress-strain relation of (a) plain and (b) confined concrete fibers .....	181
Figure 4-3 Uniaxial monotonic stress-strain models for longitudinal steel.....	181

Figure 4-4 Geometry and reinforcement details of specimen TP-21: (a) elevation, (b) cross section .....	183
Figure 4-5 Fiber representation of TP-21 .....	185
Figure 4-6 Comparison of analytical uniaxial moment-curvature with experimental data for specimen TP-21 .....	185
Figure 4-7 (a) Computational error and (b) computational time using six maximum fiber areas .....	186
Figure 4-8 Curvature distribution along column height as assumed in (a) Priestley and Park method (1987) and (b) Esmaeily-Xiao second method (2002).....	186
Figure 4-9 Geometry and reinforcement details of specimens PB01-N13, PB12-N15, and PB12-N16: (a) elevation, (b) cross section .....	187
Figure 4-10 (a) Expanding square and (b) expanding circular displacement path .....	189
Figure 4-11 Comparison of analytical force-deflection with experimental data for specimens PB01-N13 .....	189
Figure 4-12 Comparison of analytical force-deflection with experimental data (2012) for specimens PB12-N15 under expanding square path in (a) x- and (b) y-directions .....	191
Figure 4-13 Comparison of analytical force-deflection with experimental data (2012) for specimens PB12-N16 under expanding circular path in (a) x- and (b) y-directions .....	191
Figure 4-14 Curvature paths .....	193
Figure 4-15 Moment-curvature analysis of TP-21 along (a) x-axis and (b) y-axis under zero-axial force considering various curvature paths.....	194
Figure 4-16 Moment-curvature analysis of TP-21 along (a) x-axis and (b) y-axis under axial force equal to 5% analytical axial capacity of the section considering various curvature paths	194
Figure 4-17 Moment-curvature analysis of TP-21 along (a) x-axis and (b) y-axis under axial force equal to 10% of analytical axial capacity of the section considering various curvature paths .....	195
Figure 4-18 Moment-curvature analysis of TP-21 along (a) x-axis and (b) y-axis under axial force equal to 15% of analytical axial capacity of the section considering various curvature paths .....	196



Figure 4-19 Moment-curvature analysis of TP-21 along (a) x-axis and (b) y-axis under axial force equal to 20% of analytical axial capacity of the section considering various curvature paths .....	196
Figure 4-20 Force-deflection analysis of column PB01-N13 under uniaxial hysteretic lateral displacement and (a) zero axial force, (b) 5% axial force, (c) 10% axial force, (d) 15% axial force, and (e) 20% axial force.....	198
Figure 4-21 Force-deflection analysis of column PB12-N15 under expanding square displacement path and (a) zero axial force, (b) 5% axial force, and (c) 10% axial force .....	199
Figure 4-22 Force-deflection analysis of column PB12-N15 under expanding square displacement path and (a) 15% axial force and (b) 20% axial force .....	200
Figure 4-23 Force-deflection analysis of column PB12-N16 under expanding circular displacement path and (a) zero axial force, (b) 5% axial force, and (c) 10% axial force .....	201
Figure 4-24 Force-deflection analysis of column PB12-N16 under expanding circular displacement path and (a) 15% axial force and (b) 20% axial force .....	202
Figure 4-25 Force-deflection peak envelopes analysis of column PB12 under various levels of axial force and (a) uniaxial lateral displacement, (b) circular expanding lateral displacement path, and (c) square expanding lateral displacement path .....	204
Figure 4-26 Dissipated energy in reversed cyclic loading.....	205
Figure 4-27 Individual cycle energy dissipation for PB01-N13 under uniaxial lateral displacement and various axial force levels.....	205
Figure 4-28 Individual cycle energy dissipation for PB12-N15 under expanding square displacement path and various axial force levels.....	206
Figure 4-29 Individual cycle energy dissipation for PB12-N16 under expanding circular displacement path and various axial force levels.....	206
Figure 4-30 Comparison of cumulative dissipated energy for column PB01-N13 under uniaxial lateral displacement and various axial force levels.....	207
Figure 4-31 Comparison of cumulative dissipated energy for column PB12-N15 under expanding square displacement path and various axial force levels.....	208
Figure 4-32 Comparison of cumulative dissipated energy for column PB12-N16 under expanding square displacement path and various axial force levels.....	208

Figure 4-33	Geometry and reinforcement details of specimens TP-31 and TP-33: (a) elevation, (b) cross section .....	210
Figure 4-34	(a) Displacement and (b) axial load cycles for specimen TP-31 .....	211
Figure 4-35	(a) Displacement and (b) axial load cycles for specimen TP-33 .....	211
Figure 4-36	Moment-curvature analysis for specimen TP-31 .....	212
Figure 4-37	Moment-curvature analysis for specimen TP-33 .....	213
Figure 4-38	Force-deflection analysis for specimen TP-31 .....	213
Figure 4-39	Force-deflection analysis for specimen TP-33 .....	214
Figure 4-40	Axial loading pattern with $n$ triangular cycles .....	215
Figure 4-41	Axial loading pattern with (a) one cycle, (b) three cycles, (c) five cycles, (d) 10 cycles, and (e) 15 cycles .....	216
Figure 4-42	Axial force-bending moment interaction curves of the square section with $\rho_s = 0.89\%$ , considering various axial loading patterns .....	217
Figure 4-43	Axial force-bending moment interaction curves of the square section with $\rho_s = 1.58\%$ , considering various axial loading patterns .....	218
Figure 4-44	Axial force-bending moment interaction curves of the square section with $\rho_s = 2.47\%$ , considering various axial loading patterns .....	219
Figure 4-45	Axial force-bending moment interaction curves of the square section with $\rho_s = 3.56\%$ , considering various axial loading patterns .....	220
Figure 4-46	Axial force-bending moment interaction curves of the square section with $\rho_s = 3.56\%$ , considering various axial loading patterns .....	220
Figure 4-47	Axial force-bending moment interaction curves of the square section with $\rho_s = 6.33\%$ , considering various axial loading patterns .....	221
Figure 4-48	Axial force-bending moment interaction curves of the square section with $\rho_s = 8.05\%$ , considering various axial loading patterns .....	221
Figure 4-49	ACI bending moment overestimation of the square section with $\rho_s = 0.89\%$ .....	222
Figure 4-50	ACI bending moment overestimation of the square section with $\rho_s = 1.58\%$ .....	222
Figure 4-51	ACI bending moment overestimation of the square section with $\rho_s = 2.47\%$ .....	223
Figure 4-52	ACI bending moment overestimation of the square section with $\rho_s = 3.56\%$ .....	223
Figure 4-53	ACI bending moment overestimation of the square section with $\rho_s = 4.85\%$ .....	224

Figure 4-54	ACI bending moment overestimation of the square section with $\rho_s = 6.33\%$ .....	224
Figure 4-55	ACI bending moment overestimation of the square section with $\rho_s = 8.05\%$ .....	225
Figure A-1	Units tab in Options widow.....	250
Figure A-2	Data Points tab in Options window.....	251
Figure A-3	Analysis setting tab in Options window.....	252
Figure A-4	Mesh setting tab in Options window.....	252
Figure A-5	A sample window of RC-Section.....	253
Figure A-6	A sample window of material properties .....	254
Figure A-7	A sample window of monotonic material models.....	254
Figure A-8	A sample window of cyclic material models .....	255
Figure A-9	A sample window of project choosing axial force-bending moment interaction ..	255
Figure A-10	A sample window of axial force-bending moment interaction analysis .....	256
Figure A-11	A sample window of axial force-bending moment interaction analysis results...	257
Figure A-12	A sample window of project choosing the second type of moment-curvature analysis.....	258
Figure A-13	A sample window of moment-curvature analysis .....	258
Figure A-14	A sample window of moment-curvature analysis results.....	259
Figure A-15	A sample window of force-deflection analysis .....	260
Figure A-16	A sample window of force-deflection analysis .....	260

## List of Tables

Table 2-1 Numerical constants of Eqs. (3-189) to (3-192) (Riva et al. (1990)) .....	89
Table 3-1 Implemented plastic hinge methods in the computer application .....	135
Table 3-3-2 Geometrical and mechanical properties of specimens .....	156
Table 3-3 Geometrical and mechanical properties of TP-22 and TP-23 (Kawashima et al. 2001) .....	167
Table 4-1 Flexural capacity reduction of TP-21 under various curvature path and axial force level.....	197
Table 4-2 Flexural strength reduction of TP-21 at point with curvature $0.15741/m$ along the x- axis and zero curvature along the y-axis under various levels of axial force (compared to the straight path to this point) .....	197

## **Acknowledgements**

I would like to gratefully thank Dr. Asad Esmaeily, my advisor, for his guidance, support and help during my PhD studies at Kansas State University (KSU). Gratitude is also extended to the members of the supervisory committee: Dr. Sanjoy Das, Dr. Vinod Kumarappan, Dr. Hani Melhem, and Dr. Kyle Riding.

I would like to thank the members of the Department of Civil Engineering at KSU, including faculty, staff and students. In particular, I would like to thank Marta Miletić, my officemate and more than that my best friend, for being by my side during the last three years. Marta, you are the best thing happened to me at KSU. I will not forget all the happy moments that we had together in the office 2137 of Fiedler Hall.

I would like to express my deepest gratitude to my friend, Behnam Tavakkol. He was always there cheering me up and stood by me through the good times and bad times. Finally, and most importantly, I would like to thank my family specially my mother and father for their faith in me and allowing me to be as ambitious as I wanted. Your support, encouragement and love helped me to get to another achievement in my life.

## **Dedication**

This work is dedicated to my parents, Rasoul Shirmohammadi and Rezvan Shirzadi,  
and my siblings, Fariba and Mohammad Reza.

You Mean the World to Me.

# **Chapter 1 - Introduction**

## **1-1 Introduction**

Experimental and analytical studies have shown significant effects of material models, including monotonic and cyclic (hysteresis) rules, assumption on curvature distribution along a structural member, loading pattern, and the analytical strength evaluation procedure, on performance assessment accuracy of reinforced concrete (RC) columns. A primary research, sponsored by KDOT was conducted as the initial step of the present study (No. K-TRAN: KSU-11-5). A conclusion was drawn that there is a need for conducting more studies on the realistic performance of Reinforced Concrete (RC) sections and columns. The studies should have included performance of RC members under various loading scenarios, assessment of columns capacity considering confinement effect provided by lateral reinforcement, and investigation on performance of various monotonic and cyclic material models applied to simulate the realistic performance.

RC member response under various loading scenarios is a research area that has not been sufficiently addressed compared to more traditional areas in civil engineering. Loading history, pattern, intensity, and linear combination of loads, specifically lateral and axial loads in a column, can significantly affect RC members' behavior. The loading pattern of combined axial load and lateral force affects flexural and shear strength, ductility, stiffness, and energy dissipation of RC members. When exposed to dynamic excitation of any source, such as wind or earthquake, columns are subjected to a loading pattern in combined but non-proportional in lateral and axial directions, especially in earthquake excitations in near-fault regions with high accelerations of vertical and horizontal ground motions, large velocity pulses, directional effects, repetitive pulse effects, and aftershocks.

A majority of experimental research related to various parameters that affect RC member behavior has been limited to monotonic or cyclic lateral displacement (force) on columns under no or constant axial load (Jiang and Saiidi 1990, Jaradat et al. 1998, Kowalsky et al. 1999, Ridrigues et al. 2013). In an early works, the importance of concurrent amounts of axial load and bending moment was emphasized for dynamic analysis of coupled shear walls (Saatcioglu et al. 1983). A limited number of researchers, such as Gilbertsen and Moehle (1980) and Abrams (1987), considered axial load variation in RC column behavior. Abrams investigated the influence of proportionally variable axial force on flexural behavior of RC columns. He recommended additional analytical and experimental studies for a good understanding of the influence of these variations on flexural behavior of RC columns. Kreger and Linbeck (1986) considered uncoupled variations of axial and lateral force by experimentally testing a single column. They demonstrated that column behavior depends strongly on axial force history. Sadeghvaziri and Foutch (1991) analytically studied RC column behavior under nonproportionally varying axial load. They argued that “*non-proportional variations in axial load are not just another parameter that can be considered within the framework of current approaches, but that its effects are so significant that new methodology and models are needed to assess the inelastic cyclic response of RC columns under uncoupled fluctuations in axial and lateral loads.*” They concluded that axial load history significantly affects moment-curvature and axial load-flexural moment interaction curve (Saadeghvaziri 1996).

Ono et al. (1996) observed a strange failure mode in their experimental studies which they concluded may have been caused by vertical motion. Alaghebandian et al. (1998) concluded that fluctuation in axial force can cause failure, especially in low-rise buildings and interior columns. Elanashai utilized inelastic analysis of RC columns and reached the same conclusion as



Alaghebandian et al. (Papazoglou and Elnashai 1996; Ghobarah and Elnashai 1998). Ranzo et al. (1999) conducted nonlinear time-history analysis on columns and discovered that seismic codes must provide special recommendation in order to consider fluctuation in axial force due to vertical acceleration of ground motions.

During an earthquake, the majority of buildings are subjected to biaxial lateral earthquake motion in addition to vertical component of earthquake. Biaxial motion is induced in columns of an irregular building even against one-directional earthquake motions. Experimental studies and investigations of damaged structures after earthquakes have proven that damage caused by bi-directional earthquake motions is different and, in most cases, more extensive than damages caused by uniaxial earthquake motions. When cyclic seismic loading in one direction is strong enough to push a RC section into its nonlinear range, it consequently affects stiffness in that direction and the perpendicular direction. The coupling effect of two directions significantly reduces overall seismic strength of the column in some cases.

Since all methods related to seismic strength assessment of structures are based on uniaxial experimental data, in recent years researchers have investigated methods to address the biaxial effect of dynamic excitations such as earthquakes. Many experimental and analytical studies have been conducted to investigate column behavior under biaxial cyclic loading. Most analytical investigations utilize finite element modeling software such as Abaqus. Unfortunately, available commercial software, such as Abaqus or OpenSees, are not the first choice of design firms interested in assessing the real performance of existing or new RC structural members, though, because the learning curves for these applications are very steep. However, this assessment is critically important for existing structural members in relation to decisions to retrofit or replace those members.

Experimental works conducted on concrete columns under axial forces and cyclic biaxial lateral loading are presented in Qiu et al. (2002), Hsu et al. (2009), Chang (2010), Rodrigues et al. (2012a), Rodrigues et al. (2012b), and Wang et al. (2013). In addition, analytical researches, such as Sfakianakis (2002), Bonet et al. (2006), Charalampakis and Koumousis (2008), Pallares et al. (2009), and Fossetti and Papia (2012), have studied the effect of axial force and biaxial bending on composite section behavior as behavior relates to axial force and biaxial bending moment interaction. Researchers also have attempted to model cyclic behavior of composite columns under axial force and biaxial lateral forces (Lee et al. (2005), Liang (2008), and Liang (2009))

## **1-2 Objectives**

The primary objective of this research is to model and assess the behavior of concrete columns under various cyclic and monotonic loading scenarios. To achieve this goal, the following tasks must be completed:

- 1.** Evaluate the performance of concrete columns confined by conventional lateral steel or FRP under biaxial displacement paths and fluctuating axial force, benchmarked against experimental data.
- 2.** Evaluate the performance of RC columns in concrete structures located in near-fault regions.
- 3.** Assess various material monotonic models and cyclic rules for confined concrete, unconfined concrete, Fiber Reinforced Polymer (FRP), and steel by extensively studying and improving existing models or developing new models.

Develop a new model for concrete confined by FRP and steel tie/spiral.

4. Develop a new constitutive model for concrete confined by FRP and lateral steel (tie/spiral), or FRP and lateral steel.
5. Assess and improve existing plastic hinge models or develop a new model if necessary.
6. Develop window-based software to model the performance of concrete columns under various monotonic and cyclic loading scenarios in uniaxial and biaxial directions with a smooth learning curve and user-friendly interface.

### **1-3 Scopes**

This dissertation includes five chapters and an appendix that detail the performance of RC structural members with various material types and arrangements under various loading scenarios.

- Chapter 1 introduces the goals of this study and contents of the chapters.
- Chapter 2 reviews the literature through three subjects: (1) effect of lateral displacement/loading pattern on performance of RC column; (2) effect of axial loading pattern on performance of RC column; and (3) material (steel, plain concrete, confined concrete by lateral steel, FRP wrap, and both lateral steel and FRP wrap) and plastic hinge models.
- Chapter 3 introduces the analytical algorithm, material and plastic hinge models which were used in this study. In addition, a constitutive stress-strain relationship for FRP-steel-confined concrete is presented. Performance of the proposed stress-strain model is assessed through experimental data and analytical analyzes.
- Chapter 4 presents parametric studies conducted to investigate the effect of loading pattern, including lateral and axial, on performance of RC columns.

- Chapter 5 presents summary, conclusion and recommendations.
- Appendix A presents a help file for the developed computer application.

## **Chapter 2 - Literature Review**

### **2-1 Introduction**

This chapter reviews literature in three different topics; effect of lateral displacement/loading pattern on performance of RC columns, effect of axial loading pattern on performance of RC columns and material (monotonic and cyclic) and plastic hinge models.

### **2-2 Effect of Lateral Displacement/Loading Pattern on Performance of RC Members**

A comprehensive review of studies about effect of lateral displacement/loading pattern is presented, chronologically, as follows.

#### **2-2-1 Kim and Lee (2000)**

Failure of brittle material such as concrete demonstrates two major mechanisms: (a) uncracked condition and (b) cracked condition. In the uncracked condition, applied axial force and bending moment do not have any coupling effect. However, in the cracked condition, the axial force may affect curvature about the bending axis and the bending moment may influence the axial strain. The axial force and bending about the other principal axis may affect the curvature about each principal axis when the section is under axial force and bidirectional bending moment and stress is beyond the elastic range.

Kim and Lee proposed a numerical model to assess behavior of RC columns under axial and biaxial bending moments. To demonstrate validity of analytical results, they conducted a set of experimental tests in which they tested a total of 16 tied RC columns with square and rectangular cross section. Eccentricity of the axial load for all tests was 40 mm. The angle

between the principal axis and direction of eccentricity was 0, 30, and 45 for columns with square cross section and 0, 30, 45, 60, and 90 for columns with rectangular cross section.

Fafitis and Shah's (1985) model and Vebo and Ghali's (1977) stress-strain model were used to model behavior for concrete in compression and tension, respectively, in conjunction with Ottor and Naaman's (1989) cyclic stress-strain model. Stress-strain behavior of reinforcing steel bars was simulated using elastic-perfectly plastic model in conjunction with a linear cyclic model with slope equal to modulus elasticity of the steel material. Analytical results were in good agreement with experimental data. Comparisons between moment magnification factor (using the moment magnification factor to consider the slenderness effect of columns) predicted by the proposed numerical method and the American Concrete Institute (ACI) method revealed that the ACI moment magnification factor was conservative.

### **2-2-2 Sfakianakis (2002)**

Sfakianakis used an alternative fiber model with computer graphics as a computational tool to calculate stress integration. The developed model was employed to analyze conventional reinforced concrete section as well as members repaired by jacketing and steel-concrete composite sections under bidirectional bending and axial force. Due to using no iteration, Sfakianakis' method has the benefit of convergence in all cases. In order to prove the validity and functionalities of the developed method, four representative numerical examples were discussed in his work. The following assumptions were included in the proposed method: (1) Based on Bernoulli-Euler assumption, plane sections remain plane after deformation, (2) Elastic-perfectly plastic stress-strain model is used to predict steel bar behavior, (3) Tensile strength of concrete is neglected, and (4) Monotonic behavior of concrete is modeled using a stress-strain

model proposed by Tassios (1988) with parabolic initial ascending branch up to the concrete strength, followed by a descending linear branch.

### **2-2-3 Qiu et al. (2002)**

The coupling effect of two principal directions significantly decreases seismic resistance of structures. Therefore, assessment of RC column behavior under biaxial loading is a primary subject of current studies of RC structures. In order to investigate behavior of RC columns under biaxial loading, Qiu et al. (2002) conducted an experimental study that included biaxial quasi-static loading of seven RC columns. The strength and stiffness degradation, hysteretic energy dissipation, and damage index of the seven columns were analyzed considering six loading paths. According to test results, the conclusion was made that the column's capacity under biaxial bending differed significantly from the capacity of the column under uniaxial loading. Accumulative energy dissipation of the column under biaxial bending was significantly higher than the column under uniaxial loading. In addition, the plastic deformation capability of the column under biaxial loading was much lower than the plastic deformation under uniaxial loading.

### **2-2-4 Lejano (2007)**

Most RC sections design charts apply to unidirectional bending of RC sections. Utilization of Bresler's (1960) Load Contour Method and Reciprocal Load Method allows design charts to be used for bidirectional bending of RC columns. Lejano (2007) used a fiber model to predict biaxial behavior of an RC section and to develop design charts for bidirectional bending. In this fiber method, Bazant's Endochronic (1980) theory and Ciampi's model (1982) were

used to simulate the behavior of concrete and steel fibers, respectively. However, this study was limited to biaxial analysis of a square cross section with uniform and symmetrical reinforcement distribution and the effect of slenderness was ignored.

### **2-2-5 Charalampakis and Koumouis (2008)**

Charalampakis and Koumouis developed a generic fiber model algorithm to analyze an RC section under biaxial bending and axial load. The developed fiber model can be used for any arbitrary composite section. In their study, a prismatic beam with arbitrary cross section was assumed, following the Bernoulli-Euler assumption in which the plane section remains plane and perpendicular to the longitudinal axis of the beam. Using developed fiber model, Charalampakis and Koumouis addressed the following problems in their study: (1) construction of moment-curvature diagram, (2) construction of interaction curves and failure surface, and (3) determination of the deformed cross section after loading.

Failure of a three-dimensional (3D) surface of a section can be produce using four techniques: (1) conducting interaction curves with the bending moment ratio, (2) conducting load contours with the level of axial force, (3) calculating stress resultant extending along an arbitrary oriented straight line, and (4) conducting a chart of isogonic 3D curves, as used in Charalampakis and Koumouis's developed model. The stress-strain law of materials of a section can be defined using any number and any combination of linear and cubic polynomial segments in Charalampakis and Koumouis's developed fiber model. Charalampakis and Koumouis compared the calculated results of the developed fiber model were compared to results calculated by Chen et al. (2001) for an arbitrary shape cross section with a circular hole.



### **2-2-6 Papanikolaou (2012)**

Papanikolaou developed a methodology to calculate the ultimate strength and moment-curvature response of an arbitrary composite section under biaxial bending and axial load. Using the presented methodology and arbitrary material laws, any composite section with unlimited number of components and unconditionally shape complexity can be analyzed.

Papanikolaou categorized stress integration schemes into three main categories: (1) fiber integration, (2) analytical integration using closed form functions, and (3) numerical integration in a form of Gaussian sampling on a Green path integral. The third scheme was used in Papanikolaou's study due to lack of efficiency in the first two schemes. Application and validity of the presented methodology were proven through moment-curvature analysis and interaction curves of five composite sections, including the well-known composite section reported by Chen et al. (2001).

### **2-2-7 Rodrigues et al. (2012)**

In order to assess the behavior of RC columns under biaxial bending, Rodrigues et al. conducted an experimental study that included four types of full-scale quadrangular columns. A total of 24 columns were tested under constant axial force and displacement controlled condition. Six displacement paths were considered in their study, including uniaxial loading path about the weak and strong axes of the section, quadrangular, expanding square, expanding circular and expanding rhombus displacement paths. Three cycles were repeated in each level of displacement. The global behavior of these RC columns and their energy dissipation and damping capacity were discussed in their studies.

Rodrigues et al. defined four branches in the force-deflection response of an RC column: (1) pre-cracking response, (2) post-cracking response until the reinforcing steel yields, (3) post-yield hardening zone, and (4) a softening phase. According to experimental results, biaxial loading did not affect initial stiffness of the RC columns. Strength degradation in biaxial loading was higher than the strength degradation in uniaxial loading, and ultimate ductility decreased in columns under biaxial loading.

Rodrigues et al. studied the cumulative energy dissipation and individual cycle energy for all tested columns. They concluded that biaxial cumulative energy dissipation was significantly higher than uniaxial cumulative energy dissipation, but the summation of cumulative energy dissipation about two principal axes was similar to the biaxial summation of cumulative energy dissipation. The expanding circular path had maximum dissipated energy between applied displacement paths and the quadrangular path had the least dissipated energy. Energy dissipated of quadrangular path was less than the summation of dissipated energy about two principal axes. In addition to the column's geometry, the axial load level and number of cycle repetition affected total energy dissipation.

According to experimental results, the displacement path significantly affected equivalent viscous damping of the RC columns; however, the number of repetitive cycles did not affect viscous damping. The quadrangular displacement path demonstrated the highest viscous damping. Proposed expressions in literature for estimating viscous damping of RC structures were validated against experimental data, and two simplified expressions were proposed to calculate equivalent viscous damping of RC column under biaxial bending.

### **2-2-8 Rodrigues et al. (2013)**

Yield displacement differentiates behavior of an RC column in elastic and plastic regimes, and various techniques in the literature have been proposed to calculate yield displacement/curvature. In order to calculate yield displacement, Rodrigues et al. adopted the procedure originally proposed by Park (1989) to be used in conjunction with the complete cyclic response of the column.

According to experimental results achieved from a series of 24 columns under biaxial and uniaxial cyclic loading, Rodrigues et al. concluded that: (1) Biaxial loading decreases maximum strength of columns approximately 8% and 20% in the strong and weak direction of the columns, respectively. However, biaxial loading does not affect initial stiffness. (2) Ultimate ductility of a column under biaxial loading is significantly less than ultimate ductility of the column under uniaxial loading. (3) Strength degradation is more pronounced in biaxial loading than uniaxial loading. (4) Biaxial loading does not significantly affect stiffness degradation.

Finally, displacement-based performance limits were calculated using experimental data and Part 3 of Eurocode (EC) 8 that accurately predicted drift demand of columns under uniaxial loading compared to experimental results.

### **2-2-9 Dutta and Kunnath (2013)**

Based on modern seismic design codes, structures should undergo elastic behavior under minor earthquake and damage controlled avoiding collapse under severe earthquakes. However, this design philosophy is only related to service ability and ultimate limit states. Many experimental and analytical studies have been conducted to evaluate accurate seismic demands for performance-based design. However, a majority of these studies considered seismic motion

only in one principal direction. In the few studies that considered seismic motion in two perpendicular principal directions, intensity of applied ground motion in one direction was small compared to the other direction. In order to increase research of ground motion with similar intensity in both principal directions, Dutta and Kunnath assessed story drift of single-story and multi-story idealized systems under uniaxial and biaxial seismic motions. They proposed a simple and reasonably accurate hysteretic model that considered 20 far-fault ground motions. Based on results, they concluded that biaxial interaction may lead to increased drift demand. However, because they used a lumped nonlinear model, calculated results may be slightly overestimated. The period of single-story system increased under biaxial interaction, but the same trend was not demonstrated in the multi-story system.

#### **2-2-10 Bouchaboub and Samai (2013)**

Bouchaboub and Samai used finite difference method to calculate the capacity of a slender, high-strength RC column. The column in their study was subjected to bidirectional bending and axial force, and the stress-strain model in the Federation International de la Precontrainte (FIB) textbook was used to simulate behavior of concrete in compression. Tensile strength of concrete was ignored. Steel behavior was assumed to be elastic-perfectly plastic. The developed analytical method was validated by comparing calculated results and experimental data for tests conducted by Olivier Germain and Espion (2005) and Pallares et al. (2000).

### **2-3 Effect of Axial Loading Pattern on Performance of RC Members**

In this section a comprehensive review of studies about effect of axial loading pattern or in other words fluctuating axial force is presented, chronologically, as follows.

### **2-3-1 Saadeghvaziri and Foutch (1990)**

Sadeghvaziri and Foutch were the first researchers to conduct analytical studies of RC columns under non-proportional axial load and lateral force. The behavior of RC column under lateral force and non-proportional axial loading was simulated using FEM. Based on analytical results, Saadeghvaziri and Foutch concluded that non-proportional axial loading and lateral force can cause an abnormal phenomena called “negative energy” in RC columns and that hysteretic force-deflection curves are not of the Masing type. Negative energy was explained by Saadeghvaziri and Foutch in light of axial deformation. The effect of phasing in applied axial loading was also investigated; calculated results showed that hysteretic loops did not follow a unique pattern as a result of phasing.

### **2-3-2 Saadeghvaziri and Foutch (1991)**

As discussed by Saadeghvaziri and Foutch, considering the maximum vertical acceleration less than horizontal one is the lack of provisions in the seismic design of the RC structures including buildings and bridges. Based on information gathered by Saadeghvaziri and Foutch, reports of some earthquakes indicated that the vertical acceleration of an earthquake is large and the vertical acceleration can exceed the amount of the horizontal acceleration. In order to assess the effect of seismic motion’s vertical component on behavior of highway bridges, Saadeghvaziri and Foutch modeled bridge column and deck behavior using a 3-nodes element and a set of beam elements, respectively. The developed analytical model was employed to analyze several bridges under two major cases: considering horizontal motion and considering uncoupled horizontal and vertical motions. Based on analytical results, Saadeghvaziri and Foutch

concluded that hysteretic moment-curvature loops are unstable and asymmetric. Increased applied compressive axial force caused the moment and shear in the column to increase, consequently increasing the failure possibility in the column, foundation, and abutments. However, increasing tensile axial force reduced the shear and the moment of the column, possibly increasing the failure possibility of the column in shear. Saadeghvaziri and Foutch listed other undesirable effects such as greater damage in plastic hinge or transition zone, increased ductility demand, cracking of the entire cross section of RC column, possibility of buckling and pullout of reinforcing steel bars, and increased load carried by the abutments. The effects of variable and uncoupled axial and lateral forces were studied in the foundation, abutment, and connections of bridges in Saadeghvaziri and Foutch studies. Detailed results for these portions of bridges are presented in Saadeghvaziri and Foutch (1991).

### **2-3-3 Papazoglou and Elnashai (1996)**

Papazoglou and Elnashai collected field evidence from three earthquakes in addition to results from dynamic analysis considering vertical ground motion. They believed that results of previous strong earthquakes underestimated the ratio of vertical-to-horizontal peak acceleration for near-fault regions. Moreover, fluctuation of axial force was believed to potentially cause the shear and flexural failure. They categorized all evidence into two main categories: field evidence and analytical evidence. Both categories included evidence from the buildings and bridges.

Based on field evidence, the vertical component of an earthquake influences shear capacity of RC members (columns and shear wall) and creates the likely possibility of compressive failure in vertical elements such as columns and walls. The vertical component of an earthquake causes a uniform increase in the axial force of all columns of a story, considering a

uniform distribution of axial stiffness. Because overturning effect does not significantly affect interior column design, these columns are more vulnerable to compressive failure, such as interior columns in the 3-story parking building located at California State University, Long Beach, California. The buildings appear to be stiffer in vertical direction than horizontal direction; therefore, their vertical period is shorter than the horizontal period. The vertical period is not influenced greatly by lateral stiffness and building height. In the other words, during vertical motion, a wide varieties of buildings experience identical dynamic amplification.

After providing various field evidences and analytical studies, Papazoglou and Elnashai concluded that failure modes occur which cannot be explained properly considering only shear and flexural capacities. They asserted that, in such failures, the effect of axial overstressing provides more reasonable justification for observed damages. They also stated that, in addition to compressive overstressing failure, the vertical component of an earthquake may cause shear and flexural failure. The contribution of concrete in shear reduces when the section is under reduced compression or mild tension.

#### **2-3-4 Saadeghvaziri (1997)**

Sadeghvaziri categorized variation of axial load with respect to lateral force/displacement into two main categories: proportional and non-proportional. In the proportional category, the axial load and lateral force/displacement reach their extreme values at the same time and they are applied simultaneously. In the second category, axial load and lateral force/displacement are uncoupled. The axial force-moment diagram was calculated with and without considering the loading history. The flexural capacity of the section considering loading history in some level of axial load was significantly less than the value calculated without considering loading history.

Therefore, Saadeghvaziri suggested use of composite columns such as concrete-filled steel tubular columns because uniform distribution of the reinforcement causes the effect of varying axial load to be less pronounced. Otherwise, code-based axial force-moment diagrams should be modified considering the worst case of the non-proportional axial load and lateral force. Using an analytical model, a cantilever column was analyzed under proportional and non-proportional varying axial load. Comparison of obtained results from these two cases showed that ductility demand of the column increased significantly by considering non-proportional varying axial loading.

### **2-3-5 Collier and Elnashai (2001)**

Many design codes suggest use of a scaled spectral shape, originally derived for the horizontal component of an earthquake to take care of the vertical component, meaning that these design codes considered frequency contents of vertical and horizontal motions to be identical, which is incorrect. Although S-waves cause horizontal motions, the vertical component of an earthquake is associated with P-waves that have higher frequencies than S-waves. Because of this lack of design codes, Collier and Elnashai developed a new procedure to calculate the elastic and inelastic vertical vibration period considering vertical and horizontal motions. The proposed procedure requires an engineering seismology and site-specific study. Using records of past earthquakes, they concluded that the time interval between peak horizontal and peak vertical accelerations increased when the distance from the earthquake source increased. The time interval was influenced by earthquake magnitude, and for distances less than 5 km, peak vertical and peak horizontal acceleration could occur coincidentally. Utilization of a graph originally developed by Elnashai and Papazoglou (1997) and knowledge regarding horizontal



acceleration, distance, and magnitude from the earthquake source, allow vertical acceleration to be specified. Vertical accelerations also can be calculated using the equation proposed originally by Ambraseys and Simpsons (1996):

$$\text{Log}(a_v) = -1.74 + 0.273 \times M_s - 0.954 \times \log(r) + 0.076 \times S_A + 0.058 \times S_S \quad (2-1)$$

where  $M_s$  is earthquake magnitude and  $r^2 = d^2 + 4.7^2$  and  $d$  is distance from the earthquake source. Parameters  $S_A$  and  $S_S$  depend on the soil type: For rock, the parameters are equal to 0; for stiff soil,  $S_A$  is 1.0 and  $S_S$  is 0; for soft soil,  $S_A$  is 0 and  $S_S$  is 1.0.

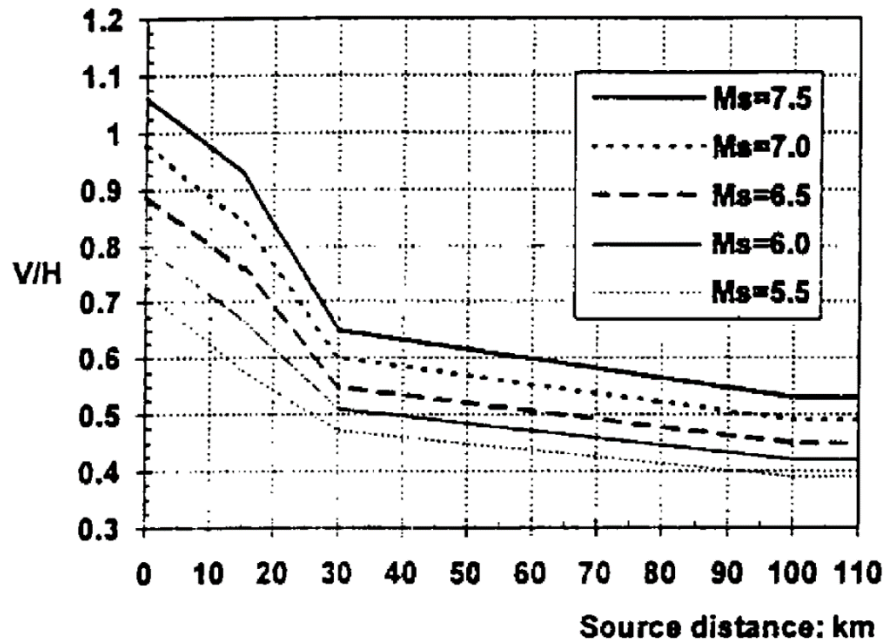


Figure 2-1 Vertical-to-horizontal earthquake GPA ratio (Elanashi and Papazoglou, 1997)

Collier and Elnashai recommended a method for calculating force caused by the vertical component of an earthquake using the vertical period and a vertical response spectrum. Based on

the observed interaction, a procedure was proposed for the combination of forces due to vertical and horizontal components of the earthquake.

### **2-3-6 Esmaeily and Xiao (2004)**

Because of overturning moment effect, columns in tall buildings and multi-column bent bridges are subjected to axial force proportional to lateral force under seismic or wind loading. However, when the tall building or bridges are located in near-fault regions, axial force acts proportional to lateral horizontal loading. Most studies conducted to assess the effect of seismic loading of structural columns have used constant level of axial force or axial force proportional to lateral loading despite considering complicated lateral loading patterns. In order to perform more studies on seismic behavior of columns under non-proportional axial force and lateral loading, Esmaeily and Xiao conducted a set of experimental tests in which they tested six large-scale RC columns with circular cross section under constant and variable axial force and cyclic and monotonic lateral loading. Based on recorded force-deflection and calculated moment-curvature responses, they concluded that peak flexural strength and displacement capacity of columns under constant level of axial force and cyclic lateral loading is similar to the flexural strength and displacement capacity for monotonic pushover loading case. However, flexural strength and displacement capacity of columns under variable axial force with identical maximum and minimum values were completely different. In addition, the variation pattern of axial force significantly affected column responses.

### **2-3-7 Esmaeily and Xiao (2005)**

In a companion paper, Esmaeily and Xiao (2005) simulated the behavior of RC columns under variable axial force using a fiber-based model, and they modeled the monotonic behavior of steel using their own proposed stress-strain model. Esmaeily and Xiao also developed a multilinear model, explained in detail in Chapter 4, to simulate cyclic behavior of steel bars. Stress-strain behavior of concrete fibers was modeled using a parabolic function in conjunction with the nonlinear cyclic model proposed by Esmaeily and Xiao. Using rectangular fibers and plastic hinge concept, force-deflection analysis of the circular section was modeled and compared to experimental data. Analytical results were in good agreement with experimental data.

### **2-3-8 Kim et al. (2011)**

Kim et al. emphasized the importance of vertical peak acceleration and that vertical-to-horizontal (V/H) acceleration ratio may exceed the value of two-thirds, as recommended by design codes. In order to investigate the effect of the vertical component of an earthquake, Kim et al. studied the effect of V/H peak ground acceleration and the time interval between arrivals of those peaks. During an earthquake, the vertical component of ground motions is caused by P-waves, and S-waves cause horizontal ground movement. P-waves' wavelength is shorter than S-waves' wavelength, or, in the other words the frequency content of P-waves is higher than S-waves. Although energy content over the frequency range of P-waves is less than the S-waves, the large amount of energy is concentrated in a narrow frequency range, causing large amplifications in a short time. Kim et al. utilized the Pacific Earthquake Engineering Research next-generation attenuation project database and other observations from the literature in order to

considered V/H ratio limited to 2.0 and time interval limited to 5s in their analytical study. They analyzed two bridges (Santa Monica Bridge and the Concept Design Example No. 4 of the Federal Administration [FHWA] designed based on AASHTO 1995) under earthquake ground motion of five near-source stations. These earthquake records had a vertical GPA greater than 0.3 and V/H ratio greater than 0.6. Using obtained analytical results, they concluded that increasing the variation of axial force caused by the vertical component of an earthquake can decrease shear capacity up to 30%. They also concluded that arrival time only minimally affects variation of axial force and consequently shear demand; in contrast, the arrival time interval has a significant effect on shear capacity. They also added that no clear correlation between the time lag and vibration period was observed.

### **2-3-9 Lee and Mosalam (2013)**

Lee and Mosalam believed that one of the primary reasons bridges fail during earthquakes in the last decades is because of lack of redundancy of structural systems. Although previous research has shown the effect of axial force on shear capacity of columns, the most critical element of bridge's structural system, current design codes have unique approaches for estimating shear capacity. Failure to consider axial force leads to bending moment capacity changes (compression increases and tension decreases) and greater shear force. Lee and Mosalam emphasized the importance of the vertical component of an earthquake and explained how design codes account for the effect of this excitation. They asserted that the two-thirds ratio of peak V/H ground acceleration, as considered in most current design codes, underestimates the effect of vertical excitation in near-fault regions. In order to address the lack of experimental justification, Lee and Mosalam studied the effect of vertical ground excitation on shear capacity

of RC bridge piers using shaking table tests. Although the effect of vertical earthquake excitation is more pronounced in a bridge comprised of small column aspect ratios, short spans, and multi-column bridge bent (Kunnath et al. 2008), Lee and Mosalam studied the single column. Isolation of high-frequency vertical excitation of axial force variation caused by overturning moment and shaking table size was mentioned as the main reason to study a single column. Vertical earthquake excitation caused fluctuating axial force in the column, resulting in degradation of shear capacity. Flexural damages occurred at the top of the column earlier than damages at the bottom of column due to large mass moment of inertia at the top. Increased scale of ground motion caused increased flexural damages at the top and bottom of the column. Shear damages occurred because of flexural yielding at the end of the column. Comparison of experimental shear force with shear capacity predicted by ACI and Caltrans Seismic Design Code (SDC) showed that the SDC predicted shear capacity more conservatively because of it neglected concrete contribution under tensile axial force.

### **2-3-10 Mwafy (2012)**

Using a fiber-based model, Mwafy (2012) investigated the effect of vertical component of earthquake in conjunction with horizontal component on seismic response of 12 medium-rise RC buildings (24-36 m). The developed analytical model was subjected to the near-field earthquake records. To avoid extreme conclusion, earthquake excitations with unusual V/H peak acceleration ratios were not considered in Mwafy's studies. Selected earthquake records were normalized to obtain equal velocity spectrum intensity in the period range of the buildings. The vertical component of an earthquake increased axial force fluctuation in the columns, potentially causing variation in column strength and stiffness because flexural and shear capacity of

columns is highly affected by axial force level. Therefore, the Zeus-NL platform (Elnahsai et al. 2010) was used for analytical simulation in order to capture the large displacement behavior of buildings under static and dynamic loading, considering material inelasticity and geometric nonlinearities. Using archived analytical results, Mwafy concluded that the vertical component of an earthquake significantly affects the seismic response of the member and structure levels. In addition, Mwafy suggested that designs of medium-rise RC buildings located at near-fault regions should consider maximum amplification of vertical ground motion. Based on Mwafy's results, the vertical ground motion effect increases when a building contains structural irregularity, and the contribution of lateral seismic action is small at higher stories.

## **2-4 Material and Plastic Hinge Models**

Analysis of RC elements or structures requires analytical material models to simulate cyclic and monotonic behavior of RC element components. These models should accurately reflect monotonic and cyclic behavior of materials. This section provides a comprehensive review of material models for monotonic and cyclic stress-strain relationships of steel, plain concrete (unconfined concrete), concrete confined by lateral steel (tie/spiral), Fiber Reinforced Polymer (FRP), or both lateral steel and FRP. In addition, current assumptions regarding curvature distribution over column height, specifically plastic hinge models are reviewed.

### **2-4-1 Monotonic Material Model**

Real monotonic material models for steel and concrete confined by various lateral reinforcements were obtained from tensile tests of steel bars and compressive tests of concrete specimens. Numerous models have been developed based on observed behavior of steel,

concrete confined by lateral steel, concrete confined by FRP, and concrete confined by both FRP and lateral steel. Some of these models are briefly discussed in this chapter.

### **2-4-1-1 Steel**

Because mild steel is generally used as reinforcing steel in concrete members, only the behavior of mild steel is discussed in this section. Actual behavior of steel bars under tensile test is shown in Figure 2-2. As illustrated in this figure, increased tensile strain caused the steel to demonstrate linear elastic behavior up to the yield point ( $\epsilon_y, f_y$ ). After that yield point, steel strength did not change significantly with increased tensile strain. This region is referred to as the yield plateau in the literature. The strain hardening region followed the second region to the ultimate strength of steel ( $f_{su}$ ). In the last region, also known as the post-ultimate stress region, steel strength decreased with increased tensile strain.

#### ***2-4-1-1-(a) Multilinear Models***

Many researchers have used multilinear models in analytical studies to simulate uniaxial behavior of steel bars. In multilinear models, steel behavior is simplified using multiple linear functions. Two examples of this type of model are shown in Figure 2-3.

One of the commonly used multilinear models is the elastic-perfectly plastic model which includes two lines. The first line has a slope equal to steel modulus of elasticity continuing to the yield point. The second line has zero-slope, as shown in Figure 2-3.

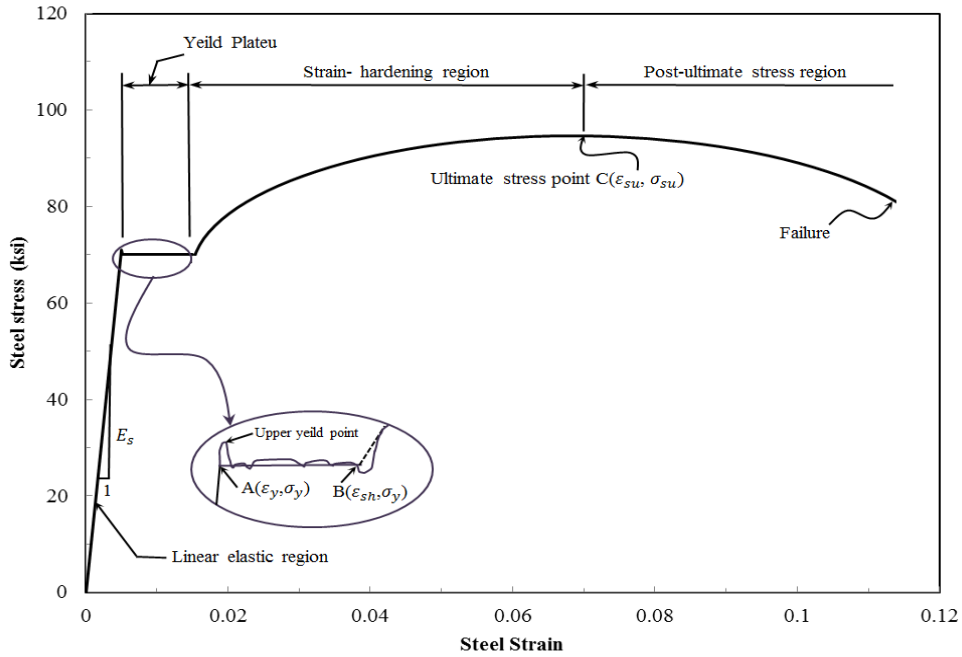


Figure 2-2 Typical monotonic curve of mild steel in tension

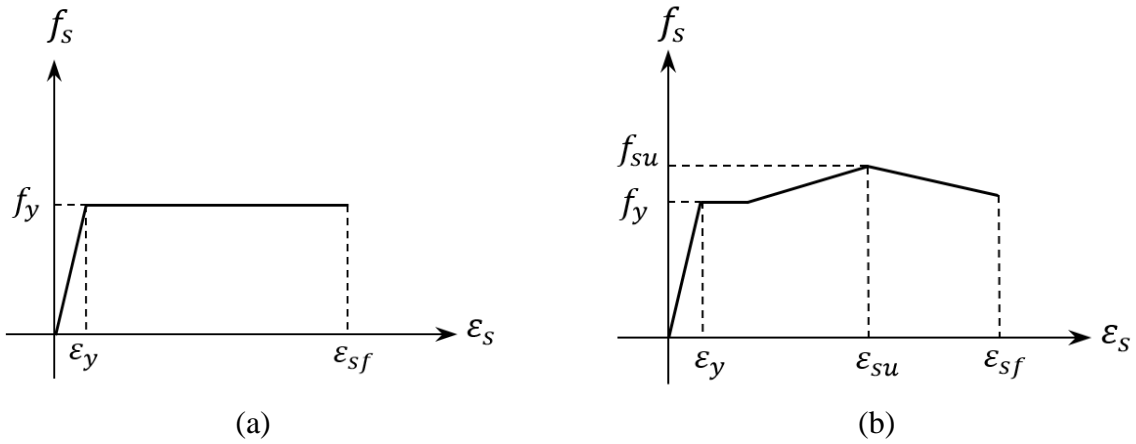


Figure 2-3 Multilinear models: (a) bilinear or elastic-perfectly plastic model and (b) quad linear model



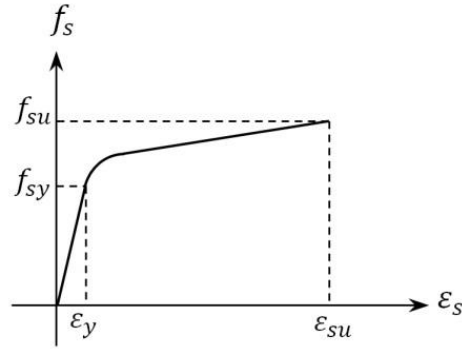


Figure 2-4 Monotonic stress-strain model for steel proposed by Menegotto-Pinto (1973)

#### **2-4-1-1-(b) Menegotto-Pinto Model**

Menegotto-Pinto's model (1973) includes a bilinear curve. The initial line with a slope of steel modulus of elasticity up to yield strength models elastic behavior of steel material. The post-yield strength is defined as a linear function with a slope equal to a portion (defined by  $b$  parameter) of the initial part's slope. However, yield plateau characterization is neglected. The Menegotto-Pinto model is summarized in the following equation:

$$\frac{f_s}{f_y} = b \times \frac{\epsilon_s}{\epsilon_y} + \frac{(1-b) \times \frac{\epsilon_s}{\epsilon_y}}{\left(1 + \left(\frac{\epsilon_s}{\epsilon_y}\right)^{R_0}\right)^{1/R_0}} \quad (2-2)$$

where  $R_0$  is the exponent that controls the transition between elastic and hardening branch.

#### **2-4-1-1-(c) Mander et al. Model (1984)**

The model of Mander et al. (1984) was developed as a result of many tension and compression coupon tests. This model, which takes into account elastic behavior, yield plateau, and strain hardening of steel material, has three main regions, as shown in Figure 2-5. The first region is a linear function with slope equal to steel's modulus of elasticity; the region ends at the

yield point with stress equal to yield stress of steel. The second region simulates yield plateau, and the third region is an ascending curve up to the maximum strength of steel, simulating the strain hardening region of steel behavior. The post-ultimate stress region is not considered in the Mander et al. model.

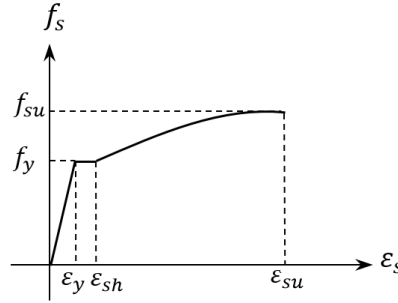


Figure 2-5 Proposed stress-strain model for reinforcing steel by Mander et al. (1984)

Stress-strain functions for these three regions can be summarized as

$$\begin{aligned}
 f_s &= E_s \times \varepsilon_s & 0 \leq \varepsilon_s \leq \varepsilon_y \\
 f_s &= f_y & \varepsilon_y \leq \varepsilon_s \leq \varepsilon_{sh} \\
 f_s &= f_{su} - (f_{su} - f_y) \times \left( \frac{\varepsilon_{su} - \varepsilon_s}{\varepsilon_{su} - \varepsilon_{sh}} \right)^P & \varepsilon_{sh} \leq \varepsilon_s \leq \varepsilon_{su}
 \end{aligned} \tag{2-3}$$

where  $\varepsilon_s$ ,  $\varepsilon_{sh}$ ,  $\varepsilon_{su}$ ,  $f_s$ ,  $f_y$ ,  $E_s$ , and  $f_{su}$  are steel strain, steel strain at commencement of strain hardening region, steel strain corresponding to ultimate strength, steel stress, steel yield stress, steel modulus of elasticity, and steel ultimate strength, respectively. Parameter  $P$  is defined as

$$P = E_{sh} \times \left( \frac{\varepsilon_{su} - \varepsilon_{sh}}{f_{su} - f_y} \right) \tag{2-4}$$

#### 2-4-1-1-(d) Balan et al. Model (1998)

The monotonic response of reinforcing steel in tension is typically assumed to be identical to its response in compression. The tensile and compressive responses were considered to be identical; therefore, the linear strength degradation of compressive response due to local buckling was ignored in Balan et al. model. Balan et al. (1998) considered two coordinate systems in order to model linear strength degradation. They considered identical curve for steel in tension and compression in engineering coordinate system, resulting in varied behavior for tension and compression in a natural coordinate system. Their proposed stress-strain curve for reinforcing steel in tension in the engineering coordinate system was

$$f_s = f_y \times \frac{(1-\rho)}{2} \times \left[ 1 + \frac{(1+\rho)}{(1-\rho)} \times \frac{\varepsilon_s}{\varepsilon_y} - \sqrt{\left( \frac{\varepsilon_s}{\varepsilon_y} - 1 \right)^2 + \delta} \right] \quad (2-5)$$

where  $\rho = E_h/E_s$  is hardening ratio and  $E_h$  is slope of asymptote in the strain hardening region. Eq. (4-4) describes a family of parallel hyperbolas with two asymptotes that depend on parameter  $\delta$ . Parameter  $\delta$  is defined as

$$\delta = \frac{\delta_0}{1-\rho} \quad (2-6)$$

where  $\delta_0$  is the area of triangle bounded by two asymptotes and the tangent to the hyperbola.

Balan et al. (1998) extended Eq. (4-4) to define the linear elastic region, yield plateau, and strain hardening behavior of reinforcing steel in a single equation in the engineering coordinate system as follows:

$$f_s = f'_y \times \frac{(1-\rho')}{2} \times \left[ 1 + \frac{(1+\rho')}{(1-\rho')} \times \frac{\varepsilon_s - \varepsilon_0}{\varepsilon'_y} - \sqrt{\left( \frac{\varepsilon_s - \varepsilon_0}{\varepsilon'_y} - 1 \right)^2 + \delta'} \right] \quad (2-7)$$

where

$$f'_y = \begin{cases} f_y & \varepsilon_s \leq \varepsilon_{sh} \\ E_s \times \varepsilon'_y & \varepsilon_s > \varepsilon_{sh} \end{cases} \quad (2-8)$$

$$\rho' = \begin{cases} 0 & \varepsilon_s \leq \varepsilon_{sh} \\ \frac{E_h}{E_s} & \varepsilon_s > \varepsilon_{sh} \end{cases} \quad (2-9)$$

$$\delta' = \begin{cases} \delta_0 & \varepsilon_s \leq \varepsilon_{sh} \\ \left( \frac{\varepsilon_{sh}}{\varepsilon_y} - 1 \right)^2 \times \delta_0 & \varepsilon_s > \varepsilon_{sh} \end{cases} \quad (2-10)$$

$$\varepsilon_0 = \begin{cases} 0 & \varepsilon_s \leq \varepsilon_{sh} \\ \left( \varepsilon_{sh} - \frac{f_y}{E_s} \right)^2 \times \delta_0 & \varepsilon_s > \varepsilon_{sh} \end{cases} \quad (2-11)$$

$$\varepsilon'_y = \frac{1}{E_s \times (1 - \rho')} \left[ (f_{su} - f_y) - (\varepsilon_{su} - \varepsilon_{sh}) \times E_s \times \rho' \right] \quad (2-12)$$

Eq. (2-7) was used to define the tension curve in the engineering coordinate system, and Eq. (2-12) converted the tensile monotonic curve:

$$\begin{aligned} \bar{\varepsilon}_s &= \ln(1 + \varepsilon_s) \\ \bar{f}_s &= \ln(1 + f_s) \end{aligned} \quad (2-13)$$

where  $\bar{\varepsilon}_s$  and  $\bar{f}_s$  are strain and stress, respectively, in the natural coordinate system.

#### **2-4-1-1-(e) Esmaily and Xiao Model (2005)**

Esmaily and Xiao's steel monotonic model simulates behavior of longitudinal reinforcement when additional detailed reinforcing steel information is available. This model takes into account yield plateau, strain hardening, and softening of steel material. As shown in Figure 2-6, four parameters ( $K_1$ ,  $K_2$ ,  $K_3$ , and  $K_4$ ) were used to simulate stress-strain behavior of various steel types. These four parameters are defined as:

$K_1$  = ratio of strain at the start of the strain hardening region to yield strain

$K_2$  = ratio of strain corresponding to ultimate strain to yield strain

$K_3$  = ratio of ultimate strain to yield strain

$K_4$  = ratio of ultimate stress to yield stress

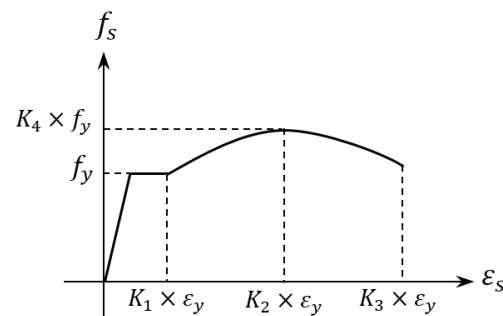


Figure 2-6 Esmaily-Xiao (2005) monotonic stress-strain model curve of steel

### 2-4-1-2 Concrete

Compressive behavior of plain or unconfined concrete is commonly obtained from compressive tests of cylinder specimens with a height-to-diameter ratio of 2. Tensile strength of plain concrete also can be obtained directly from tensile tests. However, the direct tensile test is rarely used due to difficulties associated with holding the specimen and uncertainties of secondary stress caused by the holding tools. Therefore, tensile strength can also be measured indirectly using a split-cylinder test. Experimental data has been used to develop numerous stress-strain models for unconfined concrete. A few of those models are described in the following sections.

#### 2-4-1-2-(a) Hognestad Model (1951)

The ascending portion of the stress-strain curve in Hognestad's model is defined using a parabolic function. The descending branch of the model is defined using a linear function as follows:

$$f_c = \begin{cases} f'_{c0} \times \left[ \frac{2 \times \varepsilon_c}{\varepsilon_{c0}} - \left( \frac{\varepsilon_c}{\varepsilon_{c0}} \right)^2 \right] & \varepsilon_c \leq \varepsilon_{c0} \\ f'_{c0} \times \left[ 1 - 0.15 \times \frac{\varepsilon_c + \varepsilon_{c0}}{0.0038 - \varepsilon_{c0}} \right] & \varepsilon_{c0} < \varepsilon_c \leq 0.0038 \end{cases} \quad (2-14)$$

where  $f_c$ ,  $f'_{c0}$ ,  $\varepsilon_c$ , and  $\varepsilon_{c0}$  are axial compressive stress of concrete, maximum strength of plain concrete, strain of concrete, and strain corresponding to the maximum strength of plain concrete, respectively. In Hognestad's model, fracture strain of plain concrete is assumed to be 0.0038.

#### 2-4-1-2-(b) Mander et al. Model (1988)

Mander et al. proposed a stress-strain model that considers Popovics equation as follows:

$$f_c = \begin{cases} f'_{c0} \times \left[ \frac{\frac{\varepsilon_c}{\varepsilon_{c0}} \times r}{r - 1 + \left( \frac{\varepsilon_c}{\varepsilon_{c0}} \right)^r} \right] & \varepsilon_c \leq 2 \times \varepsilon_{c0} \\ \frac{2 \times r \times f'_{c0}}{\left( \varepsilon_{sp} - 2 \times \varepsilon_c \right) \times \left( r - 1 + 2^r \right)} \times \left( \varepsilon_{sp} - \varepsilon_c \right) & 2 \times \varepsilon_{c0} < \varepsilon_c \leq \varepsilon_{sp} \end{cases} \quad (2-15)$$

where  $\varepsilon_{sp}$  is spalling strain of plain concrete, and  $r$  is defined as

$$r = \frac{E_c}{E_c - E_{sec}} \quad (2-16)$$

$E_c$  is the concrete modulus of elasticity, and  $E_{sec}$  is defined as

$$E_{\text{sec}} = \frac{f'_{c0}}{\varepsilon_{c0}} \quad (2-17)$$

### 2-4-1-3 Concrete Confined by Lateral Steel

#### 2-4-1-3-(a) Richart et al. Model (1928)

Richart et al. (1928) conducted one of the first studies on the effect of transverse reinforcement on enhancement of concrete compressive strength. Richart et al. used test results of  $100\text{ mm} \times 200\text{ mm}$  cylindrical specimens under various transverse pressures to conclude that strength and corresponding strain increases in proportion to transverse pressure increase. Based on experimental results, they proposed the following equation to predict compressive strength of confined concrete by lateral reinforcement:

$$f'_{cc} = f'_{c0} + k \times f_l \quad (2-18)$$

where  $f'_{c0}$ ,  $f_l$ ,  $f'_{cc}$ , and  $k$  are plain concrete compressive strength, transverse pressure, compressive strength of confined concrete, and experimental coefficient, respectively. Strain corresponding ( $\varepsilon_{cc}$ ) to maximum stress of confined concrete was given as

$$\varepsilon_{cc} = \varepsilon_{c0} \times \left[ 1 + 5 \left( \frac{f'_{cc}}{f'_{c0}} - 1 \right) \right] \quad (2-19)$$

where  $\varepsilon_{c0}$  is strain corresponding to maximum strength of plain concrete.

#### 2-4-1-3-(b) Mander et al. Model (1988)

The model of Mander et al. (1988) was developed analytically for circular or rectangular cross sections. Researchers have used this model to simulate monotonic behavior of concrete confined by conventional reinforcement. The RC section may contain any general confinement

type provided by spiral or circular hoops, or rectangular hoops with or without supplementary cross-tie. In this model, the effect of any confinement type is taken into account by defining an effective lateral confining pressure. Effective lateral confining pressure in this model depends on lateral and longitudinal reinforcement configuration. The model's stress-strain relationship is based on an equation proposed by Popovics:

$$f_c = f'_{c0} \times \left[ \frac{\frac{\varepsilon_c}{\varepsilon_{cc}} \times r}{r - 1 + \left( \frac{\varepsilon_c}{\varepsilon_{cc}} \right)^r} \right] \quad (2-20)$$

where  $\varepsilon_{cc}$  is strain corresponding to maximum strength of confined concrete ( $f'_{cc}$ ) calculated by

$$\varepsilon_{cc} = \varepsilon_{c0} \left[ 1 + 5 \times \left( \frac{f'_{cc}}{f'_{c0}} - 1 \right) \right] \quad (2-21)$$

$r$  is defined as

$$r = \frac{E_c}{E_c - E_{sec}} \quad (2-22)$$

and  $E_{sec} = f'_{cc} / \varepsilon_{cc}$ . Maximum strength of confined concrete is expressed as

$$f'_{cc} = f'_{c0} \times \left[ -1.254 + 2.254 \sqrt{1 + \frac{7.94 \times f'_l}{f'_{c0}}} - 2 \frac{f'_l}{f'_{c0}} \right] \quad (2-23)$$

In Eq. (2-23),  $f'_l$  is effective lateral confining pressure defined as

$$f'_l = \frac{1}{2} k_e \times \rho_s \times f_{yh} \quad (2-24)$$

where  $\rho_s$  is the ratio of volume of transverse reinforcement,  $f_{yh}$  is yield strength of the transverse reinforcement, and  $k_e$  is confinement effectiveness coefficient.  $k_e$  for a circular column can be calculated by



$$k_e = \begin{cases} \frac{\left(1 - \frac{s'}{2d_s}\right)^2}{1 - \rho_{cc}} & \text{circular hooped} \\ \frac{1 - \frac{s'}{2d_s}}{1 - \rho_{cc}} & \text{circular spiral} \end{cases} \quad (2-25)$$

$s'$ ,  $d_s$ , and  $\rho_{cc}$  are clear spacing between spiral or hoop bars, diameter of spiral or hoop, and ratio of area of longitudinal steel to area of core of section, respectively. For a rectangular section reinforced laterally by rectangular tie and cross-tie, the confinement effectiveness coefficient is defined as

$$k_e = \frac{\left(1 - \sum_{i=1}^n \frac{(w'_i)^2}{6}\right) \times \left(1 - \frac{s'}{2b_c}\right) \times \left(1 - \frac{s'}{2d_c}\right)}{1 - \rho_{cc}} \quad (2-26)$$

where  $b_c$  and  $d_c$  are core dimensions to centerlines of perimeter hoop in x- and y-directions, respectively. To predict strain corresponding to first fracture, Mander et al. used an energy balance approach by equating strain energy stored in the concrete caused by confinement to strain energy capacity of lateral reinforcement (Mander et al. 1988).

$$110\rho_s = \int_0^{\varepsilon_{cu}} f_c d\varepsilon_c + \int_0^{\varepsilon_{cu}} f_{sl} d\varepsilon_c - 0.017\sqrt{f'_{c0}} \quad (2-27)$$

where  $f_{sl}$  is stress in longitudinal steel reinforcement.

#### **2-4-1-3-(c) Cussan et al. Model (1995)**

Because proposed stress-strain models for normal-strength concrete may overestimate strength and fracture strain of high-strength concrete, Cusson and Paultre (1995) proposed a model to predict monotonic behavior of high-strength concrete confined by steel ties using

experimental results of 50 large-scale high-strength concrete-tied columns tested under eccentric loading. Cusson and Paultre considered effects of tie-yield strength, concrete compressive strength, tie configuration, and lateral and longitudinal reinforcement ratios when developing their model (Cusson and Paultre 1995). The initial part of Cusson and Paultre's stress-strain curve for confined and unconfined concrete is a relationship originally proposed by Popovics (1973). The second part of the curve is a modification of the relationship proposed by Fafitis and Shah (1985) for high-strength confined concrete. The mathematical expression of this model is

$$f_c = \begin{cases} \frac{f'_{cc} \times \frac{\varepsilon_c}{\varepsilon_{cc}} \times r}{r - 1 + \left(\frac{\varepsilon_c}{\varepsilon_{cc}}\right)^r} & \varepsilon_c \leq \varepsilon_{cc} \\ f'_{cc} \times \exp\left(k_1 \times (\varepsilon_c - \varepsilon_{cc})^{k_2}\right) & \varepsilon_c > \varepsilon_{cc} \end{cases} \quad (2-28)$$

where  $k_1$  and  $k_2$  are defined as

$$k_1 = \frac{\ln(0.5)}{(\varepsilon_{C50C} - \varepsilon_{cc})^{k_2}} \quad (2-29)$$

$$k_2 = 0.58 + 16\left(f'_{le}/f'_{c0}\right)^{1.4}$$

Maximum strength of confined concrete is calculated using the equation proposed by Press et al. (1990):

$$\frac{f'_{cc}}{f'_{c0}} = 1.0 + 2.1 \times \left(\frac{f'_l}{f'_{c0}}\right)^{0.7} \quad (2-30)$$

Effective lateral pressure ( $f'_l$ ) is calculated using equations developed by Mander et al. (1988) which consider  $f'_{hcc}$  (stress in transverse reinforcement) instead of  $f_y$ . Strain corresponding to maximum strength of confined concrete is defined as

$$\varepsilon_{cc} = \varepsilon_{c0} + 0.21 \left( \frac{f'_l}{f'_{c0}} \right)^{1.7} \quad (2-31)$$

As reported by Cusson and Paultre (1995), yield strength of lateral reinforcement develops at peak strength of concrete only for well-confined high-strength concrete specimens; therefore, peak strength of confined concrete is computed by employing an iterative process.

#### **2-4-1-3-(d) Kent and Park (1971)**

Based on experimental results, Kent and Park (1971) proposed a stress-strain model with three branches for concrete rectangular sections. The mathematical expression of the first branch is given as

$$f_c = f'_{cc} \left[ \frac{\varepsilon_c}{0.002} - \left( \frac{\varepsilon_c}{0.002} \right)^2 \right] \quad \varepsilon_c \leq 0.002 \quad (2-32)$$

Kent and Park assumed that lateral steel does not affect the shape of the first branch. The second branch of Kent and Park's stress-strain curve is given as

$$f_c = f'_{cc} [1 - Z(\varepsilon_c - 0.002)] \quad 0.002 \leq \varepsilon_c \leq \varepsilon_{20c} \quad (2-33)$$

where

$$Z = \frac{0.5}{\varepsilon_{50u} + \varepsilon_{50h} - 0.002} \quad (2-34)$$

and

$$\varepsilon_{50u} = \frac{3 + 0.002 \times f'_{cc}}{f'_{cc} - 1000} \quad (f'_{cc} \text{ in psi}) \quad (2-35)$$

$$\varepsilon_{50h} = \frac{3}{4} \rho_s \sqrt{\frac{b''}{s}} \quad (2-36)$$

In Eq. (3-35),  $\rho_s$ ,  $b''$ ,  $s$  are ratio of volume of transverse reinforcement to volume of concrete core measured to outside of hoops, width of confine core measured to outside of hoops, and transverse reinforcement spacing, respectively. The third branch of the model is

$$f_c = 0.2 \times f'_{cc} \quad \varepsilon_c > \varepsilon_{20c} \quad (2-37)$$

#### **2-4-1-3-(e) Fafitis and Shah's Model (1985)**

Fafitis and Shah (1985) initially developed a stress-strain model for a circular concrete section. They later proposed that square sections can be treated as circular sections with diameter equal to the side of square core. Effective lateral pressure caused by lateral reinforcement is defined as

$$f_l = \frac{A_{sh} \times f_{yh}}{d_c \times s} \quad (2-38)$$

where  $A_{sh}$ ,  $f_{yh}$ ,  $d_c$ , and  $s$  are total section area of the transverse reinforcement in vertical cross, yield strength of the transverse steel, core concrete diameter, and lateral spacing, respectively.

Fafitis and Shah's model includes two branches: ascending and descending branches.

Mathematical expressions of these two branches are

$$f_c = f'_{cc} \left[ 1 - \left( 1 - \frac{\varepsilon_c}{\varepsilon_{cc}} \right)^A \right] \quad 0 \leq \varepsilon_c \leq \varepsilon_{cc} \quad (2-39)$$

$$f_c = f'_{cc} \times \exp \left[ -k \times (\varepsilon_c - \varepsilon_{cc})^{1.15} \right] \quad \varepsilon_c > \varepsilon_{cc}$$

Compressive strength of confined concrete ( $f'_{cc}$ ), coefficient  $k$ , and power  $A$  are defined as

$$A = E_c \times \frac{\varepsilon_{cc}}{f'_{cc}} \quad (2-40)$$

$$k = 24.65 \times f'_{c0} \times \exp\left(-0.01 \frac{f_l}{\lambda_1}\right)$$

$$E_c = 33 \times \omega^{1.15} \times \sqrt{f'_{c0}}$$

$$\lambda_1 = 1 - 25 \left(\frac{f_l}{f'_{c0}}\right) \left(1 - \exp(-3.2 f'_{c0})\right)^9$$

#### 2-4-1-3-(f) Sakino and Sun's Model (1993)

Sakino and Sun developed a stress-strain model for circular and square section using experimental results of columns under axial loading. Their stress-strain model is given as

$$f_c = f'_{cc} \frac{AX + (D-1)X^2}{1 + (A-2)X + DX^2} \quad (2-41)$$

where  $X = \frac{\varepsilon_c}{\varepsilon_{c0}}$ ,  $A = \frac{E_c \times \varepsilon_{c0}}{f'_{cc}}$ , and  $f'_{cc}$  is calculated using the following equation:

$$f'_{cc} = \mu \times f'_{c0} + \kappa \times \rho_h \times f_{yh} \quad (2-42)$$

In above equation,  $\mu$  depends on the shape of the concrete section. For a circular section,  $\mu = 0.8$ ; for a square section,  $\mu = 1.0$ .  $\kappa$  is a coefficient that depends on the section's shape. For a square section,  $\kappa$  is defined as

$$\kappa = 1.15 \left(\frac{d''}{C}\right) \left(1 - \frac{s}{2D_c}\right) \quad (2-43)$$

where  $D_c$  and  $C$  are the center-to-center dimension of a steel hoop and transverse distance between any two anchored longitudinal bars, respectively. Strain corresponding to maximum strength of plain concrete can be calculated using the following equations:

$$\varepsilon_{c0} = \varepsilon_0 \times \begin{cases} 1 + 4.7(K-1) & K \leq 1.5 \\ 3.35 + 20(K-1.5) & K > 1.5 \end{cases} \quad (2-44)$$

where  $K = \frac{f'_{cc}}{f'_{c0}}$  and  $\varepsilon_0$  are defined as

$$\varepsilon_0 = 0.5243 \times (f'_{cc})^{1/4} \times 10^{-3}. \quad (2-45)$$

In Eq. (3-44), the concrete modulus of elasticity is calculated using the following equation:

$$E_c = 4k \left( \frac{f'_{cc}}{1000} \right)^{1/3} \times 10^5 \times \left( \frac{\gamma}{2.4} \right)^2 \quad (2-46)$$

where  $k$  is an empirical coefficient that depends on the concrete mixture material. This coefficient can be 0.9, 1.0, or 1.2.  $\gamma$  is equal to 0.75 for steel tube and 0.5 for square hoops.

Parameter  $D$  in the stress-strain function is calculated by

$$D = 1.5 - 1.68 \times 10^{-3} \times f'_{c0} + \gamma \sqrt{\frac{(K-1)f'_{c0}}{23}} \quad (2-47)$$

#### **2-4-1-3-(g) Saatcioglu and Razavi's Model (1992)**

Similar to the model proposed by Kent and Park (1971), Saatcioglu and Razavi's model includes a parabolic ascending branch and a linear descending branch. The initial branch is given as

$$f_c = f'_{cc} \left[ 2 \left( \frac{\varepsilon_c}{\varepsilon_{cc}} \right) - \left( \frac{\varepsilon_c}{\varepsilon_{cc}} \right)^2 \right]^{1+2K} \leq f'_{cc} \quad (2-48)$$

where  $K = \frac{k_1 \times f_l}{f'_{c0}}$  and  $k_1 = 6.7 \times (f_l)^{-0.17}$ .  $f_l$  is lateral pressure caused by transverse steel

reinforcement, given as

$$f_l = \frac{\sum A_s \times f_{yh} \times \sin \alpha}{s \times b_c} \quad (2-49)$$

where  $\alpha$  is the angle between transverse reinforcement and  $b_c$  is the dimension of core concrete.

$A_s$  is the total area of lateral reinforcement. Confined concrete strength ( $f'_{cc}$ ) is calculated by the following equation:

$$f'_{cc} = f'_{c0} + k_1 f_{le} \quad (2-50)$$

where  $f_{le}$  is effective lateral pressure caused by lateral reinforcement, defined as:

$$f_{le} = k_2 \times f_l \quad (2-51)$$

In Eq. (3-50),  $k_2$  is 1.0 for circular sections, and for square section is given as:

$$k_2 = 0.26 \sqrt{\left(\frac{b_c}{s}\right)\left(\frac{b_c}{s_l}\right)\left(\frac{1}{f_l}\right)} \quad (2-52)$$

where  $s_l$  is the distance between longitudinal bars. Strain corresponding to compressive strength of confined concrete is calculated by

$$\varepsilon_{cc} = \varepsilon_{c0}(1+5K) \quad (2-53)$$

#### 2-4-1-4 Concrete Confined by Fiber Reinforced Polymer

##### 2-4-1-4-(a) Saaman et al. Model (1998)

Samaan et al. expressed monotonic behavior of FRP-confined concrete by calibrating the Richard and Abbott (1975) relationship. The equation of monotonic stress-strain curve in this model is as follows:

$$f_c = \frac{(E_1 - E_2) \times \varepsilon_c}{\left[1 + \left(\frac{(E_1 - E_2) \times \varepsilon_c}{f_0}\right)^n\right]^{1/n}} + E_2 \times \varepsilon_c \quad (2-54)$$

where

$$f'_{cu} = f'_{c0} + 6.0 \times f_{lf}^{0.7} [MPa] = f'_{c0} + 3.38 \times f_{lf}^{0.7} [ksi]$$

$$E_1 = 3950 \sqrt{f'_{c0}} [MPa] = 47.586 \sqrt{1000 \times f'_{c0}} [ksi]$$

$$E_2 = 245.61 \times f_{c0}'^{0.2} + 1.3456 \times \frac{E_{frp} \times t_f}{D} [MPa] = 52.411 \times f_{c0}'^{0.2} + 1.3456 \times \frac{E_{frp} \times t_f}{D} [ksi] \quad (2-55)$$

$$f_0 = 0.872 \times f'_{c0} + 0.371 \times f_{lf} + 6.258 [MPa] = 0.872 \times f'_{c0} + 0.371 \times f_{lf} + 0.908 [ksi]$$

$$\varepsilon_{cu} = \frac{f'_{cu} - f_0}{E_2}$$

Samaan et al. used a curve-shape parameter  $n = 1.5$  for the Richard and Abbott equation.

#### **2-4-1-4-(b) Lam and Teng's Model (2003)**

Lam and Tang (2003) proposed a design-oriented stress-strain model for FRP-confined concrete. Their model contained the following basic assumptions based on test observations of FRP-confined concrete with a monotonically increasing stress-strain curve:

- The stress-strain curve includes a parabola first portion and a straight line second portion. This assumption leads to a stress-strain curve similar to models implemented in codes for unconfined concrete.
- The parabola slope at the initial point ( $\varepsilon_c = 0$ ) is equal to the slope of unconfined concrete curve ( $E_c$ ). This assumption is to account for the fact that initial stiffness of FRP-confined concrete due to the passive nature of confinement is affected by FRP.
- The first parabola portion is affected because of the presence of FRP. This assumption reflects the fact that FRP confinement is activated when concrete behavior is nonlinear.
- The slope does not change when the first portion meets the second portion.



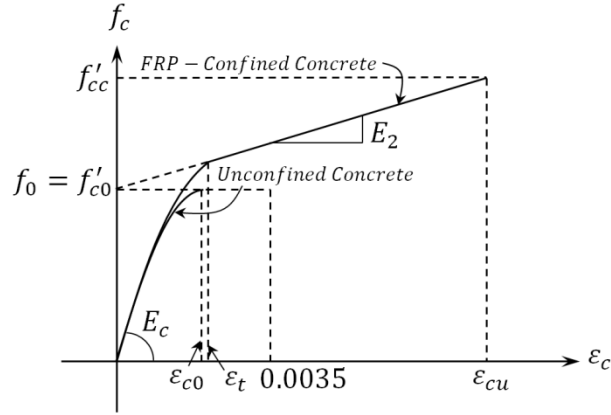


Figure 2-7 Proposed stress-strain model for FRP-confined concrete (Lam and Teng (2003))

Based on assumptions in the Lam and Teng model, the following expression is given for this stress-strain model:

$$f_c = E_c \varepsilon_c - \frac{(E_c - E_2)^2}{4f_0} \varepsilon_c^2 \quad 0 \leq \varepsilon_c \leq \varepsilon_t \quad (2-56)$$

$$f_c = f_0 + E_2 \varepsilon_c \quad \varepsilon_t \leq \varepsilon_c \leq \varepsilon_{cu}$$

where  $f_0$  is intercept of the stress axis by the linear second portion,  $\varepsilon_{cu}$  is ultimate strain, and  $\varepsilon_t$  is strain at which two portions meet, given by:

$$\varepsilon_t = \frac{2f_0}{(E_c - E_2)} \quad (2-57)$$

where  $E_2$  is the slope of the linear second portion, given by:

$$E_2 = \frac{f'_{cc} - f_0}{\varepsilon_{cu}} \quad (2-58)$$

where  $f'_{cc}$  is compressive strength of the confined concrete. To predict ultimate strain, Lam and Tang used the constitutive model proposed by Ottosen (1979). The following expression was proposed for ultimate strain in order to plot the strain enhancement ratio against the actual confinement ratio for Carbon-FRP wraps and Aramid-FRP wraps:

$$\frac{\varepsilon_{cu}}{\varepsilon_{c0}} = 1.75 + 12 \left( \frac{E_{frp} \times t}{E_{sec} \times R} \right) \left( \frac{\varepsilon_{h,rupt}}{\varepsilon_{c0}} \right)^{1.45} \quad (2-59)$$

where  $E_{sec}$ ,  $R$ ,  $E_{frp}$ ,  $t$ , and  $\varepsilon_{h,rupt}$  are second modules of elasticity at the compressive strength of unconfined concrete, radius of circular section, elastic modulus of FRP, thickness of FRP, and actual FRP hoop rupture strain, respectively. Experimental data from the present database in the literature was used to suggest the following equation for obtaining compressive strength of confined concrete:

$$\frac{f'_{cc}}{f'_{c0}} = 1 + 3.3 \frac{f_{l,a}}{f'_{c0}} \quad (2-60)$$

where  $f_{l,a}$  is confining pressure caused by FRP. To calculate  $f_0$ , Samaan et al. proposed the following equation based on experimental data (Samaan et al. 1998):

$$f_0 = 0.872 \times f'_{c0} + 0.371 \times f_l + 6.258 \text{ (MPa)} \quad (2-61)$$

Using empirical results of 63 specimens, Lam and Teng demonstrated that  $f_0$  is independent of confinement pressure and, for simplicity, they used  $f_0 = f'_{c0}$  in their model.

Lam and Teng also proposed an FRP efficiency factor defined as the ratio of actual FRP hoop rupture strain ( $\varepsilon_{h,rupt}$ ) in FRP-confined concrete to FRP rupture strain from flat coupon test ( $\varepsilon_{frp}$ ). The obtained efficiency factor equaled 0.586 for 52 CFRP-wrapped specimens out of a total of 76 specimens. Therefore, the ultimate strain of CFRP-confined concrete can be expressed as:

$$\frac{\varepsilon_{cu}}{\varepsilon_{c0}} = 1.75 + 5.53 \left( \frac{f_{l,a}}{f'_{c0}} \right) \left( \frac{\varepsilon_{frp}}{\varepsilon_{c0}} \right)^{0.45} \quad (2-62)$$

#### 2-4-1-4-(c) Berthet's et al Model (2006)

Berthet et al. (2006) presented a model based on an analytical approach. They categorized the mechanical behavior of confined concrete into two distinct parts. The first part, related to the low level of strain, is based on the theory of elasticity and strain compatibility between concrete core and composite jacket. The second part, related to the high level of strain, corresponds to pseudo-plastic behavior. This second part can be assessed using experimental data. The following steps are needed in order to obtain the stress-strain model:

- Prediction of ultimate behavior
- Modeling of the second region
- Modeling of the first region.

Using Mohr-Coulomb failure criterion, Berthet et al. proposed the following equation to determine the ultimate strength of confined concrete ( $f'_{cc}$ ):

$$f'_{cc} = f'_{c0} + k_1 \times f_{lu} \quad (2-63)$$

where  $f'_{c0}$ ,  $f_{lu}$ , and  $k_1$  are ultimate concrete strength of plain concrete, ultimate confinement pressure, and confinement efficiency, respectively. When stress equilibrium is used to obtain ultimate confinement pressure, Eq. 3-62 is represented as

$$f'_{cc} = f'_{c0} + k_1 \times \frac{t}{r} \times E_f \times \varepsilon_{fu} \quad (2-64)$$

where  $E_f$ ,  $\varepsilon_{fu}$ ,  $t$ , and  $r$  are the Young modulus of FRP jacket, ultimate circumferential strain in the jacket, jacket thickness, and radius of the concrete core, respectively. Confinement efficiency (hardening parameter) can be presented by regression analysis:

$$k_1 = 3.45 \quad 20 \leq f'_{c0} \leq 50 \text{ MPa} \quad (2-65)$$

$$k_1 = \frac{9.5}{(f'_{c0})^{1/4}} \quad 50 \leq f'_{c0} \leq 200 \text{ MPa}$$

The following expression represents ultimate axial strain ( $\varepsilon_{au}$ ) based on experimental database:

$$\varepsilon_{au} = \varepsilon_{a0} + \sqrt{2} \left( \frac{E_1}{f'_{c0}} \right)^{2/3} \times (\varepsilon_{fu} - \nu_c \varepsilon_{a0}) \quad (2-66)$$

where  $\nu_c$ ,  $E_1$ , and  $\varepsilon_{a0}$  are Poisson's ratio of plain concrete, confinement modulus, and axial strain corresponding to the change of slope from pseudo-elastic behavior to the pseudo-plastic behavior which is 0.002. Regression analysis was used to obtain the following equation for the slope of linear relationship between the pseudo-plastic branch and the confinement modulus:

$$\theta_r = 2.73E_1 - 163 \quad (2-67)$$

Reference plastic stress ( $f'_{cp}$ ) can be calculated with the following equation:

$$f'_{cp} = f'_{cc} - \theta_r \times (\varepsilon_{fu} - \varepsilon_{rp}) \quad (2-68)$$

Compressive stress for the second branch can be estimated by following equation:

$$f'_c = f'_{cc} - \theta_r \times ((\nu_c - \gamma)\varepsilon_{a0} - \varepsilon_{rp}) + \theta_r \gamma \varepsilon_a \quad \varepsilon_{ap} \leq \varepsilon_a \quad (2-69)$$

where  $\varepsilon_{ap}$  is axial plastic strain corresponding to  $\varepsilon_{rp}$ , and  $\varepsilon_a$  is axial strain.

For the first branch, Berthet et al. (2006) used the following expression proposed by Ahmad and Shah (1982) and modified by Toutanji (1999):

$$f'_c = \frac{A \times \varepsilon}{1 + b \times \varepsilon + C \times \varepsilon^2} \quad \varepsilon_{ap} \leq \varepsilon_a \quad (2-70)$$

The boundary condition of stress-strain curve was used to obtain constants  $A$ ,  $B$ , and  $C$  as follows:

$$A = E_r^* = \frac{E_c}{\nu_c} \left[ 1 + \frac{E_1}{E_c} (1 - \nu_c) \right] \quad (2-71)$$

$$B = \frac{E_r^*}{f_{cp}'} - \frac{2}{\varepsilon_{rp}} + \theta_r \frac{E_r^* \times \varepsilon_{rp}}{f_{cp}'^2}$$

$$C = \frac{1}{\varepsilon_{rp}^2} - \theta_r \frac{E_r^*}{f_{cp}'^2}$$

where  $E_c$  is Young modulus of plain concrete.

#### **2-4-1-4-(d) Teng et al. (2009)**

In 2009, Teng and his research group (Teng et al. 2009) refined the design-oriented stress-strain model originally proposed by Lam and Teng in 2003. Based on the new database compiled by Teng et al., Lam and Teng's model overestimated ultimate axial strain of concrete at high level of confinement and underestimated compressive strength at low level of confinement. In addition, the effect of confinement stiffness was only considered for the ultimate axial strain equation but was not considered in the compressive strength equation.

In their new work, Teng et al. (2009) posed two refined versions of a stress-strain model. In the first version, they updated only the ultimate axial strain and compressive strength of the original model. In the second version, they modeled the descending branch not covered in the original model. Teng et al. proposed the following expressions for ultimate axial strain and compressive strength in the first version:

$$\frac{f_{cc}'}{f_{c0}'} = C_\sigma + F_\sigma(\rho_k) \times f_\sigma(\rho_\varepsilon)$$

$$\frac{\varepsilon_{cu}}{\varepsilon_{c0}} = C_\varepsilon + F_\varepsilon(\rho_k) \times f_\varepsilon(\rho_\varepsilon)$$
(2-72)

where  $C_\varepsilon$  and  $C_\sigma$  are constant,  $F_\sigma(\rho_k)$  and  $F_\varepsilon(\rho_k)$  are functions of the confinement stiffness ratio, and  $f_\sigma(\rho_\varepsilon)$ , and  $f_\varepsilon(\rho_\varepsilon)$  are functions of the strain ratio. Based on experimental results, these functions are defined as:

$$C_\sigma = 1.0, \quad C_\varepsilon = 1.75$$

$$F_\sigma(\rho_k) \times f_\sigma(\rho_\varepsilon) = \begin{cases} 3.5(\rho_k - 1)\rho_\varepsilon & \rho_k \geq 0.01 \\ 0 & \rho_k < 0.01 \end{cases} \quad (2-73)$$

$$F_\varepsilon(\rho_k) \times f_\varepsilon(\rho_\varepsilon) = 6.5 \times \rho_k^{0.8} \times \rho_\varepsilon^{1.45}$$

For the second version of their stress-strain relationship, Teng et al. added another part to Lam and Teng's original model when  $\varepsilon_t \leq \varepsilon_c \leq \varepsilon_{cu}$ :

$$f_c = \begin{cases} E_c \varepsilon_c - \frac{(E_c - E_2)^2}{4f'_{c0}} + b \times \varepsilon_c + c & 0 \leq \varepsilon_c \leq \varepsilon_t \\ \begin{cases} f'_{c0} + E_2 \varepsilon_c & \rho_k \geq 0.01 \\ f'_{c0} - \frac{f'_{c0} - f'_{cu}}{\varepsilon_{cu} - \varepsilon_{c0}} & \rho_k < 0.01 \end{cases} & \varepsilon_t \leq \varepsilon_c \leq \varepsilon_{cu} \end{cases} \quad (2-74)$$

where  $E_2$  is defined in Lam and Teng's model (2003).  $f'_{cu}$  is defined as follows:

$$\frac{f'_{cu}}{f'_{c0}} = 3.5(\rho_k - 0.01)\rho_\varepsilon$$

$$\frac{f'_{cu}}{f'_{c0}} \geq 0.85f'_{c0} \quad \rho_k > 0 \quad (2-75)$$

$$\frac{f'_{cu}}{f'_{c0}} = 0.85f'_{c0} \quad \rho_k = 0$$

#### **2-4-1-4-(e) Lokuge's et al. Model (2011)**

The stress-strain model proposed by Lokuge et al. is based on 24 tri-axial tests on four grades of concrete (40, 60, 75, and 100 MPa) and three confining pressures (4, 8, and 12 MPa).

In order to predict the relationship between axial strain ( $\varepsilon_1$ ) and lateral strain ( $\varepsilon_2$ ), Lokuge et al.

(2011) used an equation proposed by Candappa (2000):

$$\frac{\varepsilon_2'}{\varepsilon_{cc}'} = \begin{cases} \nu_i^a \left( \frac{\varepsilon_1}{\varepsilon_{cc}} \right) & \varepsilon_1 \leq \varepsilon' \\ \left( \frac{\varepsilon_1}{\varepsilon_{cc}} \right)^a & \varepsilon_1 > \varepsilon' \end{cases} \quad (2-76)$$

where  $\varepsilon_{cc}$ ,  $\varepsilon_{cc}'$ , and  $a$  are axial strain corresponding to peak axial stress, corresponding lateral strain, and material parameter depending on uniaxial concrete length, respectively. Parameter  $a$  is approximated by:

$$a = 0.0177 f_{c0}' + 1.2818 \quad (2-77)$$

$\nu_i^a$  is initial Poisson's ratio defined in Candappa (2000) as:

$$\nu_i^a = 8 \times 10^{-6} \times (f_{c0}')^2 + 0.0002 f_{c0}' + 0.138 \quad (2-78)$$

In order to obtain axial strain corresponding to peak axial stress, Lokuge et al. used the equation suggested by Attrad and Setunge (Attrad, 1996):

$$\frac{\varepsilon_{cc}}{\varepsilon_{c0}} = 1 + (17 - 0.06 f_{c0}') \left( \frac{f_l}{f_{c0}'} \right) \quad (2-79)$$

where  $f_l$  and  $\varepsilon_{c0}$  are confining pressure and axial strain corresponding to peak uniaxial compressive strength in plain concrete (generally assumed to be 0.002), respectively.

Compressive strength of confined concrete is given as:

$$\frac{f_{cc}'}{f_{c0}'} = \left( \frac{f_l}{f_t} + 1 \right)^k \quad (2-80)$$

where  $f_t$  is tensile strength. Because the silica fume was not utilized in the work of Lokuge et al, tensile strength is given as:

$$f_t = 0.9 \times 0.32 (f_{c0}')^{0.67} \quad (2-81)$$

$k$  is a constant defined as:

$$k = 1.25 \left( 1 + 0.062 \frac{f_l'}{f_{c0}'} \right) (f_{c0}')^{-0.21} \quad (2-82)$$

Lokuge et al. expressed axial stress, axial strain, and lateral strain behavior of concrete as follows:

$$\sigma_1 = \begin{cases} 2\tau_{mp} \left( 1 - e^{-c \left( \frac{\varepsilon_1 + \varepsilon_2}{2\gamma_{mp}} \right)} \right) + f_l' & \text{Before Peak} \\ 2\tau_{mp} \left( 1 - e^{-d \left( \frac{\varepsilon_1 + \varepsilon_2}{2\gamma_{mp}} \right)^2} - d \right) + f_l' & \text{After Peak} \end{cases} \quad (2-83)$$

where  $c$  and  $d$  are material parameters depending on uniaxial concrete strength. Lokuge et al. (2011) proposed the following equations to predict these parameters based on best fit curves for each concrete strength:

$$c = -0.0427 f_{c0}' + 7.7381 \quad (2-84)$$

$$d = -0.0003 f_{c0}' - 0.0057$$

$\tau_{mp}$  and  $\gamma_{mp}$  are maximum shear stress at peak and maximum strain at peak, respectively, defined as

$$\tau_{mp} = \frac{f_{cc}' - f_l'}{2} \quad (2-85)$$

$$\gamma_{mp} = \frac{\varepsilon_{cc}' - \varepsilon_{cc}'}{2}$$

In Eq. (3-84), confining pressure  $f_l$  is obtained based on force equilibrium as follows:

$$f_l = \frac{f_{fpp} \times n \times t}{d_s} \quad (2-86)$$

where  $d_s$ ,  $f_{fpp}$ ,  $n$ , and  $t$  are diameter of the cylinder, hoop stress of the carbon fiber sheet, number of sheets, and sheet thickness, respectively.



#### 2-4-1-4-(f) *Wei and Wu's Model (2012)*

Wei and Wu (2012) proposed one of the most recent models for stress-strain relationship of concrete columns confined by FRP. This model was developed based on the large number of database from authors' own tests and tests from literature. The most unique feature of this model is its unified efficiency for use with circular, rectangular, and square sections.

Wei and Wu's model contains two parts. The first part of the model is a parabola with an initial slope in  $\varepsilon_c = 0$  equal to the elastic modulus of unconfined concrete. The first part meets smoothly with the linear second part. The following equations present these two parts:

$$f_c = \begin{cases} E_c \varepsilon_c + \frac{f_0 - E_c \varepsilon_0}{\varepsilon_0^2} \varepsilon_c^2 & 0 \leq \varepsilon_c \leq \varepsilon_0 \\ f_0 + E_2 (\varepsilon_c - \varepsilon_0) & \varepsilon_0 \leq \varepsilon_c \leq \varepsilon_{cu} \end{cases} \quad (2-87)$$

where  $\varepsilon_0$  is transitional strain calculated by the following equation:

$$\varepsilon_0 = \frac{(f_0 + f'_{cu} + E_c \varepsilon_{cu}) - \sqrt{(f_0 + f'_{cu} + E_c \varepsilon_{cu})^2 - 8f_0 E_c \varepsilon_{cu}}}{2E_c} \quad (2-88)$$

$E_2$  is the slope of the second portion, defined as:

$$E_2 = \frac{f'_{cu} - f_0}{\varepsilon_{cu} - \varepsilon_0} \quad (2-89)$$

In Eqs. (3-87) and (3-88),  $f'_{cu}$ ,  $\varepsilon_{cu}$ , and  $f_0$  are ultimate stress, ultimate strain, and transitional stress, respectively.

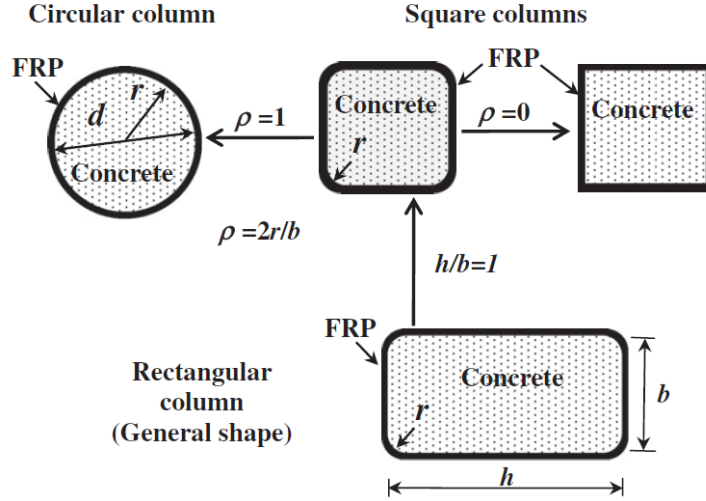


Figure 2-8 Unification of column shapes (Wei and Wu (2012))

Wei and Wu also introduced two parameters, the cross-sectional aspect ratio ( $h/b$ ) and the corner radius ratio ( $2r/b$ ), in which  $h$ ,  $b$ , and  $r$  are length of the longer side, length of the shorter side, and corner radius of a rectangular section, respectively. Wei and Wu used these two parameters to unify their model for circular, square, and rectangular columns, as shown in Figure 2-8. They used the following equation, achieved by regression of database, to obtain ultimate stress of FRP-confined concrete:

$$\frac{f'_{cu}}{f'_{c0}} = 0.5 + 2.7 \left( \frac{2r}{b} \right)^{0.4} \left( \frac{f_l}{f'_{c0}} \right)^{0.73} \left( \frac{h}{b} \right)^{-1} \quad (2-90)$$

where  $f_l$  is calculated by:

$$f_l = \frac{2E_f \varepsilon_{fu} t}{b} \quad (2-91)$$

where  $b$  is width of columns and is equal to the diameter of circular columns or the length of the smaller side of rectangular columns. Wei and Wu used regression of full database to present the following mathematical expression for calculating ultimate strain (Wei Y. Y., 2012):

$$\frac{\varepsilon_{cu}}{\varepsilon_{c0}} = 1.75 + 12 \left( \frac{f_l}{f'_{c0}} \right)^{0.75} \left( \frac{f_{30}}{f'_{c0}} \right)^{0.62} \left( 0.36 \frac{2r}{b} + 0.64 \right) \left( \frac{h}{b} \right)^{-0.3} \quad (2-92)$$

where  $f_{30}$  is concrete strength of unconfined grade C30 concrete and  $f'_{c0}$  is maximum strength of unconfined concrete. In the absence of test values, the value of  $\varepsilon_{c0}$  in Eq. 3-91 can be calculated using the equation proposed by Popovics (1973):

$$\varepsilon_{c0} = 0.000937 \sqrt[4]{f'_{c0}} \quad (2-93)$$

Regression analysis was used to present the following equation for calculating transitional stress:

$$f_0 = f'_{c0} + 0.43 \left( \frac{2r}{b} \right)^{0.68} \left( \frac{h}{b} \right)^{-1} f_l \quad (2-94)$$

#### **2-4-1-4-(g) Youssef et al. Model (2013)**

The model by Youssef et al. is based on results from large-scale tests on circular, square, and rectangular sections confined only by FRP wrap. The first part of the model is a polynomial that simulates unconfined concrete behavior. The second part of the model is a linear function of strain that can predict ascending behavior of moderate- to high-confined concrete sections and descending behavior of low- to moderate-confined concrete sections. Stress-strain equations of this model are as follows:

$$f_c = E_c \times \varepsilon_c \left[ 1 - \frac{1}{n} \left( 1 - \frac{E_2}{E_c} \right) \times \left( \frac{\varepsilon_c}{\varepsilon_t} \right)^{n-1} \right] \text{ and } n = \frac{(E_c - E_2) \times \varepsilon_t}{E_c \times \varepsilon_t - f_t} \quad 0 \leq \varepsilon_c \leq \varepsilon_t \text{ and } E_2 > 0$$

$$f_c = E_c \times \varepsilon_c \left[ 1 - \frac{1}{n} \left( \frac{\varepsilon_c}{\varepsilon_t} \right)^{n-1} \right] \text{ and } n = \frac{E_c \times \varepsilon_t}{E_c \times \varepsilon_t - f_t} \quad 0 \leq \varepsilon_c \leq \varepsilon_t \text{ and } E_2 < 0 \quad (2-95)$$

$$f_c = f_t + E_2 \times (\varepsilon_c - \varepsilon_t) \quad \varepsilon_t \leq \varepsilon_c \leq \varepsilon_{cu}$$

where for the circular section, ultimate strength and strain are calculated by the following equations:

$$\frac{f'_{cu}}{f'_{c0}} = 1.0 + 2.25 \left( \frac{f'_{yf}}{f'_{c0}} \right)$$

$$\varepsilon_{cu} = 0.003368 + 0.259 \times \left( \frac{f'_{yf}}{f'_{c0}} \right) \times \left( \frac{f'_{yf}}{E_{frp}} \right)^{0.5}$$

$$\frac{f'_t}{f'_{c0}} = 1.0 + 3.0 \left( \frac{4 \times t \times E_{frp} \times \varepsilon_{jt}}{D \times f'_{c0}} \right)^{5/4}$$

$$\varepsilon_t = 0.002748 + 0.1169 \times \left( \frac{4 \times t \times E_{frp} \times \varepsilon_{jt}}{D \times f'_{c0}} \right)^{6/7} \times \left( \frac{f'_{yf}}{E_{frp}} \right)^{0.5}$$
(2-96)

Slope of the second branch can be calculated using ultimate strain and strength ( $\varepsilon_{cu}$ ,  $f'_{cu}$ ) and strain and stress in the transition point ( $\varepsilon_t$ ,  $f_t$ ).

## 2-4-1-5 Concrete Confined by Lateral Steel and Fiber-Reinforced Polymer

### 2-4-1-5-(a) Harajli's Model (2006)

Harajli's model for the relationship between strain and strain of concrete confined with FRP contains two parts. The first part is a parabola similar to the model proposed by Scott et al. for the ascending branch of the stress-strain relationship for unconfined concrete or confined concrete with transverse steel ties:

$$f_c = f'_{c0} \left[ \frac{2\varepsilon_c}{f'_{c0}} - \left( \frac{2\varepsilon_c}{\varepsilon_{c0}} \right)^2 \right] \quad \varepsilon_c \leq \varepsilon_{c0} \quad (2-97)$$

where  $f'_{c0}$  and  $\varepsilon_{c0}$  are stress and strain at the intersection point between the first stage and the second stage.

Harajli et al. proposed the following expression for the second part of the stress-strain relationship:

$$f_c = f_{c0} + k_1 f_{lf} + k_1 f_{ls} \frac{A_{cc}}{A_g} \quad \varepsilon_c > \varepsilon_{c0} \quad (2-98)$$

where  $k_1 = 4.1$ ,  $A_{cc}$  is the area of concrete core confined with internal transverse ties, and  $A_g$  is the gross area of the column section.  $f_{lf}$  and  $f_{ls}$  are lateral passive confining pressure exerted by FRP and ordinary transverse steel on the concrete section, respectively. They are expressed as

$$f_{lf} = \left( \frac{k_{ef} \rho_f E_f}{2} \right) \varepsilon_l \quad (2-99)$$

$$f_{lf} = \left( \frac{k_{es} k_v \rho_{st} E_s}{2} \right) \varepsilon_l \leq \left( \frac{k_{es} k_v \rho_{st}}{2} \right) f_{yt}$$

In Eqs. (3-98),  $f_{yt}$  is yield strength of transverse ties and  $E_s$  is modulus of elasticity of steel.  $\rho_f$  is the volumetric ratio of FRP sheets, expressed for the circular and rectangular concrete sections as

$$\rho_f = \frac{4n_f t}{D} \quad \text{For circular concrete section} \quad (2-100)$$

$$\rho_f = \frac{2n_f t(b+h)}{bh} \quad \text{For rectangular concrete section}$$

where  $n_f$ ,  $t$ ,  $D$ ,  $b$ , and  $h$  are the number of FRP layers, design thickness of FRP fabric, diameter of circular section, smaller dimension of rectangular section, and larger dimension of rectangular section, respectively.

The term  $\rho_{st}$  is volumetric ratio of transverse steel ties or hoops (volume of ties or hoops to volume of concrete core measured to outside of hoops). Based on the approach suggested by Sheikh and Uzumeri (1982) and Mander et al. (1988), parameters  $k_{ef}$ ,  $k_{es}$ , and  $k_v$  are as follows for rectangular section using FRP:

$$k_{ef} = \frac{1 - (w_x^2 + w_y^2) / 6xy}{(1 - \rho_s)} \quad (2-101)$$

$$k_v = 1.0.$$

For a rectangular section, using hoops,  $k_{es}$ , and  $k_v$  parameters are defined as:

$$k_{ef} = \frac{1 - \sum_i (w_{xi}^2 + w_{yi}^2) / 6xy}{(1 - \rho_s)} \quad (2-102)$$

$$k_v = \frac{(1 - s' / 2x)(1 - s' / 2y)}{1 - \rho_{cc}}$$

where  $w_{xi}$  and  $w_{yi}$  are  $i^{\text{th}}$  clear distance between adjacent longitudinal bars along the horizontal x- and y-dimensions, respectively (x and y are concrete core dimensions to centerline of peripheral hoop).  $\rho_{cc}$  is the longitudinal steel ratio relative to the confined concrete core measured to outside of hoops, and  $s'$  is clear vertical spacing between lateral hoops.

Parameter  $k_v$  for circular column reinforced laterally with circular hoops and spiral is defined as

$$k_v = \frac{(1 - s' / 2d_s)^2}{1 - \rho_{cc}} \quad (2-103)$$

$$k_v = \frac{1 - s' / 2d_s}{1 - \rho_{cc}}$$

where  $d_s$  is diameter of spiral or hoop.

Stress and strain in the intersection point between the first and second part of the two-part relationship of the stress-strain model are proposed as follows:

$$f_{c0} = f_{c0}' + k_1 \varepsilon_{f0} \left( \frac{k_{ef} \rho_f E_f}{2} + \frac{k_{es} k_v \rho_{st} E_s}{2} \left( \frac{A_{cc}}{A_g} \right) \right) \quad (2-104)$$

$$\varepsilon_{c0} = \varepsilon_0 \left[ 1 + (310.57\varepsilon_{t0} + 1.9) \left( \frac{f_{c0}}{f_{c0}'} - 1 \right) \right]$$

where  $\varepsilon_{t0}$  is lateral strain equal to yield strain of transverse steel hoops, or 0.002 if no internal confinement by transverse steel is available. The stress-strain relationship for the second stage of this model is:

$$f_c = \sqrt{(K_0^2 - K)} - K_0 \quad \varepsilon_c > \varepsilon_{c0} \quad (2-105)$$

where

$$K_0 = 0.0031k_1E_{tf} - f_{c0}' - \frac{1}{2}k_1E_{ts}f_{c0}' \left( \frac{\varepsilon_c}{\varepsilon_0} + 0.9 \right) \quad (2-106)$$

and

$$\begin{aligned} E_{tf} &= k_{ef}\rho_f E_f / 2 \\ E_{ts} &= k_{es}\rho_s E_s / 2 \end{aligned} \quad (2-107)$$

#### **2-4-1-5-(b) Eid's et al. Model (2008)**

Eid et al. (2008) proposed a model to predict axial and lateral behavior of circular concrete columns with transverse steel and FRP. The proposed model integrates the contribution of FRP and transverse steel. In order to predict the behavior of confined concrete, an effective confinement index was introduced that considers transverse steel and FRP properties (mechanical and geometrical). The equation to determine maximum confined concrete stress ( $f_{cc}'$ ) and its corresponding strain ( $\varepsilon_{cc}'$ ) are derived from regression analysis of test results conducted by Legeron and Paultre (2003):

$$\frac{f_{cc}'}{f_{c0}'} = 1 + 2.4(I_e')^{0.7} \quad (2-108)$$

$$\frac{\varepsilon'_{cc}}{\varepsilon'_c} = 1 + 35(I'_e)^{1.2}$$

where  $f'_{c0}$  and  $\varepsilon'_c$  are unconfined concrete strength and its corresponding strain, respectively.

The following equation can be derived from the force equilibrium of the half cross section:

$$f'_{le} = \frac{2ef'_h}{D_c} + f'_{lf} - \Delta_p = \rho_{sy}f'_h + E_{fl}\varepsilon'_f - \Delta_p \quad (2-109)$$

where  $f'_{le}$  is effective confinement pressure at concrete peak stress, and  $e$  is thickness of the uniform equivalent steel tube that replaces discrete steel ties, given as:

$$e = \frac{k_e A_{shy}}{2 \times s} \quad (2-110)$$

where  $s$  is lateral reinforcement spacing, and  $A_{shy}$  is the total cross-sectional area of ties in  $y$ -direction.  $D_c$  is concrete core diameter, and  $f'_{lf}$  and  $\varepsilon'_f$  are lateral pressure due to FRP and FRP circumferential strain at concrete peak stress, respectively.  $E_{fl} = 2t_f E_f / D$  is measure of the FRP composite stiffness or FRP lateral modulus in which  $t_f$  and  $E_f$  are thickness and elastic modulus of FRP, respectively, and  $D$  is diameter of the whole concrete section.  $\Delta_p$  is lateral pressure due to transverse steel reinforcement, and  $\rho_{sy}$  is effective sectional ratio of the confining reinforcement, given as:

$$\rho_{sy} = \frac{k_e A_{shy}}{sD_c} \quad (2-111)$$

$f'_h$  is lateral steel stress at concrete peak stress, defined as:

$$f'_h = \begin{cases} f_{hy} & \kappa \leq 10 \\ \frac{0.25f'_{c0}}{\rho_{sy}(\kappa-1)} \geq 0.43\varepsilon'_c E_s & \kappa > 10 \end{cases} \quad (2-112)$$

where  $E_s$  is transverse steel modulus of elasticity. Parameter  $\kappa$  is defined as:



$$\kappa = \frac{f'_{c0}}{\rho_{sy} E_s \varepsilon'_c} \quad (2-113)$$

Tangential (tensile) strain of composite ( $\varepsilon'_f$ ) and tangential strain of transverse steel ( $\varepsilon'_h$ ) can be assumed to be equal in elastic range, as for  $\varepsilon_f$  and  $\varepsilon_h$ . Strain in transverse steel can be expressed as a function of the concrete secant's Poisson's ratio corresponding to peak stress ( $\nu'_{cc}$ ) and the concrete's secant modulus elasticity at peak stress ( $E'_{ccl}$ ):

$$\varepsilon'_h = \nu'_{cc} \varepsilon'_{cc} - \frac{(1 - \nu'_{cc})}{E'_{ccl}} f'_e \quad (2-114)$$

where

$$E'_{ccl} = \alpha \frac{f'_{cc}}{\varepsilon'_{cc}} \quad \alpha \geq 1 \quad (2-115)$$

Substituting Eq. 3-107 into Eq. 3-113 yields:

$$\frac{\varepsilon'_h}{\varepsilon'_c} = \left( 1 + 35 (I'_e)^{1.2} \right) \left( \nu'_{cc} - \frac{1 - \nu'_{cc}}{\alpha} \times \frac{I'_e}{\left( 1 + 2.4 \times (I'_e)^{0.7} \right)} \right) \quad (2-116)$$

Legeron and Paultre's study (2003) concluded that steel-confined concrete  $\nu'_{cc}$  is equal to 0.43 and  $\alpha = 0.11$ . In another study, Xia and Wu (2003) proposed the following equation for  $\nu'_{cc}$  for FRP-confined concrete:

$$\nu'_{cc} = 10 \left( \frac{f'_{c0}}{E_{fl}} \right)^{0.9} \quad (2-117)$$

In order to consider the effect of transverse steel on  $\nu'_{cc}$ , the following modified equation was proposed:

$$v_{c0} \leq v'_{cc} = 10 \left( \frac{f'_{c0}}{E_{fl} + \rho_{sy} E_s \gamma_{sf}} \right)^{0.9} \leq 0.5 \quad (2-118)$$

where  $v_{c0}$  is concrete Poisson's ratio and  $\gamma_{sf} = \varepsilon_{ly} / \varepsilon_{fu}$ , which is 0.133 for concrete confined by transverse steel only. Based on regression analysis of experimental data and Eq. 3-115:

$$\frac{\varepsilon'_h}{\varepsilon'_c} = v'_{cc} + \eta \times I'_e \quad (2-119)$$

where  $\eta$  is given as

$$\eta = 29.8 \times v'_{cc} - 3.56. \quad (2-120)$$

When considering force equilibrium at the half cross section, the equation for effective confinement index ( $I_e$ ) is given as

$$I_e = \frac{\rho_{sy} f_h}{f'_{c0}} + \frac{E_{fl} \varepsilon_f}{f'_{c0}} \quad (2-121)$$

where  $f_h = E_s \times \varepsilon_h \leq f_{hy}$ . When  $\varepsilon_f$  is equal to actual FRP rupture strain ( $\varepsilon_{fu,a}$ ), the effective confinement index is at its maximum level:

$$I_{e,max} = \frac{\rho_{sy} f_{hy}}{f'_{c0}} + \frac{E_{fl} \varepsilon_{fu\xi}}{f'_{c0}} \quad (2-122)$$

Integration of Eqs. 3-118 and 3-120 yields

$$I'_e = \begin{cases} I'_{e1} = \frac{v'_{cc}}{\kappa_1 - \eta} \leq I'_{e2} & \kappa_1 > \eta \\ I'_{e2} = \frac{v'_{cc} f'_{c0} + \kappa_2 \rho_{sy} f_{hy}}{f'_{c0} (\kappa_2 - \eta)} \leq I_{e,max} & \kappa_1 \leq \eta \text{ and } \kappa_2 > \eta \\ I_{e,max} & \kappa_1 \leq \eta \end{cases} \quad (2-123)$$

where  $\kappa_1$  and  $\kappa_2$  are defined as:

$$\kappa_1 = \frac{f'_{c0}}{\rho_{sy} E_s \varepsilon'_c + E_{fl} \varepsilon'_c} = \frac{E'_c}{E_{fl} + E_{sl}} \quad (2-124)$$

$$\kappa_2 = \frac{f'_{c0}}{E_{fl}\epsilon'_c} = \frac{E'_c}{E_{fl}}$$

where  $E'_c = f'_{c0}/\epsilon'_c$  is concrete secant modulus at peak stress and  $E_{st} = E_s \times \rho_{sy}$  is transverse steel stiffness.

Experimental data of various studies showed that adjustment of Lam and Teng's proposed model (2003) allows ultimate concrete strength ( $f'_{cu}$ ) and strain ( $\epsilon'_{cu}$ ) of concrete confined with FRP or FRP and transverse steel to be predicted using the following expressions:

$$\frac{f'_{cu}}{f'_{c0}} = 1 + 3.3 \left( \frac{\rho_{sy} f_{hy}}{f'_{c0}} + \frac{E_{fl} \epsilon_{fu\xi}}{f'_{c0}} \right) \geq \frac{f'_{cc}}{f'_{c0}} \quad (2-125)$$

$$\frac{\epsilon'_{cu}}{\epsilon'_c} = 1.56 + 12 \left( \frac{\rho_{sy} f_{hy}}{f'_{c0}} + \frac{E_{fl} \epsilon_{fu\xi}}{f'_{c0}} \right) \left( \frac{\epsilon_{fu,a}}{\epsilon'_c} \right)^{0.45}$$

The first stage, or pre-peak branch, of the stress-strain curve is expressed by Sargin's (1971) proposed equation, with modification as follows:

$$f_c = \frac{a\epsilon'_c}{1 + b\epsilon'_c + z\epsilon'^2_c} \quad (2-126)$$

$$a = E_{ct} \quad b = \frac{E_{ct}}{f'_{cc}} - \frac{2}{\epsilon'_{cc}} + \frac{E_{ct} E_{cu} \epsilon'_{cc}}{(f'_{cc})^2} \quad z = \frac{1}{(\epsilon'_{cc})^2} - \frac{E_{ct} E_{cu}}{(f'_{cc})^2}$$

where  $E_{ct}$  is tangent elasticity modulus of concrete and  $E_{cu}$  is slope of the curve after the peak, given as:

$$E_{cu} = \frac{f'_{cu} - f'_{cc}}{\epsilon'_{cu} - \epsilon'_{cc}} \quad (2-127)$$

#### **2-4-1-5-(c) Lee et al. Model (2010)**

In the study by Lee et al., an experimental work was conducted on 24 specimens under compressive load with various types of confinements. Based on experimental results,

compressive response of the confined concrete column could not be obtained by adding the confinement effect of FRP and transverse steel reinforcement due to differences in FRP and steel behavior. Using the test data, a set of empirical equations to predict the stress-strain response of concrete column confined with FRP and transverse steel was proposed.

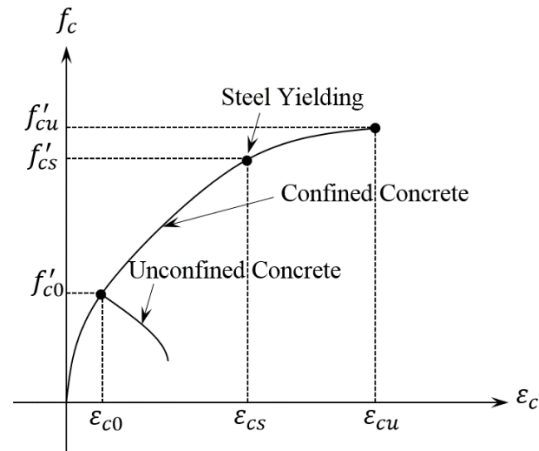


Figure 2-9 Monotonic stress-strain model proposed by Lee et al. for FRP steel spiral-confined concrete

The proposed model considers the role of transverse reinforcement and the FRP jacket to predict the stress-strain response of the confined concrete column subjected to a compressive load. In this three-part model (Figure 2-9) for concrete confined by spiral and FRP, the first part of the model is a parabolic equation beginning with a slope equal to the modulus of elasticity of plain concrete. The first part is followed by a polynomial function after a strain equal to the strain of unconfined concrete at maximum compressive strength. The confining effect of FRP and spiral steel on the compressive strength of concrete is demonstrated by the second part of the curve which ends at the yield point of the steel spiral. The effect of the steel spiral remains

constant, and the effect of FRP confinement increases to the ultimate strain of FRP-spiral-confined concrete in the remaining part of the curve. The formulae of this model are as follows:

$$\begin{aligned}
 f_c &= E_c \times \varepsilon_c + (f'_{c0} - E_c \times \varepsilon_{c0}) \times \left( \frac{\varepsilon_c}{\varepsilon_{c0}} \right)^2 & 0 \leq \varepsilon_c \leq \varepsilon_{c0} \\
 f_c &= f'_{c0} + (f_{cs} - f'_{c0}) \times \left( \frac{\varepsilon_c - \varepsilon_{c0}}{\varepsilon_{cs} - \varepsilon_{c0}} \right)^{0.7} & \varepsilon_{c0} \leq \varepsilon_c \leq \varepsilon_{cs} \\
 f_c &= f_{cs} + (f'_{cu} - f_{cs}) \times \left( \frac{\varepsilon_c - \varepsilon_{cs}}{\varepsilon_{cu} - \varepsilon_{cs}} \right)^{0.7} & \varepsilon_{cs} \leq \varepsilon_c \leq \varepsilon_{cu}
 \end{aligned} \tag{2-128}$$

where

$$\varepsilon_{cs} = \varepsilon_{cu} \left\{ 0.85 + 0.03 \times \left( \frac{f_{lf}}{f_{ls}} \right) \right\} \text{ and } f_{cs} = 0.95 \times f_{cu} \quad f_{lf} \geq f_{ls} \tag{2-129}$$

$$\varepsilon_{cs} = 0.7 \times \varepsilon_{cu} \text{ and } f_{cs} = f'_{cu} \times \left( \frac{\varepsilon_{cs}}{\varepsilon_{cu}} \right)^{0.4} \quad f_{lf} < f_{ls}$$

Ultimate strength and strain are calculated using the following equations:

$$\begin{aligned}
 f_{cu} &= f'_{c0} \times \left( 1 + 2 \frac{f_{lf} + f_{ls}}{f'_{c0}} \right) \\
 \varepsilon_{cu} &= \varepsilon_{c0} \times \left( 1.75 + 5.25 \left( \frac{f_{lf} + k_s \times f_{ls}}{f'_{c0}} \right) \times \left( \frac{\varepsilon_{frp}}{\varepsilon_{c0}} \right)^{0.45} \right)
 \end{aligned} \tag{2-130}$$

where  $k_s = 2 - f_{lf}/f_{ls}$  for  $f_{lf} < f_{ls}$  and  $k_s = 1$  for  $f_{lf} \geq f_{ls}$ .  $\varepsilon_{frp}$  is the rupture strain of FRP.

#### **2-4-1-5-(d) Hu et al. Model (2010)**

In accordance with the concept of passive confinement, Hu et al. proposed a model for concrete columns confined with FRP and transverse steel. Axial stress and strain can be

calculated from each actively confined stress-strain curve by adopting the stress-strain relationship proposed by Popovics (1973):

$$\frac{f_c}{f'_{cc}} = \frac{(\varepsilon_c / \varepsilon'_{cc}) \times \gamma}{\gamma - 1 + (\varepsilon_c / \varepsilon'_{cc}) \times \gamma} \quad (2-131)$$

where  $\gamma = E_c / (E_c - f'_{cc} / \varepsilon'_{cc})$ .  $E_c$  is Young's modulus of the concrete;  $f'_{cc}$  and  $\varepsilon'_{cc}$  are peak stress and strain of the actively confined concrete, respectively;  $f_c$  and  $\varepsilon_c$  are stress and strain of the passively confined concrete curve, respectively. Peak stress and strain are calculated as:

$$\begin{aligned} f'_{cc} &= f'_{c0} + \Delta f'_{ccFRP} + \Delta f'_{ccTRA} \\ \varepsilon'_{cc} &= 1 + 5 \left( \frac{f'_{cc}}{f'_{c0}} - 1 \right) \end{aligned} \quad (2-132)$$

where

$$\begin{aligned} \Delta f'_{ccFRP} &= 3.5 \times f_{lf} \\ \Delta f'_{ccTRA} &= f'_{c0} \left( 2.254 \sqrt{1 + 7.94 \frac{f_{ls}}{f'_{c0}}} - 2 \frac{f_{ls}}{f'_{c0}} - 2.254 \right) \end{aligned} \quad (2-133)$$

In Eq. (3-132),  $f_{ls}$  and  $f_{lf}$  are given as:

$$\begin{aligned} f_{lf} &= \frac{2E_f t_f \varepsilon_l}{d} \\ f_{ls} &= \begin{cases} \frac{2k_e E_s \varepsilon_l A_{sp}}{s \times d_c} & \varepsilon_l < \varepsilon_{sy} \\ \frac{2k_e f_{sy} A_{sp}}{s \times d_c} & \varepsilon_l \geq \varepsilon_{sy} \end{cases} \end{aligned} \quad (2-134)$$

where  $k_e$  is a confinement-effectiveness coefficient proposed by Mander et al. (1988).  $d$  is diameter of the cross section,  $d_c$  is diameter of core concrete, and  $\varepsilon_l$  is lateral strain that can be calculated using the following equation:

$$\frac{\varepsilon_c}{\varepsilon_{c0}} = 0.85 \left[ \left( 1 + 0.75 \left( \frac{\varepsilon_l}{\varepsilon_{c0}} \right) \right)^{0.7} - \exp \left( -7 \frac{\varepsilon_l}{\varepsilon_{c0}} \right) \right] \times \eta \quad (2-135)$$

where

$$\eta = \begin{cases} 1 + 8 \times f_{lf} / f_{c0}' & \text{For FRP Confined Concrete} \\ 1 + 8 \times f_{lf} / f_{c0}' + \beta_{TRS} \times f_{ls} / f_{c0}' & \text{For FRP - Steel Confined Concrete} \end{cases} \quad (2-136)$$

$\beta_{TRS}$  is defined as:

$$\beta_{TRS} = \frac{23.5}{\sqrt{\frac{k_{steel}}{k_{FRP}}}} \quad (2-137)$$

where  $k_{steel} = E_s A_{sp} / \pi d_c$  and  $k_{FRP} = E_f t_f s / \pi d$ .

## 2-4-2 Cyclic Material Models

Cyclic behavior of reinforcing steel and concrete, especially core concrete, significantly affects RC member cyclic behavior modeling. The following section presents cyclic rules proposed in the literature to simulate cyclic behavior of reinforcing steel, concrete confined by conventional lateral steel, and FRP.

### 2-4-2-1 Steel

#### 2-4-2-1-(a) Linear Hysteretic Model

A linear hysteretic model uses a linear function with slope equal to modulus elasticity of steel in order to model unloading and reloading branches of steel's cyclic behavior. Stiffness degradation is not considered in this model; therefore, calculated results using the linear hysteretic model are not as accurate as results obtained using a more realistic hysteretic model.

The monotonic model used in conjunction with the linear model as the envelope of the hysteretic model may or may not consider the strain hardening effect.

#### 2-4-2-1-(b) Ramberg-Osgood Model

The Ramberg-Osgood equation is given as

$$\varepsilon_s - \varepsilon_{si} = \frac{f_s}{E_s} \left( 1 + \left| \frac{f_s}{f_{ch}} \right|^{r-1} \right) \quad (2-138)$$

where  $\varepsilon_s$ ,  $\varepsilon_{si}$ ,  $f_s$ ,  $E_s$ ,  $f_{ch}$ , and  $r$  are steel strain, steel strain at zero stress at the beginning of loading, steel stress, steel modulus of elasticity, stress dependent on yield strength and plastic strain of steel from previous loading, and parameters depending on the loading run number.

#### 2-4-2-1-(c) Balan et al. Model

Balan et al. developed a macroscopic cyclic model. The backbone of this model is expressed as

$$f_s = f_y' \frac{(1-\rho')}{2} \left[ 1 + \frac{(1+\rho')}{(1-\rho')} \times \frac{\varepsilon_s - \varepsilon_s'}{\varepsilon_y'} - \sqrt{\left( \frac{\varepsilon_s - \varepsilon_s'}{\varepsilon_y'} - 1 \right)^2 + \delta'} \right] \quad (2-139)$$

where

$$f_y' = \begin{cases} f_y & \varepsilon_s - \varepsilon_0 \leq \varepsilon_{sh} \\ E_s \times \varepsilon_y' & \varepsilon_s - \varepsilon_0 > \varepsilon_{sh} \end{cases} \quad (2-140)$$

$$\rho' = \begin{cases} 0 & \varepsilon_s - \varepsilon_0 \leq \varepsilon_{sh} \\ \frac{E_h}{E_s} & \varepsilon_s - \varepsilon_0 > \varepsilon_{sh} \end{cases} \quad (2-141)$$



$$\delta' = \begin{cases} \delta_0 & \varepsilon_s - \varepsilon_0 \leq \varepsilon_{sh} \\ \left( \frac{\varepsilon_{sh} - 1}{\varepsilon_y} \right)^2 \times \delta_0 & \varepsilon_s - \varepsilon_0 > \varepsilon_{sh} \end{cases} \quad (2-142)$$

and

$$\varepsilon_0' = \begin{cases} \varepsilon_0 & \varepsilon_s - \varepsilon_0 \leq \varepsilon_{sh} \\ \varepsilon_0 + \left( \varepsilon_{sh} - \frac{f_y}{E_s} \right) & \varepsilon_s - \varepsilon_0 > \varepsilon_{sh} \end{cases} \quad (2-143)$$

$$\varepsilon_y' = \frac{1}{E_s(1-\rho')} \left[ (f_{su} - f_y) - (\varepsilon_{su} - \varepsilon_{sh}) E_s \rho' \right] \quad (2-144)$$

Differentiation of the envelope equation with respect to the strain leads to the tangent modulus on the envelope curve in the engineering coordinate:

$$E_t = \frac{E_s}{2} (1-\rho) \left[ \frac{(1+\rho)}{(1-\rho)} - \frac{\left( \frac{\varepsilon_s - \varepsilon_0}{\varepsilon_y'} - 1 \right)}{\sqrt{\left( \frac{\varepsilon_s - \varepsilon_0}{\varepsilon_y'} - 1 \right)^2 + \delta'}} \right] \quad (2-145)$$

Balan et al. considered three types of reversals:

- Reversal from yield plateau
- Reversal from strain hardening region
- Reversal from reversal curves.

Complete and incomplete reversals follow the same rules. The only difference between these three types of reversals is amplitude parameter. When an unloading/reloading occurs, stress-strain behavior of steel is simulated using a hyperbolic branch. Mathematical formulation of this branch in the engineering coordinate is given as:

$$f_s = {}^k f_y \frac{(1-\rho)}{2} \left[ 1 + \frac{(1+\rho)}{(1-\rho)} \times \frac{\varepsilon_s - {}^k \varepsilon_r}{{}^k \varepsilon_r} - \sqrt{\left( \frac{\varepsilon_s - {}^k \varepsilon_r}{{}^k \varepsilon_y} - 1 \right)^2} + {}^k \delta \right], \quad (k=0,1,\dots,n) \quad (2-146)$$

where  ${}^k \varepsilon_r$ ,  $\rho = E_h / {}^k E_u$ ,  ${}^k E_u$ ,  ${}^k f_y$ , and  ${}^k \varepsilon_y$  are reversal strain, instantaneous hardening, unloading modulus, instantaneous yield stress, and strain, respectively. Superscripts  $k$  in this formula indicate the unloading/reloading cycle number. All parameters with superscripts  $k$  are updated after each unloading/reloading cycle. Instantaneous stress and strain are calculated using the following equations:

$${}^k f_y = {}^k E_u \times {}^k \varepsilon_y, \quad (k=0,1,\dots,n) \quad (2-147)$$

where

$${}^k \varepsilon_y = \varepsilon_y \frac{\rho}{(1-\rho)} {}^k \varepsilon_0, \quad (k=0,1,\dots,n) \quad (2-148)$$

and

$${}^k \varepsilon_0 = {}^k \varepsilon_r - \frac{{}^k f_r}{{}^k E_u}, \quad (k=0,1,\dots,n) \quad (2-149)$$

In Eqs. (3-146) to (3-148),  ${}^k \varepsilon_0$ ,  $\varepsilon_y$ ,  ${}^k f_r$ , and  ${}^k \varepsilon_r$  are strain at the intersection of the instantaneous unloading asymptote and strain axis after  $k$ -reversal, initial yield strain in the engineering coordinate, stress, and stress after  $k$ -reversal. In the unloading/reloading branch equation,  ${}^k \delta$  is degradation parameter, defined as:

$${}^k \delta = \frac{\delta_0}{1-\rho} \left[ 1 + {}^k a \left( \frac{{}^k \varepsilon_p}{{}^k \varepsilon_y} \right)^2 \right], \quad (k=0,1,\dots,n) \quad (2-150)$$

where  ${}^k \varepsilon_p$  is plastic strain amplitude and  $\delta_0$  is initial value of  $\delta$  given as:

$$\delta_0 = \begin{cases} 0.005 & \text{Ordinary Steel (Grade 40 and 60)} \\ 0.01 & \text{High-Strength Steel} \end{cases} \quad (2-151)$$

and  ${}^k a$  is amplitude parameter, given as:

$${}^k a = \begin{cases} 6 & \frac{{}^k f_r - {}^{k-1} f}{f_y} \geq 2 \\ 3 & \frac{{}^k f_r - {}^{k-1} f}{f_y} < 2 \end{cases} \cdot \quad (2-152)$$

#### **2-4-2-1-(d) Esmaily and Xiao's Model (2005)**

Esmaily and Xiao's hysteretic model (2005) for steel is a multilinear model. At the reversal point, the unloading path is a linear function with a slope equal to modulus of elasticity of steel material. The Bauschinger effect is taken into account in this model by changing the slope of the first unloading branch into a portion of steel's modulus of elasticity. In order to more realistically simulate cyclic behavior of steel material, this ratio and the strain at which the slope change occurs differ in the second (tensile strain and compressive stress) and fourth (compressive strain and tensile stress) quarters compared to values in the first (tensile strain and stress) and third (compressive strain and stress) quarters. Hysteretic behavior of steel material can be changed using five ratios ( $P_1$ ,  $P_2$ ,  $P_3$ ,  $R_1$ , and  $R_2$ ) in Esmaily-Xiao's model. Stress-strain mathematical expressions of this model in one of the Point 1, 2, and 3, as shown in Figure 2-10 are defined by considering the previous stress and strain state ( $\varepsilon_p, f_p$ ).

At Point 1, no unloading/reloading had previously occurred; therefore, the envelope curve (monotonic model) is followed. At Point 2, the reversal branches are defined mathematically as:

$$f = \begin{cases} f_p + E_s (\varepsilon_s - \varepsilon_p) \leq f^{+Line(\varepsilon)} & \varepsilon > \varepsilon_p - \frac{f_p + P_1 f_y}{E_s} \\ P_1 f_y + P_3 E_s \left( \varepsilon - \varepsilon_p + \frac{f_p + P_1 f_y}{E_s} \right) \leq f^{-Line(\varepsilon)} & \varepsilon \leq \varepsilon_p - \frac{f_p + P_1 f_y}{E_s} \end{cases} \quad (2-153)$$

where

$$f^{+Line(\varepsilon)} = \left( \frac{f_u - P_4 f_y}{2\varepsilon_u} \right) \varepsilon + \frac{f_u + P_4 f_y}{2} \quad (2-154)$$

$$f^{-Line(\varepsilon)} = \left( \frac{f_u - P_4 f_y}{2\varepsilon_u} \right) \varepsilon - \frac{f_u + P_4 f_y}{2} \quad (2-155)$$

In Eqs. (2-153) to (2-155),  $f_u$ ,  $f_y$ , and  $\varepsilon_u$  are ultimate strength, yield strength, and rupture strain of steel, respectively.

At Point 3, the stress-strain reversal branch is similar to Point 2, with one exception:

$$f = P_1 f_y + P_2 E_s \left( \varepsilon - \varepsilon_p + \frac{f_p + P_1 f_y}{E_s} \right) \leq f^{-Line(\varepsilon)} \quad \varepsilon \leq \varepsilon_p - \frac{f_p + P_1 f_y}{E_s}. \quad (2-156)$$

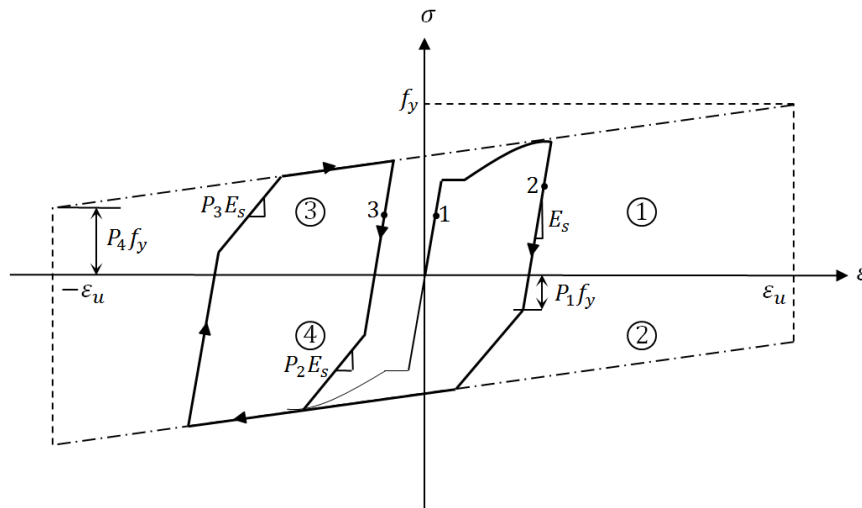


Figure 2-10 Esmaily and Xiao's cyclic model

## 2-4-2-2 Concrete

### 2-4-2-2-(a) Linear Model

Cyclic behavior of plain and confined concrete can be modeled using a linear model in which unloading and reloading curves are simplified using a line with a slope equal to the modulus of elasticity of the plain concrete. The linear cyclic model is shown in Figure 2-11. Although the linear model was developed to simulate hysteretic behavior of plain and concrete confined by lateral steel reinforcement, the linear model can also be used to model hysteric behavior of concrete confined by FRP or lateral steel and FRP.

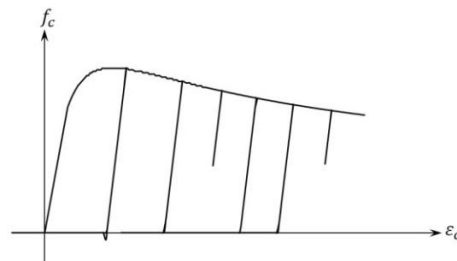


Figure 2-11 Linear cyclic model

### 2-4-2-2-(b) Park et al. Model (1972)

Kent and Park developed a cyclic model to model cyclic behavior of plain concrete and concrete confined by lateral steel. In this model, the unloading/reloading curve is approximated by a bilinear function. Although the envelope curve (monotonic model) for compressive behavior of concrete is represented by Kent and Park's function for concrete confined by lateral steel reinforcement, this model can be used in conjunction with any monotonic model as its envelope curve. Park et al. model is shown in Figure 2-12.

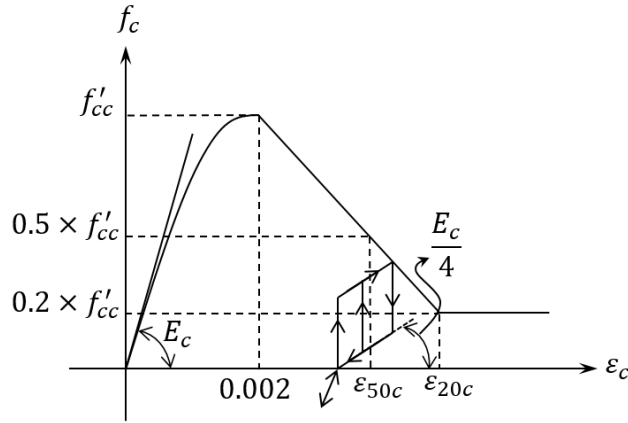


Figure 2-12 Park et al. model for hysteretic behavior of concrete

**2-4-2-2-(c) Kuramoto and Kabeyasawa Model (1995)**

Kuramoto and Kabeyasawa developed a linear model in which the slope of unloading/reloading branch can be tuned as needed, as shown in Figure 2-13. In this figure,  $\sigma_B$  is compressive strength of cover concrete (or plain concrete) and  $K$  is confinement coefficient. Initial stiffness of plain and confined concrete is considered to be equal to plain concrete modulus of elasticity, and secondary stiffness of plain and confined concrete is defined as a portion of initial stiffness.

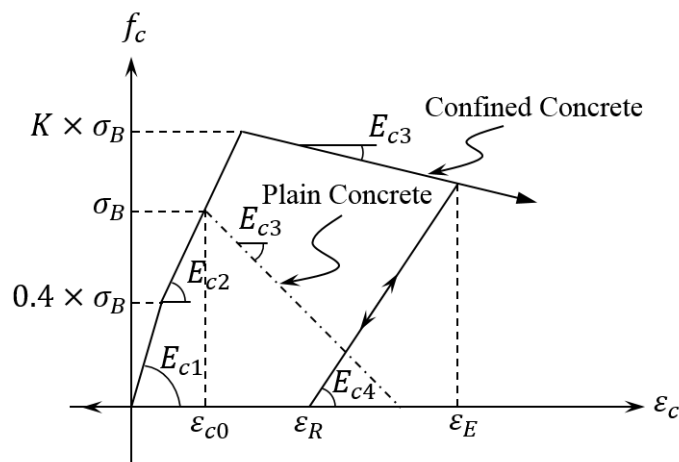


Figure 2-13 Kuramoto and Kabeyasawa model for hysteretic behavior of concrete

#### **2-4-2-2-(d) Mander et al. Model (1984)**

Mander et al. modified the hysteretic model developed by Takiguchi et al. to be suitable for plain and confined concrete. In the Mander et al. model, shown in Figure 2-14, the unloading path follows a concave-upward parabolic path with a zero-slope at the strain-axis. Tensile strength of concrete can be taken into account considering a linear path with a slope of plain concrete modulus of elasticity. With increased strain, stress remains zero up to the last strain corresponding to zero stress, after which point strain will grow in a linear reloading path with a slope equal to plain concrete modulus of elasticity in the strain-axis.

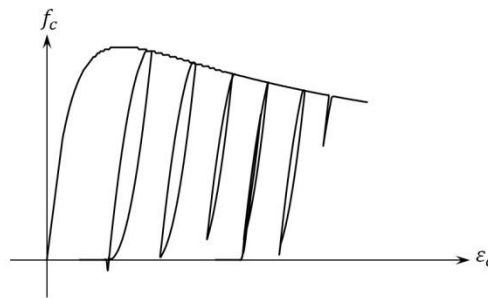


Figure 2-14 Mander et al. (1984) model for hysteretic behavior of concrete

#### **2-4-2-2-(e) Esmaily-Xiao Model (2005)**

In Esmaily-Xiao's cyclic model, shown in Figure 2-15, the unloading path follows a parabolic path that is concave-upward with a slope of  $E_{c2}$  on the envelope curve (monotonic curve). The monotonic model is followed for ascending and descending within the elastic range of concrete. With decreased strain at the unloading path, stress decreases to zero, after which point if the tensile strength is ignored, stress remains zero; otherwise, the stress decreases to

tensile strength using a linear function with a slope of  $E_{c1}$ . The mathematical expression of unloading branch is given as:

$$f_c = \frac{E_{c1}^2}{4f_{cc}'} \left( \varepsilon - \varepsilon_p - \frac{2\sqrt{f_{cc}' f_p}}{E_{c2}} \right)^2 \leq f_{cc}' \quad \varepsilon > \varepsilon_p - \frac{2\sqrt{f_{cc}' f_p}}{E_{c2}} \quad (2-157)$$

$$f_c = 0 \quad \varepsilon \leq \varepsilon_p - \frac{2\sqrt{f_{cc}' f_p}}{E_{c2}}$$

where  $f_c$ ,  $\varepsilon$ ,  $\varepsilon_p$ ,  $f_p$ ,  $E_{c1}$ , and  $f_{cc}'$  are stress, strain, strain and stress at the point from which unloading begins, initial stiffness of reloading branch, and maximum compressive strength, respectively.

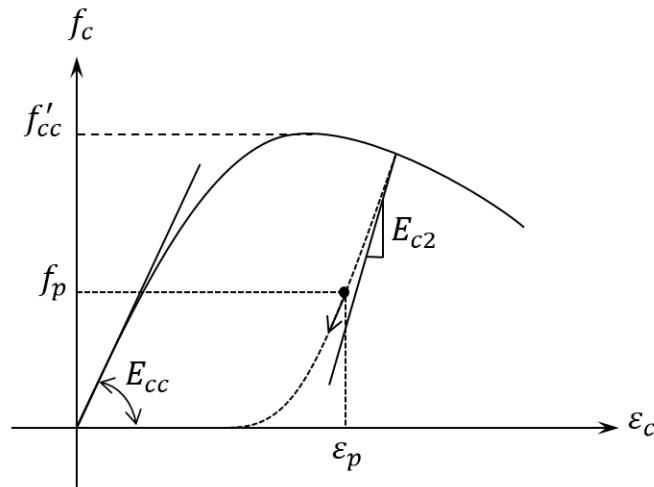


Figure 2-15 Esmaeily-Xiao hysteretic model for concrete, descending branch

With increased strain, the stress remains zero until the latest strain corresponding to zero stress; then stress increases following a concave-downward parabolic with a slope of  $E_{c1}$  at the strain-axis, as shown in Figure 2-16. The following parabolic function is followed for ascension from a point with strain  $\varepsilon_p$  and stress  $f_p$ :



$$f_c = -\frac{E_{c1}^2}{4f_{cc}'} \left( \varepsilon - \varepsilon_p + \frac{2f_{cc}'}{E_{c1}} - \frac{2\sqrt{f_{cc}'(f_{cc}' - f_p)}}{E_{c1}} \right)^2 - E_{c1} \left( \varepsilon - \varepsilon_p + \frac{2f_{cc}'}{E_{c1}} - \frac{2\sqrt{f_{cc}'(f_{cc}' - f_p)}}{E_{c1}} \right) \quad (2-158)$$

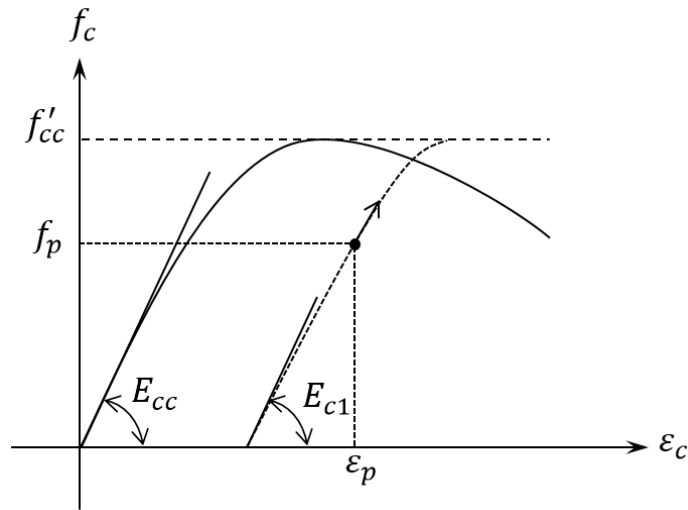


Figure 2-16 Esmaeily-Xiao hysteretic model for concrete, ascending branch

#### 2-4-2-2-(f) Shao, Zhu, and Mirmiran Model (2006)

Shao et al. developed a model for predicting behavior of FRP-wrapped concrete cylinders using experimental data. Experimental data was developed by testing 24 concrete cylinders with dimensions of 152 mm by 305 mm tall. Cylinders were wrapped with carbon or glass FRP and then loaded cyclically. During cylinder testing, the discovery was made that using one layer of FRP wrap was only beneficial in increasing cylinder ductility but failed to increase compressive strength (Zhao et al. 2006). Researchers also discovered that the Glass-FRP caused the cylinder to have increased ductility, but Carbon-FRP caused ultimate strengths to increase more than Glass-FRP (Zhao et al. 2006). The concluding observation from testing showed that a thick wrap

would potentially cause the cylinder to fail during unloading because the FRP squeezes the cylinder after loading.

After completing testing on 24 cylinders, a model was developed by Shao et al. to explain observed cyclic behavior. The model is a bilinear curve. The concrete core's modulus governs the first part of the stress-strain curve and the FRP jacket controls the latter part of the curve. The stiffness of each part is a primary factor in the curve's response, given by:

$$f_c = \frac{(E_1 - E_2)\varepsilon_c}{\left[1 + \left(\frac{(E_1 - E_2)\varepsilon_c}{f_o}\right)^n\right]^{1/n}} + E_2\varepsilon_c \quad (2-159)$$

where  $E_1$  and  $E_2$  are slopes of the response, given by:

$$E_1 = 3950\sqrt{f'_{co}} \quad (2-160)$$

$$E_2 = 245.61f'_{co}{}^{0.2} + 1.3456\frac{E_j t_j}{D}$$

where  $E_j$  is the modulus of elasticity of FRP,  $t_j$  is jacket thickness, and  $f'_{co}$  is unconfined strength of the concrete. In addition,  $n$  is 1.5 and  $f_o$  and  $f_r$  are given by:

$$f_o = 0.872f'_{co} + 0.371f_r + 6.258 \quad (2-161)$$

$$f_r = \frac{f_j t_j}{D}$$

where  $f_j$  is tensile strength of the wrap. Ultimate strength of FRP-confined concrete is given by:

$$f'_{cu} = f'_{co} + 6.0f_r{}^{0.7} \quad (2-162)$$

which can be used to find ultimate strain using

$$\varepsilon_c = \frac{f'_{cu} - f_o}{E_2} \quad (2-163)$$

The unloading branch of the response curve was found by developing a model for the secant modulus, given by:

$$E_{Secu} = \frac{f_{un}}{\varepsilon_{un} - \varepsilon_{pl}} \quad (2-164)$$

where  $f_{un}$  and  $\varepsilon_{un}$  are stress and strain at unloading, respectively, and  $\varepsilon_{pl}$  is the plastic strain, given by:

$$\varepsilon_{pl} = \varepsilon_{un} - \frac{f_{un}}{E_{secu}} \quad (2-165)$$

Shao et al. discovered a linear correlation between the secant modulus of unloading and  $E_c$ . Analyzing data, a tri-linear model was adopted for  $E_{secu}$ , given by:

$$\frac{E_{secu}}{E_1} = \begin{cases} 1, 0 \leq \frac{f_{un}}{f'_{co}} < 1 \\ -0.44 * \frac{f_{un}}{f'_{co}} + 1.44, 1 \leq \frac{f_{un}}{f'_{co}} < 2.5 \\ 0.34, \frac{f_{un}}{f'_{co}} > 2.5 \end{cases} \quad (2-166)$$

Using the above correlation, the unloading response was determined by the following equations:

$$x = \frac{\varepsilon_c - \varepsilon'_{un}}{\varepsilon_{pl} - \varepsilon'_{un}} \quad (2-167)$$

$$f_c = \frac{(1-x)^2}{(1+2x)^2} f'_{un}$$

#### **2-4-2-2-(g) Lam and Teng Model (2009)**

Lam and Teng used the monotonic model proposed for stress-strain behavior of confined concrete with FRP under monotonic loading as an envelope curve for their cyclic model. Based on experimental works, Lam and Teng concluded that the unloading path for FRP-confined concrete is highly nonlinear except in the initial loading stage. They highlighted two primary observations:

- The degree of nonlinearity or curvature of the unloading path increases by increasing the strain.
- The slope of the unloading path at zero stress usually is nonzero; when the unloading strain increases, this value consequently increases.

Based on Lam and Teng's observations, Shao's cyclic stress-strain model is inadequate for predicting the unloading path because he considered only a small range of strain in his studies. The following equation describes the unloading path in Lam and Teng's model:

$$\sigma_c = a\varepsilon_c^\eta + b\varepsilon_c + c \quad (2-168)$$

where

$$a = \frac{\sigma_{un} - E_{un,0}(\varepsilon_{un} - \varepsilon_{pl})}{\varepsilon_{un}^\eta - \varepsilon_{pl}^\eta - \eta\varepsilon_{pl}^{\eta-1}(\varepsilon_{un} - \varepsilon_{pl})} \quad (2-169)$$

$$b = E_{un,0} - \eta\varepsilon_{pl}^{\eta-1}(\varepsilon_{un} - \varepsilon_{pl})$$

$$c = -a\varepsilon_{pl}^\eta - b\varepsilon_{pl}$$

In Eqs. (3-168),  $\eta$  is an exponent and  $E_{un,0}$  is slope of the unloading path at zero stress, defined as

$$\eta = 350\varepsilon_{un} + 3$$

$$E_{un,0} = \min \left\{ \begin{array}{l} \frac{0.5f_{c0}'}{\varepsilon_{un}} \\ \frac{\sigma_{un}}{\varepsilon_{un} - \varepsilon_{pl}} \end{array} \right. \quad (2-170)$$

Based on Lam and Teng's observations from experimental work, they used a linear function as a main part of the reloading path, which continues with a parabola in order to reach the monotonic envelope curve. The defined linear portion of the reloading path is

$$\sigma_c = \sigma_{re} + E_{re}(\varepsilon_c - \varepsilon_{re}) \quad \varepsilon_{re} \leq \varepsilon_c \leq \varepsilon_{ref} \quad (2-171)$$

where

$$E_{re} = \frac{\sigma_{new} - \sigma_{re}}{\varepsilon_{ref} - \varepsilon_{re}} \quad \varepsilon_{re} \leq \varepsilon_c \leq \varepsilon_{ref} \quad (2-172)$$

In Eqs. (3-170) and (3-171),  $\varepsilon_{ref}$  is reference strain depending on the number of cycles. In order to evaluate the degree of stress deterioration under repeated unloading/reloading cycles and define the reloading path, the reference strain must be defined as follows:

$$\varepsilon_{ref,1} = \varepsilon_{un,env} \quad \text{and} \quad \sigma_{ref,1} = \sigma_{un,env}$$

$$\varepsilon_{ref,n} = \begin{cases} \varepsilon_{ref,n-1} & \varepsilon_{un,n} \leq \varepsilon_{ref,n-1} \\ \varepsilon_{un,n} & \varepsilon_{un,n} > \varepsilon_{ref,n-1} \end{cases} \quad (2-173)$$

$$\sigma_{ref,n} = \begin{cases} \sigma_{ref,n-1} & \varepsilon_{un,n} \leq \varepsilon_{ref,n-1} \\ \sigma_{un,n} & \varepsilon_{un,n} > \varepsilon_{ref,n-1} \end{cases}$$

When the reference strain is defined,  $\sigma_{new}$  is calculated using linear portion. Once the linear portion is calculated, the parabolic portion is defined. The following assumptions define the second portion:

- (a) The parabola starts from the reference point  $(\varepsilon_{ref}, \sigma_{new})$ .
- (b) The initial slope of the parabola is equal to  $E_{re}$ .
- (c) The slope of the parabola at the point which reaches the monotonic curve is equal to the envelope curve defined by the monotonic curve.

The parabola expression is as follows:

$$\sigma_c = A\varepsilon_c^2 + B\varepsilon_c + C \quad \varepsilon_{ref} \leq \varepsilon_c \leq \varepsilon_{ret,env} \quad (2-174)$$

where  $A$ ,  $B$ , and  $C$  are constants that must be determined.  $A$ ,  $B$  and  $C$  are calculated as follows:

$$B = E_{re} - 2A\varepsilon_{ref}$$

$$C = \sigma_{new} - A\varepsilon_{ref}^2 - B\varepsilon_{ref} \quad (2-175)$$

As mentioned, the first linear portion continues with the parabolic portion in order to obtain the envelope curve. However, in the following cases the line portion continues to the envelope curve:

Case (1) - When  $\varepsilon_{un,env} \leq 0.001$ , so  $\varepsilon_{un,env} = \varepsilon_{ret,env,n}$  for any value  $n$ .

Case (2) - When  $\varepsilon_{un,env} > 0.001$ : for  $n=1$ ,  $\varepsilon_{ret,env,1} = \varepsilon_{un,env}$  if  $\sigma_{re,1} \geq 0.85 \times \sigma_{un,env}$  and

$\varepsilon_{ret,env,n-1} = \varepsilon_{un,env}$  if both  $\sigma_{re,1} \geq 0.85 \times \sigma_{un,env}$  and  $\varepsilon_{ret,env,1} = \varepsilon_{un,env}$  are satisfied.

For Cases (1) and (2), the following equation must be used to calculate the slope of the linear portion:

$$E_{re} = \frac{\sigma_{un,env} - \sigma_{re}}{\varepsilon_{un,env} - \varepsilon_{re}} \quad \varepsilon_{re} \leq \varepsilon_c \leq \varepsilon_{ref} . \quad (2-176)$$

#### **2-4-2-2-(h) Varma, Barros and Sena-Cruz Model (2009)**

Varma and Barros (2009) proposed a stress-strain model to model CFRP-confined, short, circular concrete columns under cyclic and monotonic loading. The theoretical cyclic stress-strain model proposed for cyclic loading is based on a three-sectioned monotonic model. The three zones (I, II, and III) are defined by a linear section, a nonlinear transition section, and another nonlinear transition section. The third section (Zone III) is the only zone significantly influenced by FRP. These regions are illustrated in Figure 2-17. Zone I uses the following equations for the region  $0 \leq \varepsilon_c \leq \varepsilon_{cp}$ :

$$\begin{aligned} f_c &= E_{ci} \times \varepsilon_c \\ E_c &= E_{ci} \\ \varepsilon_{cp} &= \beta \times \varepsilon_{c0,UPC} \end{aligned} \quad (2-177)$$

where  $E_{ci}$  is initial modulus of elasticity for the concrete evaluated experimentally or by applicable code equations and  $\beta=0.4$ .  $\varepsilon_{c0,UPC}$  is strain corresponding to axial compressive strength of unconfined, plain concrete. Zone II uses the following equations for the region  $\varepsilon_{cp} \leq \varepsilon_c \leq \varepsilon_{cQ}$ :

$$f_c = f_{ca} \times (\varepsilon_c - \varepsilon_{ca}) \left[ E_{ca} + A |\varepsilon_c - \varepsilon_{ca}|^R \right]$$

$$E_c = E_{ca} + A(R+1) |\varepsilon_c - \varepsilon_{ca}|^R$$

$$R = \frac{E_{ca} - E_{c,sec}}{E_{c,sec} - E_{cb}} \quad \text{and} \quad A = \frac{E_{c,sec} - E_{ca}}{|\varepsilon_{cb} - \varepsilon_{ca}|^R} \quad (2-178)$$

$$E_{c,sec} = \frac{f_{cb} - f_{ca}}{\varepsilon_{cb} - \varepsilon_{ca}}$$

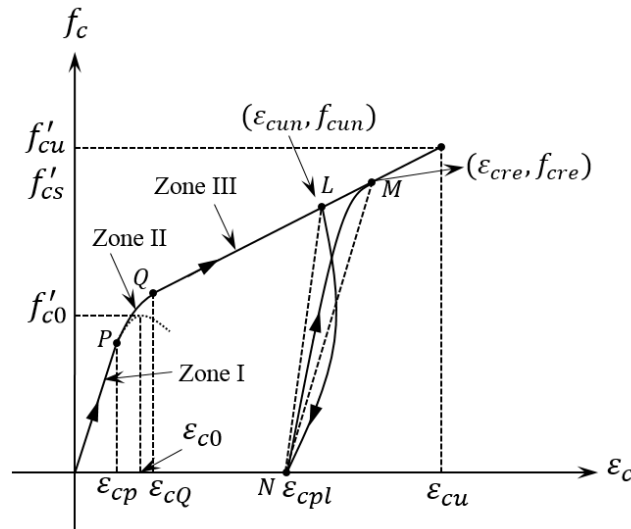


Figure 2-17 Schematic of FRP-confined envelope curve

The transition zone begins from the end of Zone I ( $\varepsilon_{ca}$ ,  $f_{ca}$ ) and ends at the start of Zone III ( $\varepsilon_{cb}$ ,  $f_{cb}$ ). In Figure 2-17, these points are labeled  $P$  and  $Q$ , respectively. Zone II uses the following equations for the region  $\varepsilon_{cQ} \leq \varepsilon_c \leq \varepsilon_{cu}$ :

$$f_c = f_{c0,UPC} + k_1 f_l$$

$$\varepsilon_c = \varepsilon_{c0,UPC} \left[ 1 + k_2 \left( \frac{f_c}{f_{c0,UPC}} - 1 \right) \right] \quad (2-179)$$

$$f_l = f_{fl} + f_{sl} \times \frac{A_{cc}}{A_g}$$

Equations for Zone III (confined concrete) are taken from Harajli's (2006) paper. The remaining equations associated with Varma et al. (2009) model are described in Section 2-4-1-5-(a). The cyclic model was developed to predict four loading conditions:

- Complete unloading and complete reloading ( $A$  to  $B$  to  $C$  to  $D$ )
- Partial unloading and complete reloading ( $A$  to  $B'$  to  $C'$  to  $D'$ )
- Complete unloading and partial reloading ( $A$  to  $B$  to  $E'$ )
- Random loading ( $A$  to  $B'$  to  $E''$  to  $F'''$ )

These four unloading and reloading cases are shown in Figure 2-18. Shifts in stress and strain (denoted as  $\Delta\varepsilon_c$  and  $\Delta f_c$ ) are commonly observed in a confined concrete cyclic loading cycle because of change in stiffness (moduli) in which the reloading branch always rejoins the loading curve at a higher strain than the unloading strain.



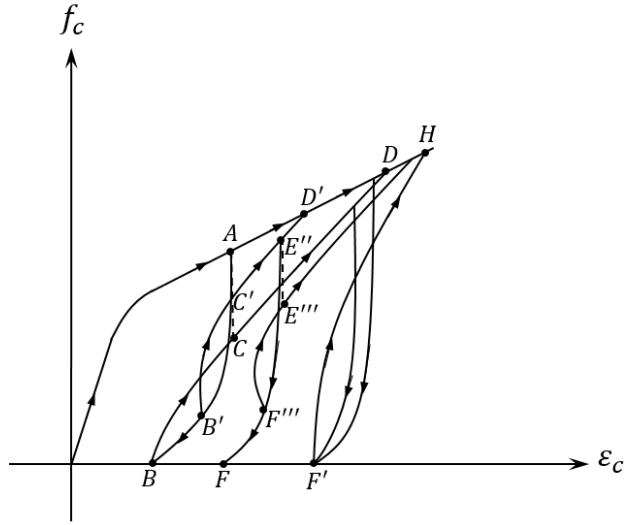


Figure 2-18 Schematic of FRP-confined concrete cyclic model

The unloading portion of the cyclic stress-strain model uses the same equations as the transition zone (Zone II) equations. Points B, C, and D represent the three points of interest in a complete reloading cycle. This curve is represented by

$$f_{cnew} = f_{cum} - \Delta f_c \quad \text{From B to C}$$

$$E_{cnew} = \frac{f_{cnew}}{\epsilon_{un} - \epsilon_{cpl}} \quad \text{From B to C}$$

$$f_{cre} = E_c \times \epsilon_{cre} \quad \text{From C to D}$$

$$\epsilon_{cre} = \epsilon_{cum} + \Delta \epsilon_c \quad \text{From C to D}$$

$$E_{cre} = E_c \times \epsilon_{cre} \quad \text{From C to D}$$

(2-180)

where

$$\epsilon_{cpl} = \epsilon_{cum} - \frac{f_{cum}}{E_{csecu}}$$

$$\Delta f_c = 0.14 f_{cum,g} \left( \left| \frac{\epsilon_{cum,g}}{\epsilon_{cu}} \right| \right)^{0.15}$$

(2-181)

$$\Delta \varepsilon_c = 0.19 \times \varepsilon_{cun}$$

where  $\varepsilon_{cpl}$  is concrete plastic strain,  $f_{cnew}$  is new value of stress corresponding to the unloading strain ( $\varepsilon_{cun}$ ), and  $f_{cun}$  is stress on FRP-confined concrete at unloading before load reversal. Equations from Points C to D (denoted with subscript “cre”) correspond to returning stress, strain, and modulus of elasticity.

Partial unloading allows for complete or partial reloading. Both curves calculate modified intermediate ( $C'$ ) and returning points ( $D'$ ). Stresses and strains associated with partial unloading are assumed to be between the envelope curve and the complete unloading curve. Varma et al. (2009) denotes these partial points with an asterisk. Partial unloading equations are as follows:

$$f_{cnew}^* = f_{cun} - \Delta f_c \frac{\varepsilon_{cun} - \varepsilon_{cro}}{\varepsilon_{cun} - \varepsilon_{cpl}} \quad \text{From } B' \text{ to } C'$$

$$E_{cnew}^* = \frac{f_{cnew}^* - f_{cro}}{\varepsilon_{cun} - \varepsilon_{cro}} \quad \text{From } B' \text{ to } C'$$

$$\varepsilon_{cre}^* = \varepsilon_{cun} - \Delta \varepsilon_c \frac{\varepsilon_{cun} - \varepsilon_{cro}}{\varepsilon_{cun} - \varepsilon_{cpl}} \quad \text{From } C' \text{ to } D'$$

$$E_{cre}^* = E_c \times \varepsilon_{cre}^* \quad \text{From } C' \text{ to } D'$$

$$f_{cre}^* = f_c \times \varepsilon_{cre}^* \quad \text{From } C' \text{ to } D'.$$
(2-182)

In addition, experimental results revealed that an imaginary unloading strain ( $\varepsilon_{cun}^*$ ) was valid to connect the “previous envelope unloading strain and the envelope reloading strain” (Varma et al. 2009) for future load responses of a partial unloaded curve.

$$\varepsilon_{cun}^* = \varepsilon_{cun} + \left( \frac{\varepsilon_{ce'} - \varepsilon_{cun}}{\varepsilon_{cre} - \varepsilon_{cpl}} \right) (\varepsilon_{cre} - \varepsilon_{cun})$$
(2-183)

### 2-4-3 Plastic Hinge Models

Plastic hinge length of RC members is defined as the length over which a concrete section experiences severe damage. Three physical zones in the plastic hinge of RC members include longitudinal steel yielding, concrete crushing, and curvature concentration zone (Jiang et al. (2014)). Extensive damage of the plastic hinge zone, typically occurring at sections with bending moment larger than bending moment corresponding to section yielding, can be observed in the following forms: comprehensive crushing of the concrete cover, concrete core damage, inelastic buckling of longitudinal steel, and lateral steel yielding or FRP rupture (Ho and Pam 2003). For practical purposes, equivalent plastic hinge length,  $L_p$ , is defined as the length over which plastic deformation occurs with constant distribution of plastic curvature. This constant curvature, known as maximum plastic curvature,  $\phi_p$ , is assumed to be equal to the difference between maximum curvature,  $\phi_m$ , and yield curvature,  $\phi_y$  :

$$\phi_p = \phi_m - \phi_y \quad (2-184)$$

However, plastic rotation can be related to  $L_p$  and  $\phi_p$  as follows:

$$\theta_p = \theta_p \times L = (\theta_m - \theta_y) \times L_p \quad (2-185)$$

The assumption is made that plastic rotation,  $\theta_p$  is concentrated at mid-height of the plastic hinge. Therefore, plastic displacement at the top of the cantilever,  $\Delta_p$  can be obtained by the following expression:

$$\Delta_p = \Delta_{\max} - \Delta_y = \theta_p (1 - 0.5 \times L_p) = (\phi_m - \phi_y) \times L_p \times (L - 0.5 \times L_p) \quad (2-186)$$

where  $L$  is column length,  $\Delta_{\max}$  is maximum displacement at the top of the cantilever, and  $\Delta_y$  is yield displacement given by the following equation:

$$\Delta_y = \phi_y \times L^2 / 3 \quad (2-187)$$

The presented procedure to determine  $L_p$  with respect to  $\Delta_{max}$  and  $\Delta_y$  has been implemented in many researches to determine plastic hinge length from moment-curvature and lateral load-lateral displacement relationships.

RC member plastic hinge research can be categorized according to variables such as the type of reinforcing material (FRP/steel), concrete strength, section geometry, and load pattern. Work presented herein consisted of studies categorized based on their consideration of the effect of load patterns on plastic hinge determination:

- No axial load
  1. Monotonic lateral load/displacement
  2. Cyclic lateral load/displacement
- Constant axial load
  1. Monotonic lateral load/displacement
  2. Cyclic lateral load/displacement
    - Uniaxial
    - Biaxial
- Variable axial load
  1. Cyclic lateral load/displacement
    - Uniaxial
    - Biaxial

However, few researches have been applicable to RC members under variable axial load (Blakeley et al. (1971), Hachem et al. (2003), Esmaily et al. (2005), Phan et al. (2007), Mortezaei et al. (2012), and Mortezaei (2014)) or biaxial lateral load/displacement (Hachem et

al. (2003), Esmaily et al. (2005), Alemdar (2010), and Biskinis et al. (2010)). Among reviewed papers in the current study, the only method applicable to all possible load patterns, including constant and variable axial loading with monotonic and cyclic biaxial lateral load/displacement, is presented in research reported by Esmaily et al. (2005). Assuming that load pattern considerably affects RC member behavior, additional experimental and analytical studies should be undertaken to provide increased understanding of the behavior of the plastic hinge region of RC columns subjected to various load patterns. For example, investigation of variable axial load effects on the behavior of structural elements is essential because observations from previous earthquakes have indicated that structures subjected to near-fault ground motions experience more severe damage compared to structures under far-fault ground motions. Following, it is a review of existing plastic hinge models.

#### **2-4-3-1 No Axial Load-Monotonic Lateral Load/Displacement**

Cohn et al. (1963) tested two series of five two-span continuous reinforced concrete beams under monotonic concentrated load. Steel ratios at critical sections differed in each beam specimen. Calculated plastic hinge lengths from test data were within the range of  $0.3d$  to  $0.9d$  where  $d$  is effective depth of the beam section.

Mattock (1965) tested 37 simple-span beams under concentrated load. Test variables included concrete strength, beam depth, amount and yield point of reinforcement, and distance from point of maximum moment to point of zero moment. Based on test results for identical degrees of reinforcement,  $((q - q') / q_b)$  plastic hinge length increased with increased ratio  $z / d$  where  $q = \rho \times f_y / f_c'$  is tension reinforcement index,  $q' = \rho' \times f_y / f_c'$  is compression

reinforcement index,  $q_b = \rho_b \times f_y / f_c'$  is tension reinforcement for balanced ultimate strength conditions,  $z$  is distance from section of maximum moment to adjacent section of zero moment (in.),  $d$  is distance from extreme compressive fiber to centroid of tensile reinforcement (in.),  $\rho$  and  $\rho'$  are tensile and compressive steel ratios, respectively,  $f_y$  is yield point stress of tension reinforcement, and  $f_c'$  is concrete cylinder strength. In addition, for the same ratio  $z/d$ , plastic hinge length decreased with increased degree of reinforcement. By analyzing test data, Mattock proposed the following equation to estimate plastic hinge length:

$$L_p = \frac{d}{2} \left[ 1 + \left( 1.14 \sqrt{\frac{z}{d}} - 1 \right) \times \left( 1 - \frac{q - q'}{q_b} \right) \sqrt{\frac{d}{16.2}} \right] \quad (2-188)$$

Corley et al. (1966) presented test results of 40 simple-span beams under concentrated load. These tests were an extension of tests conducted by Mattock (1965). Test variables included size of specimens, confinement of concrete in compression, moment gradient, tensile reinforcement ratio, and size of loaded area. Based on test results of this study, the following equation was proposed for plastic hinge length:

$$L_p = \frac{d}{2} + \frac{0.2Z}{\sqrt{d}} \quad (2-189)$$

where  $z$  is the distance along the span from section of maximum moment to adjacent section of zero moment (in.) and  $d$  is the distance from extreme compression fiber to centroid of tension reinforcement (in.).

Riva et al. (1990) derived an expression to estimate plastic hinge length using a computer lumped-plasticity program, STRUPL-LC. A parametric study on 56 simply supported and 32 cantilevered reinforced and pre-stressed concrete beams tested under monotonic distributed or point loads was conducted. Variables of this study included section shape, mechanical

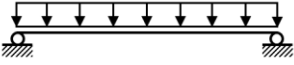
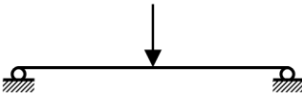
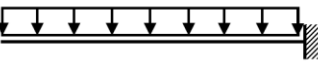
percentage of tension steel,  $q$ , mixed reinforcing steel,  $\gamma$ , load distribution, structural configuration, boundary conditions, and pre-stressing cable layout. Terms  $q$  and  $\gamma$  are defined as follows:

$$q = \frac{A_p \times f_{pu} + A_s \times f_{sl}}{b_w \times d \times f'_c} \quad (2-190)$$

$$\gamma = \frac{A_p \times f_{pu}}{A_p \times f_{pu} + A_s \times f_{sl}}$$

where  $f_{pu}$  is ultimate pre-stressing steel stress,  $f_{sl}$  is reinforcing steel stress at the limiting strain,  $f'_c$  is concrete compressive strength,  $d$  is effective depth of the section,  $b_w$  is web width of the section,  $A_s$  is the reinforcing steel area, and  $A_p$  is the pre-stressing steel area.

Table 2-1 Numerical constants of Eqs. (3-189) to (3-192) (Riva et al. (1990))

Beam Model	A	B	C	D	E	F	G	$f(\gamma)$
	0.58	3.0	3.5	3.0	5.0	6.5	0.5	$(1 - 0.50\gamma^{3/2})^{1/10q}$
	0.39	7.0	6.5	5.0	5.4	0.0	0.75	$(1 - 0.75\gamma^{3/2})^{1/10q}$
	0.25	7.0	8.0	6.0	2.8	0.0	0.8	$1 - 0.80\gamma$

Three plastic hinge length equations were defined for three states of  $\phi_p / \phi_{py}$ , where  $\phi_p$  is plastic curvature and  $\phi_{py}$  is yielding curvature. These three stages and corresponding plastic hinge length equations are:

1. From cracking to yielding limit state ( $\phi_p / \phi_{py} \leq 1.0$ ). In this stage, plastic hinge length increases from zero to its maximum value at yielding limit state.

$$\frac{L_P}{z} = \left( A - \frac{B}{1000 \times q} \right) \times \left( \frac{\phi_p}{\phi_{py}} \right)^{c/100q} \times \left( \frac{b'}{b_w} \right)^{-p/1000q^2} \times f(\gamma) \quad (2-191)$$

2. From yielding to reinforcement strain-hardening ( $1.0 \leq \phi_p / \phi_{py} \leq 7.0$ ). In this stage plastic hinge length drastically decreases.

$$\frac{L_P}{z} = \left( A - \frac{B}{1000 \times q} \right) \times \left( \frac{\phi_p}{\phi_{py}} \right)^{-(0.9-0.8\gamma)} \times \left( \frac{b'}{b_w} \right)^{-p/1000q^2} \times f(\gamma) \quad (2-192)$$

3. Ultimate limit state ( $\phi_p / \phi_{py} > 7.0$ ). In this stage, plastic hinge length increases up to the value corresponding to the ultimate limit state.

$$\frac{L_P}{z} = \left( \frac{E}{100} + \frac{F}{1000} \times \frac{\phi_{pu}}{\phi_{py}} \right) \times \left( \frac{b}{b_w} \right)^G \quad (2-193)$$

where  $L_P$  is plastic hinge length,  $z$  is abscissa of the contraflexure point, and  $b$  and  $b'$  are compression flange and tension flange width, respectively. A, B, C, D, E, F, G, and  $f(\gamma)$  approximated by regression analysis are based on bending moment distribution. These values correspond to various loading and support conditions, as shown in Table 2-1.

Zhao et al. (2011) used FEM to study plastic hinge length involving three physical zones: rebar yielding, concrete crushing, and curvature concentration. In their study,  $L_{sy}$ ,  $L_{cs}$ ,  $L_{pc}$ , and  $L_{pcs}$  were defined as maximum length of the rebar yielding zone, concrete crushing zone, curvature increasing zone, and curvature localization zone, respectively. The curvature increasing zone is the region in which increased curvature and insignificant increase in other parts are observed. The curvature localization zone is the region of curvature concentration during plastic rotation. Zhao et al. believed that dominant deformation in plastic hinge is flexural, so members with small aspect ratio were not considered. A parametric study to evaluate the effect of yield strength



of reinforcing steel ( $f_y$ ), strain hardening stiffness of steel bar ( $E_{sh}$ ), compressive strength of concrete ( $f_c'$ ) shear span of beam ( $z$ ), effective depth of beam ( $d$ ), tension and compression reinforcement ratios ( $\rho_s$  and  $\rho_{sc}$ , respectively), tension rebar diameter ( $d_b$ ), and aspect ratio  $z/h$  on  $L_{sy}$ ,  $L_{cs}$ ,  $L_{pc}$ , and  $L_{pcs}$  was conducted. Results of this study indicated that  $L_{sy}$  has the maximum value compared to lengths of other zones: Its value is less than two times the effective depth. Empirical plastic hinge lengths reported in the literature were close to  $L_{sy}$  and  $L_{pc}$  but different from  $L_{cs}$  and much larger than  $L_{pcs}$ . Results of this study indicated a clear trend of increasing  $L_{cs}$ ,  $L_{sy}$ ,  $L_{pc}$ , and  $L_{pcs}$  with an increase in beam aspect ratio, effective depth, and strain hardening stiffness of steel bar for normal range of strain hardening stiffness. However,  $L_{sy}$ ,  $L_{pc}$  did not show a clear trend of increased  $f_y$  unless the effect of strain hardening stiffness of steel bar was considered. In this case,  $L_{sy}$ ,  $L_{pc}$  increased with an increase in  $f_y$ ,  $L_{sy}$ , and  $L_{pc}$  increased with an increase in  $\rho_s$  before rebar yielding and concrete crushing point, after which the opposite trend was observed. For smaller values of  $d_b$ , increase in  $d_b$  caused an increase in  $L_p$ . However, for bars with a very large diameter,  $L_{sy}$ ,  $L_{pc}$  increased if  $f_c'$  increased. For smaller values of  $\rho_{sc}$ , no significant trend was observed, while for larger values of  $\rho_{sc}$ , length of yielding zone increased when  $\rho_{sc}$  increased. A comparison of numerical results of this study and those of available empirical studies indicated that plastic hinge length given by Paulay and Priestley yielded the closest value to plastic hinge length obtained from this study. In addition, proposed models by Corley, Mattock, and Sawyer overestimated plastic hinge length for  $E_{sh}$  less than or equal to zero and underestimated plastic hinge length for  $E_{sh}$  greater than zero. Among

the studied parameters,  $\rho_s$ ,  $\rho_{sc}$ ,  $E_{sh}$ , and  $d$ , had the most significant effect on plastic hinge length.

Zhao et al. (2014) tested five groups of simply supported reinforced concrete beams with rectangular cross sections under two symmetrical monotonic loads. Test results indicated that equivalent plastic hinge length was approximately equal to beam depth ( $h$ ) for all specimens tested in this study.

Gopinath et al. (2014) conducted a parametric study on 173 test data from the literature to determine plastic hinge length of simply supported beams under central point loading. Variable parameters included strength of concrete, yield strength of steel reinforcement, geometrical dimensions of beams, reinforcing ratio, support conditions, and load configuration. Based on results of this study,  $L_p$  decreases with an increase in beam depth and reinforcement percentage does not affect plastic hinge length. Among the studied variables, effective depth of the beam had the largest correlation with plastic hinge length. The proposed equation to predict plastic hinge length is as follows:

$$L_p = \frac{2 \times z \times (M_u - M_y)}{M_u} \quad (2-194)$$

Variable parameters are defined in Figure 2-19  $M_y$  and  $M_u$  are yield moment and ultimate moment, respectively, given by the following equations:

$$\begin{aligned} M_y &= 0.87 \times f_y \times A_{st} \times (d - 0.42 \times X_y) \\ M_u &= 0.87 \times f_y \times A_{st} \times (d - 0.42 \times X_u) \end{aligned} \quad (2-195)$$

where  $f_y$  and  $A_{st}$  are yield strength and area of tension reinforcement, respectively.  $X_y$  and  $X_u$  are neutral axis depth at yield load and ultimate load, respectively.

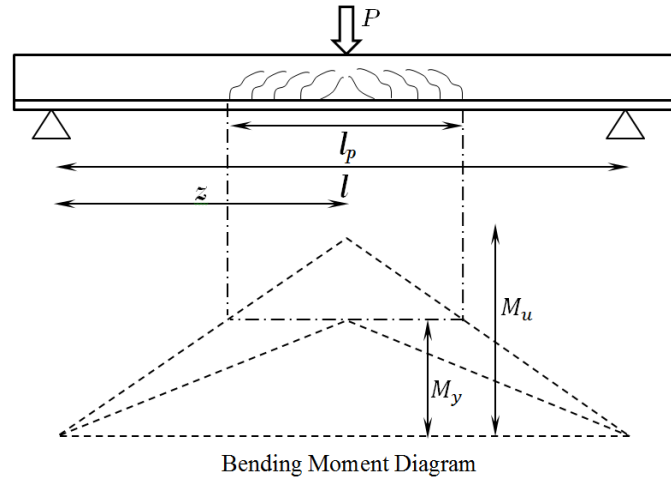


Figure 2-19 Determination of plastic hinge length based on bending moment diagrams  
(Gopinath et al. (2014))

#### 2-4-3-2 No Axial Load-Cyclic Lateral Load/Displacement

Thompson et al. (1980) developed a computer program to investigate the effect of variables such as longitudinal prestressing and non-prestressed steel ratio and distribution, transverse steel amount, and cover thickness on curvature ductility of prestressed and partially prestressed rectangular concrete beams. In order to assess accuracy of the developed analytical model, test results from other studies were compared to results obtained from the analytical model in this study. Tests were conducted on beam-column assemblies, and earthquake loading was simulated by reversing the direction of vertical loads at the beam ends. Assuming a rectangular distribution of curvature along the plastic hinge length, the measured equivalent plastic hinge lengths of beam specimens were approximately one-half the overall section depth ( $h/2$ ).

### 2-4-3-3 Constant Axial Load-Monotonic Lateral Load/Displacement

Chan et al. (1955) conducted 23 tests on RC frame assemblies under monotonic constant axial load on columns and monotonic bending moment. The influence of axial load level and lateral binding ratio on plastic hinge length was studied. Because the axial load level was high in all tests, primary failure was due to compression. Analysis of test data indicated that plastic hinge length does not vary significantly when varying the steel ratio for fixed-end beams. Analysis also showed that plastic hinge length had an average value of  $0.4 \times S$ , where  $S$  is the distance between the point of maximum moment and the point of contraflexure. In addition to the columns, plastic hinge length increased with an increase in axial load level. However, for normal rectangular frameworks, plastic hinge length did not exceed  $0.7 \times S$ .

Baker et al. (1964) developed an equation to estimate plastic hinge length based on test results of 32 beams under monotonic bending moment with or without axial loading. Test variables included grade of concrete and steel, steel ratio, single loads and double loads, axial force, shear magnitude, transverse binding, and compression steel ratio. The proposed plastic hinge equation is as follows:

$$L_p = k_1 \times k_2 \times k_3 \times \left(\frac{z}{d}\right)^{1/4} d \quad (2-196)$$

where  $z$  is the distance of critical section to point of contraflexure and  $d$  is effective depth of the section.

$$k_1 = \begin{cases} 0.7 & \text{For Mild Steel} \\ 0.9 & \text{For Cold-Worked Steel} \end{cases} \quad (2-197)$$

$$k_2 = \left(1 + 0.5 \frac{P}{P_u}\right)$$

where  $P$  is applied axial force and  $P_u$  is maximum compressive force which the member could sustain without any bending moment.

$$k_3 = \begin{cases} 0.6 & \text{When cube Strength} = 6000 \text{ psi} \\ 0.9 & \text{When cube Strength} = 2000 \text{ psi} \end{cases} \quad (2-198)$$

For normal values of  $z/d$ , the value of  $L_p$  lies within  $0.2 \times d$  and  $0.4 \times d$ .

Paulay and Priestley (1992) proposed an equation to predict plastic hinge length as a function of column length ( $L$ ), longitudinal steel reinforcement diameter ( $d_b$ ), and yield strength of steel reinforcement ( $f_y$ ):

$$L_p = 0.08L + 0.022d_b f_y \quad (MPa). \quad (2-199)$$

The average value of  $L_p$  for typical columns and beams can be approximately taken as  $0.5 \times h$ , where  $h$  is the section depth. The theoretical value of plastic hinge length obtained from integration of curvature distribution did not include “tensile strain penetration” length into the footing. Eq. (3-198) considers “tensile strain penetration” phenomenon and steel strains due to inclined flexure-shear cracking.

Mendis (2001) compared plastic hinge length measured experimentally to those estimated by nine existing expressions. Test results were adopted from experimental work Mendis (1986) conducted on nine simply supported beams subjected to axial load, shear, and bending moment. In this experimental work, the effect of compression and tension reinforcement ratio, transverse steel spacing, shear span ratio, and axial load level on plastic hinge length was evaluated. Axial load ranged from 175 to 50,100 KN, while balance axial load on the axial load-moment interaction curve for test specimens was approximately 100 KN. Test results showed that plastic hinge length increases with increased shear span ratio, compression, and tension reinforcement ratio and decreases with increased transverse steel ratio. Results also showed that plastic hinge

length is insensitive to axial load level. According to test data of this study, all beams subjected to axial load had constant plastic hinge length and were approximately equal to  $0.4 \times d$ , where  $d$  is effective depth of the beam cross section. Compared to other plastic hinge length expressions reviewed in this study, the predicted plastic hinge length using the expression recommended by ACI Committee 428 in 1968 best matches experimentally observed plastic hinge lengths for low axially-loaded columns and high-strength concrete beams (up to 80 MPa).

#### 2-4-3-4 Constant Axial Load-Cyclic Lateral Load/Displacement-Uniaxial

Park et al. (1977) performed tests on 10 prestressed and non-prestressed reinforced concrete beam-columns and beam assemblies with approximately full-size members subjected to static cyclic loading. The frame was loaded as depicted in Figure 2-20. Cyclic loading was simulated by reversing direction of vertical loads on the beams.

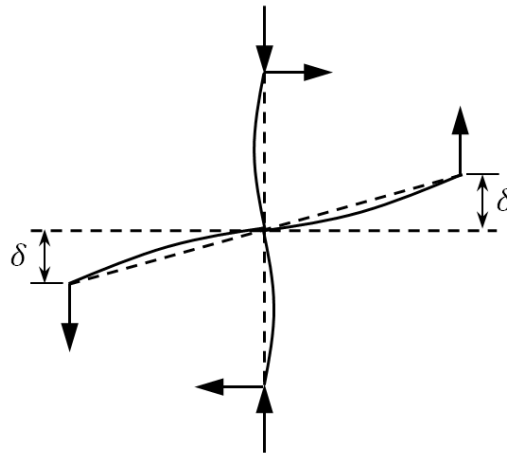


Figure 2-20 Frame loading

Based on test results, measured plastic hinge length was independent from prestressing steel with an average value of half the overall section depth ( $h/2$ ).

Park et al. (1982) tested four square reinforced concrete columns under constant axial load and reversal lateral displacement. Test variables included axial load levels varying between 0.2 and 0.6 and lateral steel reinforcement ratio. Test results indicated that measured equivalent plastic hinge lengths have an average value of  $0.42 \times h$  and are not influenced by the axial load level in which  $h$  is the overall section depth. Plastic hinge length is equal to  $0.4 \times h$ . Baker and Amarakone (1965) and Corley and Gene (1966) proposed equations that predict larger values for plastic hinge lengths compared to measured plastic hinge lengths in this study. Corley's equation provides more accurate results at higher axial load levels compared to Baker's equation.

The results of experimental work conducted at the University of Canterbury (Gill et al. 1979, Potangaroa et al. (1979), Ghee et al. (1981), Davey et al. (1975), Munro et al. (1976) and Heng et al. 1978) indicated that plastic hinge length does not depend on the axial load level with a value between  $0.35 \times H$  and  $0.65 \times H$ , where  $H$  is the overall depth of the sections. Mander (1983) performed further investigations on experimental results of the aforementioned tests and suggested that plastic deformation is due to moment gradient and yield penetration of longitudinal bars. Test results of four hollow RC columns subjected to constant axial load and cyclic lateral displacement and previous studies led Mander to propose the following equation to predict equivalent plastic hinge length:

$$L_p = L_{py} + 0.06 \times L \tag{2-200}$$

$$L_{py} = 0.32 \sqrt{d_b}$$

where  $L$  is column length and  $d_b$  is the longitudinal bar diameter in mm. The first and second terms of Eq. (3-199) denote the contribution of yield penetration and spread of plasticity along the member length due to the moment gradient, respectively.

Zahn (1985) tested 14 columns with circular, hollow circular, and square sections under constant axial compressive load ( $P$ ) and reversible horizontal load. Axial load ratio differed for each specimen. Plastic hinge length calculated using Priestley and Park's (1987) equation and plastic hinge length observed from tests in the current study were compared. The comparison indicated that Priestley's equation overestimates  $L_p$  for square columns with diagonal bending and hollow circular columns. In addition, for axial load ratios less than 0.3, Priestley's equation gives larger values for  $L_p$  compared to experimental values. Because overestimating plastic hinge length is not conservative, Zahn suggested that, for columns with low axial loads, a reduction factor should be applied to Priestley's equation as follows:

$$L_p = \begin{cases} \left(0.08l + 6d_b\right) \left(0.5 + 1.67 \frac{P}{f'_c A_g}\right) & \frac{P}{f'_c A_g} < 0.3 \\ 0.08l + 6d_b & \frac{P}{f'_c A_g} > 0.3 \end{cases} \quad (2-201)$$

where  $l$  is column length and  $d_b$  is the diameter of longitudinal reinforcing bars (mm). However, for hollow circular columns with one ring of reinforcing bars and no confinement through the tube walls, a reduction factor of 0.25 should be applied to Priestley's equation as follows:

$$L_p = 0.06l + 4.5d_b \quad (2-202)$$

As noted in their study, additional experimental data is required to validate equations proposed for plastic hinge length, especially columns with  $d_b \neq 16$ .

Priestley et al. (1987) derived an equation for plastic hinge length based on test results of RC bridge columns under constant axial load and inelastic cyclic lateral displacement. Test variables included cross-sectional shape, column aspect ratio, axial load level, confining reinforcement ratio, yield strength, and configuration. Axial load ratio for solid columns was between 0.2 and 0.7 and between 0.1 and 0.3 for hollow columns. Curvature distribution was



assumed to be constant along the plastic hinge length. Yield penetration and shear spread of plasticity were also considered. Curvature distributions along column lengths for all columns specimens were measured, and the following relationship to estimate plastic hinge length was proposed:

$$L_p = 0.08L + 6d_b \quad (2-203)$$

where  $L$  is the distance from point of contraflexure of the column to the section of maximum moment, and  $d_b$  is the bar diameter (mm). The calculated mean value of the plastic hinge for all tests was approximately  $0.5 \times h$ , where  $h$  is gross section depth in the direction of seismic loading.

Tanaka et al. (1990) tested eight RC columns under constant axial and cyclic lateral loading. Test variables included axial load level, shear span-to-depth ratio, lateral reinforcement configuration, and anchorage details. Axial load levels varied from  $0.1 \times f'_c \times A_g$  to  $0.3 \times f'_c \times A_g$ , where  $f'_c$  and  $A_g$  are compressive strength and gross section area of the concrete column. Based on observations from the aforementioned tests, the conclusion was made that plastic hinge length increases when axial load level increases. Observed plastic hinge length was within the range  $0.4 \times H$  to  $0.75 \times H$ , where  $H$  is overall depth of the column section.

Sheikh et al. (1993) used test data of four high-strength and six normal-strength concrete column large-scale specimens with prismatic and nonprismatic sections subjected to constant large axial load level ranging from 0.47 to 0.77 and reversal lateral load. In this study, observed plastic hinge lengths, including effects of yield penetration into the stub, were within the range of  $0.85 \times h$  to  $1.1 \times h$ , with an average value of  $1.02 \times h$ . In addition, results indicated that plastic hinge length is insensitive to axial load level, reinforcement steel configuration, concrete strength, and confining steel ratio.

Dodd et al. (2000) used a shake table to test 14 cantilever circular bridge concrete columns under simulated earthquake loads. Test variables included the column's aspect ratio, axial load ratio, base flexibility, base input motions, and the effect of initial low-level shaking on column response to subsequent higher-level shakes. Axial load ratios varied from 0.05 to 0.45. Equivalent plastic hinge length was assumed to be equal to the length over which curvature distribution is constant. Experimental results indicated that plastic hinge length increases with increased axial load level. Zahn et al. (1986) suggested that, for axial-load ratios less than 0.3, a reduction factor of  $0.5 + 1.6 \times P / f'_c A_g$  should be applied to the plastic hinge length equation proposed by Priestley et al. (1992). The conclusion was made that plastic hinge length values calculated with Zahn's recommendation are conservative and show good agreement with values obtained from tests of this study, especially for lower axial loads. However, Priestley's equation yields conservative values for tall and medium columns, but it overestimates plastic hinge length for short columns. The authors of this study suggested that no reduction factor should be used for an axial load ratio of 0.4.

Panagiotakos et al. (2001) used test results of 875 RC members under uniaxial bending moment with or without axial load to investigate plastic hinge length of RC columns. Test variables included test specimen geometry, reinforcement ratio and configuration, concrete strength, steel type, and axial load level. The axial load ratio varied from 0 to 0.95. After analyzing data of the 875 tests, the following expressions were revised from Paulay and Priestley's (1992) equation to estimate plastic hinge length in this study:

For cyclic loading

$$L_{pl,cy} = 0.12L_s + 0.014a_{sl}d_b f_y \quad (MPa) \quad (2-204)$$

For monotonic loading

$$L_{pl,mon} = 0.18L_s + 0.021a_{sl}d_b f_y \quad (MPa) \quad (2-205)$$

where  $f_y$  is yield strength of tension reinforcement (MPa),  $L_s$  is shear span of the member,  $d_b$  is the diameter of compression longitudinal reinforcement.  $a_{sl}$  is 0 when no bar pullout is present from the anchorage zone beyond the section of maximum moment;  $a_{sl}$  is 1 when bar pullout is present.

Ho et al. (2003) investigated the plastic response of high-strength reinforced concrete (HSRC) columns using test results of four column specimens subjected to low axial load level and reverse cyclic displacement excursions. Based on experimental results of this study, plastic hinge length of HSRC columns under low axial load does not exceed the depth of the column cross section and is not affected by the lateral reinforcement ratio. Plastic hinge length, including “stub effect” length, was suggested to be equal to overall depth of the column cross section ( $h$ ).

Binici et al. (2008) developed an analytical model to investigate ductility of plastic hinge zones of RC columns after FRP retrofitting. Obtained results of the proposed model were verified against results of numerical analysis and test results, and a parametric study was conducted to derive an equation for plastic hinge length. Carbon-FRP and Glass-FRP confined RC columns subjected to constant axial load ratio between 0.1 and 0.4 with column aspect ratio ( $L/R$ ) of 10, longitudinal reinforcement ratio between 0.01 and 0.04, and cyclic lateral displacement excursions were selected for the parametric study. The following equation was proposed to calculate plastic hinge length:

$$\frac{L_p}{L} = 0.077 + 8.16 \frac{d_b}{L} \quad (2-206)$$

where  $d_b$  is the longitudinal bar diameter. Plastic hinge length calculated by Eq. (3-205) was shown to correlate well with observed plastic hinge lengths of 59 column specimens under constant axial load and cyclic lateral displacement.

Berry et al. (2008) proposed an equation to estimate plastic hinge length using experimental data of 37 large-scale circular columns. All test columns were confined by spiral reinforcement and subjected to cyclic lateral loading and constant axial load less than  $0.3 \times f'_c \times A_g$ , where  $f'_c$  is concrete compressive strength and  $A_g$  is the gross section area of the column. Shear deformation was disregarded due to the typical aspect ratio of bridge columns of this study. After conducting a parametric study, the following equation was proposed to calculate plastic hinge length:

$$L_p = 0.0375L + \frac{0.12f_y d_b}{\sqrt{f'_c}} \quad (MPa) \quad (2-207)$$

where  $L$  is the distance between the point of maximum moment at the column base to the point of zero moment at the column top, and  $f_y$  and  $d_b$  are yield strength and diameter of longitudinal reinforcing steel, respectively. The second term of Eq. (3-206) reflects the strain penetration effect, normalized with respect to  $\sqrt{f'_c}$  in order to consider the effect of concrete strength on bond strength.

Bae et al. (2008) conducted four tests on full-scale concrete columns subjected to reverse cyclic displacement excursions and axial load levels from moderate to high in order to study the effect of axial load and shear span-depth ratio ( $L/h$ ) on plastic hinge length. Using a concrete compression strain method and considering bar slip, shear, and flexural displacement, an expression to estimate plastic hinge length was proposed. In order to reflect the stub confinement effect,  $0.25h$  was subtracted from the length corresponding to strains greater than compressive

reinforcing bar strains. As a result, plastic hinge length increased with increased  $L/h$  for high levels of axial loads (axial load ratio  $>0.2$ ). However, for low levels of axial loads (axial load ratio  $\geq 0.2$ ), the effect of  $L/h$  on plastic hinge length was not significant and plastic hinge length was approximately equal to the constant value of  $0.25 \times h$ . For high values of axial load, plastic hinge length increased with an increase in axial load level. For all axial load levels, plastic hinge length increased when longitudinal reinforcement ratio ( $A_s/A_g$ ) increased. The following equation was proposed to estimate plastic hinge length:

$$\frac{L_p}{h} = \left[ 0.3 \left( \frac{P}{P_0} \right) + 3 \left( \frac{A_s}{A_g} \right) - 0.1 \right] \left( \frac{L}{h} \right) + 0.25 \geq 0.25 \quad (2-208)$$

where

$$P_0 = 0.85 f'_c (A_g - A_s) + f_y A_s \quad (2-209)$$

where  $P$  is the applied axial load,  $A_s$  is area of tension reinforcement,  $A_g$  is gross area of concrete section,  $L$  is the distance from critical section to point of contraflexure,  $f'_c$  is compressive strength of concrete, and  $h$  is overall depth of the column. Bae et al. suggested that the specified plastic hinge length in ACI 318-05 is not conservative for columns subjected to high axial loads. They recommended an increase in column length from  $h$  to  $1.5 \times h$  in order to require the use of closely-spaced ties.

Qinghua et al. (2008) implemented five plastic hinge models to develop a computer program that investigates the accuracy of calculated damage indices, such as ultimate curvature of critical section. Twelve quasistatic tests on bridge pier specimens, simulated by the computer program, were subjected to monotonic or cyclic lateral loading and a constant axial load. Axial load ratio varied between 0.7 and 0.19 in these tests. The implemented plastic hinge models included Priestley and Park, Chang-Mander, Japanese code, and Esmaily-Xiao's first and

second models. Details of these models are presented in the study by Qinghua et al. (2008). Results of this study showed that although calculated residual displacement does not depend on the implemented plastic hinge model, the ultimate curvature value is highly dependent on it. A comparison between calculated values of ultimate curvature with various plastic hinge models showed that Esmaily-Xiao's second model and the Japanese code model provide minimum and maximum values, respectively. All calculated ultimate curvatures were less than experimental ultimate curvatures except when Japanese code was implemented. Based on results, Chang-Mander's model and Esmaily-Xiao's first model gave most accurate values for ultimate curvature, and Chang-Mander's and Esmaily-Xiao's second model more accurately computed maximum tensile strength of outmost longitudinal steel compared to the other three models. Among the five studied models, Japanese code and the Priestly-Park model provided most accurate results compared to experimental data. All five plastic hinge models underestimated maximum compression strain of the core concrete and overestimated maximum tensile strain of longitudinal steel, resulting in great statistic discreteness in calculated cycle fatigue indices by the program. Qinghua et al. (2008) concluded that the Japanese code model is the most conservative among the five models. Qinghua et al. concluded that the Priestly-Park model is easy to use, appropriate for high bridge piers, and sufficiently reliable. They suggested the Chang-Mander model as a second recommendation.

Gu et al. (2011) suggested an equation for plastic hinge length estimation based on test results from 29 FRP-confined circular concrete columns subjected to simulated seismic load with axial load ratio between 0.05 and 0.65. Due to a small lateral-steel ratio, confinement provided by lateral reinforcement could be neglected in these tests. No lap splice was observed in the plastic hinge region. Results of this study indicated that plastic hinge length increases with

increased FRP confinement at low confinement ratio and decreases at high confinement ratio. However, the type of confining FRP does not significantly affect plastic hinge length. The proposed equation to calculate plastic hinge length is as follows:

$$L_p = (0.59 - 2.3\lambda_f + 2.28\lambda_f^2)L + 0.022f_y d_b \quad \text{where } \lambda_f > 0.1 \quad (2-210)$$

where  $\lambda_f$  is the confinement ratio,  $L$  is column height,  $d_b$  is the diameter of longitudinal reinforcement (mm), and  $f_y$  is yield strength of longitudinal reinforcement (MPa). Due to lack of test data for confinement ratios less than 0.1, Eq. (3-209) is applicable only when  $\lambda_f > 0.1$ . The general form of this equation, adopted from Paulay and Priestley (1992), was modified to consider the effect of FRP confinement. For  $\lambda_f = 0$ , the original form of the Paulay and Priestley (1992) equation for plastic hinge length should be used as follows:

$$L_p = 0.08L + 0.022f_y d_b \quad \text{where } \lambda_f = 0. \quad (2-211)$$

Jiang et al. (2014) used analytical and experimental studies to evaluate the confining effect of FRP on plastic hinge length. Tests were conducted on seven RC square columns under constant axial load and monotonic lateral displacement with axial load ratio of 0.35. These columns were confined with FRP with various confining ratios. The proposed equation for plastic hinge length is a modified version of the Gu et al. (2011) equation in order to be applicable to circular and rectangular columns. This expression consists of two terms:  $L_{p0}$  which represents the normal plastic hinge adopted from the Paulay and Priestley (1992) model, and  $L_{pc}$  which represents the FRP confining effect. Because the proposed equation by Gu et al. (2011) is applicable to circular columns, the reduction factor  $k_s = \left(\frac{2r}{b}\right)^{0.72}$ , in which  $b$  and  $r$  are column width and corner radius, respectively, is multiplied by the second term. This reduction factor is

applied because the FRP confinement effect on plastic hinge in circular columns is more comparable to rectangular or square columns (Wu and Wang, 2009; Wu and Wei, 2010; Wei and Wu, 2012).

$$L_p = L_{p0} + \left(\frac{2r}{b}\right)^{0.72} \times L_{pc} \quad (2-212)$$

where

$$L_{p0} = 0.08L + 0.022d_b f_y \quad (2-213)$$

in which  $L$  is column height and  $d_b$  and  $f_y$  are diameter and yield strength of longitudinal reinforcement, respectively.

$$L_{pc} = \begin{cases} 3.028\lambda_f & 0 \leq \lambda_f < 1 \\ 0.51 - 2.3\lambda_f + 2.28\lambda_f^2 & 0.1 \leq \lambda_f < 0.5 \end{cases} \quad (2-214)$$

where  $\lambda_f$  is the confinement ratio defined as  $\lambda_f = f_l / f_{c0}$ , in which  $f_{c0}$  is cylindrical compressive strength of unconfined concrete.

$$f_l = \frac{2E_f \varepsilon_{fu} t}{b} \quad (2-215)$$

where  $E_f$ ,  $\varepsilon_{fu}$ , and  $t$  are elastic modulus, ultimate tensile strain, and thickness of FRP jacket, respectively. Based on findings of Jiang et al. (2014) studies, the effect of FRP jacketing on plastic hinge length depends on the level of confinement. Plastic hinge length increases for low level of confinement and decreases for high level of confinement, confirming findings of the study by Gu et al. (2011). Because tests were conducted under larger axial load compared to other studies, Jiang et al. concluded that, at zero-confinement, test results match better with results predicted by Ho's (2003) plastic hinge length equation compared to results of Paulay and Priestly's (1992) equation.

#### **2-4-3-5 Constant Axial Load-Cyclic Lateral Load/Displacement-Biaxial**

Biskinis et al. (2010) developed an expression for plastic hinge length based on experimental data from 1540 cyclic or monotonic uniaxial tests. The proposed equation is



applicable to RC beams, rectangular columns, members with T-, H-, U-, or hollow rectangular sections and rectangular walls. Biskinis et al. (2010) acknowledged that the proposed model is also on the safe side for biaxial loading. Flexural failure was the dominant failure mode in all tests. The proposed equation for plastic hinge length

For cycling loading with earthquake resistance detailing:

$$L_{pl,cy} = 0.2h \left[ 1 + \frac{1}{3} \min \left( 9, \frac{L_s}{h} \right) \right] \quad (2-216)$$

For monotonic loading with or without earthquake resistance detailing:

$$L_{pl,mon} = h \left[ 1.1 + 0.04 \min \left( 9, \frac{L_s}{h} \right) \right] \quad (2-217)$$

where  $h$  is cross section depth and  $L_s$  is shear span.

Alemdar (2010) used results of 72 dynamic and static tests of modern bridge columns to propose two equations to estimate plastic hinge length. In this study, two methods were used to determine plastic hinge length. One method used maximum drift capacity and the other method utilized curvature distribution along the column length. All tests had axial load ratio of less than or equal to 0.3. Multivariable regression analysis of test data was used to propose the following equations for plastic hinge length:

Based on maximum drift capacity:

$$\frac{L_p}{d} = \frac{1}{5} + \frac{3f_y d_b}{500\sqrt{f'_c}} + \frac{L}{1000} \quad (psi \text{ and } in) \quad (2-218)$$

Based on curvature distribution:

$$\frac{L_p}{d} = \frac{3}{10} + \frac{f_y d_b}{1000\sqrt{f'_c}} + \frac{L}{2500} \quad (psi \text{ and } in). \quad (2-219)$$

#### **2-4-3-6 Variable Axial Load-Cyclic Lateral Load/Displacement-Uniaxial**

Blakeley (1971) performed four tests on full-scale precast, pre-stressed concrete beam-column assemblies subjected to static cyclic lateral and variable axial loading. Plastic hinge location and confining steel ratio were the test variables. Observed equivalent plastic hinge length in columns and beams tested in this study were approximated as one-half of the overall depth of the member ( $h/2$ ).

Phan et al. (2007) tested three one-third scale bridge columns on a shake table. Two of the three columns were tested under near-fault ground motions and the other column was tested under far-fault ground motions. Axial load ratio was 8% for all specimens, and the two columns tested under near-fault ground motions were reinforced with various amounts of longitudinal and lateral steel reinforcements. Paulay and Priestley's equation was used to calculate plastic hinge length. This equation was found to be conservative for all specimens. Plastic hinge lengths measured from the specimen's plastic displacements were larger than lengths calculated using Paulay and Priestley's equation. Columns subjected to near-fault and far-fault ground motions had identical plastic hinge length.

Mortezaei et al. (2012) performed a numerical study, including nonlinear analysis of 1350 FRP-confined RC columns, to investigate plastic hinge region length for near-fault and far-fault earthquakes. Variables in this study included axial load level, high-depth ratio, longitudinal reinforcement ratio, and earthquake characteristic. Based on conclusions from this study, for axial load ratio less than 0.2 ( $P/P_0 \leq 0.2$ ), plastic hinge length remains almost constant, or  $0.65 \times h$  for far-fault and  $0.55h$  for near-fault earthquakes. For higher values of axial load, plastic hinge length increases with increased axial load level. Although the effect of height-depth ratio on plastic hinge length at low levels of axial load ( $P/P_0 \leq 0.2$ ) was not significant, plastic hinge length increases with increased height-depth ratio at higher axial load levels. Columns with high

longitudinal reinforcement ratio developed longer plastic hinge length. Results of this study showed that columns subjected to far-fault earthquakes have longer plastic hinge length compared to columns subjected to near-fault earthquakes. FRP jacketing also increases plastic hinge length.

Recommended equations to approximate plastic hinge length are as follows:

$$\frac{L_p}{h} = \left[ 0.4 \left( \frac{P}{P_0} \right) + 3 \left( \frac{A_s}{A_g} \right) - 0.1 \right] \left( \frac{H}{h} \right) + 0.65 \geq 0.65 \quad \text{For far-fault earthquake}$$

$$\frac{L_p}{h} = \left[ 0.4 \left( \frac{P}{P_0} \right) + 3 \left( \frac{A_s}{A_g} \right) - 0.1 \right] \left( \frac{H}{h} \right) + 0.55 \geq 0.55 \quad \text{For near-fault earthquake}$$

(2-220)

where  $P$  is applied axial load,  $P_0$  is nominal axial load capacity,  $h$  is overall depth of the column,  $A_s$  is the area of tension reinforcement,  $A_g$  is the gross area of concrete section, and  $H$  is the distance between the critical section and contraflexure point. Proposed plastic hinge length equations in this study were adopted from Bae and Bayrak's (2008) study with an adjustment to consider shear deformation, deformation caused by bar slip, and flexural deformation.

Mortezaei (2014) analytically investigated plastic hinge length of RC columns under near-fault ground motions by simulating 936 RC columns under variable axial loading and cyclic lateral loading/displacement using a finite element program. Variable parameters included axial load ratio, height-depth ratio, and strength of concrete. Analytically obtained results were verified against experimental results from literature. Results indicated that at low level of axial loads (less than 0.2),  $L_p$  is almost constant and equal to  $0.55h$ . At higher axial load ratios,  $L_p$  increases with increased axial load levels. In addition, the observation was made that an increase in height-depth ratio did not cause significant increase in  $L_p$  for axial load ratios less than or equal to 0.2.  $L_p$  increased as height-depth ratio increased at higher axial load levels. RC columns

under near-fault axial loading also exhibited longer plastic hinge length compared to columns subjected to far-fault ground motions. The following equation for plastic hinge length was proposed based on obtained numerical results:

$$\frac{L_p}{h} = 0.85 \left[ 1 + 0.45 \left( \frac{P}{P_0} \right) \right] \left( \frac{H}{h} \right)^{0.2} \times k \quad \text{For } P/P_0 > 0.2 \quad (2-221)$$

$$\frac{L_p}{h} = 0.55 \quad \text{For } P/P_0 \leq 0.2$$

where  $h$  is overall column depth,  $P$  is applied axial load,  $P_0$  is nominal axial load capacity, and  $H$  is the distance from critical section to point of contraflexure. Coefficient,  $k$ , depends on concrete strength,  $f'_c$ , as follows:

$$K = \begin{cases} 0.65 & \text{When } f'_c = 32.5 \text{ MPa} \\ 0.85 & \text{When } f'_c = 32.5 \text{ MPa} \\ 0.85 - 0.01(f'_c - 12.5) & \text{When } 12.5 \text{ MPa} < f'_c < 32.5 \text{ MPa} \end{cases} \quad (2-222)$$

#### 2-4-3-1 Variable Axial Load-Cyclic Lateral Load/Displacement-Biaxial

Hachem et al. (2003) tested four circular reinforced concrete bridge columns under bidirectional earthquake loading subjected to near-fault and far-fault ground motions. The average axial load level was approximately  $0.06f'_cA_g$ , where  $f'_c$  and  $A_g$  are compressive strength and gross section area of the concrete column, respectively. Observed plastic hinge length after testing was approximately  $0.75D$ , in which  $D$  is the column section diameter. Values of observed plastic hinge lengths were close to values predicted by the Priestley et al. (1992) equation.

Esmaily et al. (2005) developed a computer program to investigate the effect of axial load level and its pattern on lateral behavior of bridge piers. Based on Esmaily et al. findings,

the level of axial load and its pattern significantly affects column behavior. Methods developed by Esmaily et al. are applicable to biaxial monotonic and cyclic lateral loading and displacement cases with variable or constant axial loading. Curvature distribution was assumed to be linear between the first yield point (concrete or longitudinal bar) and the critical section in the first method.  $L_p$ , defined as the length over which transition occurs, is the distance between the first yield point and the critical section. In this method,  $L_p$  is given by:

$$L_p = l \left( 1 - \frac{M_y}{M_u} \right) \quad (2-223)$$

where  $l$  is total length,  $M_y$  is the yield moment for the existing axial load, and  $M_u$  is the moment at the critical section.

For the second method, curvature distribution along the column at various hinge regions is shown in Figure 2-21.

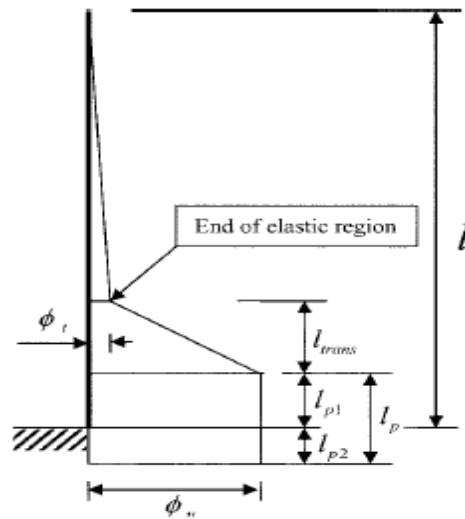


Figure 2-21 Assumption of curvature distribution along column height

In Figure 2-21,

$$l_{p1} = \begin{cases} D & \text{for length to depth ratio} \leq 12.5 \\ 0.08l & \text{for length to depth ratio} > 12.5 \end{cases} \quad (2-224)$$

where  $D$  is the column's section depth in direction of analysis.

$$l_{p2} = 0.15f_s d_b \quad (2-225)$$

in which  $f_s$  is maximum tensile stress of the section at the column-footing interface and  $d_b$  is the longitudinal bar diameter. The value of  $l_{p1}$  (plastic length) is constant, but  $l_{p2}$  (stress penetration length) changes at each step of analysis due to variation of  $f_s$ . The value  $l_{trans}$  (transition length) is not constant and varies as the length of the elastic part changes with changes in loading and displacement.

Plastic hinge lengths recommended by codes include:

I. ACI-ASCE committee 428 on limit design (1968):

$$l_p > \begin{cases} R_\varepsilon \left( \frac{d}{4} + 0.03zR_m \right) \\ R_\varepsilon d \end{cases} \quad (2-226)$$

where

$$R_m = \frac{M_m - M_\varepsilon}{M_u - M_e}$$

$$R_\varepsilon = \frac{0.044 - \varepsilon_{cue}}{\varepsilon_{cu0} - \varepsilon_{cue}} \quad (2-227)$$

$$z = \frac{4M_m}{4V_z + \sqrt{\omega M_m R_m}}$$

$d$  is the distance from extreme compression fiber to centroid of section reinforcement,  $\varepsilon_{cue}$  is elastic component of maximum compressive strain in concrete at ultimate resisting moment and axial load,  $\varepsilon_{cu0}$  is basic maximum compressive strain in concrete to which a value in the range 0.003 to 0.004 is assigned,  $M_m$  is maximum moment in a length of member,  $M_u$  is ultimate

resisting moment concurrent with ultimate resisting axial load,  $M_e$  is elastic-limit resisting moment,  $V_z$  is shear adjacent to a concentrated load or reaction at a section of maximum moment, and  $\omega$  is the uniformly distributed load at a section of maximum moment. If  $\omega$  and a concentrated load (or reaction) at this section act in opposite directions,  $\omega = 0$  should be used.

The following are AASHTO guide specifications for Load and Resistance Factor Design (LRFD) of seismic bridge design (2007):

For columns framing into a footing, an integral bent cap, oversized shaft, or cased shaft:

$$L_p = 0.08L + 0.15f_{ye}d_{bl} \geq 0.3f_{ye}d_{bl} \quad (2-228)$$

For noncasted prismatic pile shafts:

$$L_p = 0.08H' + D^* \quad (2-229)$$

For horizontally isolated flared columns:

$$L_p = G_f + 0.3f_{ye}d_{bl} \quad (2-230)$$

where  $L$  is the length of column from point of maximum moment to point of moment contraflexure (in.),  $f_{ye}$  is expected yield strength of longitudinal column reinforcing steel bars (ksi),  $d_{bl}$  is nominal diameter of longitudinal column reinforcing steel bars (in.),  $D^*$  is diameter of circular shafts or cross-sectional dimension in direction under consideration for oblong shafts (in.),  $H'$  is the length of pile shaft/column from point of maximum moment to point of contraflexure above ground (in.), and  $G_f$  is the gap between the isolated flare and soffit of the bent cap (in.).

The institute research committee on ultimate load design of concrete structures (1962) proposes

$$L_p = k_1 \times k_2 \times k_3 \times \left(\frac{z}{d}\right)^{1/4} d \quad (2-231)$$

where

$$k_1 = \begin{cases} 0.7 & \text{for mild steel} \\ 0.9 & \text{for cold-worked steel} \end{cases}$$

$$k_2 = 1 + 0.5 \left( \frac{P}{P_u} \right) \quad (2-232)$$

$$k_3 = 0.9 - \frac{0.3}{0.25} (f'_c - 11.7)$$

where  $P$  is the ultimate axial load for the member (allowing for the bending moment when present),  $P_u$  is the ultimate capacity of the member for axial load when no bending moment acts,  $z$  is the distance of critical section to point of contraflexure, and  $d$  is effective depth of the section.



## **Chapter 3 - Analytical Models and Algorithm**

### **3-1 Introduction**

Performance of reinforced concrete sections with arbitrary cross-sectional shapes has been studied by many a number of researchers (Yen 1991, Yau 1993, Rodriguez and Aristizabal-Ochao 1999, Fafitis 2000, Sfakianakis 2002, Bonet et al. 2004, Sousa and Muniz 2007, Charalampakis 2008, Rosati et al. 2008, Papanikolau 2012) in an attempt to develop new methods and algorithms and small computer applications to calculate axial force-bending moment interaction surface of a section. Monotonic loading was employed in these studies to construct the failure surface of a section; however, when exposed to a dynamic excitation such as wind, tornado, or earthquake, columns can be subjected to combined non-proportional bilateral and axial directions which is more pronounced in earthquake excitations, specifically in near-fault regions with high vertical and horizontal ground accelerations, large velocity pulses, directional effects, repetitive pulse effects, and aftershocks.

Estimation of available force and displacement capacity, energy dissipation, and inflicted damage on a structural element or occurrence of a certain limit state with reasonable accuracy requires a realistic prediction of structure performance. Accuracy of analytical predictions depends on the employed analytical methods and implemented material models, constitutive laws hysteresis rules, and distribution of curvature along the member. Detailed finite element analysis using available commercial software such as ABAQUS or open source software such as OpenSees has a steep learning curve and is not the first choice for a design engineer who prefers less sophisticated approaches.

Most small computer applications are limited to section analysis under a constant axial load, monotonic and very few cyclic, unilateral displacement or force. In order to fulfill the need for a simple, yet accurate analytical tool for performance assessment of reinforced concrete columns, a computer program was developed that uses relatively simple analytical methods and material models to accurately predict the performance of reinforced concrete structures under various loading conditions, including cyclic lateral displacement under a non-proportionally variable axial load (Esmaeily and Xiao 2005, Esmaeily and Peterman 2007). However, it was limited to circular, rectangular, and hollow circular/rectangular sections and uniaxial lateral curvature or displacement.

The computer program described in this study is the next generation of the aforesaid program with additional functionality and options. Triangulation of the section allows opportunity for cross-sectional geometry. Biaxial lateral curvature/displacement/force combined with any sequence of axial load provides opportunity to analyze the performance of a reinforced concrete column under any load and displacement path. Use of unconventional reinforcement, such as FRP, in lateral as well as longitudinal direction is another feature of this application.

Accuracy of various material models, hysteresis rules, and other assumptions for behavior simulation of a reinforced concrete member tested under a certain loading pattern can be examined by the developed computer program.

Performance of the developed computer application was assessed through various types of analysis for RC members compared to respected experimental data, including moment-curvature analysis of a hollow square cross section, force-deflection analysis of an oval section under axial force and uniaxial lateral displacement and a square section under axial force and

biaxial lateral displacements, and axial force-bending moment interaction surface for a square section.

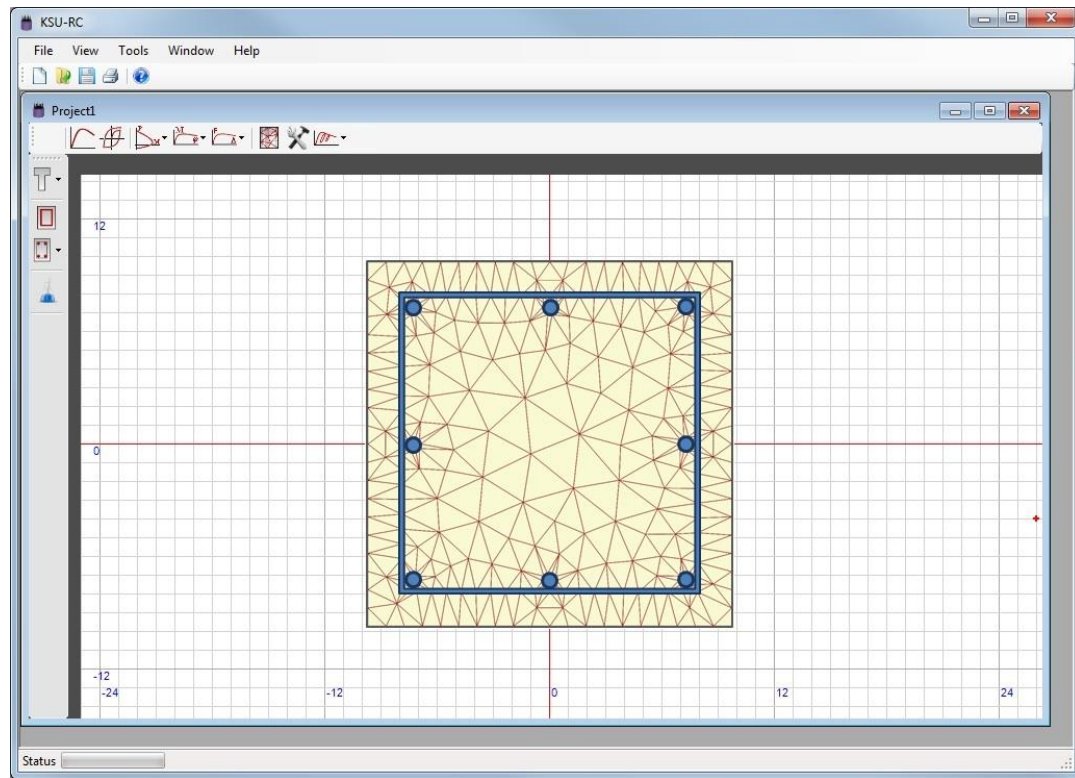


Figure 3-1 Main window of the developed window-based computer application

### 3-1 Applied Analytical Method and Assumptions

The primary goal of this study was to develop a user-friendly, simple, and accurate computer program capable of analyzing the performance of RC columns with any cross section, reinforced by conventional or unconventional reinforcement in lateral and/or longitudinal directions under any load/displacement pattern. The main window of this computer application is shown in Figure 3-1. The load/displacement pattern can be a combination of independent biaxial curvature or moment with any axial load pattern in a moment-curvature analysis, or independent

biaxial lateral displacement or force under an independently variable axial load. Behavior of an arbitrary-shaped section under various loading scenarios was modeled using the Bernoulli-Euler assumption in which plane sections remain plane after deformation. The arbitrary-shape section may consist of various materials and reinforcements, and the section may have any hole/opening. Constitutive material in the arbitrary-shape section may have any monotonic and cyclic behavior.

Analysis was based on fiber modeling of the section effectively used by others (Prakash et al. 1993, Mazzoni et al. 2006). When a fiber model is used to analyze a beam or column, the cross section of the member is divided into smaller elements. When these elements are viewed in relation to the length of the beam, they appear as long ‘fibrous’ elements, hence the name ‘Fiber Modeling’. The stress and strain on each of these smaller elements is analyzed. When the stress and strain on each element is known, the axial load and moment effects on that element are easily found. After all of these smaller elements are analyzed, the axial loads and moments from each element are added together to determine the forces on the cross section as a whole. The accuracy of the analysis depends upon the size of each small element. As the cross section of the member is divided into more elements, the smaller these elements become, the more accurate the analysis.

Fiber modeling is a type of finite element analysis. Fiber modeling has two general assumptions which separate it from finite element analysis. The first assumption is that as the beam or column member bends, the cross section of the member always remains plane to the longitudinal axis of the member.

The second assumption is that the deformation of each fiber is linear across each fiber of the cross section. These two assumptions are general and cover the majority of fiber models. It is

possible, however, to implement a fiber analysis which does not follow one or both of these assumptions.

Analysis addressed by the developed computer application includes (i) construction of code-based 3D axial force-bending moment interaction surface for RC columns with conventional lateral steel reinforcement using American Concrete Institute stress-block (ACI 318-11), (ii) construction of axial force-bending moment interaction surface using material models for meshed RC columns laterally reinforced by steel, FRP, or steel and FRP assuming a constant strain at the extreme compressive fiber, (iii) construction of real axial force-bending moment failure surface considering material models for meshed RC columns laterally reinforced by steel, FRP, or steel and FRP with or without considering the axial force loading pattern, (iv) code-based biaxial moment-curvature analysis for RC columns with conventional lateral steel reinforcement considering ACI stress-block, (v) biaxial moment-curvature analysis considering the meshed section, including use of proper material models with any pattern of curvature in the two lateral directions and any variation of axial load, and (vi) biaxial force-deflection analysis using proper material models and a plastic hinge method, with displacement patterns in two lateral directions and arbitrary axial load pattern.

### **3-2 Cross Section**

As mentioned earlier, a fiber-based method was employed to analyze RC sections in the developed computer application. In the triangular mesh algorithm used in the computer application, various components of a column's section are defined as separate regions. Each region is divided into a number of fibers and each fiber, depending on the material and location of the region, follows a particular cyclic rule and a monotonic material model as the envelope

curve of the cyclic model. Longitudinal bars are considered separately in the model with distinct monotonic and cyclic rules and load history. Triangular meshing caused the cross section of a beam-column to have an arbitrary shape with or without holes/opening. The composite section can be reinforced longitudinally by steel/FRP bars and laterally by conventional steel (tie/spiral), FRP warps, or lateral steel and FRP warps. The effect of lateral reinforcement was indirectly taken into account in modeling because uniaxial stress-strain behavior of the region enclosed by lateral reinforcement is affected by lateral reinforcement. FRP warps can have stiffness in axial and lateral directions, depending on the orientation of FRP fibers. The effect of FRP warps with fibers only in hoop direction was modeled indirectly through the stress-strain relationship of concrete regions. The fiber arrangement of a composite section is shown in Figure 3-2, which includes four regions: (i) steel or FRP bars, (ii) section core region, (iii) region between FRP warps and lateral steel reinforcement (or cover concrete for conventionally reinforced sections), and (iv) FRP wraps region.

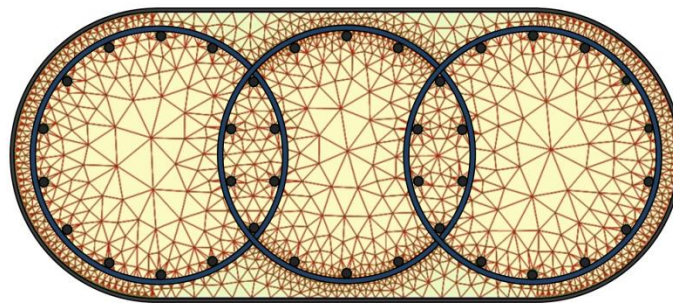


Figure 3-2 Composite section

Distribution of longitudinal reinforcement can be evenly distributed or costume distribution. Lateral reinforcement can be provided by conventional lateral reinforcement (tie/spiral), FRP warps, or FRP warps and steel lateral reinforcement. However, the FRP wrap

may have stiffness in only the hoop direction, thereby providing confinement for the concrete section or the hoop and longitudinal directions. In the latest case, FRP stiffness contributes to the axial and flexural capacity of the RC section.

### **3-3 Material Properties**

Mechanical properties of materials, including concrete, steel in longitudinal and lateral directions, FRP wraps, and FRP longitudinal bars, are provided in the computer application. Concrete strength, as measured in the lab or desired for analysis, must be provided. For steel material, yield strength and modulus of elasticity are provided as basic mechanical properties, assuming symmetric behavior for steel in tension and compression. Because behavior of FRP wraps in tension and compressive directions may not be similar in general, tensile and compressive strength and modulus of elasticity of FRP wraps must be individually provided.

### **3-4 Material Models**

#### **3-4-1 Monotonic Material Models**

A number of widely-used existing material models were implemented in the computer application in order to model uniaxial monotonic behavior of fibers with various materials. For plain/unconfined concrete, the Mander et al. model (Mander et al. 1988) for low to medium strength concrete and Cusson and Paultre's model (1995) for high-strength concrete were implemented into the program. For concrete confined by steel lateral reinforcement, the Mander et al. model (1988) for low to medium strength concrete and Cusson and Paultre's model (1995) for high-strength concrete were chosen because of their accuracy in predicting the behavior of circular and rectangular concrete columns with various longitudinal and lateral steel configurations.

The Mander et al. model (1988) was developed analytically for circular or rectangular cross sections under monotonic, cyclic static or dynamic loading. The RC section may have any general confinement type provided by either spiral or circular hoops, or rectangular hoops with or without supplementary cross-tie. In this model, the effect of any confinement type was taken into account by defining an effective lateral confining pressure that depends on lateral and longitudinal reinforcement configuration. To predict strain corresponding to first fracture, Mander et al. used an energy balance approach by equating strain energy stored in the concrete caused by confinement to strain energy capacity of the lateral reinforcement (Mander et al. 1988). The stress-strain relationship of the Mander et al. model is based on an equation proposed by Popovics (1973). Many researchers have used Mander et al. model to simulate model monotonic behavior of concrete confined by conventional reinforcement. Because proposed stress-strain models for normal-strength concrete may overestimate the strength and fracture strain of high-strength concrete, Cusson and Paultre (1995) proposed their model to predict monotonic behavior of high-strength concrete confined by steel ties, using experimental results of 50 large-scale high-strength concrete tied columns tested under eccentric loading. Cusson and Paultre also considered effects of tie-yield strength, concrete compressive strength, tie configuration, and lateral and longitudinal reinforcement ratios when developing their model (Cusson and Paultre 1995). Cusson and Paultre's stress-strain curve for confined and unconfined concrete consists of two parts. The initial part is a relationship originally proposed by Popovics (1973), and the second part is a modification of the relationship proposed by Fafitis and Shah (Fafitis and Shah 1985) for high-strength confined concrete. As reported by Cusson and Paultre (1995), yield strength of lateral reinforcement is developed at the peak strength of concrete only for well-confined high-strength concrete specimens; therefore, peak strength of confined



concrete was computed by employing an iterative process in this model. Formulas of these two models are provided in Chapter 3.

Samaan et al. (1998) and Youssef et al. (2007) models were chosen as representative models for concrete confined by FRP. Samaan et al. developed a bilinear stress-strain model for FRP-confined concrete based on 30 cylindrical specimens tested under uniaxial compression loading (Samaan et al. 1998). They used a four-parameter relationship originally proposed by Richard and Abbott (1975) to model initial behavior of FRP-confined concrete. Calculating the fracture strain and its corresponding stress, the initial curve is followed by a line connecting the initial part to the fracture point.

Youssef et al. (2007) used results of an experimental program that included large-scale circular, rectangular, and square short columns confined by carbon-FRP and E-glass-FRP warps in order to develop a stress-strain model for concrete confined by FRP. This model is applicable for predicting monotonic behavior of low- to high-confined concrete. The initial relationship of this model is a polynomial function followed by an ascending or descending linear part that represents low- and moderate- to high-strength confinement, respectively.

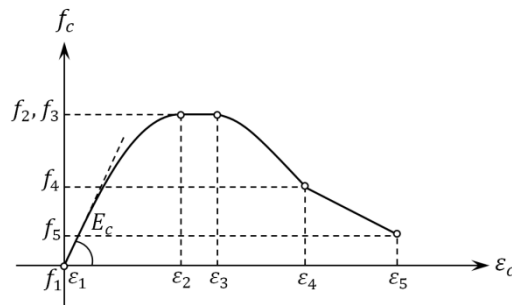


Figure 3-3 Example of “custom model” for plain or confined concrete

For concrete confined by FRP and conventional lateral steel, Kawashima et al. (2000), Lee et al. (2009), and Shirmohammadi et al. (2014) models were implemented in the computer

program. Kawashima et al. stress-strain model was developed by combining the Hoshikuma et al. (1997) model for concrete confined by steel tie reinforcement and the Hostani et al. (1998) model for concrete confined by carbon-FRP. The initial part of this model is a polynomial followed by a linear path. The linear part of this model can be ascending or descending depending on the confinement ratio of the concrete section (Kawashima et al. 2000). Lee et al. (2009) presented a comprehensive stress-strain model for concrete confined internally by lateral steel and externally by FRP wraps based on experimental results of 24 concrete cylinders subjected to compression. The Lee et al. model consists of three polynomials: a second-order polynomial function, a polynomial at strain corresponding to plain concrete strength, and a polynomial at the point representing the lateral steel yield point (Lee et al. 2009). In order to estimate ultimate stress and corresponding strain, Lam and Teng (Lam and Teng 2003) equations were modified by introducing two new parameters based on experimental results from Lee et al. Shirmohammadi et al. developed a constitutive stress-strain relationship to model the behavior of concrete confined by FRP and lateral steel. They used Thorenfeldt et al. (1987) stress-strain relationship which is the modified version of Popovics' (1973) equation. Using experimental data, Shirmohammadi et al. proposed two equations for ultimate strain and corresponding stress for FRP and steel confined concrete. The formulations of monotonic stress-strain models for concrete confined by FRP or FRP and conventional lateral steel are provided in Chapter 3.

Concrete tensile strength can be considered by assuming a linear equation with a slope equal to modulus of elasticity of plain concrete in all aforementioned monotonic models. In addition these models, a custom model option was added to the developed program. Using custom model functionality, users can implement and use their own model, including linear and second-order polynomial segments for various regions of cross section. Custom Model may

include up to five segments, and each segment may be linear or polynomial. An example of a Custom Model for plain or concrete confined by steel is shown in Figure 3-3. This monotonic model consists of four segments; the first and third segments are polynomial, and the second and last segments are linear.

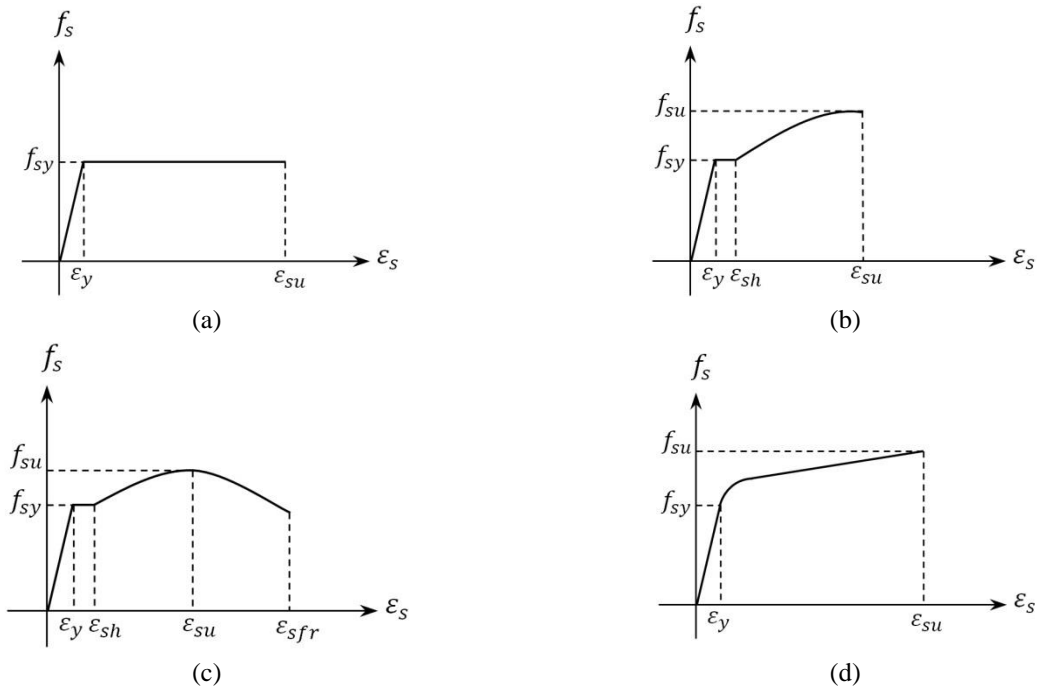


Figure 3-4 Implemented steel stress-strain models in computer application: (a) elastic-perfectly plastic model, (b) Mander et al. model (1984), (c) Esmaily-Xiao model (2005), and (d) Menegotto-Pinto model (1973)

For steel, a plastic-perfectly plastic model, Mander et al. model (1984), Esmaily-Xiao model (2005), and Menegotto-Pinto model (1973) were implemented in the computer application. Figure 3-4 shows these four steel monotonic models. When no information except yield strength and modulus of elasticity is available, the plastic-perfectly plastic stress-strain model can be used for monotonic behavior of longitudinal steel bars. Esmaily and Xiao's steel monotonic model can be employed to model behavior of longitudinal reinforcement when additional detailed information about reinforcing steel is available. Stress-strain behavior of

various types of steel can be simulated using four parameters ( $K_1$ ,  $K_2$ ,  $K_3$ , and  $K_4$ ). Yield plateau, strain hardening, and softening of steel material were taken into account in this model (Esmaily and Xiao 2015). The hardening and softening branch of steel monotonic model can be estimated using coefficients proposed by Esmaily and Xiao (2002) when no information is available except steel yield strength and modulus of elasticity. Based on tensile experiments of steel bars, Esmaily and Xiao proposed the ultimate strain ( $\epsilon_{su}$ ) and strength ( $f_{su}$ ) for steel to be equal to  $24.9 \times \epsilon_{sy}$  and  $1.3 \times f_{sy}$ , respectively (Esmaily and Xiao 2002).

The Mander et al. model (1984) was developed as a result of a variety of tension and compression tests. This model takes into account elastic behavior, yield plateau, and strain hardening of steel material. Menegotto-Pinto's model (1973) includes a bilinear curve. The initial line has the slope of steel modulus of elasticity up to yield strength, thereby modeling elastic behavior of steel material, and post-yield strength is defined as a linear function with a slope equal to a portion (defined by  $b$  parameter) of the initial part's slope. Yield plateau characterization is neglected in Menegotto-Pinto's monotonic model.

A bilinear model was used in the computer application to model uniaxial behavior of FRP. The slope of tensile and the slope of compressive branches were equal to tensile modulus and compressive modulus of elasticity of FRP wraps, respectively.

### **3-4-1 Cyclic Material Models**

Various cyclic models were implemented in the computer application to model cyclic behavior of materials in a composite section. A sample form of cyclic rules is shown in **Error! eference source not found..** Cyclic behavior of plain concrete can be modeled using a linear model with a slope equal to the modulus of elasticity of concrete, or models developed by

Mander et al. (1984) and Esmaily and Xiao (2005). For cyclic behavior of concrete confined by conventional lateral steel, Mander et al. and Esmaily-Xiao cyclic rules were implemented in the developed computer application (Figure 3-5). All these cyclic models can work with any monotonic model as an envelope curve. In the Mander et al. cyclic model, the unloading path follows a concave-upward parabolic path with a zero-slope at the strain-axis. Tensile strength of concrete can be taken into account considering a linear path with a slope of plain concrete modulus of elasticity. With increased strain, stress remains zero up to the last strain corresponding to the zero stress, after which point strain grows in a linear reloading path with a slope equal to plain concrete modulus of elasticity in the strain-axis (Mander et al. 1984). In Esmaily-Xiao's cyclic model, the unloading path follows a parabolic path which is concave-upward with a slope of  $E_{c2}$  on the envelope curve (monotonic curve). This model may account for the tensile strength of concrete. With decreased strain at the unloading path, stress decreases to zero, after which point, if the tensile strength is ignored, stress remains zero; otherwise, stress decreases to tensile strength using a linear function with a slope of  $E_{ct}$ . With increased strain, stress remains zero up to the latest strain corresponding to zero stress and then stress increases, following a concave-downward parabolic with a slope of  $E_{c1}$  at the strain-axis (Esmaily and Xiao 2005). Cyclic behavior of concrete confined by FRP or lateral steel and FRP can be modeled by a linear cyclic model with a slope equal to the modulus of elasticity of plain concrete. Mander et al. (1984) and Esmaily-Xiao (2005) cyclic models were originally developed to model cyclic behavior of concrete confined by lateral steel; however, they can also be applied to model cyclic behavior of concrete confined by FRP or FRP and lateral steel. The Esmaily-Xiao and linear cyclic models for confined concrete are shown in Figure 3-5 in which the Mander et al. confined concrete monotonic model is used as the envelope curve.

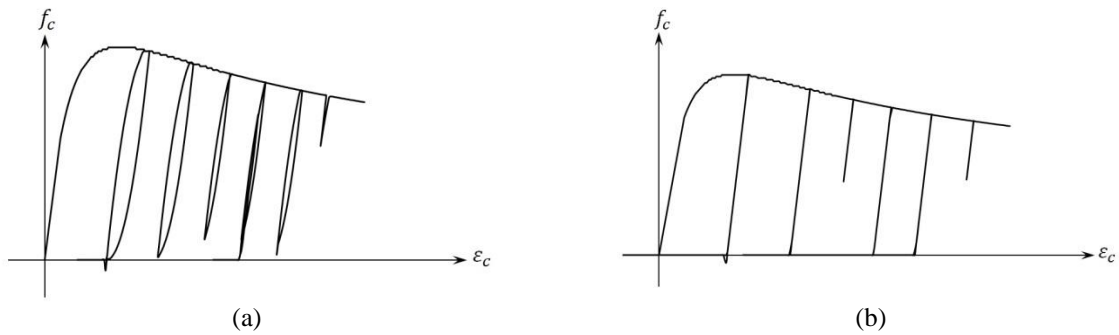


Figure 3-5 Implemented confined concrete cyclic models: (a) Esmaily-Xiao model, (b) linear model

For steel, Menegotto-Pinto's model (1973), Esmaily-Xiao's model (2005), and a linear model with a slope equal to the modulus of elasticity of steel were implemented into the developed computer program. Menegotto-Pinto's model has a bilinear backbone curve, as previously explained. Cyclic response of steel material was defined using a nonlinear equation. The shape of unloading and reloading curves are defined by three parameters:  $R_0$ ,  $a_1$ , and  $a_2$ . Because of numerical stability and realistic predictions, many researchers have used this model as a basis to propose new models for steel material.

Esmaily-Xiao's hysteretic model for steel is a multilinear model. At the reversal point, the unloading path is a linear function with a slope equal to modulus of elasticity of steel material. The Bauschinger effect is taken into account in this model by changing the slope of the first unloading part into a portion of steel's modulus of elasticity beyond a certain stress (Esmaily and Xiao 2005). In order to realistically simulate cyclic behavior of steel material, this ratio and the strain at which the slope change occurs are different in the second (tensile strain and compressive stress) and fourth (compressive strain and tensile stress) quarters from their values in the first (tensile strain and stress) and third (compressive strain and stress) quarters. Esmaily-

Xiao's model uses five ratios ( $P_1$ ,  $P_2$ ,  $P_3$ ,  $R_1$ , and  $R_2$ ) to change the hysteretic behavior of steel material. Unlike Menegotto-Pinto's model, linear and Esmaily-Xiao's cyclic models can be used in conjunction with any steel monotonic model as an envelope curve. Figure 3-6 shows Esmaily-Xiao's and Menegotto-Pinto's cyclic models for steel material. In Figure 3-6(a), Esmaily-Xiao's monotonic model is used as an envelope curve of Esmaily-Xiao's cyclic model. The Menegotto-Pinto cyclic model is used in conjunction with Menegotto-Pinto's monotonic model in Figure 3-6(b).

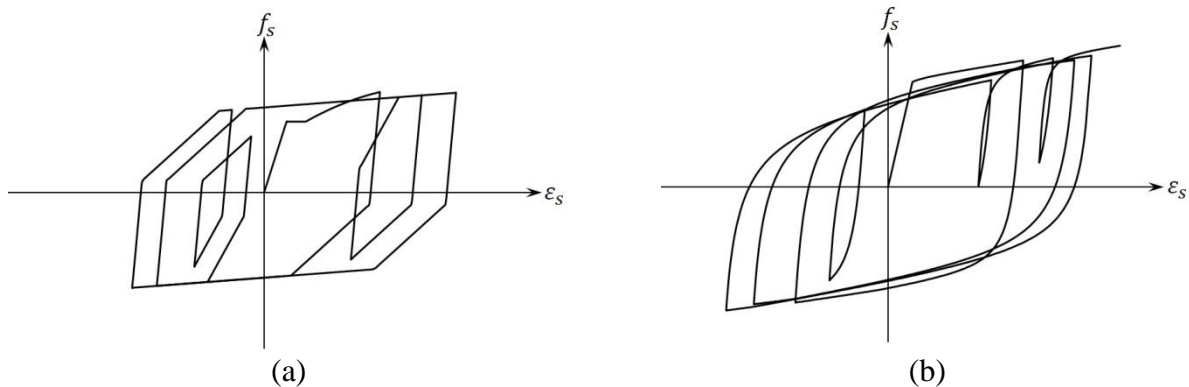


Figure 3-6 Implemented steel cyclic models: (a) Esmaily-Xiao model, (b) Menegotto-Pinto model

### 3-5 Analysis

Because shear deformation is not modeled in the computer application, beam-column specimens should not be shear-critical. A beam column specimen was modeled cantilever considering fix support at the bottom of the specimen. Axial force and lateral forces/displacements were assigned to the top of the column. The centroid of a composite section was calculated with respect to a global x- and y-axis considered in the program. Considering

curvature in x- and y-direction, uniaxial strain of fibers was calculated using the following equations:

$$\begin{aligned}\varepsilon_{si} &= \varphi_x \times y_{si} - \varphi_y \times x_{si} - D \\ \varepsilon_{ci} &= -(\varphi_x \times y_{ci} - \varphi_y \times x_{ci} - D) \\ \varepsilon_{fi} &= \varphi_x \times y_{fi} - \varphi_y \times x_{fi} - D\end{aligned}\tag{4-1}$$

In the above equations,  $\varepsilon_{si}$ ,  $\varepsilon_{ci}$ , and  $\varepsilon_{fi}$  are uniaxial strain at steel bar, concrete fiber, and FRP fiber, respectively.  $x_i$ ,  $y_i$ ,  $\varphi_x$ , and  $\varphi_y$  are locations of  $i^{\text{th}}$  fiber with respect to x- and y-axis of the global coordinate system, respectively, and  $D$  is strain at the global coordinate's centroid (Figure 3-7).

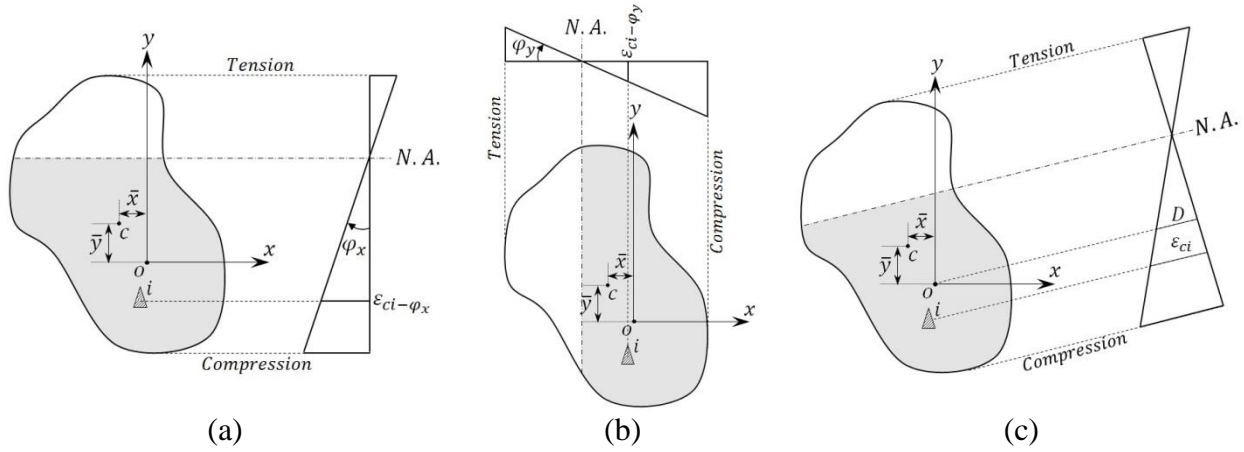


Figure 3-7 Calculation of fiber's strain under biaxial bending

When strains of all concrete and FRP fibers and longitudinal bars were calculated, stress of fibers and bars were calculated through cyclic and monotonic models defined for each fiber or bar as follows:

$$\sigma_{si} = \text{Steel Cyclic Model}(\text{Steel Monotonic Model}, \varepsilon_{si}, \varepsilon_{si}^p, \sigma_{si}^p, \varepsilon_{un}, \sigma_{un})\tag{4-2}$$



$$\sigma_{ci} = \text{Concrete Cyclic Model}(\text{Concrete Monotonic Model}, \varepsilon_{ci}, \varepsilon_{ci}^p, \sigma_{ci}^p, \varepsilon_{um}, \sigma_{um}, \varepsilon_{RO}, \sigma_{RO})$$

$$\sigma_{fi} = \text{FRP Cyclic Model}(\text{FRP Monotonic Model}, \varepsilon_{fi}, \varepsilon_{fi}^p, \sigma_{fi}^p)$$

where  $\sigma_{si}$ ,  $\sigma_{ci}$ , and  $\sigma_{fi}$  are stresses in  $i^{\text{th}}$  steel/FRP bar, concrete fiber, and FRP fiber, respectively. Stress in each fiber depends on current strain ( $\varepsilon_i$ ), previous strain and stress of that fiber ( $\varepsilon_i^p, \sigma_i^p$ ), strain and stress of the last point reached on the monotonic model ( $\varepsilon_{um}, \sigma_{um}$ ) and in concrete fibers, and strain and stress of the last point reached in the unloading branch ( $\varepsilon_{RO}, \sigma_{RO}$ ).

When the axial force and bending moments have stresses of all fibers and bars, the axial force and bending moments are calculated using the following equations:

$$P = \iint_A \sigma \, dx dy = \int_A \sigma \, dA \quad (4-3)$$

$$M_x = \int_A \sigma \times (y - \bar{y}) \, dA \quad (4-4)$$

$$M_y = \int_A \sigma \times (x - \bar{x}) \, dA$$

Using discrete fibers, the above equations can be written in the following discrete format:

$$P = \sum_{i=1}^{n_s} A_{si} \times \sigma_{si} + \sum_{i=1}^{n_c} A_{ci} \times \sigma_{ci} + \sum_{i=1}^{n_f} A_{fi} \times \sigma_{fi}$$

$$M_x = \sum_{i=1}^{n_s} A_{si} \times \sigma_{si} \times (y_{si} - \bar{y}) + \sum_{i=1}^{n_c} A_{ci} \times \sigma_{ci} \times (y_{ci} - \bar{y}) + \sum_{i=1}^{n_f} A_{fi} \times \sigma_{fi} \times (y_{fi} - \bar{y}) \quad (4-5)$$

$$M_y = \sum_{i=1}^{n_s} A_{si} \times \sigma_{si} \times (x_{si} - \bar{x}) + \sum_{i=1}^{n_c} A_{ci} \times \sigma_{ci} \times (x_{ci} - \bar{x}) + \sum_{i=1}^{n_f} A_{fi} \times \sigma_{fi} \times (x_{fi} - \bar{x})$$

In the above equations,  $A_{si}$ ,  $A_{ci}$ , and  $A_{fi}$  are the area of  $i^{\text{th}}$  steel/FRP bar,  $i^{\text{th}}$  concrete fiber, and  $i^{\text{th}}$  FRP fiber, respectively.  $\bar{x}$  and  $\bar{y}$  are the distances of the cross section of beam-column specimen centroid along x- and y-direction, respectively.

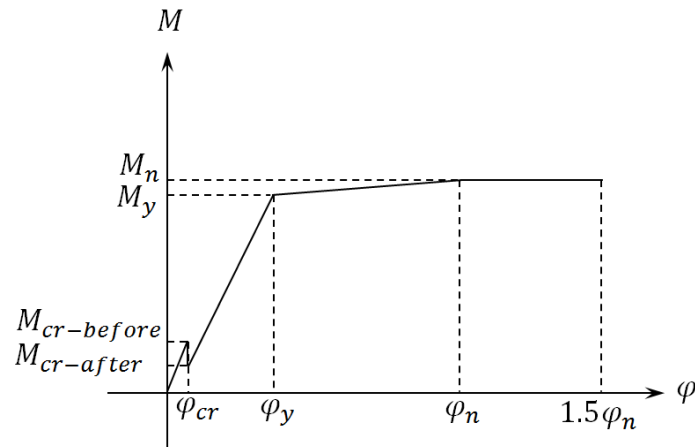


Figure 3-8 Displacement-controlled code-based moment-curvature curve

### 3-5-1 Moment-Curvature Analysis

In the developed computer application, monotonic moment-curvature analysis was performed with consideration of the code-based method and material models. Code-based monotonic moment-curvature analysis can be conducted for RC beam-columns laterally reinforced by conventional lateral steel and longitudinally reinforced by steel bars only. However, exact monotonic and cyclic moment-curvature analysis considering material models can be performed for concrete beam-columns with any longitudinal and lateral reinforcement.

In code-based moment-curvature analysis, the “ACI stress-block” is used without considering the confinement effect. In this analysis, the angle of neutral axis with respect to x-axis should be given to the computer application. The approximate code-based moment-curvature graph contains four essential points. The first point is related to the starting point of which curvature and moment are equal to zero. The second point is related to the “First Crack.” For displacement control analysis (Figure 3-8), when the curvature changes step-by-step and

moment is calculated, the bending moment drops when a crack develops. Therefore, at the same curvature ( $\varphi_{cr}$ ), two moments are present: the moment before ( $M_{cr-before}$ ) and the moment right after the crack ( $M_{cr-after}$ ). For force-controlled analysis (Figure 3-9), when curvature related to a given moment is calculated at the first crack point, the curvature jumps to a new curvature immediately following the first crack, thereby demonstrating the presence of two curvatures: one before the first crack and one after the first crack. The third point of the code-based moment-curvature graph is related to “Steel Yield,” at which point the steel bars initially yield. The last point is related to “Ultimate Strength,” which considers the code-based ultimate strength of an RC section.

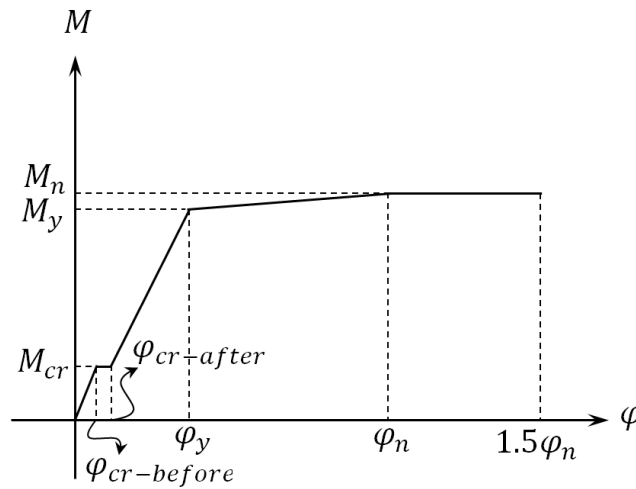


Figure 3-9 Force-controlled code-based moment-curvature curve

In moment-curvature analysis using material models, the curvature-path along x- and y-axis is known and the ultimate bending moment along x- and y-axis are calculated using material models. Having  $\varphi_x$  and  $\varphi_y$  in each step during an iterative process, the value of  $D$  is calculated to set axial force equal to the applied axial force at the top of the beam-column specimen. Next,

bending moments along the x- and y-axis are calculated using Eq. (5-5). Unlike code-based moment-curvature analysis, the developed computer application can perform monotonic and cyclic moment-curvature analysis using material models.

### 3-5-2 Force-Deflection Analysis

Two methods can be employed to calculate flexural deformation of an RC beam-column. In the first method, flexural deformation analysis of an RC beam-column specimen is conducted using the finite element approach. This approach has high computational demands. In Finite Element Method (FEM), displacement approximation has a significant role in the accuracy of force-deflection results. When curvature of the critical section (at the bottom of the beam-column specimen) falls into the descending branch of the moment-curvature curve, the corresponding stiffness matrix becomes negative definite and adaptive methods (resorting trial-error) must be employed to capture force-deflection results (Esmaily and Xiao 2002).

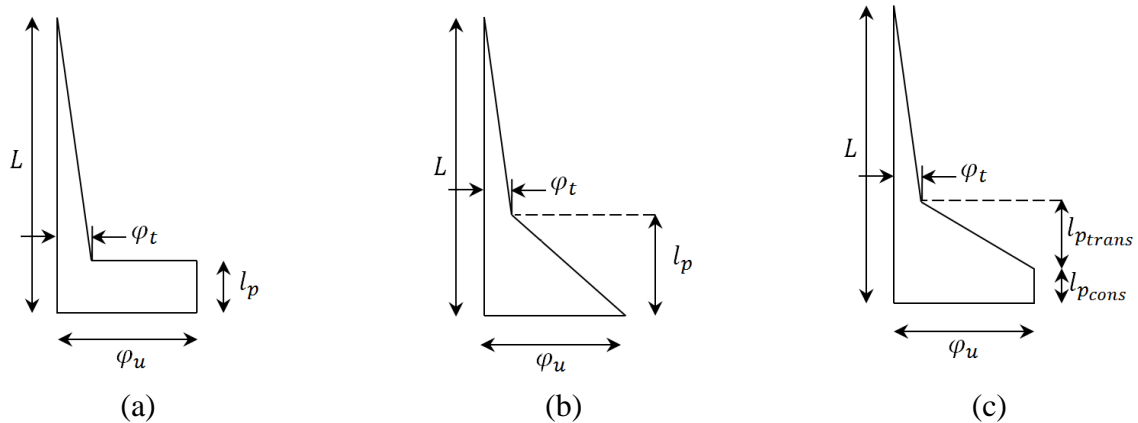


Figure 3-10 Curvature distributing along column height as assumed in (a) Priestley and Park and Priestley and Park revised by Xiao's methods, (b) Esmaily's first method, and (c) Esmaily's second method

Table 3-1 Implemented plastic hinge methods in the computer application

Method	Plastic Hinge Length
Priestly and Park (1987)	$l_p = 0.08 \times L + \xi \times f_{sy} \times d$ , $\xi = 0.022 \text{ mm}(0.15 \text{ in.})$
Priestly and Park Revised by Xiao (Esmaily and Xiao 2002)	$l_p = 0.08 \times L + \xi \times \sigma_s \times d$ , $\xi = 0.022 \text{ mm}(0.15 \text{ in.})$
Esmaily First Method (Esmaily and Xiao 2002)	$l_p = L \times \left(1 - \frac{M_{yield}}{M_u}\right)$ , $\phi_t = \phi_{yield} \times \left(\frac{M_u}{M_{yield}}\right) \times \frac{(L - l_p)}{L}$
Esmaily Second Method (Esmaily and Peterman 2007)	$l_p = l_{pcons} + l_{ptrans}$ , $l_{pcons} = l_{p1} + l_{p2}$ , $l_{p1} = \begin{cases} D & L/D \leq 12.5 \\ 0.08 \times L & L/D > 12.5 \end{cases}$ $l_{p2} = \xi \times \sigma_s \times d$ , $\xi = 0.022 \text{ mm}(0.15 \text{ in.})$ $l_{ptrans} = L - \frac{M_{yield}}{M_u} \times (L + l_{p2}) - l_{p1}$

In the second method to calculate flexural deformation of an RC beam-column, the plastic hinge concept of the critical section (or transition area) and a proper curvature distribution along the beam-column specimen height are employed to solve the force-deflection problem when curvature falls into the descending branch of the moment-curvature curve. In the plastic hinge approach, column height is divided into two elastic and plastic elements. Depending on the curvature distribution method, the length of the transition area (plastic hinge length) may or may not change during force-deflection analysis. Total displacement at the top of a column is a summation of elastic and plastic deformation caused by elastic and plastic elements, respectively.

In the developed computer application, the second approach was employed to perform force-deflection analysis of an RC beam-column under constant or variable axial force and cyclic or monotonic lateral forces/displacements. Nearly 30 plastic hinge models are available in the literature, of which Priestley and Park's model (Priestley and Park 1987), Esmaily's first and second model, and Xiao's model (Esmaily and Xiao 2002) were implemented into the window-based computer program. Although a majority of existing plastic hinge models in the literature were developed considering uniaxial behavior of RC columns, experimental evidences have

confirmed plastic hinge length is not affected by biaxial loading (Rodrigues et al. 2013); therefore, the plastic hinge models developed based on uniaxial testing are applicable for biaxial force-deflection analysis. Priestley and Park's plastic hinge length depends on column height, longitudinal steel yield strength, and rebar diameter. Curvature distribution was considered to be uniform along the plastic hinge length, and axial force effect was not taken into account in Priestley and Park's model. Xiao (Esmaily and Xiao 2002) later modified Priestley and Park's plastic hinge length by employing maximum tensile stress at longitudinal bars instead of steel yield strength. These plastic hinge models work well for RC columns under constant axial force and monotonic lateral force/displacement.

Esmaily's first plastic hinge method considered a linear distribution along transition zone or plastic hinge length. Plastic hinge length applied in this model depends on yield moment and moment at critical section at each step of loading. Therefore, axial force effect and cyclic and monotonic behavior of all materials are taken into account in calculation of plastic hinge length. Esmaily's first plastic hinge length may increase by decreasing the ratio of yield moment to moment of critical section. Plastic hinge length simulates severe damage at column footing; therefore, it cannot be decreased after formation (Esmaily and Xiao 2002).

In Esmaily's second plastic hinge model, divides the transition zone into two parts. Curvature distribution along the part closet to the critical section is assumed to be uniform. The length of this part is constant and is equal to the section depth for columns with high to depth ratio of less than 12.5; otherwise, it is equal to  $0.08 \times L$ , where  $L$  is the column height. Curvature distribution along the second part is assumed to be linear; its length depends on existing axial force and level of lateral force. Esmaily's first and second models work more accurately compared to Priestley and Park and Priestley and Park-Revised by Xiao models for RC columns

under variable axial force and cyclic lateral force/displacement (Esmaily and Xiao 2002). Curvature distribution along column height as assumed in aforesaid models is shown in Figure 3-10 and their formulation is summarized in Table 3-1.

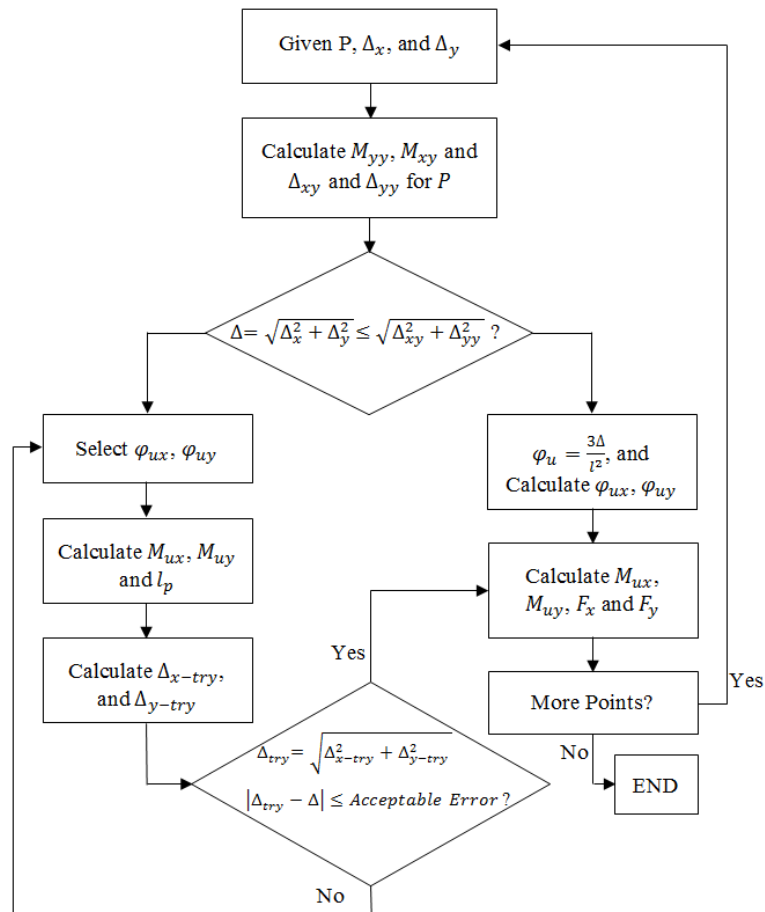


Figure 3-11 Force-deflection analysis flowchart

The developed computer application can conduct biaxial force-deflection analysis. Axial force and lateral forces/displacements are applied at the top of columns. For each combination of axial force and lateral displacement in the x- and y-direction using two sets of trial-error process for  $D$ ,  $\varphi_x$  and  $\varphi_y$ , axial force and lateral displacements are set to the applied values. Force-deflection analysis of an RC section under constant or variable axial force and cyclic or

monotonic lateral displacements can be conducted using aforesaid plastic hinge models implemented in the developed computer application. A simplified flowchart for force-deflection analysis of an RC column under axial force and biaxial lateral displacements is shown in Figure 3-11.

### **3-5-3 Axial Force-Bending Moment Interaction Curves**

Three types of axial force-moment interaction 3D surface of an RC section can be conducted using the developed computer program. In the first type, or code-based axial force-moment interaction 3D surface, axial force-moment analysis is performed considering the ACI stress-block concept without considering the confinement effect applied by lateral reinforcement. Compressive strain in the extreme concrete fiber is assumed to be 0.003. Considering a specific angle for neutral axis with respect to the x-axis, for each level of axial force through an iteration process, curvature along the neutral axis is changed to converge to a curvature resulting in the considered axial force. When curvature is changed, strain at the global coordinate's centroid is changed to maintain strain at the extreme compressive concrete fiber equal to 0.003. Code-based axial force-moment analysis can be performed only for concrete sections reinforced laterally by lateral steel reinforcement and longitudinally by steel bars. There are two methods to calculate the ACI interaction curve as follows:

In the first method, the strain at the extreme concrete fiber is equal to 0.003. The curvature along the analysis axis is increased from zero to the point that strain at the extreme tensile steel bars becomes equal to 0.005. Then the curvature is decreased in a way that strain at the extreme steel fiber remains 0.005.



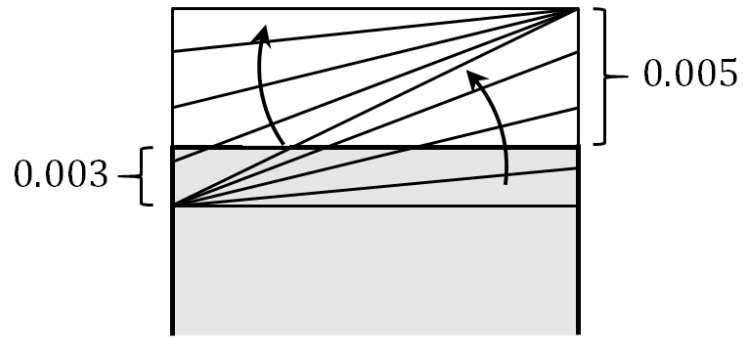


Figure 3-12 Curvature change in Method 1

In the second method, the strain at the extreme concrete fiber is kept constant and equal to 0.003 and the curvature will increase to the point and the section fails.

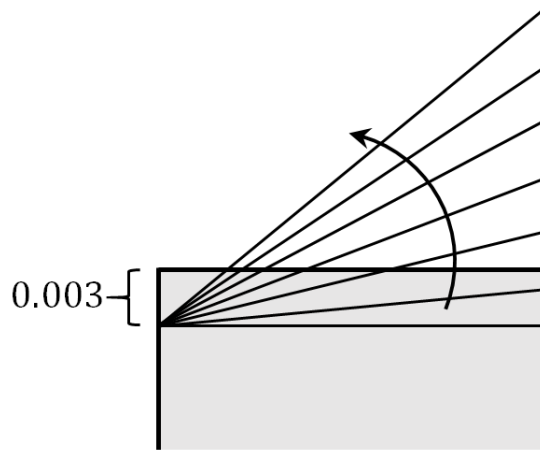


Figure 3-13 Curvature change in Method 2

The second type of axial force-moment interaction surface is calculated considering user-selected material models for plain concrete, confined concrete, reinforcing steel, and FRP. This type of interaction surface can be calculated for a concrete section confined by conventional steel

(tie/spiral), FRP wraps, or FRP wraps and conventional steel. Strain at extreme compressive fibers is assumed to be constant and can be defined by the user.

The third type of interaction 3D surface is referred to as axial force-bending moment interaction failure surface in the literature. Four techniques were employed in the literature to construct the 3D failure surface of a composite section: (i) interaction curve considering constant or variable ratio of curvature along x- and y-axis (constant neutral axis orientation), (ii) interaction curve for a given ratio of bending moment in x- and y-direction, (iii) bending moment constant for a constant given axial force, and (iv) generation of triplets stress resultant extending an oriented strength line. The first technique (constant neutral axis orientation) was utilized in the developed computer application.

In various algorithms developed by researchers to calculate failure surface, ultimate moment capacity of an RC section is defined as the maximum moment in monotonic moment-curvature analysis considering constant axial force (not considering the loading pattern of axial force). However, columns exposed to a dynamic excitation are subjected to a loading pattern in combined but non-proportional lateral and axial directions. Consideration of axial force loading pattern when calculating bending capacity of an RC section is essential in structure columns located in near-fault regions.

The developed computer application is capable of generating the failure surface of a composite section using proper material models with or without considering the axial force loading pattern. To calculate the failure surface of a section while considering the axial force loading pattern for a specific neutral axis orientation and axial force level ( $P$ ), a moment-curvature analysis was performed considering the pattern of axial force against curvatures along x- and y-directions. The maximum moment was selected as the ultimate capacity of the section

in that level of axial force. The axial force loading pattern includes a number of points with various curvature along the x- and y-axis and axial force coefficient ( $\varphi_x$ ,  $\varphi_y$ ,  $ac$ ). The axial force coefficient ( $ac$ ) for any combination of x- and y- curvature cannot exceed 1.0, meaning that the maximum compressive axial force ( $ac \times P$ ) in that pattern is equal to the specified level of axial force ( $P$ ). The axial force coefficient may consider more than -0.1, meaning that the maximum tensile axial force capacity of the section should not be considered more than  $0.1 \times P$ . Sinusoidal and triangular axial force loading patterns are shown in Figure 3-14.

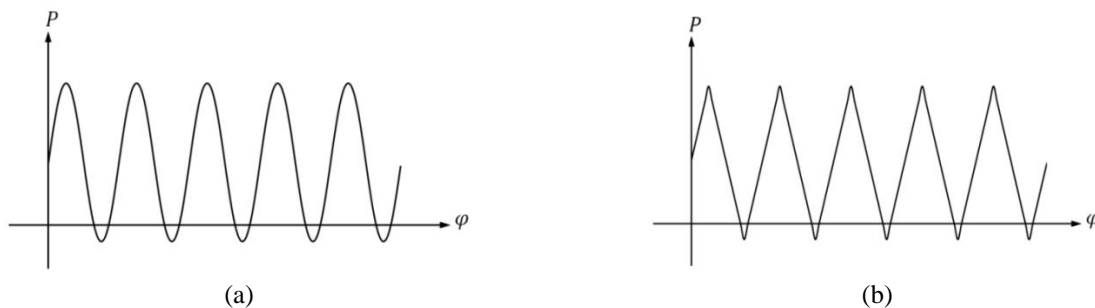


Figure 3-14 (a) Sinusoidal and (b) triangular axial force loading pattern

### 3-6 Validation Examples

This section presents the performance and applicability of the developed computer application using four examples in which analytical results by the program are compared to experimental results from tests conducted on the respected specimen. The first example investigates computer application accuracy to predict moment-curvature response of a reinforced concrete section. In the second and third validation examples, computer application performance for predicting the force-deflection response of two columns with their respected cross sections is illustrated. The fourth test investigates computer application capability in constructing the failure surface of a square section and interaction curves using the ACI stress-block concept.

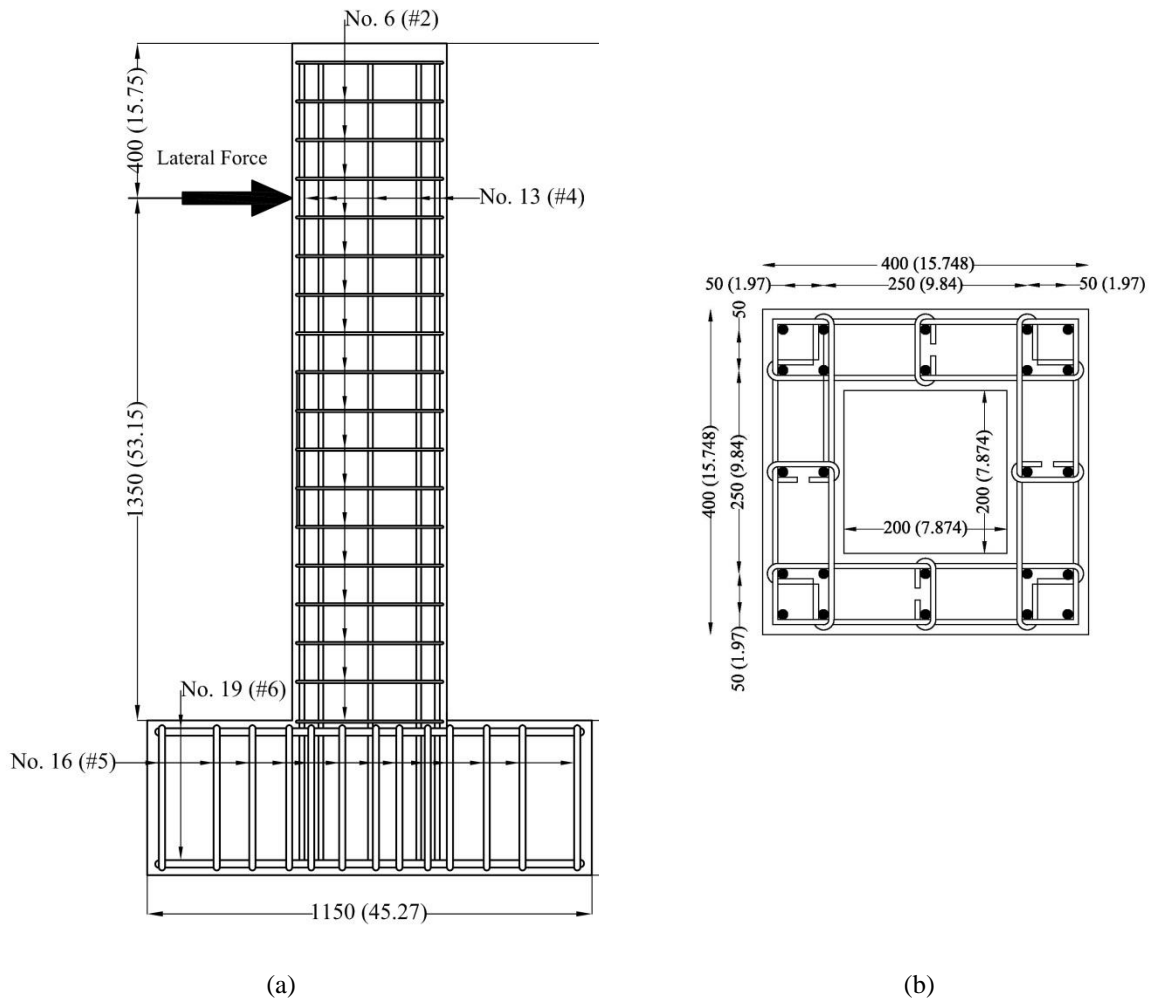


Figure 3-15 Geometry and reinforcement of the specimen TP-36; (a) elevation, (b) cross section

### 3-6-1 Moment-Curvature Analysis

The developed window-based computer application was employed to conduct moment-curvature analysis of a hollow square cross section. The hollow square section, as shown in Figure 3-15, had a width of 400 mm (15.748 in.), cover width of 50 mm (1.97 in.), and hole width of 200 mm (7.874 in.). Cylinder strength of concrete was 29.7 MPa (4.05 ksi). The column specimen was reinforced longitudinally with 24 No. 13 (24 #4) Grade SD295A (yield strength

was 374 MPa (54.24 ksi)), giving the specimen a longitudinal ratio of 2.53%. The longitudinal steel rebar arrangement is shown in Figure 3-15. The transverse reinforcing steel was Grade SD295A with yield strength of 363 MPa (52.64 ksi). Lateral reinforcement was a No. 6 (#2) with center-to-center spacing of 100 mm (3.93 in.), giving the specimen volumetric lateral reinforcement of 1.23%.

The column specimen was tested under constant axial force of 230 kN (51.71 kips) and cyclic uniaxial lateral force. Bending moment and curvature were measured at the column footing. Additional details regarding experimental setup are presented in Kawashima et al. (2001).

The Mander et al. model (1988) for unconfined and confined concrete was employed in order to model monotonic behavior of concrete fibers located in the cover and core concrete, respectively. The Mander et al. model was developed for circular and rectangular cross sections without a hole/opening. An equivalent rectangular section without an opening was considered in order to use this model to simulate monotonic behavior of confined concrete in a rectangular section with a hole/opening. Dimensions of the equivalent rectangular section were similar to the original section; however, only the outer layer of longitudinal and lateral reinforcement original section were considered as longitudinal and lateral reinforcement of the equivalent section. Maximum strength, ultimate strain, and fracture strain of confined concrete in the hollow rectangular section was calculated considering the equivalent rectangular section in the Mander et al. model (1988). Tensile strength for confined and unconfined concrete was assumed to be 10% of the plain concrete compressive strength. Linear cyclic behavior with a slope of plain concrete modulus of elasticity was considered for unconfined and confined concrete fibers.

Menegotto-Pinto's model (1973) was used to model cyclic and monotonic behavior of longitudinal steel bars. The monotonic curve backbone coefficient ( $b$ ) in Menegotto-Pinto's model was set to 0.01. Cyclic parameters  $R_0$ ,  $a_1$ , and  $a_2$  were considered 2.0, 2.0, and 0.09, respectively.

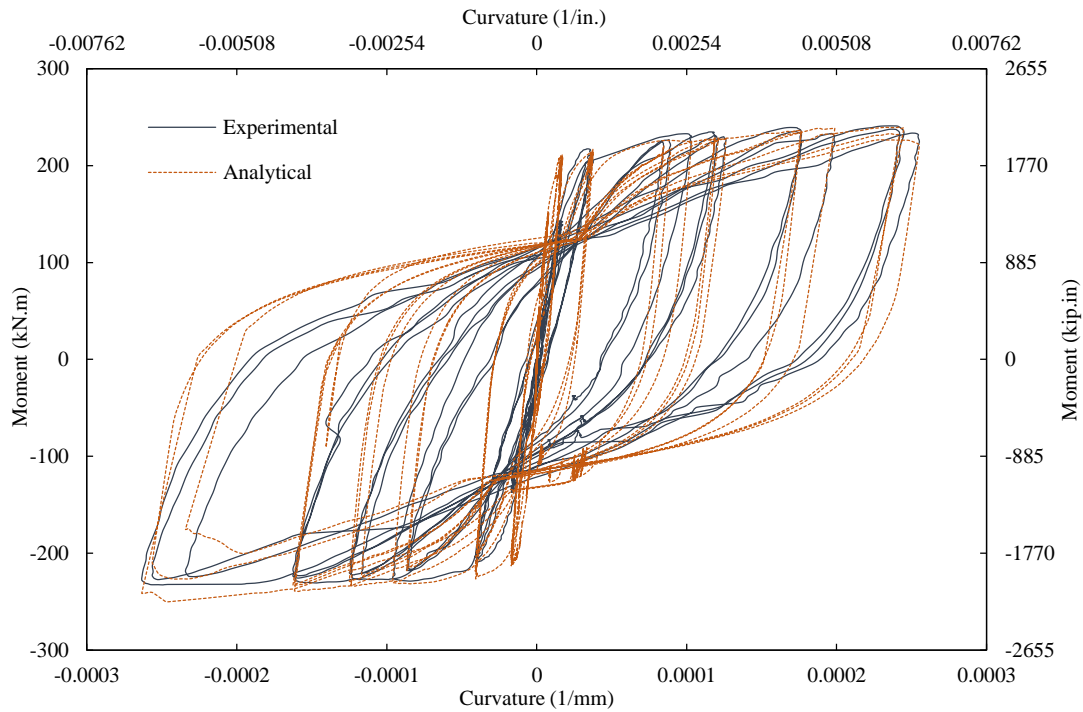


Figure 3-16 Comparison of analytical and experimental moment-curvature response curves for the hollow square cross section (TP-36)

Experimental and calculated moment-curvature curves at the bottom of the column specimen are shown in Figure 3-16. As demonstrated in the figure, great agreement exists between experimental data and analytical results calculated by the developed window-based computer application.

## 3-6-2 Force-Deflection Analysis

### 3-6-2-1 Reinforced Concrete Column under Axial Force and Uniaxial Lateral Force

The developed fiber-based computer application was employed for force-deflection analysis of an oval section (TP-9) under constant axial force and uniaxial cyclic lateral force, tested by Fujikura et al. (1998). Geometrical properties of the oval section are shown in Figure 3-17 in SI and imperial systems (numbers in parenthesis). The column specimen was reinforced longitudinally with 38 No. 10 (38 #3) Grade SD295, giving the specimen a longitudinal ratio of 0.83%. The longitudinal steel bar arrangement is shown in Figure 3-17. Lateral reinforcement was provided using No. 6 (#2) with center-to-center spacing of 150 mm (5.905 in.), giving the specimen volumetric lateral reinforcement of 0.9%. Cylinder strength of concrete ( $f'_{c0}$ ) was 22.7 MPa (3.292 ksi) and yield strength of longitudinal and lateral steel was 379 MPa (54.97 ksi) and 380 MPa (55.114 ksi), respectively. The oval section was under constant axial force of 160 kN (35.97 kips) and lateral uniaxial force in x-direction. Additional details regarding experimental setup are presented in Fujikura et al. (1998).

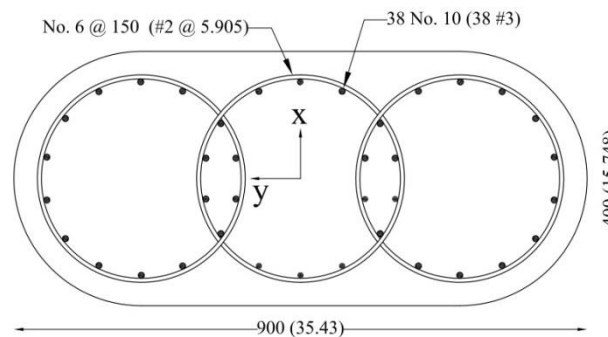


Figure 3-17 Oval cross section (TP-9)

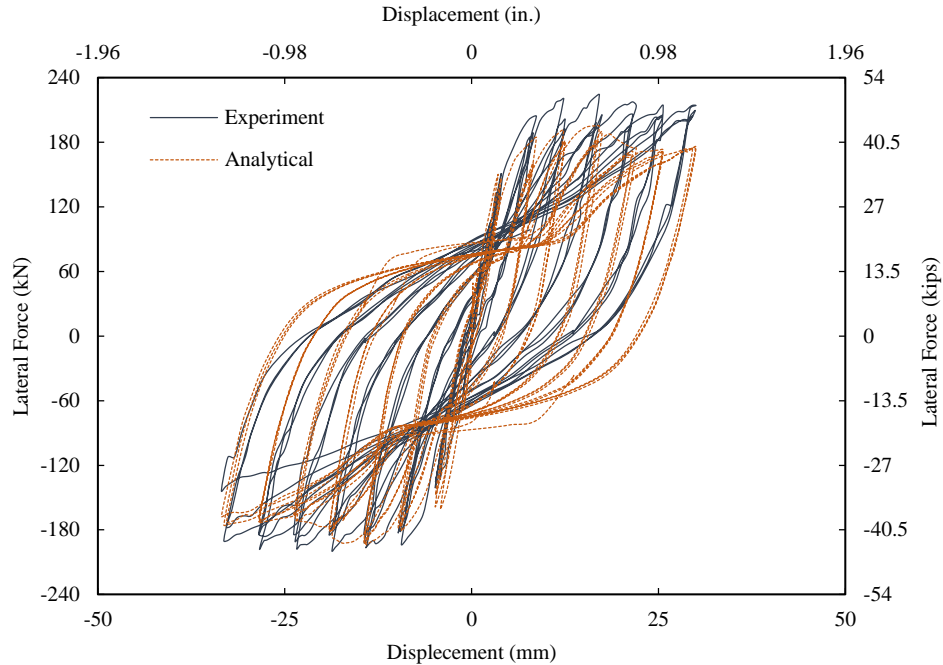


Figure 3-18 Comparison of analytical and experimental force-deflection response curves for oval section

In order to model the behavior of confined concrete, the Mander et al. model and linear cyclic model were used as monotonic and cyclic rules, respectively. Ultimate strain, stress, and fracture strain of confined concrete in the oval section were calculated considering only one of the circular hoops in the oval section as an equivalent section. Diameter of the equivalent cross section was equal to the width of the oval section (400 mm (15.748 in.)). It was reinforced longitudinally and laterally using 14 No. 10 (14 #3) and No. 6 @ 150 mm (#2 @ 5.905 in.).

For plain concrete (located at the cover), the Mander et al. monotonic model and linear cyclic model were employed. Menegotto-Pinto's monotonic and cyclic models modeled longitudinal reinforcement behavior. The monotonic curve backbone coefficient ( $b$ ) in Menegotto-Pinto's model was set to 0.01. Cyclic parameters  $R_0$ ,  $a_1$ , and  $a_2$  were considered 2.0, 2.0, and 0.09, respectively. Esmaily's first plastic hinge method (Esmaily and Xiao 2005) was



employed as curvature distribution along the specimen height. As shown in Figure 3-18, fiber-based analysis predicted cyclic force-deflection of the oval section with reasonable accuracy.

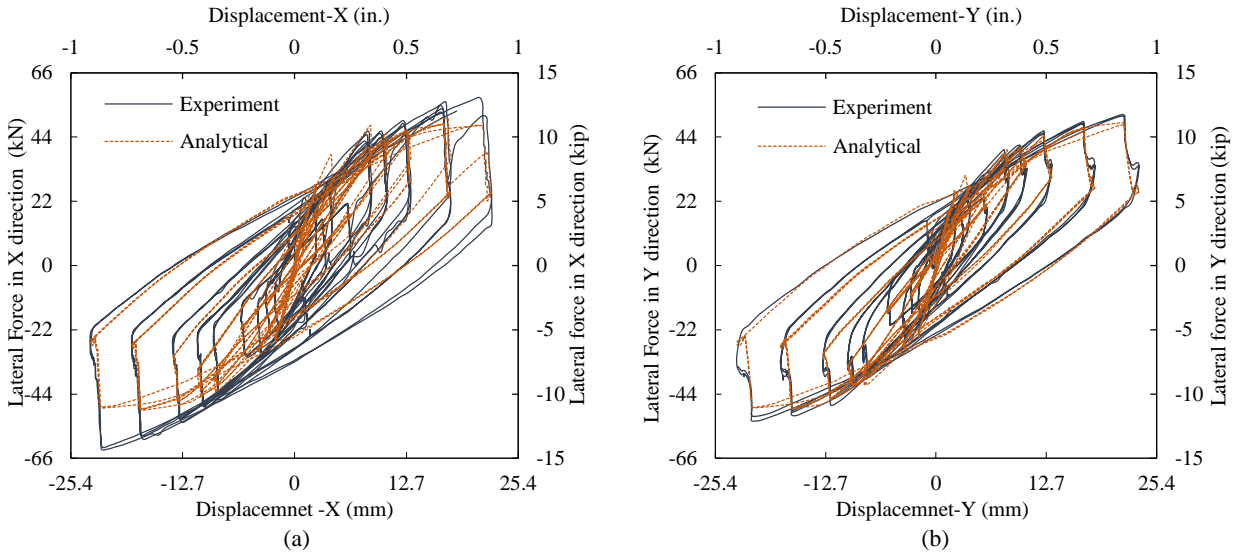


Figure 3-19 Comparison of analytical force-deflection with experimental data for specimen PB12-N15 in (a) x-, and (b) y-direction under expanding square path

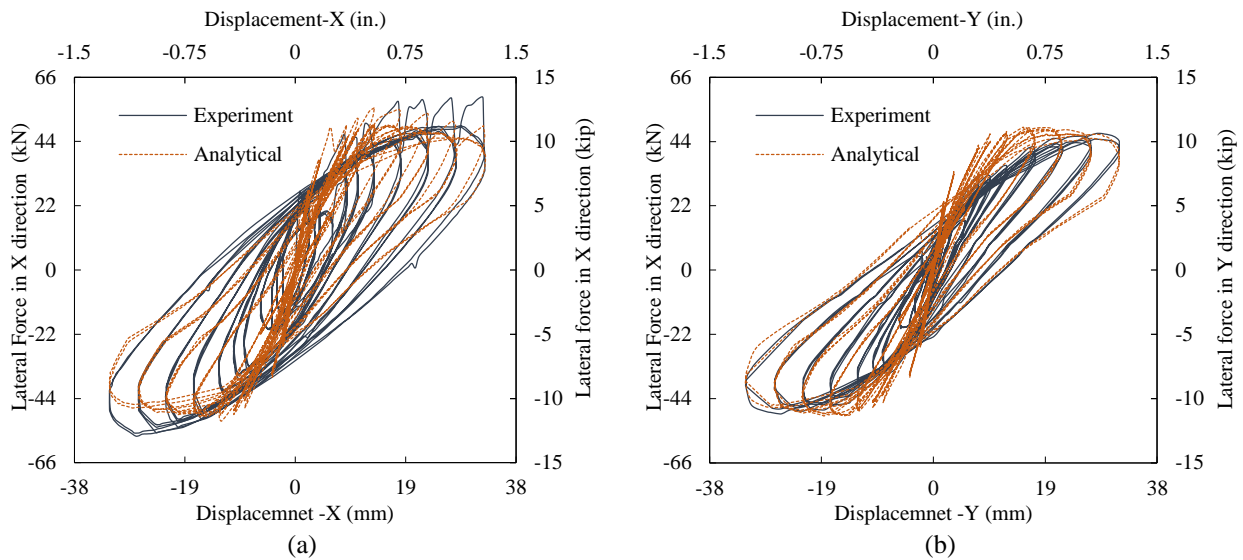


Figure 3-20 Comparison of analytical force-deflection with experimental data for specimens PB12-N16

### 3-6-2-2 Reinforced Concrete Column under Axial Force and Biaxial Lateral Force

The second example of force-deflection analysis is related to biaxial analysis of specimens PB12-N15 and PB12-N16 from experimental work by Rodrigues et al. (2012). In that work, specimens PB12-N15 and PB12-N16 were tested under expanding square and circular displacement paths, respectively, and constant axial force at approximately 10% of theoretical axial capacity (equal to  $P_0 = A_g \times f'_{c0}$ , where  $P_0$ ,  $f'_{c0}$  and  $A_g$  are theoretical axial capacity, plain concrete compressive strength, and gross cross-sectional area, respectively). These two specimens had a square cross section with a dimension of 300 mm (11.81 in.), and they were reinforced longitudinally using eight No. 12 bars in European standard (No. 12 bar diameter is 12 mm (0.472 in.)), giving the specimen a longitudinal ratio of 1.01%. Lateral reinforcement was provided by No. 6 bars in European standard with a step of 150 mm (5.9 in.) (No. 6 bar diameter is 6 mm (0.236 in.)), giving the specimen volumetric lateral reinforcement of 0.21%. Cylinder strength of concrete ( $f'_{c0}$ ) was 21.57 MPa (3.13 ksi), and steel reinforcement grade in the longitudinal and lateral direction was A400NR-SD (European standard).

Monotonic behavior of longitudinal bars was modeled using an idealized bilinear model. Because no information was available concerning the monotonic curve of reinforcing steel material, as recommended by Esmaily and Xiao (2002), the ultimate strain ( $\epsilon_{su}$ ) and strength ( $f_{su}$ ) for steel was considered to be  $24.9 \times \epsilon_{sy}$  and  $1.3 \times f_{sy}$ , respectively. The linear model was used to model cyclic behavior of longitudinal bars with linear unloading-reloading stiffness.

For confined and unconfined concrete fibers, the Mander et al. model (1988) for confined and unconfined concrete was used, respectively. Cyclic behavior of concrete fibers was considered linear with a slope equal to the modulus of elasticity of plain concrete. Priestly and

Park's plastic hinge method (1987) was employed as curvature distribution along the specimen height.

Experimental and analytical force-deflection curves of specimens PB12-N15 and PB12-N16 are shown in Figure 3-19 and Figure 3-20, respectively. As demonstrated in these figures, predicted results are in good agreement with experimental data.

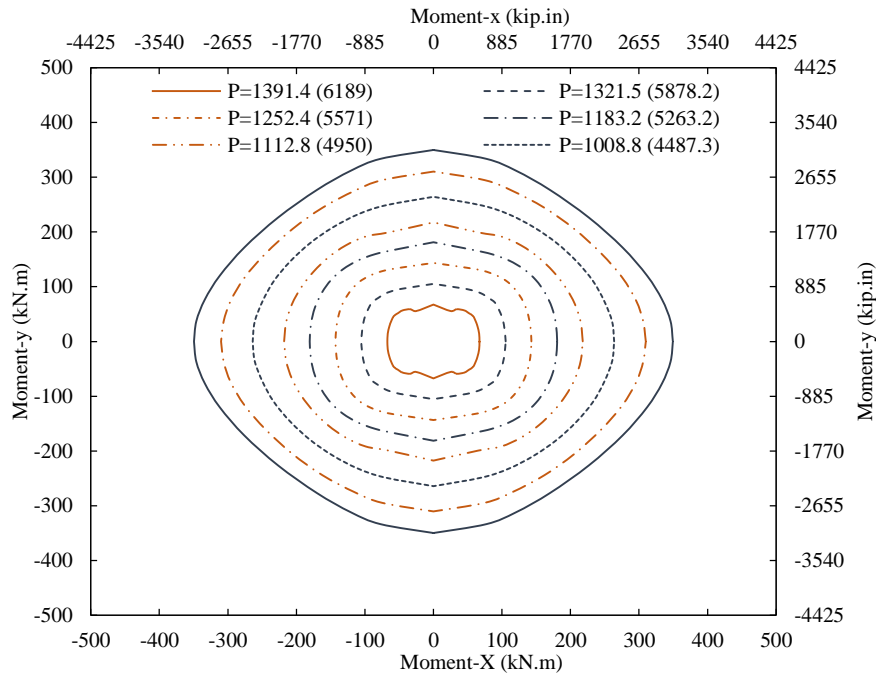


Figure 3-21 Failure curves for square section

### 3-6-3 Axial Force-Bending Moment Interaction Curves

The axial force-bending moment failure surface was constructed for a square cross section beam-column specimen with a dimension of 400 mm (15.75 in.). The square cross section was reinforced longitudinally using 20 No. 13 (20 #4), giving the specimen a longitudinal ratio of 1.58%. Lateral reinforcement was provided by No. 6 (#2) steel rebar with lateral spacing of 70 mm (2.75 in.), giving the specimen volumetric lateral reinforcement of 0.57. Cylinder

strength of concrete was 35.9 MPa (5.207 ksi), and yield strength of longitudinal and lateral steel was 363 MPa (52.65 ksi) and 368 MPa (53.37 ksi), respectively.

Actual interaction curves and failure surface of the square section are demonstrated in Figure 3-21 and Figure 3-22, respectively. To construct these plots, confined and unconfined concrete models of Mander et al. were used to model the behavior of confined and unconfined concrete fibers. The Menegotto-Pinto model was applied to model cyclic and monotonic behavior of longitudinal steel bars. Monotonic ( $b$ ) and cyclic coefficients ( $R_0$ ,  $a_1$ ,  $a_2$ ) in Menegotto-Pinto's model were considered 0.01, 2.0, 2.0, and 0.09, respectively.

In addition to actual failure surface, axial force-bending moment interaction 3D surface of the square section was calculated considering the ACI-stress block method (ACI 318-11). In Figure 3-23 and Figure 3-24, the red and blue dots are related to the ACI-interaction surface with consideration of reduction factors and ACI-interaction surface without reduction factors.

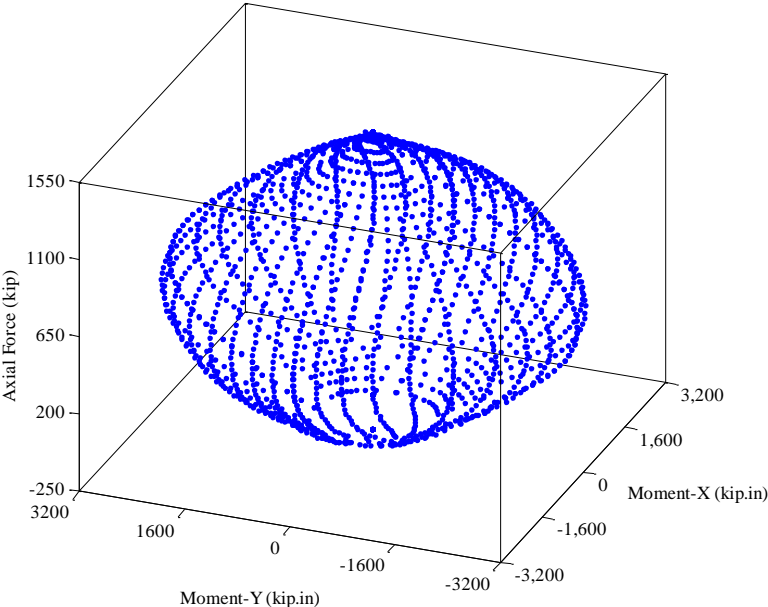


Figure 3-22 Failure-surface of square section

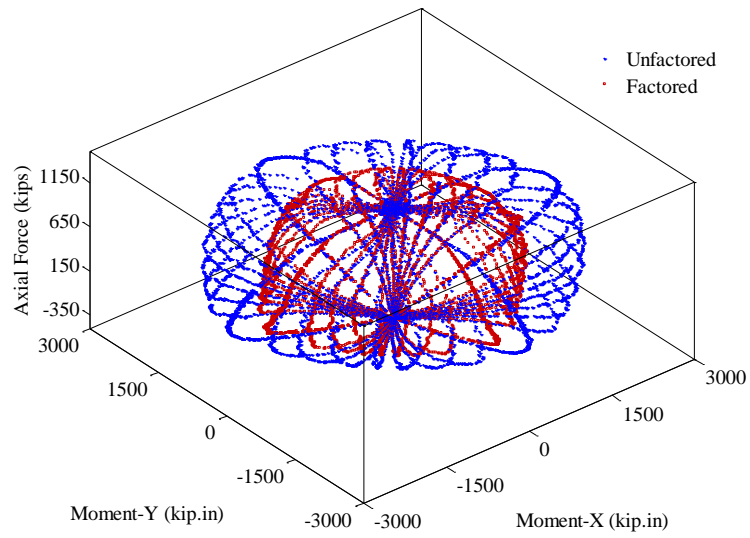


Figure 3-23 ACI Axial force-bending moment interaction surface

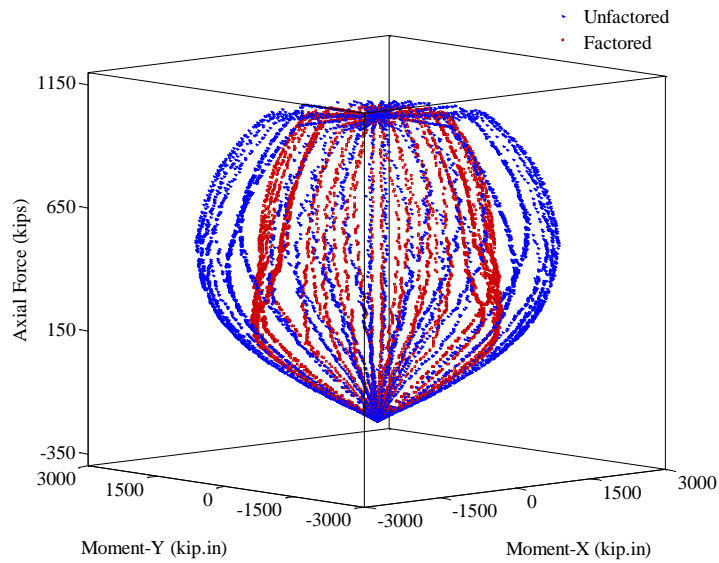


Figure 3-24 ACI Axial force-bending moment interaction surface

### **3-7 Developing New Model for Circular Concrete Column Confined by FRP and Conventional Lateral Steel**

FRP application to enhance ductility, flexural strength, and shear capacity of existing deficient concrete structures has increased during the last two decades. Therefore, various aspects of FRP-confined concrete members, specifically monotonic and cyclic behavior of concrete members confined and reinforced by FRP, have been studied in many research programs, resulting in proposal of various monotonic models for concrete confined by only FRP. Ozbakkalogu et al. (2013) reported 88 monotonic models for FRP-confined concrete circular sections until year 2011. They categorized these models into two design-oriented and analysis-oriented groups based on Lam and Teng's suggested categorization (Lam and Teng 2003). Using selected statistical indicators, model performances were assessed compared to reliable experimental data. According to their investigation, models by Lam and Teng (2003) and Tamuzs et al. (2006) most accurately predict ultimate strength and strain of FRP-confined concrete (Ozbakkalogou et al. 2013).

FRP wrapping is typically used to confine existing concrete members containing conventional lateral steel reinforcement (tie/spiral). The confining effect of lateral steel reinforcement in analytical studies has been uniquely considered in various models. A majority of related models consider confinement due to FRP and ignore the effect of conventional lateral steel reinforcement. Shao et al. (2005) used the model proposed by Samaan et al. (1998) that utilizes concrete confined only by FRP to conduct a fiber-based analysis of concrete specimens confined by FRP and tie. Although the amount of lateral steel reinforcement was not negligible in their test specimens, they ignored its confining effect and achieved a reasonably good agreement between experimental data and analytical results.

The model by Kawashima et al. (2000) was the first model to consider the confining effects of FRP and conventional lateral steel reinforcement. Harajli et al. (2006) consequently proposed a novel model for circular and rectangular concrete columns confined by FRP and conventional lateral steel. Eid and Paultre (2008) proposed a relatively complicated model requiring numerous parameters with good accuracy compared to experimental data. Based on test results from 24 specimens, Lee et al. (2009) proposed a new empirical model to predict monotonic behavior of concrete confined by FRP and steel spiral in circular sections. Chastre and Silva (2010) proposed a model for circular sections using Ricard and Abbott (1975) stress-strain relationship. Pellegrino and Modena's model (2010) was proposed for circular and rectangular sections confined by FRP with or without lateral steel reinforcement. Recently, Hu and Seracino (2013) proposed a constitutive model using Popovics (1973) equation and modified Mander et al. (1988) equations to predict peak stress and corresponding strain for concrete confined by FRP and lateral steel reinforcement. However, their model does not predict ultimate stress and its corresponding strain, two important parameters of monotonic models.

A majority of models have been based on experimental data from tests performed only by originators. Performance of these models in prediction of experiments conducted by others degrades considerably, as discussed later, as proven by a comparison of models proposed for conventional confined concrete (Esmaeily and Lucio 2006). Exploration of existing model performances for predicting the behavior of several tested specimens shows a need for improvement of existing algorithms. The model proposed in the current study is a step in this direction.

In addition to the proposed model, performance of four representative models in the literature was assessed in this study. Two of the four models (Samaan et al. 1998; Youssef et al.

2007) were proposed for concrete confined only by FRP but used as a model in analytical studies for concrete confined by FRP and lateral steel. The other two models (Kawashima et al. 2000; Lee et al. 2009), originally proposed for concrete confined by FRP and lateral steel, were chosen because of their easy-to-use equations and accuracy in predicting experimental monotonic behavior of specimens confined by FRP and lateral steel.

The new model proposed in this study was developed for concrete confined by FRP and conventional lateral steel. Performance of the proposed model and the four representative models from literature was compared to experimental data from four independent databases. These specimens were reinforced laterally by FRP wraps and steel tie/spiral and tested under monotonic concentric loading by Demers and Neale (1999), Eid and Paultre (2008), and Lee et al. (2009).

In order to demonstrate the accuracy of the proposed model compared to the four aforesaid models, a blind verification was performed using nonlinear moment-curvature analysis and experimental moment-curvature response of two specimens not used to calibrate the proposed model. These two specimens originated from experimental works performed by Kawashima (2001). They were reinforced by Carbon-FRP and steel tie laterally and were tested under constant axial load and cyclic lateral force.

### **3-7-1 Proposed Stress-Strain Curve**

Most concrete members retrofitted or designed using FRP wraps contain internal lateral steel reinforcement. Core concrete in these members is under the confining action of steel tie/spiral and FRP wraps. However, due to limited experimental data from tests conducted by the originator, proposed models for concrete confined by FRP or FRP and tie/spiral do not provide a



reasonably accurate prediction of specimen behavior tested by other researchers. Use of these models to analyze performance of columns confined by FRP and lateral steel underestimates or, in some cases, overestimates section capacity related to flexibility and flexural strength. Development of the proposed model for concrete confined by internal steel and external FRP lateral reinforcement is an attempt to address the aforesaid issue.

Axial stress-strain behavior of concrete confined by FRP and lateral steel (tie/spiral) was obtained using the Thorenfeldt et al. equation (1987). This equation is a modified version of the Popovics (1973) equation which describes stress-strain behavior of unconfined concrete (Popovics 1973). This equation works well for normal-weight concrete. In addition, many researchers have used this equation to simulate stress-strain behavior of concrete confined by conventional steel reinforcement. Hu and Seracino (2013) used Popovics' equation for monotonic behavior of concrete confined by FRP and lateral steel. The Thorenfeldt equation is as follows:

$$\frac{f_c}{f'_{cu}} = \frac{n \cdot (\varepsilon_c / \varepsilon_{cu})}{n - 1 + (\varepsilon_c / \varepsilon_{cu})^{nk}} \quad (2-3)$$

where  $n = E_c / (E_c - f'_{cu} / \varepsilon_{cu})$ .  $E_c$  is the modulus of elasticity of the concrete,  $f_c$  and  $\varepsilon_c$  are axial stress and axial strain of confined concrete, respectively,  $\varepsilon_{cu}$  and  $f'_{cu}$  are ultimate strain and ultimate stress of confined concrete, respectively, and Thorenfeldt parameter  $k = 0.8$ .

Many equations for calculating the modulus of elasticity of concrete are proposed in the literature. In this study, ACI equations were used because of their relative accuracy in providing the modulus of elasticity of concrete. ACI concrete modulus of elasticity equations for normal-weight concrete is as follows:

$$E_c = 4700\sqrt{f'_{c0}} \quad (MPa) \quad (2-4)$$

$$E_c = 57000\sqrt{f'_{c0}} \quad (psi)$$

where  $f'_{c0}$  is compressive strength of unconfined concrete.

Table 3-3-2 Geometrical and mechanical properties of specimens

Specimen	$D$ (m)	$f'_{c0}$ (MPa)	$\epsilon_{c0}$	FRP			TSR				$f'_{cu}$ (MPa)	$\epsilon_{cu}$
				$t$ (mm)	$E_{frp}$ (GPa)	$f_{fu}$ (MPa)	Type	$f_{ys}$ (MPa)	$s$ (m)	$d_b$ (mm)		
U25-2 (Demers and Neale, 1999)	0.3	25	0.002	0.9	84	3937	Tie	400	0.15	11.3	36.6	0.0104
U40-3 (Demers and Neale, 1999)	0.3	40	0.0027	0.9	84	3937	Tie	400	0.3	6.4	54.8	0.0065
C2NP2C (Eid and Paultre, 2008)	0.303	31.7	0.002	0.762	78	3350	Spiral	456	0.065	11.3	49.6	0.0124
C4NP4C (Eid and Paultre, 2008)	0.303	31.7	0.002	1.524	78	3350	Spiral	456	0.1	11.3	69.38	0.0243
C2MP4C (Eid and Paultre, 2008)	0.303	50.8	0.0024	1.524	78	3350	Spiral	456	0.065	11.3	92.08	0.0188
A3NP2C (Eid and Paultre, 2008)	0.303	31.7	0.002	0.762	78	3350	Tie	602	0.07	9.5	50.6	0.0124
S2F2 (Lee et al., 2009)	0.15	36.2	0.0024	0.22	250	4510	Spiral	1200	0.02	5	92.68	0.038
S2F3 (Lee et al., 2009)	0.15	36.2	0.0024	0.33	250	4510	Spiral	1200	0.02	5	108.0	0.039
S2F4 (Lee et al., 2009)	0.15	36.2	0.0024	0.44	250	4510	Spiral	1200	0.02	5	115.7	0.0384
S2F5 (Lee et al., 2009)	0.15	36.2	0.0024	0.55	250	4510	Spiral	1200	0.02	5	150.8	0.043
S4F2 (Lee et al., 2009)	0.15	36.2	0.0024	0.22	250	4510	Spiral	1200	0.04	5	74.77	0.0225
S4F3 (Lee et al., 2009)	0.15	36.2	0.0024	0.33	250	4510	Spiral	1200	0.04	5	88.8	0.029
S4F4 (Lee et al., 2009)	0.15	36.2	0.0024	0.44	250	4510	Spiral	1200	0.04	5	104.2	0.032
S4F5 (Lee et al., 2009)	0.15	36.2	0.0024	0.55	250	4510	Spiral	1200	0.04	5	123.6	0.036
IRCC. 1.1L (Benzaid et al., 2010)	0.16	9.51	.00377		34	50	ie	235	.01	8	0.59	.01593
IRCC. 2.1L (Benzaid et al., 2010)	0.16	9.51	.00377		34	50	ie	235	.014	8	9.17	.01475
IPCC. 1L (Benzaid et al., 2010)	0.16	5.93	.00273		34	50	ie	235	.014	8	9.63	.01278
II.RCC.1.1L (Benzaid et al., 2010)	0.16	8.24	.00302		34	50	ie	235	.0141	8	5.84	.00737
II.RCC.2.1L (Benzaid et al., 2010)	0.16	8.24	.00302		34	50	ie	235	.0142	8	9.18	.0935
II.RCC.1.3L (Benzaid et al., 2010)	0.16	8.24	.00302		34	50	ie	235	.0143	8	01.5	.1372
II.RCC.2.3L (Benzaid et al., 2010)	0.16	8.24	.00302		34	50	ie	235	.014	8	9.35	.1344
II.PCC. 3L (Benzaid et al., 2010)	0.16	9.46	.00169		34	50	ie	235	.014	8	2.91	.00727

### 3-7-2 Peak Stress and Strain in Confined Concrete

Ultimate strength and corresponding strain are important parameters in a stress-strain model. Major parameters affecting ultimate strength and corresponding strain of confined concrete include (i) cross-sectional dimension, (ii) lateral steel reinforcement bar area, (iii) lateral reinforcement spacing, (iv) FRP thickness, (v) FRP tensile strength, (vi) compressive strength of unconfined concrete, and (vii) FRP modulus of elasticity and/or FRP rupture strain.

Coefficients and factors in the following equation for the ultimate strength of concrete confined by FRP and conventional lateral reinforcement are based on regression analysis of a set of 22 experimental studies. Geometrical and mechanical properties of these specimens are presented in Table 3-3-2. All specimens were wrapped by CFRP with fibers primarily in the hoop direction. CFRP-wrapped specimens with stiffness in the longitudinal direction and a few specimens in Demers and Neale (1999) that were damaged before the compression test have been excluded. Behavior of concrete confined by lateral steel and FRP wraps was notably different from concrete confined by lateral steel and FRP tube because a part of FRP tube's lateral strain originated from its Poisson's ratio. Therefore, concrete-filled CFRP tube specimens with internal transverse steel reinforcement also have been excluded.

$$\frac{f'_{cu}}{f'_{c0}} = 1.1 + 2.5 \left( \frac{f'_{lf}}{f'_{c0}} \right)^{0.8} \times \left( \frac{f'_{ls}}{f'_{c0}} \right) + 3.5 \left( \frac{f'_{ls}}{f'_{c0}} \right)^{0.2} \left( \frac{d_c^2}{D^2} \right)^4 \quad (2-5)$$

where

$$f'_{lf} = \frac{2 \times t_f \times f_{yf}}{D} \quad (2-6)$$
$$f'_{ls} = \frac{2 \times A_{st} \times f_{ys}}{s \times d_c}$$

In Eqs. (3-234) and (3-235),  $t_f$ ,  $f_{yf}$ ,  $A_{st}$ ,  $f_{ys}$ , and  $s$  are FRP thickness, ultimate strength of FRP, transverse steel cross section area, steel yield strength, and transverse steel spacing, respectively. The confining mechanism for concrete confined by FRP and lateral steel is shown in Figure 3-25. Relationships between the second and third terms of Eq. 4-224 with experimental ultimate strength of confined concrete are shown in Figure 3-26 in which normalized experimental ultimate strength of confined concrete from the 14 specimens has reasonable linear correlation with the second and third terms of Eq. 4-224.

The second important parameter of the stress-strain curve is the ultimate strain of confined concrete, beyond which confined concrete is assumed to fail. Ultimate strain is a function of ultimate confining pressure by FRP and conventional steel. FRP jacketing and its mechanical properties significantly affect the ultimate strain of confined concrete. Experimental data monitoring showed the conventional reinforcement correlation between FRP jacketing confinement and confinement. The following equation is proposed for ultimate strain of confined concrete:

$$\frac{\varepsilon_{cu}}{\varepsilon_{c0}} = 2.0 + 6.5 \times \left( \frac{f_{lf}}{f'_{c0}} \right)^{0.7} \times \left( \frac{f_{ls}}{f'_{c0}} \right)^{0.7} + 6.0 \times \left( \frac{f_{ls}}{f'_{c0}} \right)^{0.04} \left( \frac{s}{0.5 \times D} \right)^{-0.8} \times \left( \frac{E_{frp}}{f'_{c0}} \right)^{0.5} \quad (2-7)$$

where  $E_{frp}$  is FRP modulus of elasticity. Parameters  $f_{ls}$  and  $E_{frp}$  are provided in Eq. (3-236) to consider properties related to FRP jacketing. The second term is primarily related to FRP confinement, and the third term primarily relates to the confining effect of lateral steel. For two specimens with identical lateral steel ratio, ultimate strain provided by the specimen with smaller lateral steel spacing is higher than the specimen with larger lateral steel bar area and spacing. Therefore, the lateral spacing effect is considered in the third term of the proposed equation for

ultimate strain as an individual term in addition to confining pressure caused by lateral steel reinforcement. The relationship between the second and third terms of Eq. (3-236) with experimental ultimate strain is shown in Figure 3-27, which demonstrates a reasonable linear correlation between normalized experimental ultimate strain and the second and third term of Eq. 4-226. Figure 3-28 shows a sample of the proposed stress-strain curve for concrete confined by FRP and lateral steel.

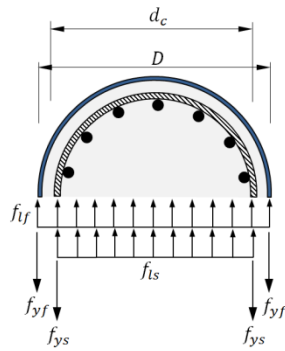


Figure 3-25 Confining mechanism for concrete confined by FRP and lateral steel

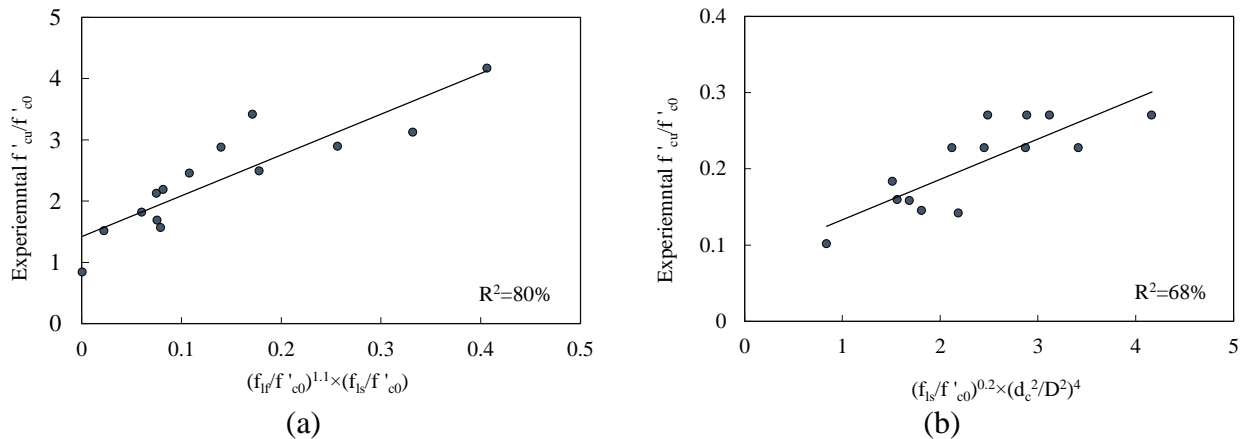


Figure 3-26 Relationship between (a) second and (b) third term of confinement effectiveness and experimental ultimate stress

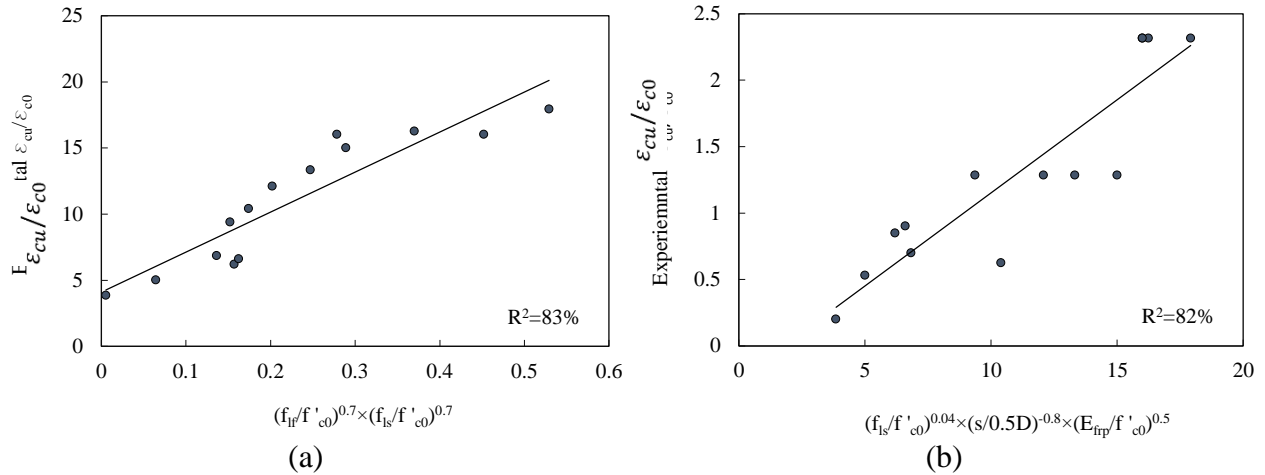


Figure 3-27 Relationship between (a) second, and (b) third term of confinement effectiveness and experimental ultimate strain

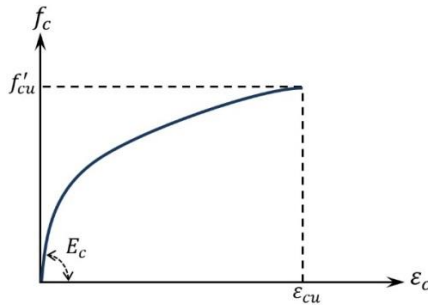


Figure 3-28 Proposed stress-strain curve for confined concrete by FRP and lateral steel

### 3-7-3 Validation

#### 3-7-3-1 Validation of the Proposed Model in Prediction of Concentric-Uniaxial Monotonic Stress-Strain Response

Figure 3-29 to Figure 3-33 show predicted monotonic uniaxial concentric stress-strain curves for specimens S2F2, S2F3, S4F2, A3NP2C, and U25-2, respectively, using the four models and the model proposed in this paper. In the model by Kawashima et al. (2000), the initial part of the model is a polynomial function ending at  $\epsilon_t$ , followed by the second part of the model that ends at a strain corresponding to ultimate strength ( $\epsilon_{cu}$ ). For specimens S2F2 and

S2F3, the calculated  $\varepsilon_t$  is greater than  $\varepsilon_{cut}$ ; therefore, the model by Kawashima is not presented in Figure 3-29 and Figure 3-30. For specimens S2F2 and S2F3 (Figure 3-29 and Figure 3-30, respectively) with considerable lateral steel reinforcement, models by Samaan and Youssef underestimate the ultimate strength and ultimate strain. The model by Lee, calibrated against and proposed based on their own test data, works generally well for these two specimens, as expected.

For specimen S4F2 (Figure 3-31) with less lateral steel reinforcement ratio compared to the first two specimens, Samaan's model underestimates the ultimate strength and overestimates ultimate strain. Youssef's model underestimates the ultimate strength and strain of the specimen S2F4 and the first two specimens (S2F2 and S2F3). The Kawashima model underestimates ultimate strain and overestimates strength of the concrete section for specimen S4F2.

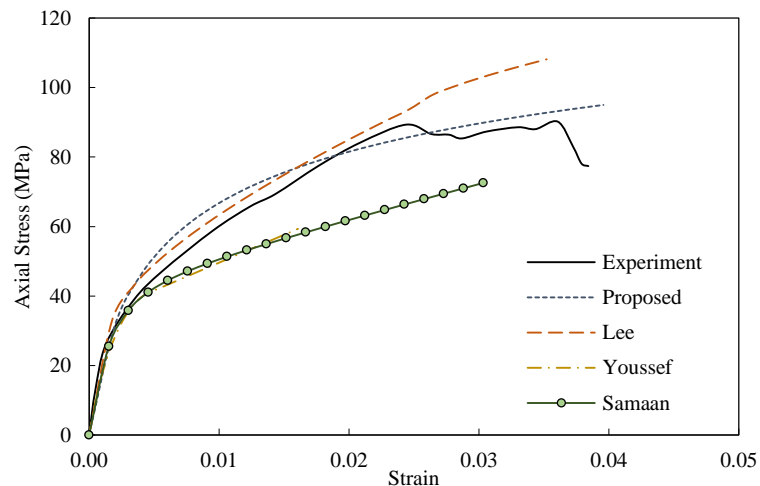


Figure 3-29 Comparison of confinement models to experimental stress-strain of S2F2 (monotonic concentric)

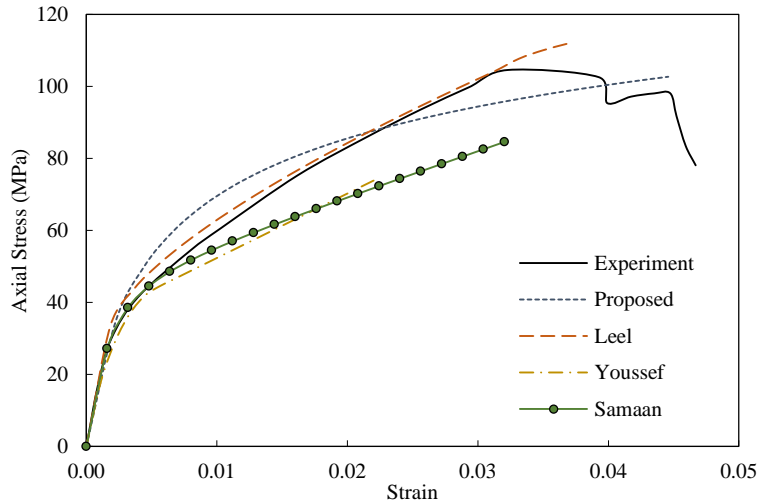


Figure 3-30 Comparison of confinement models to experimental stress-strain of S2F3 (monotonic concentric)

For A3NP2C specimen (Figure 3-32), all models except those proposed by Samaan and Kawashima provide a reasonably accurate prediction of the ultimate strain of confined concrete. The Samaan model significantly overestimates the ultimate strength and strain of A3NP2C. For the last specimen, U25-2, predicted ultimate strength and strain by all models differ significantly from experimental values.

As shown in Figure 3-29 to Figure 3-33, the proposed model has good agreement with experimental results for specimens S2F2, S2F3, S4F2, and A3NP2C. Although the model slightly overestimates the ultimate strength for specimen U25-2 (Figure 3-33), its overall performance is better than the other four models.

Predicted normalized ultimate strength and strain of confined concrete by the proposed model and the four aforesaid models versus experimental results are shown in Figure 3-34 and Figure 3-35, respectively. Because ultimate strain predicted by the Kawashima model is less than transition strain, predicted ultimate strength and strain for specimens S2F2, S2F3, S2F4, and



S2F5 are not plotted in these figures. As demonstrated in Figure 3-34, the proposed model has an overall margin of error less than the four representative models for predicting ultimate strength of confined concrete.

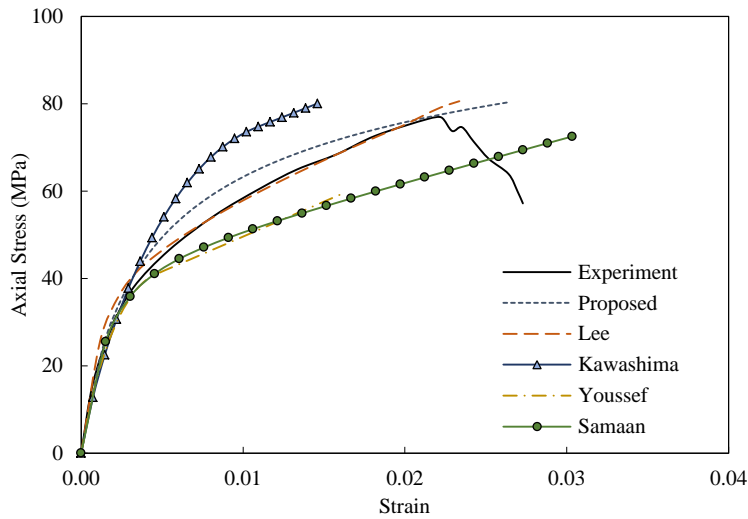


Figure 3-31 Comparison of confinement models to experimental stress-strain of S4F2 (monotonic concentric)

As shown in Figure 3-35, variability of the predicted ultimate strain versus experimental data is higher than variability of predicted ultimate strength versus experimental data. Normalized ultimate strains predicted by the proposed model show a good correlation with normalized experimental ultimate strain. In addition, the proposed model has a smaller margin of error than the four representative models for predicting ultimate strain of confined concrete. The overall margin of error for ultimate strain and strength is 20% and 15%, respectively.

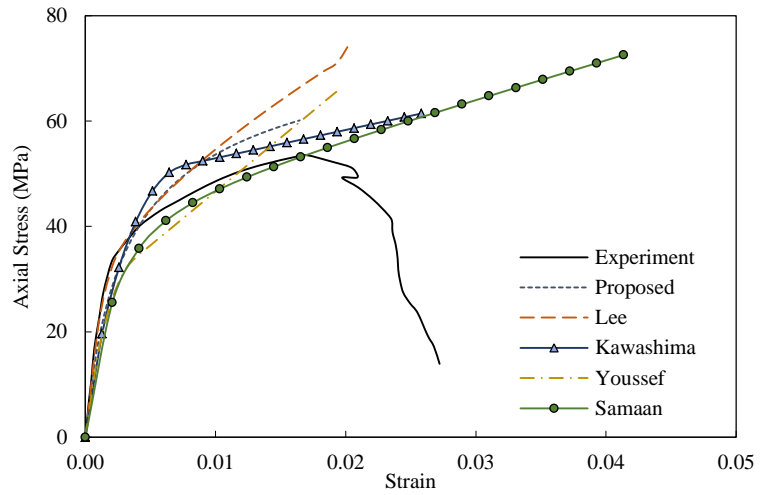


Figure 3-32 Comparison of confinement models to experimental stress-strain of A3NP2C (monotonic concentric)

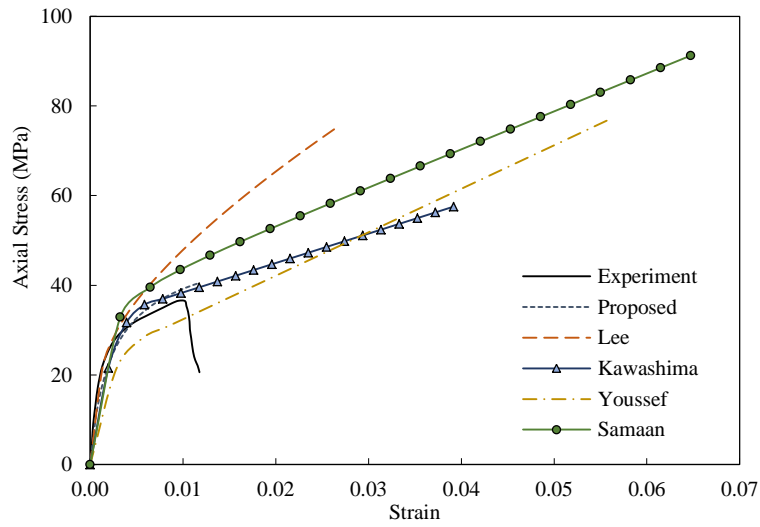


Figure 3-33 Comparison of confinement models to experimental stress-strain of U25-2 (monotonic concentric)

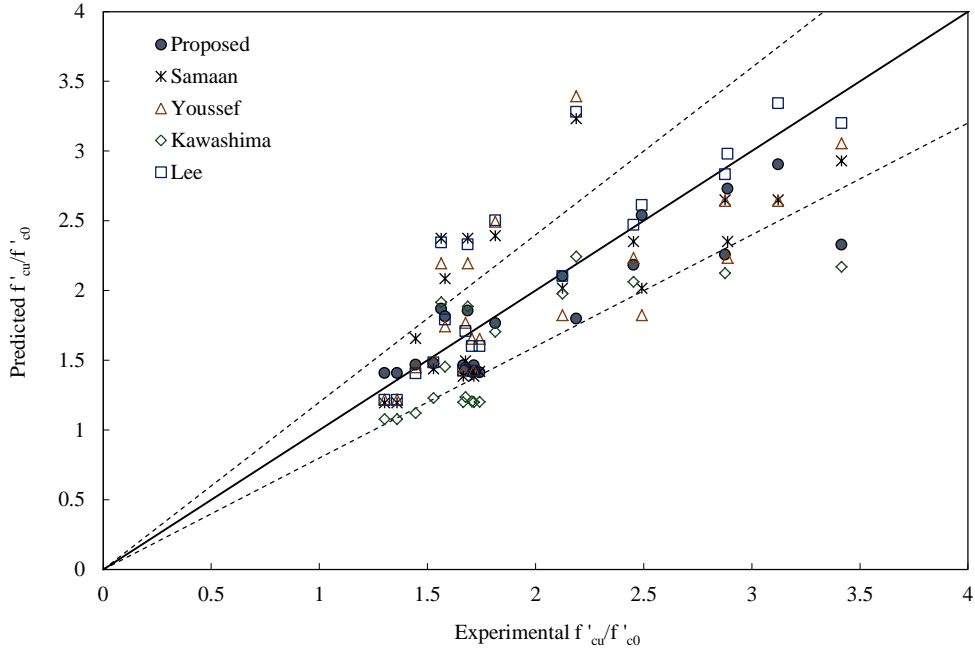


Figure 3-34 Predicted versus experimental ultimate strength

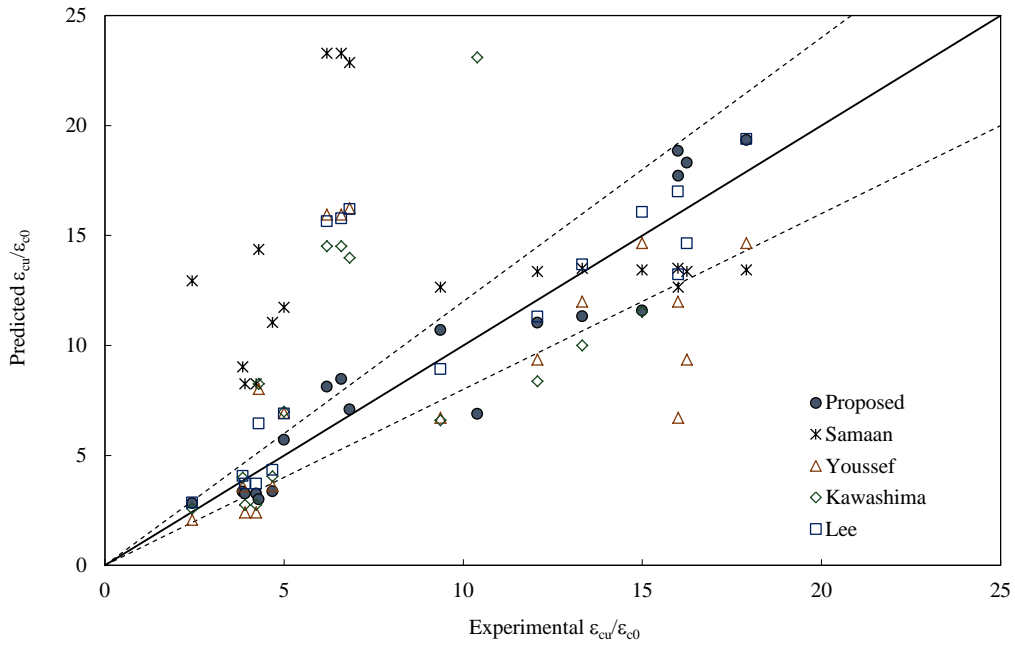


Figure 3-35 Predicted versus experimental ultimate strain

### **3-7-3-2 Validation of the Proposed Model in Response Prediction of a Member under Combined Axial and Lateral Load**

For further verification of the proposed model, experimental data was used from two specimens not used for model calibration. Geometrical and mechanical properties of these specimens are presented in Table 3-3. These two specimens were tested under cyclic lateral load. Experimental data included the moment and curvature at the column-footing interface extracted from data recorded by local displacement transducers and/or strain gauges affixed to the main bars, applied lateral force, and displacement and axial force recorded at the top of the columns (Kawashima et al. 2001). Moment-curvature analysis is preferred for accuracy assessment of material's monotonic behavior since no assumption on curvature distribution along the column height is required. The proposed model and other aforesaid models were implemented into a fiber-based moment-curvature analysis and results were compared to experimental data. All other factors except the material model for confined concrete were unchanged in the analytical process, including the monotonic stress-strain relationship of steel, cyclic rules for steel, and plain and confined concrete.

Analytical procedure is based on a nonlinear fiber-based model in which a section is divided into several parts and the column or beam is divided into several segments. Individual fiber behavior is then simulated using a proper monotonic model and cyclic rule. Computational efficiency of this method is greater than efficiency of the FEM to model flexural behavior of concrete members (Rodrigues et al. 2013). Figure 3-36 shows a circular section of mesh used in fiber-based analysis in this study. The cross section of beam or beam-column was divided into core concrete, cover concrete, longitudinal steel, and FRP fibers. The cross section of the fiber-elements in this study was triangular in accordance with the meshing procedure used in the analytical procedure.

Table 3-3 Geometrical and mechanical properties of TP-22 and TP-23 (Kawashima et al. 2001)

Specimen	TP-22	TP-23
Diameter (mm)	400	400
Longitudinal reinforcement	12 No. 16	12 No. 16
Longitudinal steel yield strength (MPa)	374	374
Tie Reinforcement	No. 6 @ 5.9	No.6 @ 5.9
Tie steel yield strength (MPa)	363	363
Fiber Type	CFRP	CFRP
FRP Thickness (mm)	0.11	0.22
FRP modulus of elasticity (GPa)	266	266
FRP fracture Strain	0.0163	0.0163
Unconfined compressive strength (MPa)	30	27.5

In order to address analytical needs of this study, a windows-based computer application was developed. As the next version of a program developed to analyze performance of reinforced concrete columns under various load patterns, the developed computer application is capable of biaxial nonlinear monotonic and cyclic moment-curvature and force-deflection analysis under any load and displacement pattern (Esmaeily and Peterman 2007).

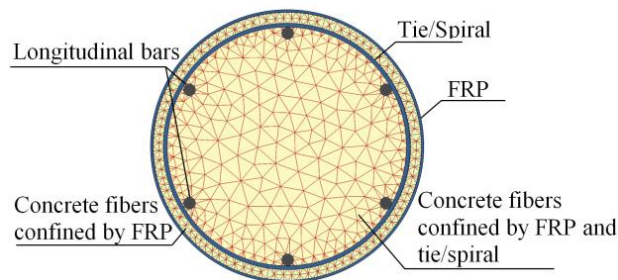


Figure 3-36 Fiber representation of circular section

As shown in Figure 3-36, four types of fiber elements are specified for a concrete section confined by FRP and lateral steel: (i) concrete fibers confined by FRP and lateral steel located at the section core, (ii) concrete fibers confined only by FRP (cover concrete for a conventionally reinforced section), (iii) longitudinal reinforcement bars, and (iv) FRP fibers.

Moment-curvature analysis was conducted for two sections: TP-22 and TP-23 (Kawashima et al. 2001). Geometrical and material properties of these two sections are listed in Table 3-3. FRP wraps used in specimens TP-22 and TP-23 were horizontal, thereby acting only in the lateral/hoop direction with no stiffness in the longitudinal direction.

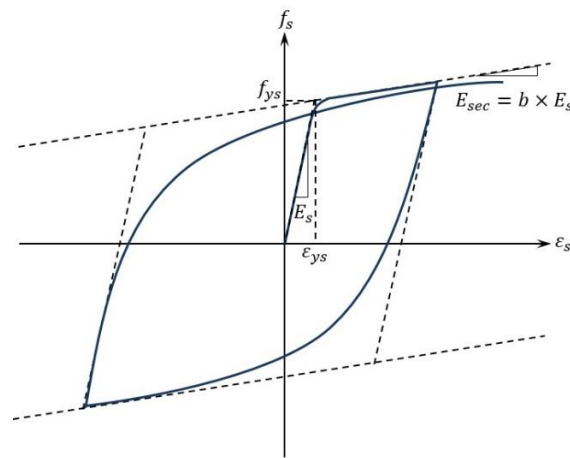


Figure 3-37 Menegotto-Pinto monotonic and cyclic model

The three fiber types (Types i, ii, and iii) followed monotonic and cyclic models and rules. In order to analyze section behavior, three cyclic models for steel were implemented in the developed window-based computer application, including linear-cyclic model, Esmaily's cyclic model (Esmaily and Peterman 2007; Esmaily and Xiao 2005), and Menegotto-Pinto's cyclic model (1973). When all other parameters remained unchanged, predicted behavior using Menegotto-Pinto and Esmaily's models was generally closer to experimental data. The

Menegotto-Pinto model includes four parameters for setting monotonic and cyclic behavior of steel. As shown in Figure 3-37, monotonic behavior of steel is bilinear in the Menegotto-Pinto model. The first part of the monotonic model is a line with a slope equal to the modulus of elasticity of steel, ending at the steel yield point. It is followed by the second line with a specific slope set by the first parameter of the Menegotto-Pinto model ( $b$ ) set to 0.01. Cyclic parameters of the Menegotto-Pinto model,  $R_0$ ,  $a_1$ , and  $a_2$ , were considered 2.0, 2.0, and 0.09, respectively (Menegotto and Pinto 1973).

In order to model behavior of concrete confined only by FRP (concrete fibers located between lateral steel reinforcement and FRP, referred to as cover concrete for conventionally reinforced sections), Youssef's and Samaan's stress-strain models were used in this study. Considering functionalities of various models, the Samaan model is used for concrete fibers located in the cover concrete region only when behavior of core concrete fibers are predicted by the same model.

Maximum uniaxial compressive strength of a concrete fiber predicted by the Samaan model, which considers only FRP, for specimens TP-22 and TP-23 was larger than the ones predicted by Kawashima, Lee, and Youssef models in which effects of FRP and lateral steel were considered (Figure 3-38). Because real FRP confinement for a section is less than confinement provided by FRP wrap and steel lateral reinforcement, the Samaan model cannot logically be used as monotonic behavior of concrete fibers located at the cover region when the Kawashima, Lee, or Youssef model is used for monotonic behavior of core-section fibers. Therefore, the Youssef model is used for monotonic behavior of concrete fibers located at the cover region, and the Kawashima, Lee, Youssef or proposed models are used for monotonic behavior of core-concrete fibers.

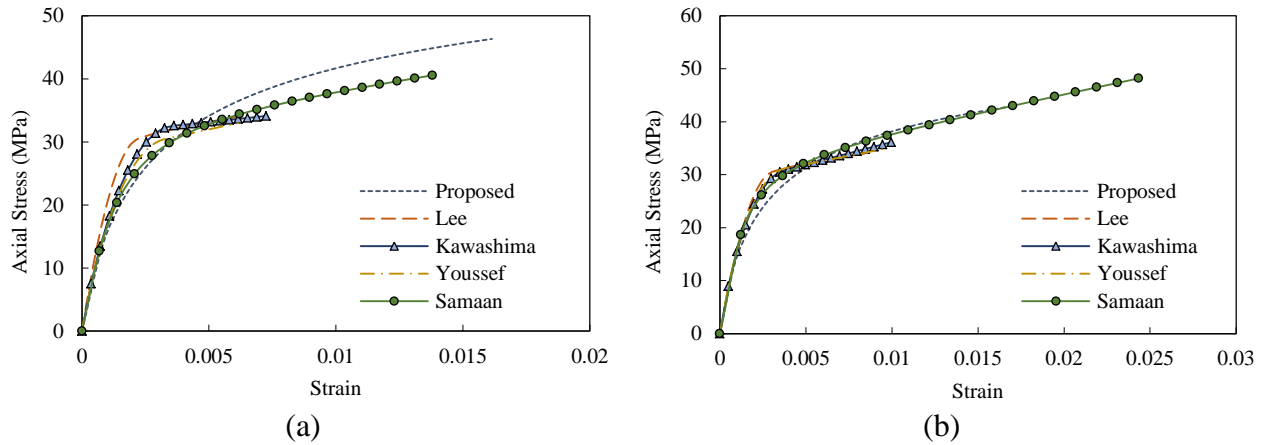


Figure 3-38 Analytical stress-strain of (a) TP-22 (with one layer of CFRP) and (b) TP-23 specimen (with two layers of CFRP) (monotonic concentric)

Cyclic behavior of FRP-confined fibers is considered linear with a slope equal to the modulus of elasticity of plain concrete.

Monotonic models developed to predict behavior of concrete columns confined by FRP can be categorized into two groups. In the first group, the effect of existing internal lateral steel reinforcement (tie/spiral) is ignored. In the second group, however, this effect is implemented. The Samaan and Youssef models represent the first group, and the Kawashima, Lee, and proposed models represent the second group. Similar to FRP-confined only fibers, cyclic behavior of fibers confined by FRP and lateral steel is also considered linear with a slope equal to the modulus of elasticity of plain concrete.

Analytical results obtained from the five models (Samaan, Youssef, Kawashima, Lee, and the proposed model) are compared to experimental results for specimens TP-22 and TP-23 in Figure 3-39 and Figure 3-40, respectively. Throughout all analytical processes, only the monotonic model for core concrete and cover concrete changed.



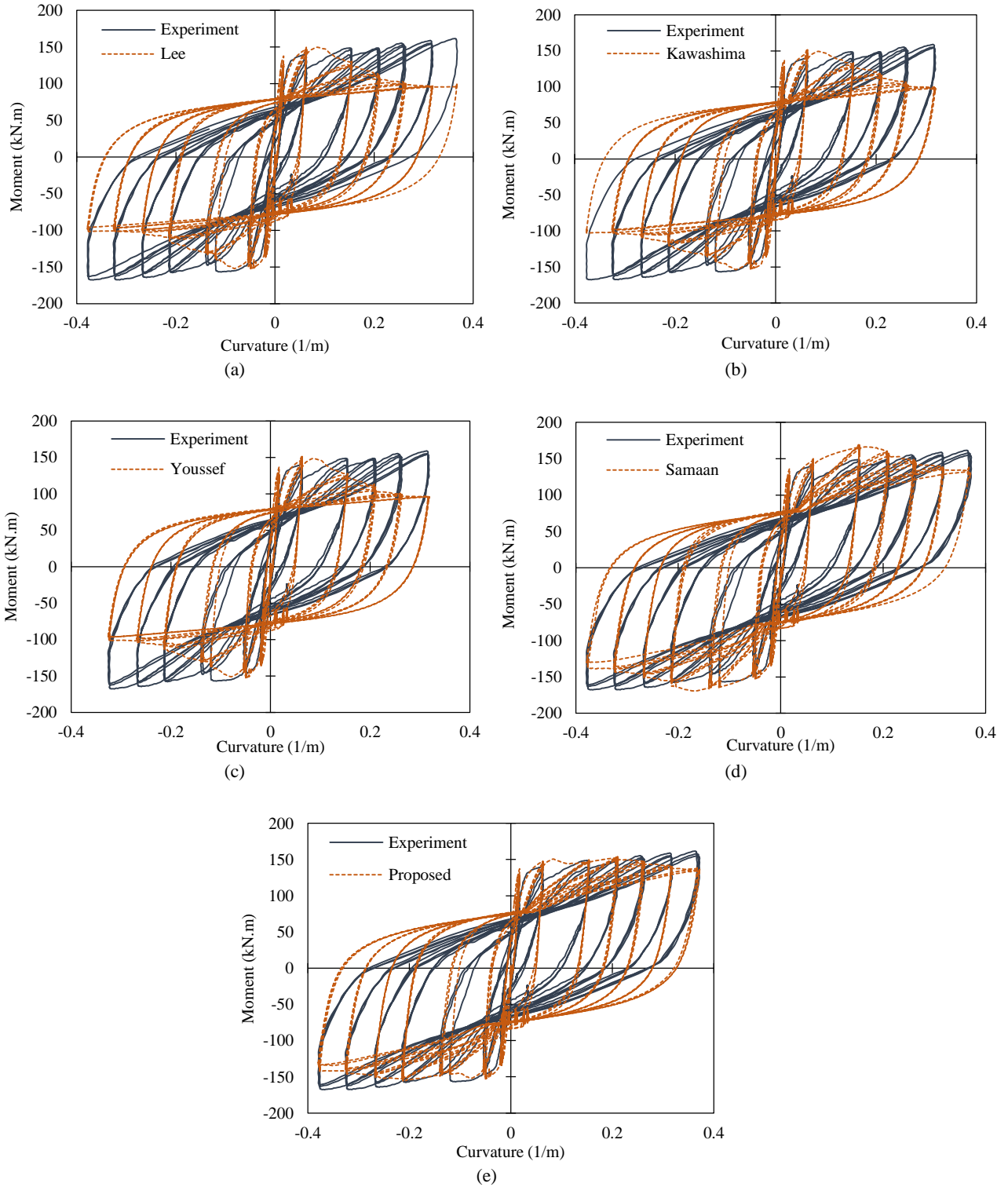


Figure 3-39 Moment-curvature analysis for TP-22 (with one layer of CFRP) using (a) Lee, (b) Kawashima, (c) Youssef, (d) Samaan, and (e) proposed model for confined concrete

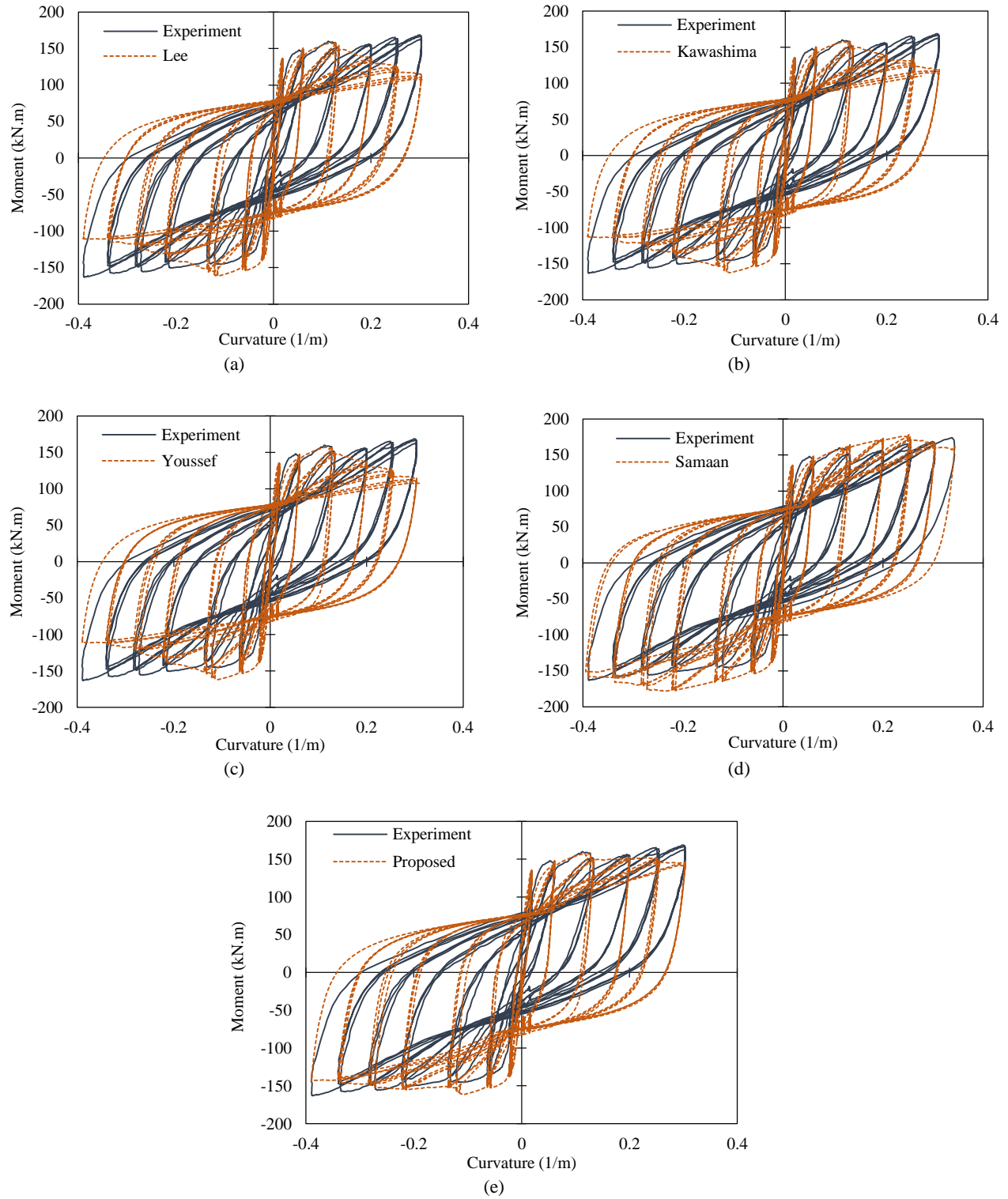


Figure 3-40 Moment-curvature analysis for TP-23 (with two layers of CFRP) using (a) Lee, (b) Kawashima, (c) Youssef, (d) Samaan, and (e) proposed model for confined concrete

Monotonic behavior, cyclic rules of steel, and cyclic rules for fibers located at cover and core regions remained unchanged. The term “performance” refers to the ability of the analytical procedure to predict real behavior of the specimen. The closer the prediction is to the real values, the higher the performance of the model. Stiffness degradation and Bouschinger effect are primarily affected by the steel hysteretic model when the level of axial force is low. Therefore, in order to compare experimental data and analytical results, the envelope of flexural moment in analytical and experimental hysteretic moment-curvature curves was compared. The closer the predicted analytical envelope is to the experimental, the higher the performance. The moment-curvature envelope of specimens TP-22 and TP-23 are shown in Figure 3-41.

As shown in Figure 3-39 and Figure 3-40, Youssef, Kawashima, and Lee models have almost the same prediction for specimens TP-22 and TP-23. Moment capacity of the section dropped significantly after curvature 0.1 and 0.15 (1/m) in specimens TP-22 and TP-23, respectively. Although Kawashima and Lee models are proposed for concrete confined by FRP and lateral steel, their predictions are more realistic for a specific range of FRP and steel lateral reinforcement. As shown in Figure 3-39, the predicted moment capacity of a section is closer to the experimental moment for a section with two layers of FRP (higher FRP ratio) compared to a section with only one layer of FRP (lower FRP ratio).

Although the Samaan model was developed for concrete confined only by FRP, performance of this model for specimens TP-22 and TP-23 was better than performance of the Kawashima and Youssef models, considering the confinement effect of FRP and lateral steel reinforcement. Performance of the Samaan model improved by increasing the number of FRP layers, as shown in Figure 3-40. For other stress-strain models, ultimate strain of confined concrete was lower than the one predicted by the Samaan model. Therefore, confined concrete

fibers began failing in a curvature less than 0.1 (1/m); when the Samaan model was used, curvature at the start of failing for concrete fibers was higher than 0.15 (1/m). As shown in Figure 3-34, the Samaan model overestimates ultimate compressive strain of specimens confined by FRP and lateral steel for 55% when considering the confinement effect of FRP only. The Samaan model was proposed using concrete-filled FRP tube specimens, and the effect of FRP tube Poisson's ratio on lateral FRP strain was ignored. Therefore, the Samaan model overestimated ultimate strain of specimens TP-22 and TP-23 when considering the confinement effect provided only by FRP, thereby leading to better performance compared to other models.

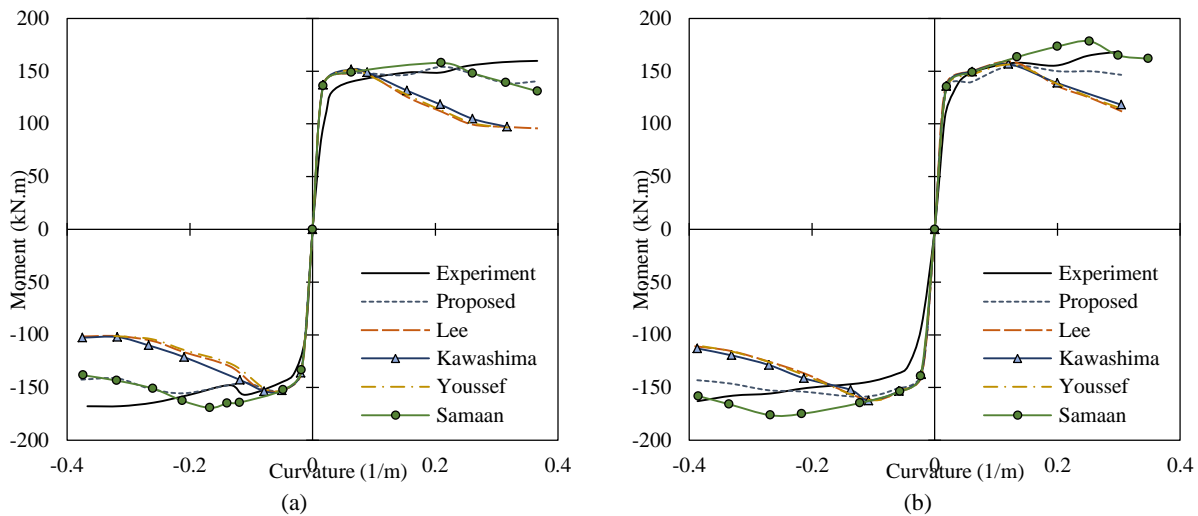


Figure 3-41 Moment-curvature envelope of (a) specimen TP-22 (with one layer of CFRP) and (b) specimen TP-23 (with two layers of CFRP)

The proposed model works reliably well for specimens TP-22 and TP -23, as shown in Figure 3-39 and Figure 3-40. Versatility of the proposed model was enhanced by four independent experimental databases. Compared to other models, the proposed model calculated moment capacity of TP-22 and TP-23 specimens conservatively closer to the experimental data.

### 3-8 Summary

A fiber-based method was employed to analyze RC sections, and a number of monotonic and cyclic material models from the literature were implemented in a developed computer application. Because the developed computer application utilizes triangular meshing, a column's cross section can have any arbitrary shape. Monotonic and cyclic rules of materials can be unconditionally complex. The developed window-based computer application can be used for:

- Construction of 3D axial force-bending moment interaction surface for RC columns with conventional lateral steel reinforcement using the ACI stress-block (code-based),
- Construction of axial force-bending moment interaction surface using proper material models for RC columns laterally reinforced by steel, FRP, or steel and FRP assuming constant strain at extreme compressive fiber,
- Construction of real axial force-bending moment failure surface considering proper material models for RC columns laterally reinforced by steel, FRP, or steel and FRP with or without considering the axial force loading pattern. Ultimate moment capacity of an RC section is defined as the maximum moment in monotonic moment-curvature analysis with constant or variable axial force,
- Moment-curvature analysis for RC columns with conventional lateral steel reinforcement considering ACI stress-block (code-based),
- Biaxial moment-curvature analysis considering proper material models under any pattern of curvature in the two lateral directions and arbitrary axial load pattern,

- Biaxial force-deflection analysis using proper material models and plastic hinge method under any pattern of lateral displacement in the two lateral directions and an arbitrary axial load pattern.

Accuracy of the developed computer application's calculated results was assessed through validation examples in which analytical predictions were compared to experimental results. Calculated results demonstrated a close agreement with the experimental data. The effect of axial and lateral forces' loading pattern in two lateral directions as it pertains to the response of concrete columns confined by conventional lateral steel reinforcement, FRP, or lateral steel and FRP can be captured using proper monotonic and cyclic material models and assumption on curvature distribution along the column height. In addition, accuracy of existing monotonic and cyclic material models and curvature distribution assumption (plastic hinges methods) can be assessed through various types of analysis when experimental data is available.

In order to obtain a more versatile model for the stress-strain relationship of concrete confined by FRP and lateral steel, a new monotonic model was developed using four independent experimental databases, utilizing specimens tested under concentric monotonic axial load. Compared to other models, predictions by the proposed model showed good agreement with experimental data for the specimens.

Blind verification of the proposed model was also conducted using experimental data from two concrete sections not used to calibrate this model. Because experimental data of these two sections included moment and curvature at the column-footing interface, a fiber-based moment-curvature analysis was conducted using the proposed model and the other four models of monotonic behavior of confined concrete fibers. Use of four independent databases to develop the proposed model demonstrated increased versatility and accuracy in performance prediction,

especially ultimate failure condition, ultimate strength, and overall stress-strain response compared to existing models in the literature.

This model and other representative models were implemented in a windows-based computer program which is explained in detail in Chapter 4. This application can analyze the load/displacement pattern and flexural performance of a reinforced concrete section or structural members with various cross-sectional geometry, type, and arrangement of reinforcement in longitudinal and lateral directions.

## **Chapter 4 - Parametric Study on Load History and Pattern**

### **4-1 Introduction**

Loading history, pattern, intensity, and linear combinations of loads, specifically lateral and axial loads, can significantly affect RC column behavior (Sadeghvaziri and Fouch 1991, Lee et al. 2009). During an earthquake, a majority of buildings are subject to biaxial lateral earthquake forces and variable cyclic axial force. Biaxial motion is induced in columns of irregular buildings, even against one-directional earthquake motions. Experimental studies and investigations of damaged structures after earthquakes have proven that damage caused by bidirectional earthquake motion differs from and, in most cases, is more extensive than damage caused by uniaxial earthquake motions (Marante and Flórez-López 2002, Rodrigues et al. 2013).

This chapter discusses the effect of lateral displacement/loading pattern and variable axial force on performance of RC members. The effect of lateral displacement/loading pattern was investigated in relation to performance of RC members' flexural capacity and energy dissipation. In addition, a new axial force-bending moment interaction curve was conducted that considered maximum bending capacity of the section in a moment-curvature analysis with variable axial loading.

### **4-2 Effect of Lateral Displacement/Loading Pattern on Performance of RC Members**

#### **4-2-1 Analytical Model**

In order to assess performance of RC column behavior under various loading scenarios, a computer application was developed for nonlinear analysis of RC columns under uniaxial lateral



forces/displacements and axial loading. Functionalities of this computer application are explained in detail in Chapter 4.

A typical RC column was simulated using a nonlinear fiber-based model in which a cross section of an RC column was divided into a number of fibers, including confined concrete fibers at the section core enclosed by lateral reinforcement, plain concrete fibers at the section cover, and longitudinal steel fibers. Other researchers have effectively utilized the fiber-based model to simulate flexural behavior of RC columns (Esmaeily and Xiao 2005, Shao et al. 2005). Figure 4-1 shows fiber representation of a square cross section with triangular mesh.

For columns with conventional geometry, deformation compatibility was considered by the classical Bernoulli-Euler rule of plane sections remaining plane after deformation. Each fiber was assigned to the proper monotonic stress-strain model in which cyclic rules for hysteretic performance and confining effects were considered when applicable.

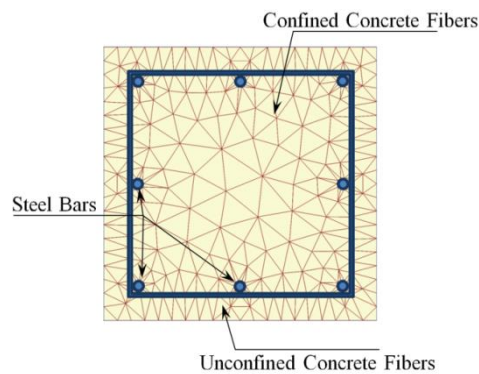


Figure 4-1 Fiber representation of a square cross section

In the present study, the model developed by Mander et al. (1988) was employed to model uniaxial behavior of concrete fibers confined by tie in compression. This model can be

used to model normal-weight concrete in circular and rectangular sections confined by spiral, circular, or rectangular tie with or without cross ties. Uniaxial monotonic behavior of unconfined (plain) concrete fibers was modeled using the model developed by Mander et al. (1988). The equation related to the first part of this model for plain concrete was identical to the equation used for confined concrete by assuming zero lateral pressure; the second part was a line connecting strengths that corresponded to a strain of  $2 \times \varepsilon_{c0}$  ( $\varepsilon_{c0}$  is axial strain in unconfined concrete corresponding to maximum compressive stress of plain concrete) and the point of concrete spalling ( $\varepsilon_{csp}$ ) with zero strength. Tensile behavior of confined and unconfined concrete fibers was modeled by a linear stress-strain relationship with a slope equal to the modulus of elasticity of plain concrete. Fibers were shown to lose their tensile or compressive strength after the first failure in tension or compression. Tensile strength of concrete is generally less than 20% of the compressive strength, and it can be obtained experimentally using a tension test or a split-cylinder test. In addition, a bending test of a plain concrete beam can be used to obtain tensile strength of concrete, known as the modulus of rupture. When experimental data is unavailable, tensile strength of concrete is commonly calculated using equation  $f_r = 0.7\sqrt{f'_{c0}}$  (MPa), proposed by the ACI. Tensile strength of plain concrete, for which no direct experimental value exists, has commonly been considered to be approximately 10% of the standard compressive strength. Cyclic behavior of confined and unconfined concrete fibers was assumed to be linear with a slope equal to the modulus of elasticity of plain concrete. The effect of lateral reinforcement was taken into account using the proper stress-strain model for concrete confined by lateral reinforcement, namely stirrups. Monotonic and hysteretic stress-strain relationships of confined and plain concrete fibers are shown in Figure 4-2.

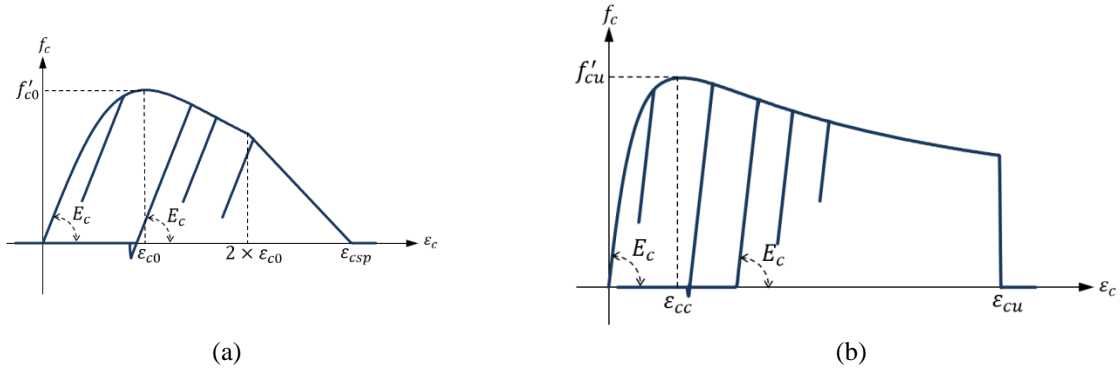


Figure 4-2 Monotonic and hysteretic stress-strain relation of (a) plain and (b) confined concrete fibers

In order to model uniaxial monotonic behavior of longitudinal steel bars, four models were assessed in the presented study: idealized bilinear model, Menegotto-Pinto’s model (1973), Esmaeily’s model (Esmaeily and Xiao 2005), and the model by Mander et al. model (1984) (Figure 4-3). These models were selected because of their widespread usage and numerical stability. The initial line in the idealized bilinear curve had a slope equal to the steel modulus of elasticity ( $E_s$ ), followed by the second line with a specific slope calculated with consideration of fracture strength ( $f_{sf}$ ) and fracture strain ( $\epsilon_{sf}$ ) of steel material.

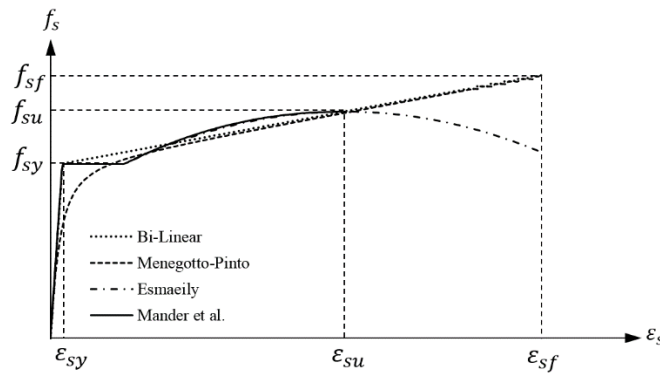


Figure 4-3 Uniaxial monotonic stress-strain models for longitudinal steel

The Menegotto-Pinto model (1973) had a bilinear backbone curve, and the initial line had the slope of steel modulus of elasticity up to yield strength ( $f_{sy}$ ). The post-yield linear function had a slope equal to a portion of steel modulus of elasticity, defined as hardening ratio. The first line of the Menegotto-Pinto model was connected to the second line using a transition curve with curvature  $R_0$ . The effect of yield plateau was ignored. Esmaeily's monotonic model (Esmaeily and Xiao 2005) accounted for effects of strain hardening and softening of longitudinal steel using four parameters ( $K_1, K_2, K_3, K_4$ ). These parameters defined the ratio of ultimate and fracture stress and strain with respect to yield strength and strain ( $\epsilon_{sy}$ ), respectively. In the model by Mander et al.(1984), only the strain hardening effect was considered, and the ultimate point (point with maximum strength) was defined as the fracture point of the steel material.

When no information was available regarding uniaxial behavior of the reinforcing steel except yield strength ( $f_{sy}$ ), the ultimate strain ( $\epsilon_{su}$ ) and strength ( $f_{su}$ ) for longitudinal steel were considered to be  $24.9 \times \epsilon_{sy}$  ( $\epsilon_{sy}$  is the yield strain of steel) and  $1.3 \times f_{sy}$ , respectively, as recommended by Esmaeily and Xiao (2005).

Utilization of Menegotto-Pinto's (1973) and linear hysteretic models to predict hysteretic behavior of longitudinal steel bars of columns under uniaxial and biaxial lateral forces, respectively, provided results with the closest agreement to experimental data. The linear cyclic model used in this study had linear unloading and reloading with a slope equal to the steel modulus of elasticity. Unlike the linear cyclic model, Menegotto-Pinto's model accounted for the Bauchinger effect during unloading and reloading cycles.

## 4-2-2 Validation of Analytical Model

### 4-2-2-1 Moment-Curvature Analysis

Moment-curvature analysis is the preferred analysis to assess accuracy of material behavior because no assumption of curvature distribution along the column height (plastic hinge model) is required. To the author's knowledge, no experimental biaxial moment-curvature curve exists in the literature; therefore, to verify accuracy of moment-curvature response performed in this study, unidirectional cyclic moment-curvature analysis of a circular section (specimen TP-21) was compared to existing experimental data (Yoneda et al. 2001).

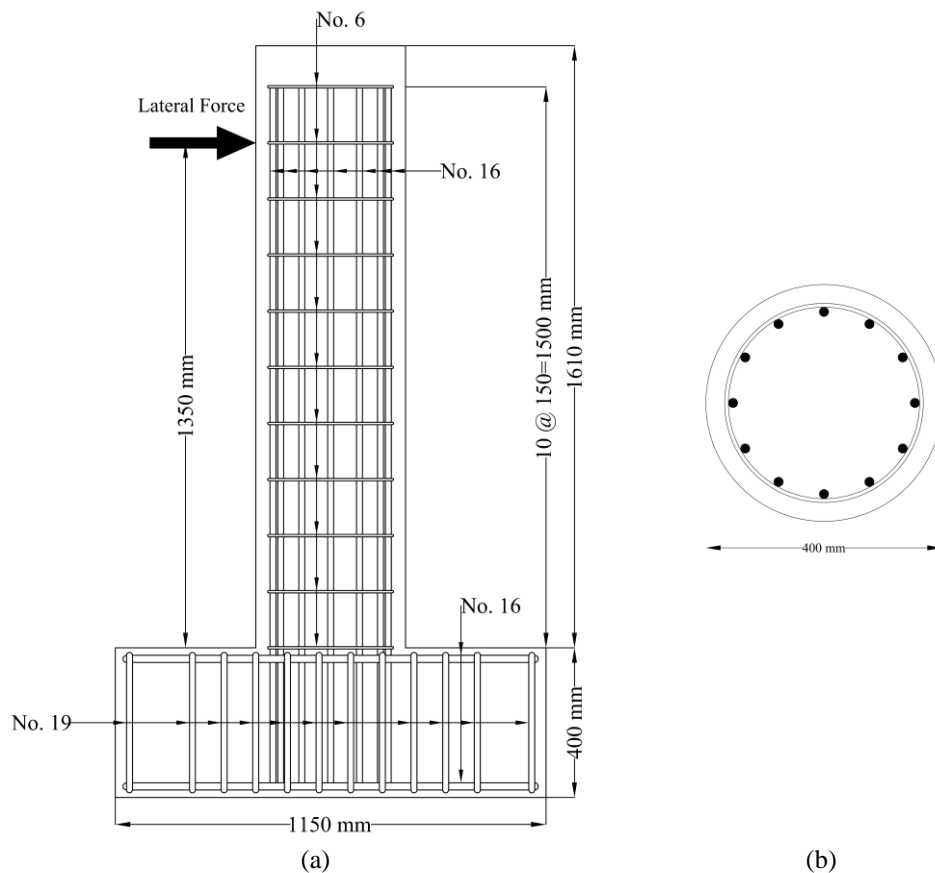


Figure 4-4 Geometry and reinforcement details of specimen TP-21: (a) elevation, (b) cross section

The circular column had a diameter of 400 mm and a clear cover of 25.4 mm. This specimen was reinforced longitudinally using 12 No. 16 evenly distributed steel bars, Grade SD295 (nominal yield strength in tension is 374 MPa) and reinforced laterally using No. 6 steel tie, Grade 295, with 150 mm spacing. Details of longitudinal and lateral reinforcement of specimen TP-21 are shown in Figure 4-4. The strength of plain concrete was 30 MPa. The column specimen was tested under constant axial force of 185 kN and reversed cyclic uniaxial lateral force. Detailed information regarding experimental setup is presented in Yoneda et al. (2001).

Fiber representation of the circular cross section is shown in Figure 4-5. The model by Mander et al. (1988) was used in conjunction with the linear cyclic rule to model behavior of confined and unconfined concrete fibers. Based on moment-curvature responses obtained using the three monotonic and cyclic models for reinforcing steel bars, the Menegotto-Pinto model was selected to simulate behavior of longitudinal steel fibers when a section is under uniaxial cyclic loading. The monotonic curve backbone coefficient ( $b$ ) in the Menegotto-Pinto model was set to 0.01, and cyclic parameters  $R_0$ ,  $a_1$ , and  $a_2$  were considered 2.0, 2.0, and 0.18, respectively. Cyclic moment-curvature analysis of specimen TP-21, obtained by the developed analytical model, was compared to experimental data in Figure 4-6. In this figure, the purple dashed line and the blue solid line demonstrate calculated analytical results and measured experimental data, respectively. As shown in Figure 4-6, flexural capacity of the circular section was accurately predicted using the analytical model.

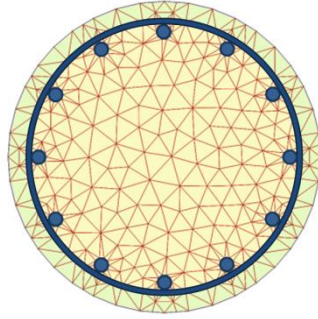


Figure 4-5 Fiber representation of TP-21

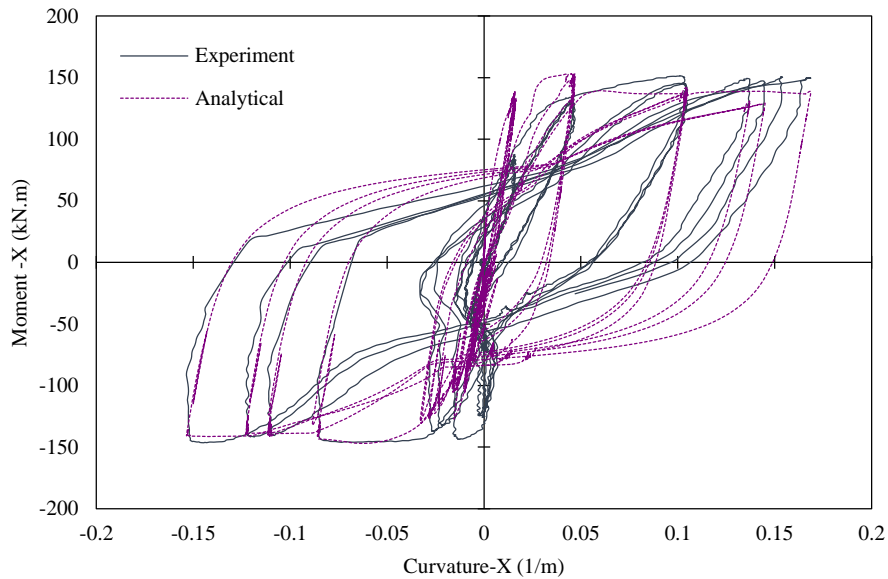


Figure 4-6 Comparison of analytical uniaxial moment-curvature with experimental data for specimen TP-21

In order to explore the effect of mesh size on accuracy of results, the maximum fiber area was set to a series of values from  $0.5\text{ cm}^2$  to  $4\text{ cm}^2$ . Refinement of the mesh did not have a considerable effect on the general moment-curvature curve. Therefore, the bending moment of the point with maximum positive curvature was compared to the experimental value for the various mesh sizes. As shown in Figure 4-7, the difference was less than 2% for all mesh sizes.

Although accuracy improved by decreasing the margin from 2% to approximately 1.17%, when mesh size decreased from  $4\text{ cm}^2$  to  $0.5\text{ cm}^2$ , the computational time increased approximately 250%, as shown in Figure 4-7.

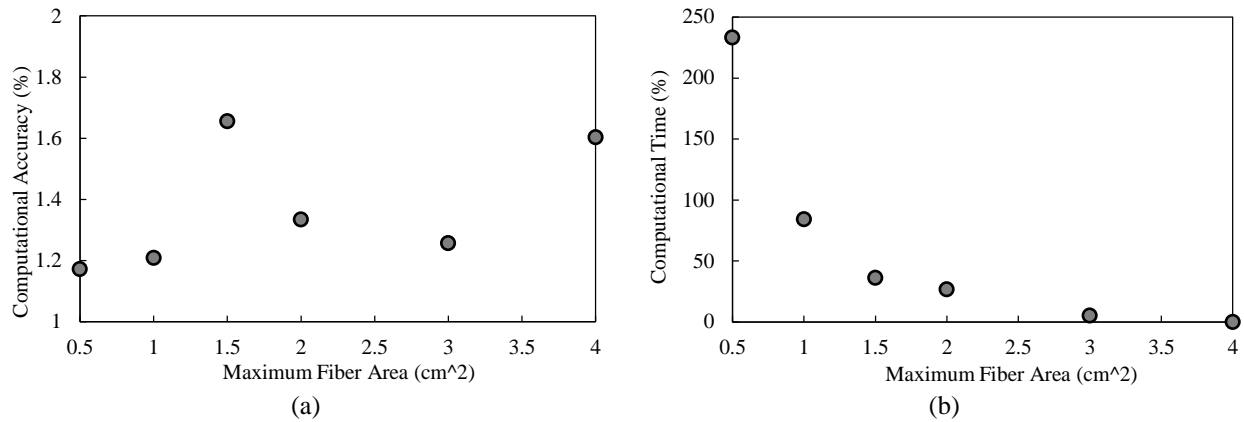


Figure 4-7 (a) Computational error and (b) computational time using six maximum fiber areas

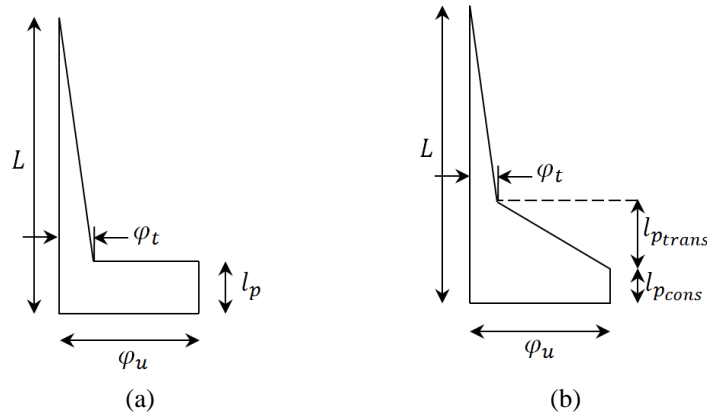


Figure 4-8 Curvature distribution along column height as assumed in (a) Priestley and Park method (1987) and (b) Esmaily-Xiao second method (2002)

#### 4-2-2-1 Force-Deflection Analysis

The force-deflection response of a column can be evaluated using two approaches. In the first approach, flexural deformation of column is calculated using the Finite Element Method (FEM) in which curvature of the critical section (with maximum moment) falls into the



descending branch of the moment-curvature curve. The corresponding stiffness matrix does not remain positive-definite, and displacement-controlled adaptive methods are needed to capture the force-deflection response (Esmaily and Xiao 2004). Accordingly, computational demand increases significantly in this approach.

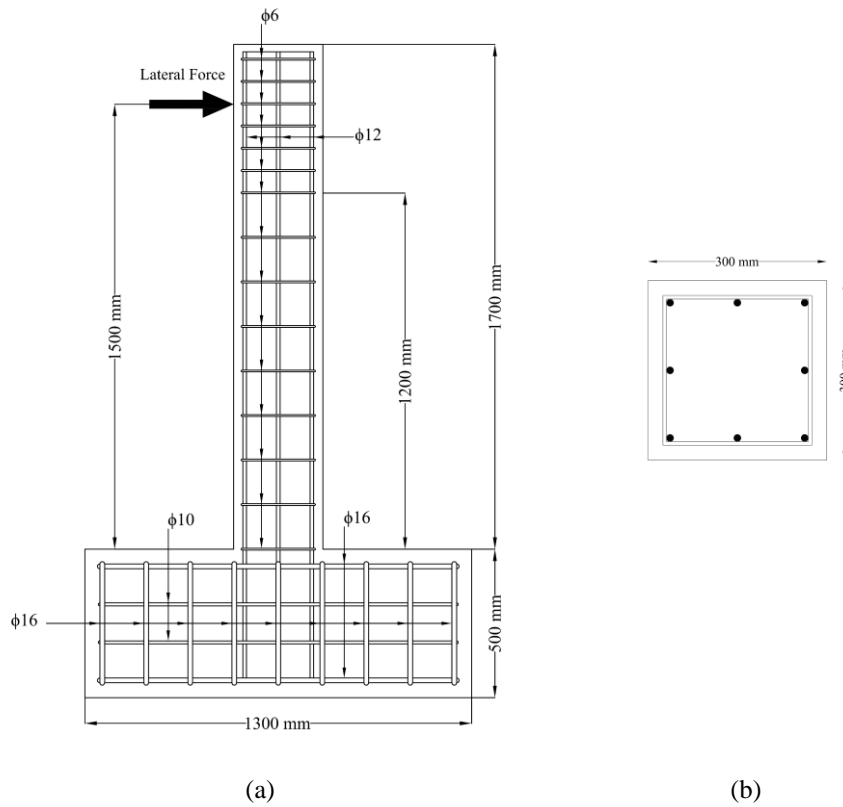


Figure 4-9 Geometry and reinforcement details of specimens PB01-N13, PB12-N15, and PB12-N16: (a) elevation, (b) cross section

In the second approach, a plastic hinge method with proper curvature distribution along the beam-column height is employed to calculate the force-deflection response when curvature falls into the descending branch of the moment-curvature curve. Considering the plastic hinge model, curvature distribution along the column height is divided into two regions. Curvature

distribution in the top region (as shown in Figure 4-8) is linear, leading to elastic deformation of the RC column's tip; whereas curvature distribution along the bottom region (plastic hinge region denoted as plastic hinge length) may not be linear, leading to plastic deformation at the top of the column. Plastic hinge length depends on the curvature distribution model and may or may not change during force-deflection analysis. Total displacement at the top of the RC column is a summation of elastic and plastic deformations.

In this study, the second approach was employed to perform force-deflection analysis of an RC column specimen. Although a majority of existing plastic hinge models in the literature was developed considering uniaxial behavior of RC columns, experimental evidence has confirmed that plastic hinge length is not affected by biaxial loading (Rodrigues et al. 2013). The Priestley and Park (1987) model, Esmaily-Xiao's first and second models (Esmaily and Xiao 2002), and Xiao's model (Esmaily and Xiao 2002) were used to calculate uniaxial and biaxial force-deflection response of three RC columns (PB01-N13, PB12-N15, and PB12-N16) tested by Rodrigues et al. (2012). The columns had a 300×300 mm square cross section. Lateral reinforcement was provided by No. 6 bars of the European standard (diameter of 6 mm) with step of 150 mm starting at 1.2 m from the bottom of the columns. For longitudinal reinforcement, eight No. 12 bars in European standard were evenly distributed (diameter of 12 mm). Reinforcement details of these specimens are shown in Figure 4-9, and experimental setup is presented in Rodrigues et al. (2012). The specimens were subjected to constant axial force at approximately 10% of their theoretical section capacity,  $A_g \times f'_{c0}$ , where  $f'_{c0}$  and  $A_g$  are plain concrete compressive strength and gross cross section area, respectively. Plain concrete strength was approximately 21.57 MPa, and the grade of steel reinforcement in longitudinal and transverse directions was A400NR-SD (European standard). Specimens PB01-N13, PB12-N15,

and PB12-N16 were subjected to uniaxial, biaxial expanding square, and circular lateral displacement paths, respectively. Applied expanding square and circular paths are shown in Figure 4-10.



Figure 4-10 (a) Expanding square and (b) expanding circular displacement path

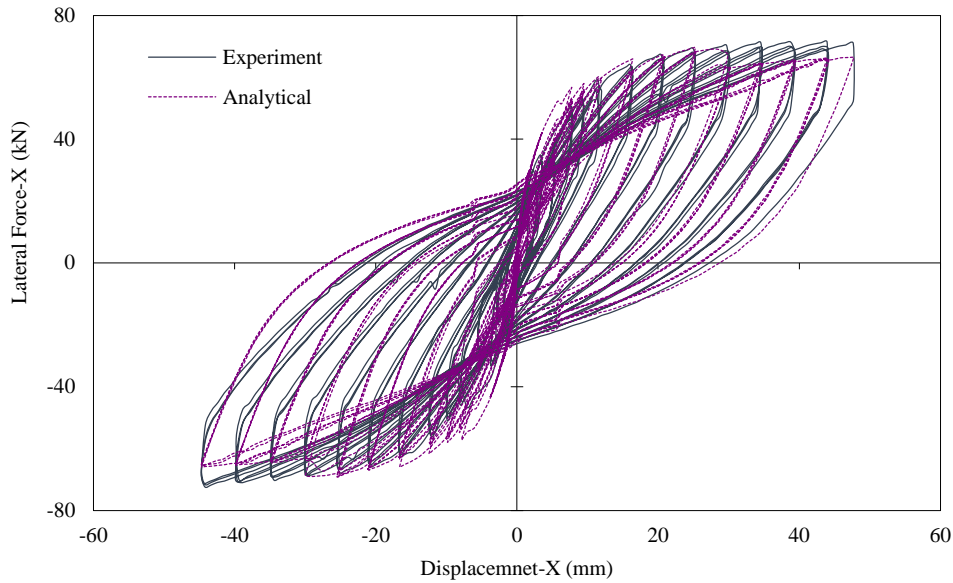


Figure 4-11 Comparison of analytical force-deflection with experimental data for specimens PB01-N13

Compared to various monotonic and hysteretic steel material models, results predicted using Menegoto-Pinto monotonic and hysteretic models showed the closest agreement with

experimental data for the column under uniaxial lateral displacement. For columns under biaxial lateral displacements, idealized bilinear monotonic model and linear cyclic model led to closest agreement between experimental data and calculated results.

During comparison of plastic hinge models, the Priestly and Park model (Park and Priestley 1987) showed closer agreement with experimental data for columns under biaxial lateral displacements; whereas, Esmaily-Xiao's second plastic hinge method calculated an analytical force-deflection response in closer agreement with experimental data when the column was under uniaxial lateral displacement. Priestly and Park (1987) proposed a constant plastic hinge length dependent ( $l_p$ ) on column height ( $L$ ), yield strength of longitudinal reinforcement, and diameter of longitudinal bars. Curvature distribution along the plastic hinge length was considered to be constant. Esmaily-Xiao's second plastic hinge length included two parts. The first part ( $l_{pcons}$ ) was a constant length depending on column height, maximum longitudinal steel stress, and longitudinal steel bar diameter. The second part ( $l_{ptrans}$ ) increased linearly when the yield section (section experiencing yield moment) moved upward (Esmaily and Xiao 2005). Curvature distribution along column height as assumed in Priestly and Park (1987) and Esmaily-Xiao's second models is shown in Figure 4-8. In this figure,  $\varphi_u$  is curvature next to the footing and  $\varphi_t$  is curvature at the end of elastic region, equal to yield curvature in Priestly and Park's model (1987). Analytical force-deflection prediction of the PB01-N13 column subjected to constant axial force and uniaxial displacement is compared to experimental data in Figure 4-11. The dashed purple line and blue solid line represent calculated results and experimental data, respectively. As shown in this figure, predicted analytical results were in close agreement with measured experimental data.

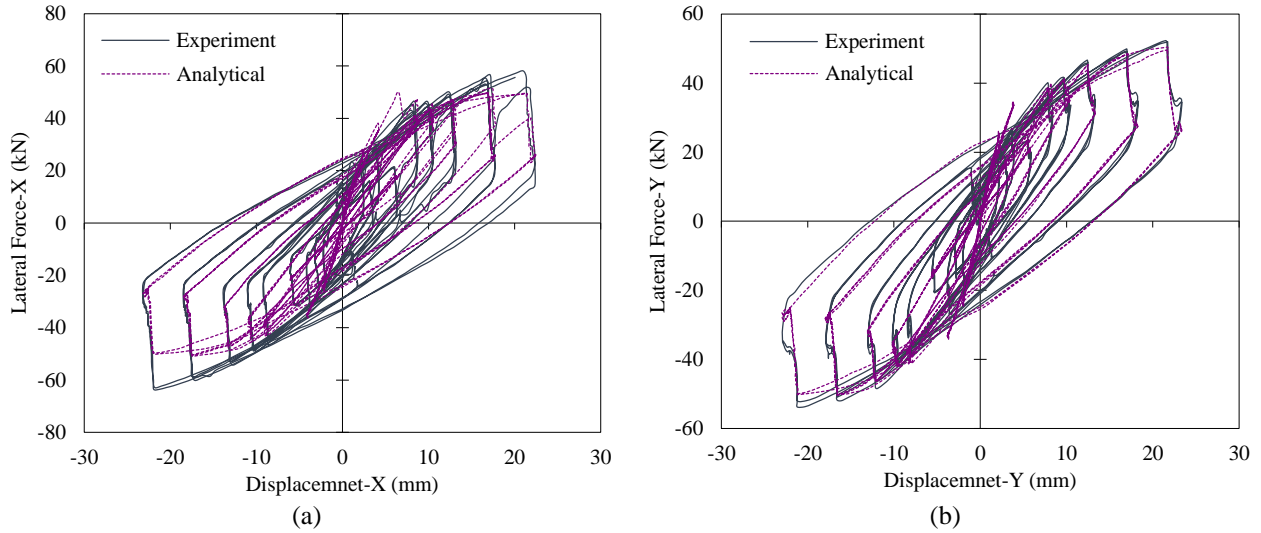


Figure 4-12 Comparison of analytical force-deflection with experimental data (2012) for specimens PB12-N15 under expanding square path in (a) x- and (b) y-directions

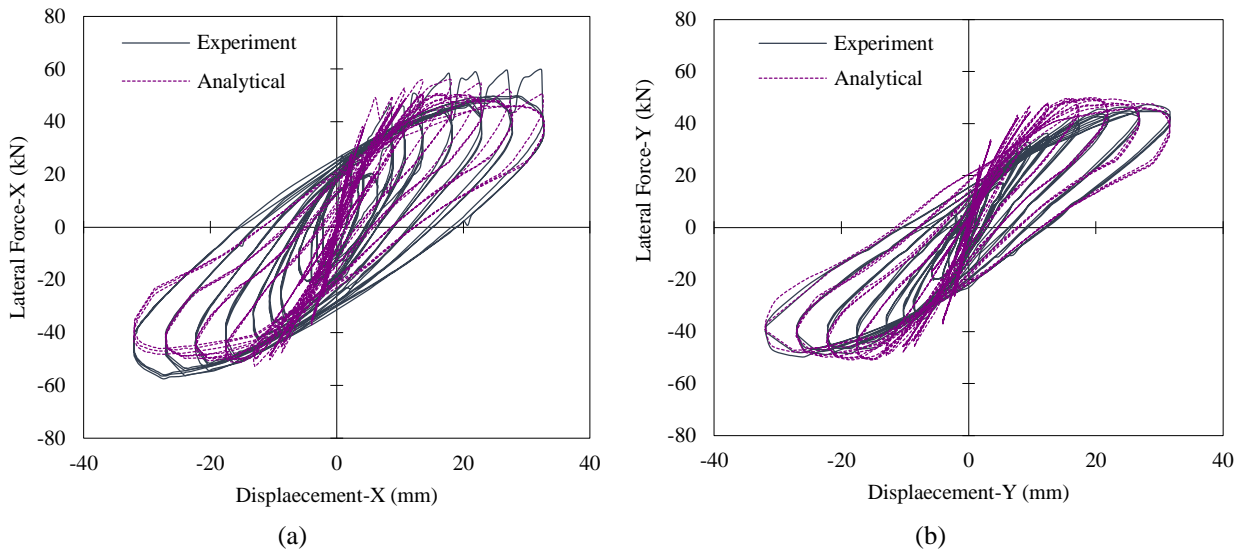


Figure 4-13 Comparison of analytical force-deflection with experimental data (2012) for specimens PB12-N16 under expanding circular path in (a) x- and (b) y-directions

Figure 4-12 shows force-deflection curves of analytical and experimental results obtained for specimen PB12-N15 subjected to the expanding square displacement path. The obtained force-deflection curve of specimen PB12-N16 under expanding circular path in x- and y-

directions was compared to experimental data, as shown in Figure 4-13. In general, analytical results showed good agreement with experimental data.

The calculated results confirmed the reasonable accuracy and validity of the analytical model to predict moment-curvature and force-deflection of RC columns under axial force and uniaxial or biaxial lateral forces/displacements with any pattern.

### **4-2-3 Vital Consideration of Biaxial Analysis**

Assessment of the effect of biaxial lateral displacement/force pattern and axial load variation on performance of RC columns in terms of flexural strength, ductility, and energy dissipation is required for a realistic prediction of column capacity. In order to demonstrate the importance of considering the biaxial load pattern on flexural performance of RC columns, monotonic moment-curvature analysis was conducted for section TP-21, considering various curvature paths. To investigate the effect of axial load level on uniaxial and biaxial performance of columns; lateral force strength and energy dissipation of columns PB01-N13, PB12-N15, and PB12-N16 under “uniaxial”, “expanding square”, and “expanding circular” displacement paths, as shown in Figure 4-10, were calculated. The axial load level varied from 0% to 20% of the theoretical section capacity ( $A_g \times f'_{c0}$ ) of the section in all cases.

#### **4-2-3-1 Moment-Curvature Analysis of RC Columns under Various Curvature Paths**

The developed analytical model was validated in the cyclic moment-curvature test of the column specimen, TP-21. As shown in Figure 4-6, flexural capacity (moment-curvature envelope) of column specimen TP-21 was predicted accurately. Monotonic moment-curvature

analysis of section TP-21 was performed considering seven curvature paths and five levels of axial force. Beginning at a point with zero curvature in x- and y-directions, seven curvature paths were considered in order to reach the point with curvature  $0.15741/m$  along the x-axis and zero curvature along the y-axis. Curvature paths are shown in Figure 4-14. In Path 1, the column experienced uniaxial bending; in other paths, the column was subjected to biaxial bending.

Bending moments induced along x- and y-directions considering curvature paths are shown in Figure 4-15 to Figure 4-19 for section TP-21 under constant axial force equal to 0, 5%, 10%, 15%, and 20% of the theoretical section capacity ( $A_g \times f'_{c0}$ ), respectively. As demonstrated in the figures, when compressive axial force increased, initial flexural capacity of the section increased for all paths. Section capacity along the x-axis decreased when curvature increased along the y-axis, referred to as the “coupling effect” in the literature. For curvature along the y-axis, even a small value caused reduction in flexural capacity of the section along the x-axis; this reduction was more pronounced at higher levels of axial loading.

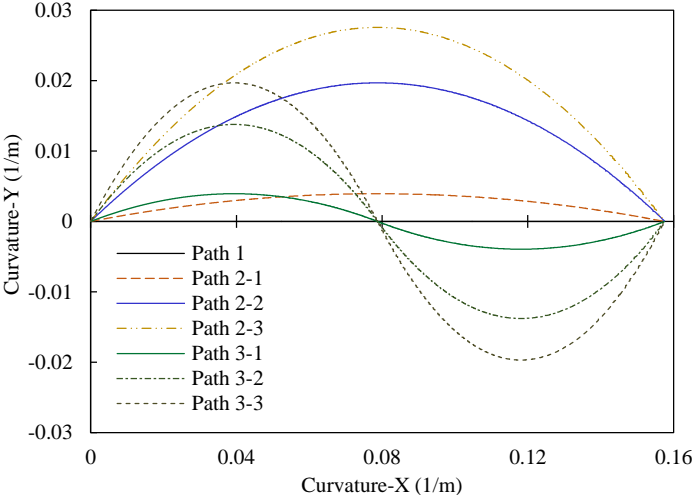


Figure 4-14 Curvature paths

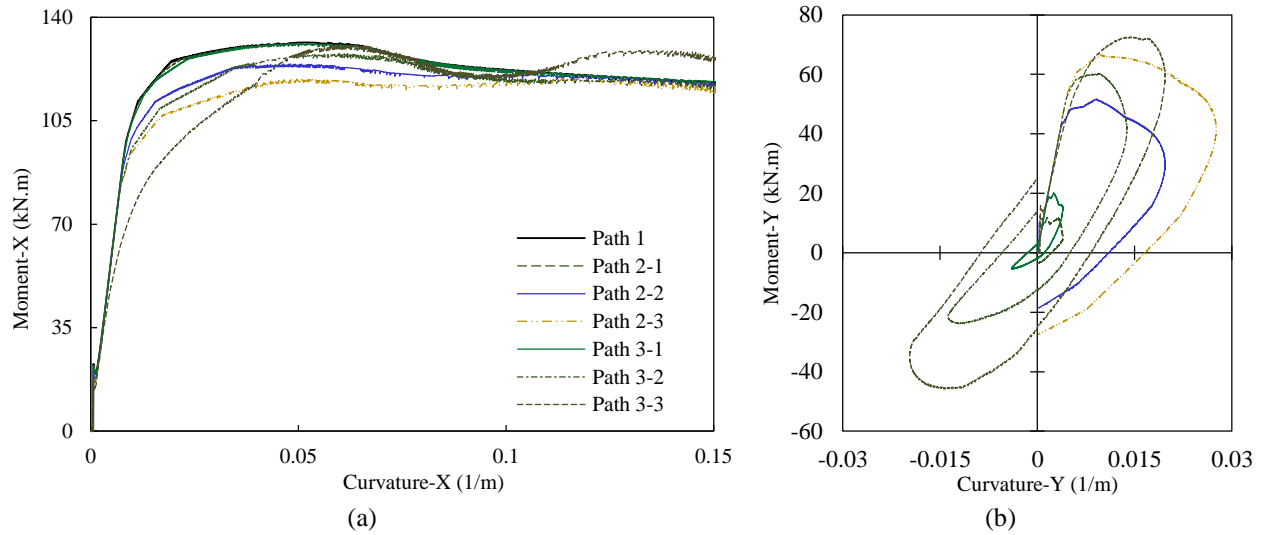


Figure 4-15 Moment-curvature analysis of TP-21 along (a) x-axis and (b) y-axis under zero-axial force considering various curvature paths

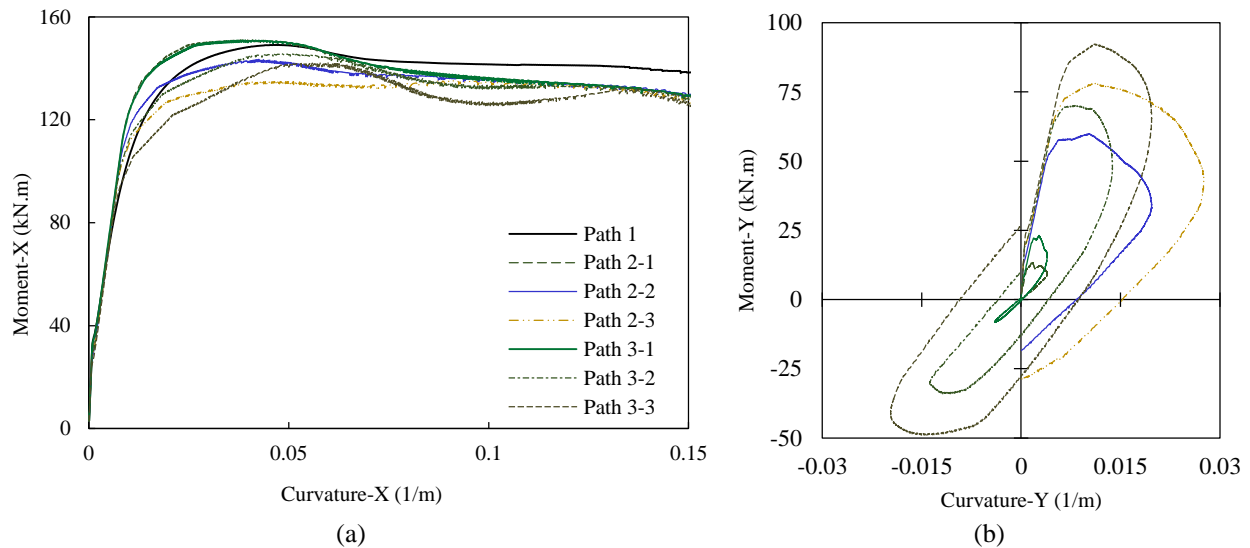


Figure 4-16 Moment-curvature analysis of TP-21 along (a) x-axis and (b) y-axis under axial force equal to 5% analytical axial capacity of the section considering various curvature paths

The reduction percentage of flexural capacity, or maximum strength in x-direction, for each level of axial force is summarized in Table 4-1 (the reduction percentage is calculated with



respect to Path 1 (uniaxial curvature path)). In this table, negative and positive signs indicate decrease and increase in ultimate flexural capacity of the RC section, respectively. Flexural capacity of the section in the x-direction decreased, with the exception of two cases of increased flexural capacity related to 5% axial force. As shown in Table 4-1, the effect of curvature path for reducing flexural capacity of the section increased significantly when the applied axial force level increased.

Under zero axial force, the flexural capacity reduction percentage was 1.01 for Path 3-3; however, this percentage increased to 15.64 when the section was subjected to axial force equal to 20% of analytical axial capacity of the section. The highest decrement in flexural capacity along the x-axis was observed under Path 2-3 and Path 3-3.

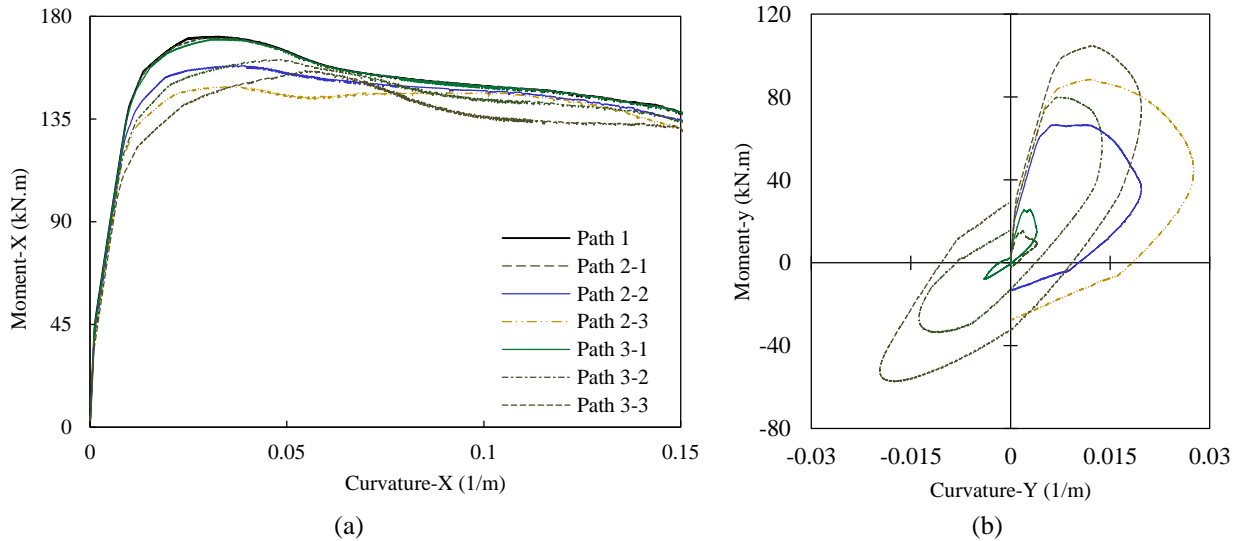


Figure 4-17 Moment-curvature analysis of TP-21 along (a) x-axis and (b) y-axis under axial force equal to 10% of analytical axial capacity of the section considering various curvature paths

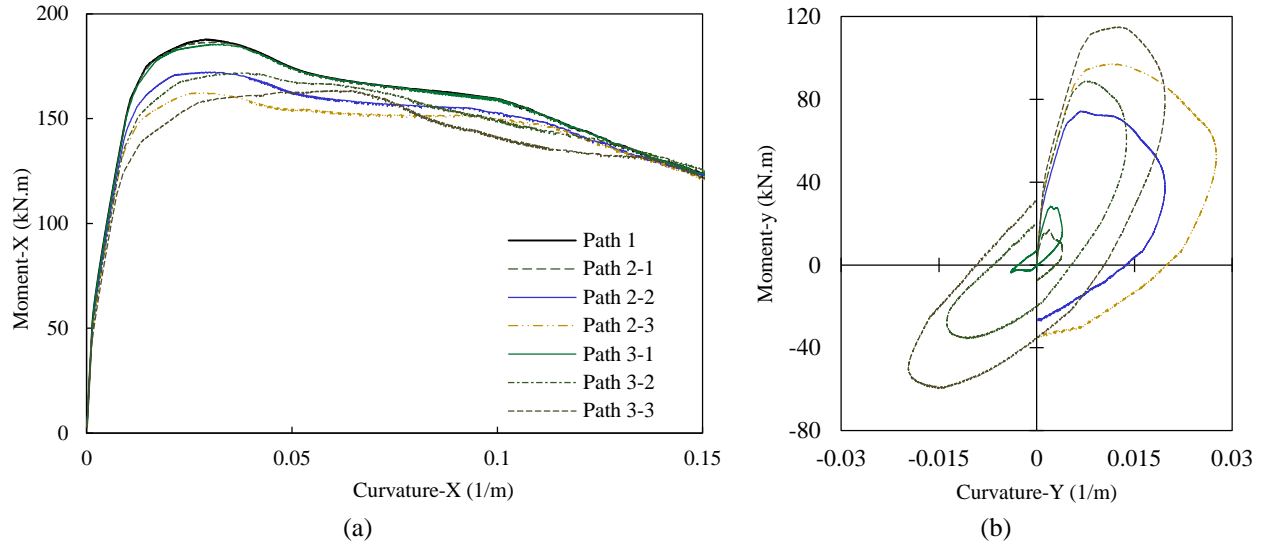


Figure 4-18 Moment-curvature analysis of TP-21 along (a) x-axis and (b) y-axis under axial force equal to 15% of analytical axial capacity of the section considering various curvature paths

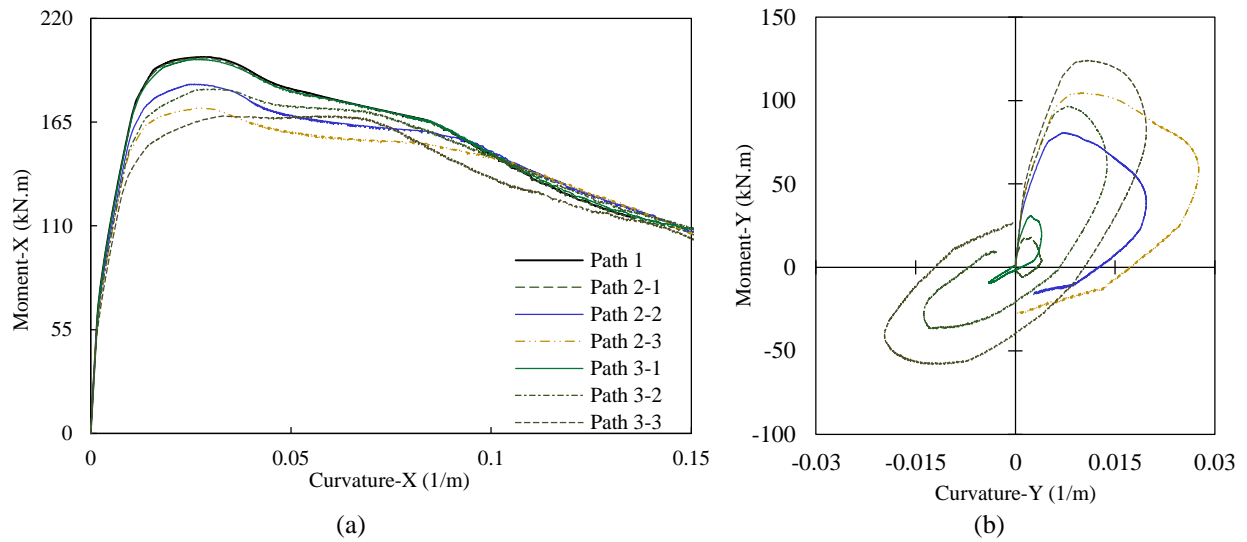


Figure 4-19 Moment-curvature analysis of TP-21 along (a) x-axis and (b) y-axis under axial force equal to 20% of analytical axial capacity of the section considering various curvature paths

In order to clearly demonstrate the effect of load history, the flexural strength percentage of the RC section at the last point with curvature  $0.15741/m$  along the x-axis and zero curvature along the y-axis for all six paths are listed in Table 4-2. Although the section experienced identical curvature along the x-axis and y-axis at the last point in all six paths, flexural strengths

differed significantly depending on the passed curvature path. In Table 4-2, negative and positive signs indicate decrease and increase of final flexural strength of the RC section at the last point of the paths as compared to the straight path as the control path, thereby indicating dependency of the column flexural strength on load pattern and history. The load path affected strength of the concrete section at the exact final point in addition to its effects on energy dissipation. For the section under zero axial force and Path 3-3, the coupling effect caused 6.68% increase of final flexural strength. However, final flexural strength of the section, experiencing Path 3-3 and 20% axial force, decreased almost 17% compared to the final flexural strength of the section with Path 1. The presented study is an attempt to show the effect of load history and pattern on flexural strength of RC columns. However, additional experimental and analytical work is needed before any solid change in design procedure can be proposed.

Table 4-1 Flexural capacity reduction of TP-21 under various curvature path and axial force level

Loading Path	Percentage of Axial Force				
	0	5	10	15	20
Path 2-1	-0.27	+1.32	-0.35	-0.73	-0.21
Path 2-2	-5.49	-3.75	-7.45	-8.30	-7.24
Path 2-3	-9.19	-9.32	-12.81	-13.59	-13.62
Path 3-1	-0.31	+1.15	-0.664	-1.27	-0.63
Path 3-2	-2.82	-2.35	-5.87	-8.55	-8.55
Path 3-3	-1.01	-4.69	-8.73	-12.95	-15.64

Table 4-2 Flexural strength reduction of TP-21 at point with curvature  $0.15741/m$  along the x-axis and zero curvature along the y-axis under various levels of axial force (compared to the straight path to this point)

Loading Path	Percentage of Axial Force				
	0	5	10	15	20
Path 2-1	+0.24	-7.11	+0.19	+0.41	-10.97
Path 2-2	-0.68	-6.19	-2.28	-0.22	-7.41
Path 2-3	-1.37	-8.90	-5.72	-2.53	-12.33
Path 3-1	+0.80	-8.50	+0.18	+0.41	-8.58
Path 3-2	-0.55	-10.46	-3.70	+0.61	-6.99
Path 3-3	+6.68	-7.09	-7.74	-3.15	-16.99

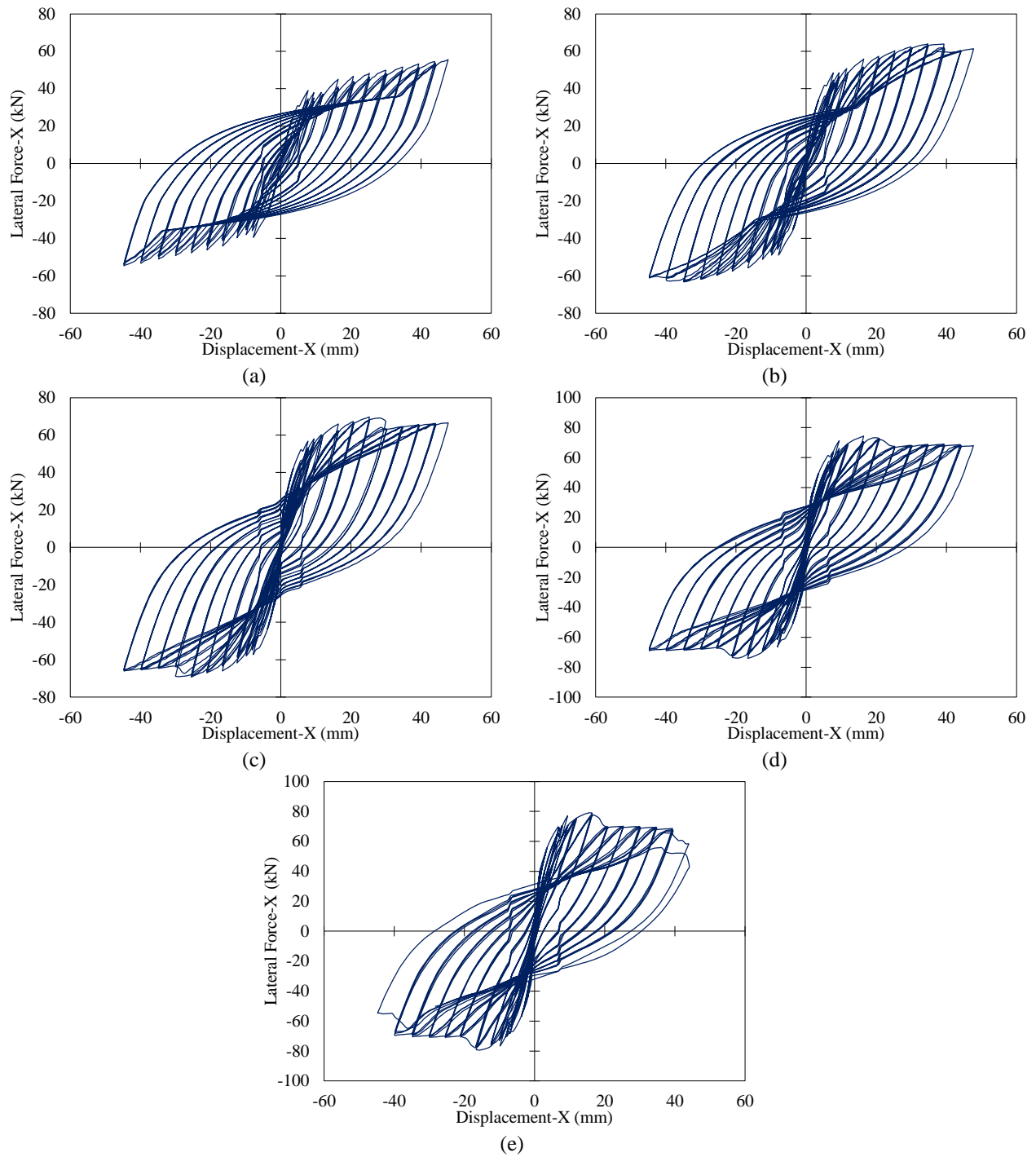


Figure 4-20 Force-deflection analysis of column PB01-N13 under uniaxial hysteretic lateral displacement and (a) zero axial force, (b) 5% axial force, (c) 10% axial force, (d) 15% axial force, and (e) 20% axial force

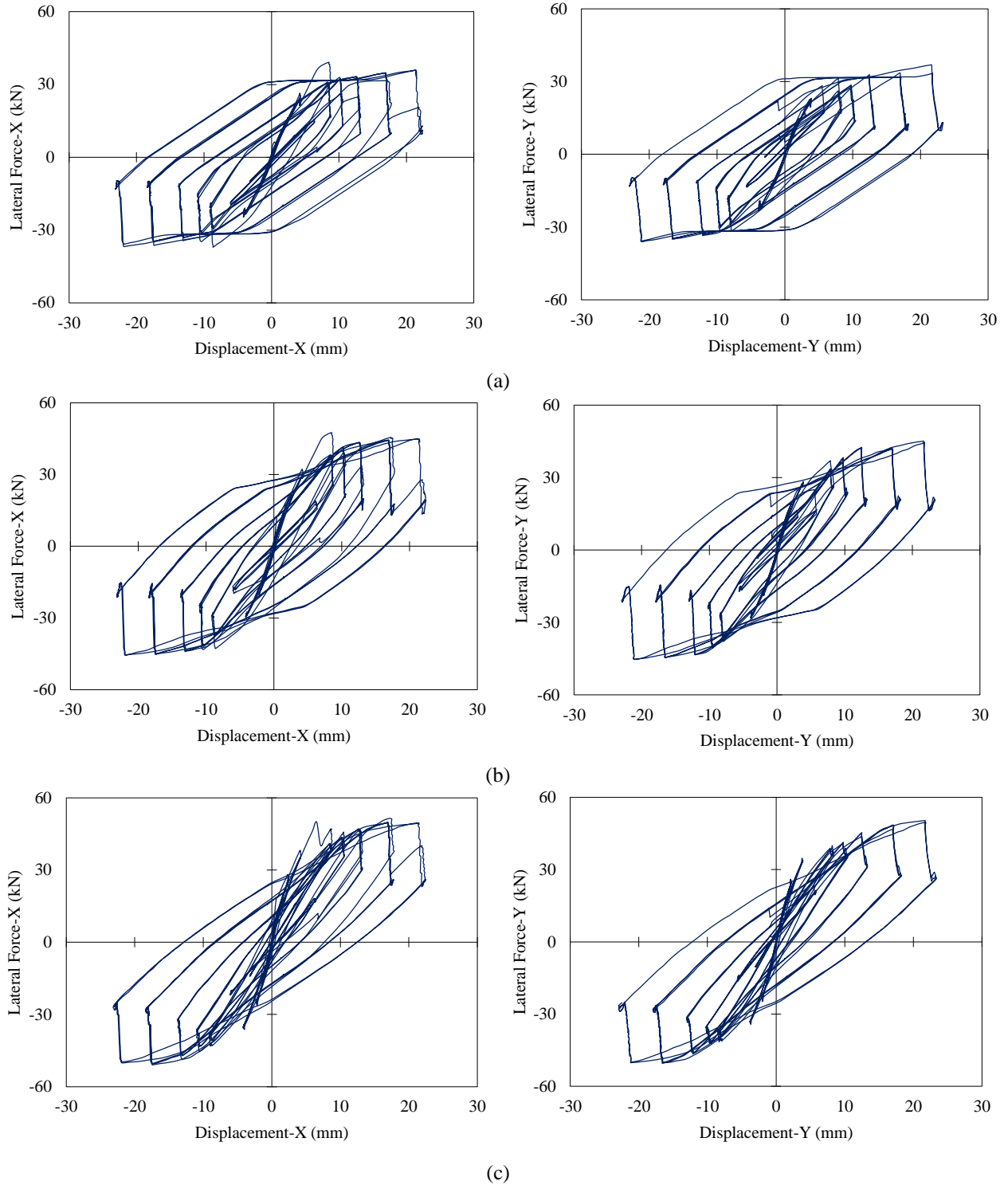


Figure 4-21 Force-deflection analysis of column PB12-N15 under expanding square displacement path and (a) zero axial force, (b) 5% axial force, and (c) 10% axial force

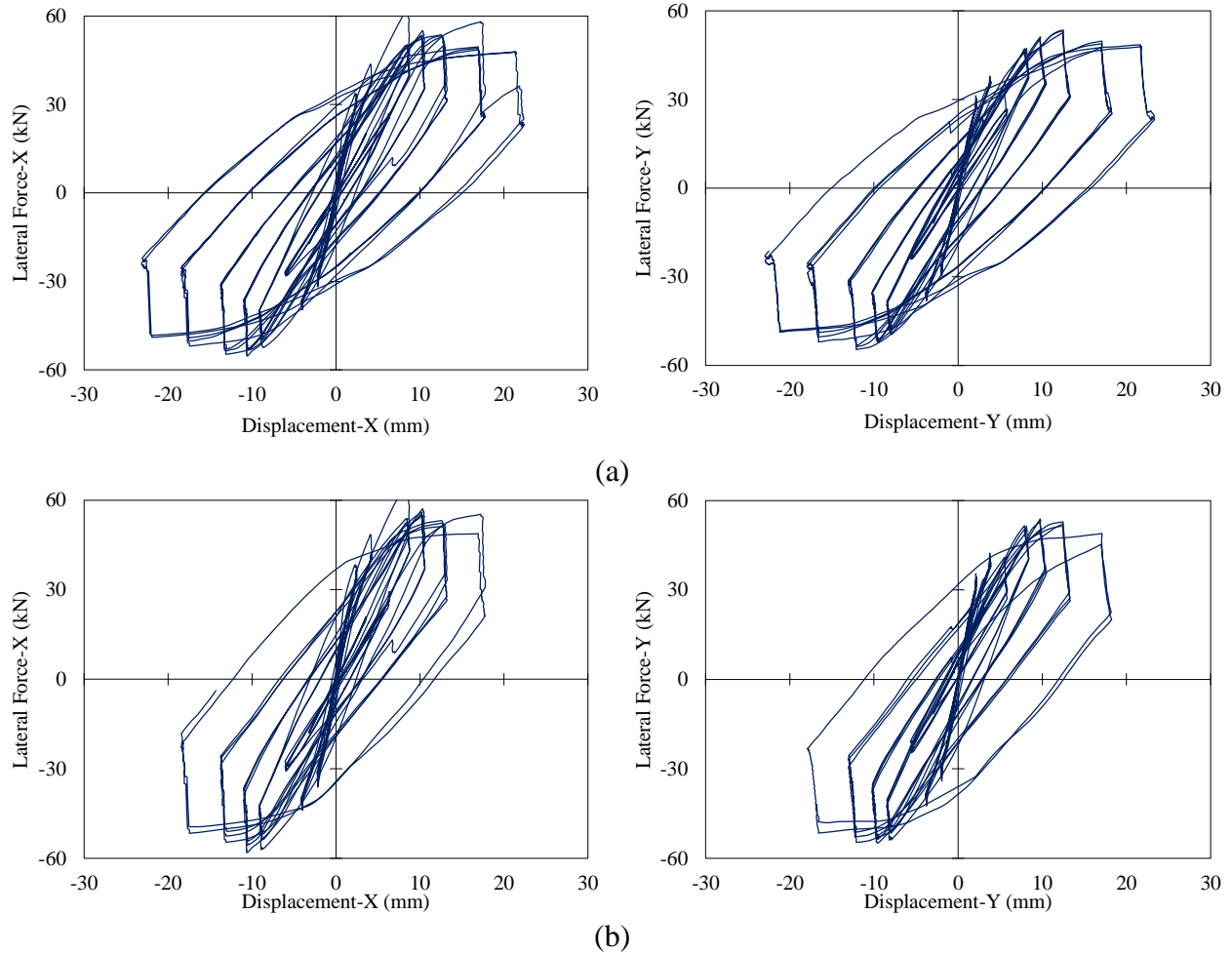


Figure 4-22 Force-deflection analysis of column PB12-N15 under expanding square displacement path and (a) 15% axial force and (b) 20% axial force

#### 4-2-3-1 Force-Deflection Analysis of RC Columns under Various Loading Paths

General force-deflection performance of PB01-N13, PB12-N15, and PB12-N16 columns was evaluated considering various axial force levels. Calculated results in terms of general hysteretic force-deflection performance are presented in Figure 4-20 to Figure 4-24 for PB01-N13, PB12-N15, and PB12-N16 columns under uniaxial, expanding square, and expanding circular displacement path, respectively.

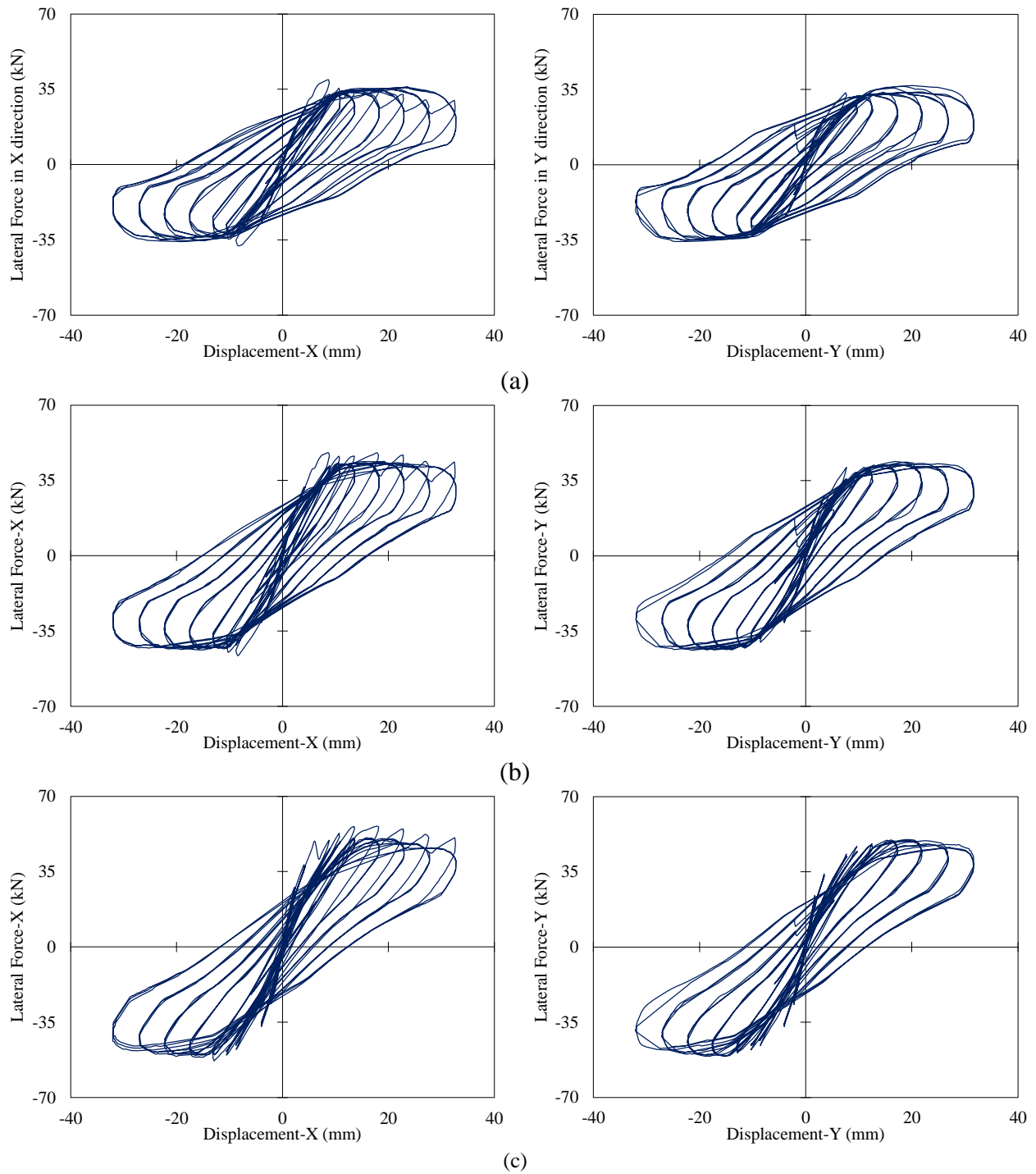


Figure 4-23 Force-deflection analysis of column PB12-N16 under expanding circular displacement path and (a) zero axial force, (b) 5% axial force, and (c) 10% axial force

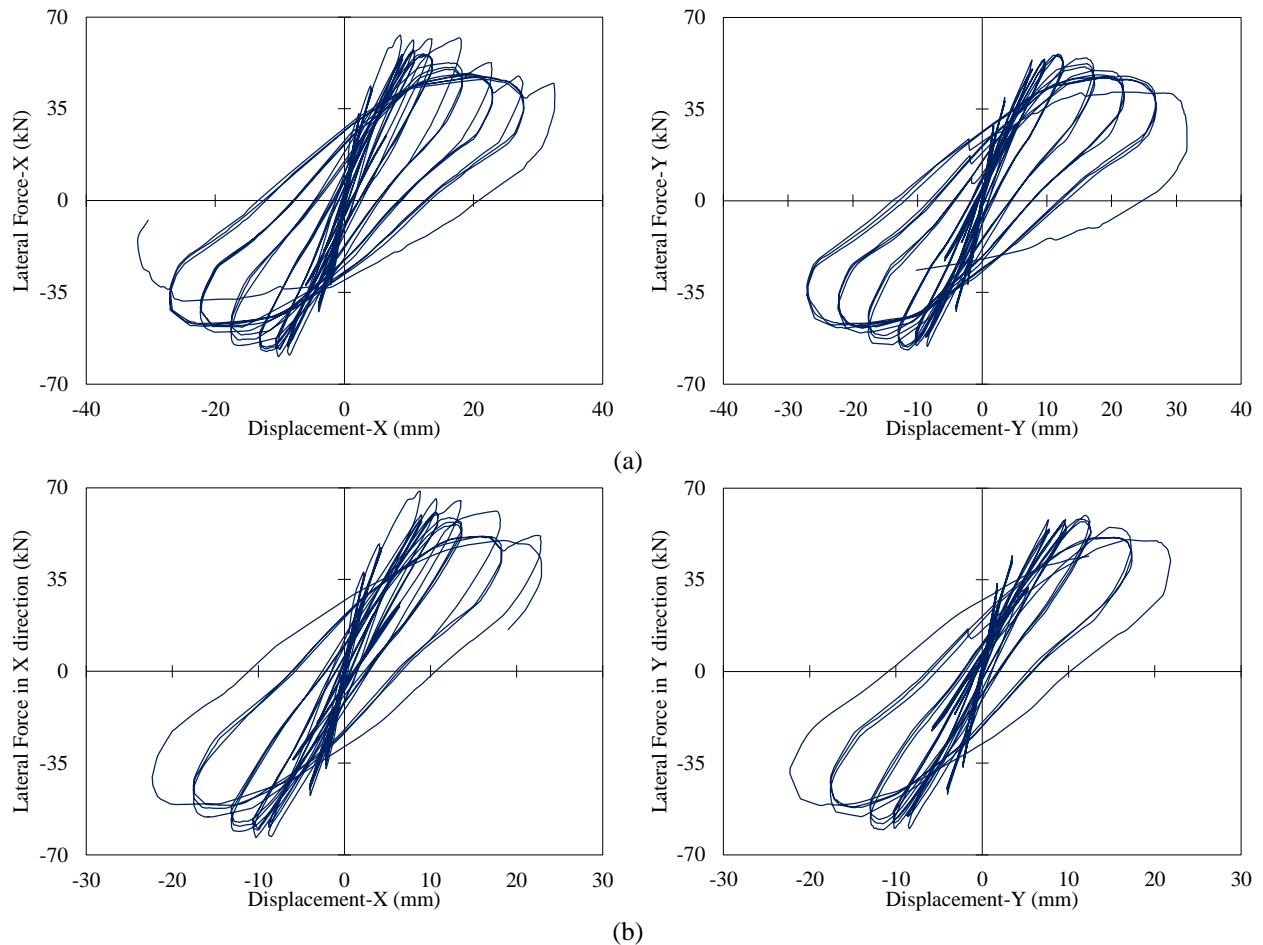


Figure 4-24 Force-deflection analysis of column PB12-N16 under expanding circular displacement path and (a) 15% axial force and (b) 20% axial force

Force-deflection envelopes of columns PB01-N13, PB12-N15, and PB12-N16 under various levels of axial force and uniaxial lateral displacement, expanding square and expanding circular lateral displacement paths, respectively, are shown in Figure 4-25. As demonstrated in Figure 4-25, maximum lateral force increased for all three paths when the axial force level increased.

Increasing axial force level from 0 to 20% of analytical axial capacity of the section resulted in a 41.5% increase in lateral force when the column was under uniaxial lateral displacement path. For columns under expanding square displacement path, the lateral force



increment was 70.0% and 45.0% in x- and y-directions, respectively. These incremental percentages were 75.4% and 54.3% for columns under expanding circular displacement path. The incremental percentages for these three paths highlighted the role of lateral displacement path and axial force level in specifying required lateral capacity of the section.

Because the level of axial force was more pronounced in performance of columns under biaxial lateral displacements, biaxial analysis of structures located at near-fault regions is vital.

Individual cycle energy dissipation of the column under three displacement paths and various axial force levels was calculated. Energy dissipated in each cycle was equal to the area enclosed in the hysteresis loop, as shown in Figure 4-26. For columns PB01-N13, PB12-N15, and PB12-N16 under uniaxial, expanding square and circular displacement path, energy dissipation of 9, 7, and 8 individual cycles is shown in Figure 4-27, Figure 4-28, and Figure 4-29, respectively, for five levels of axial force.

As shown in Figure 4-27, dissipated energy in all individual cycles increased with increasing axial force level when columns were under uniaxial lateral displacement. However, dissipated energy of individual cycles for columns under expanding square and circular displacement paths followed no specific trend. For column PB12-N15 under expanding square displacement path and axial force equal to the 20% of analytical axial capacity of the section, force-deflection analysis was performed up to maximum drift of 18.25 mm because axial capacity of the section could not reach the applied axial force (248.13 kN) when a majority of concrete fibers failed in compression. Therefore, the dissipated energy bar related to the maximum drift of 25 mm is not shown in Figure 4-28. Similarly, the last dissipated energy bars are not shown in Figure 4-29.

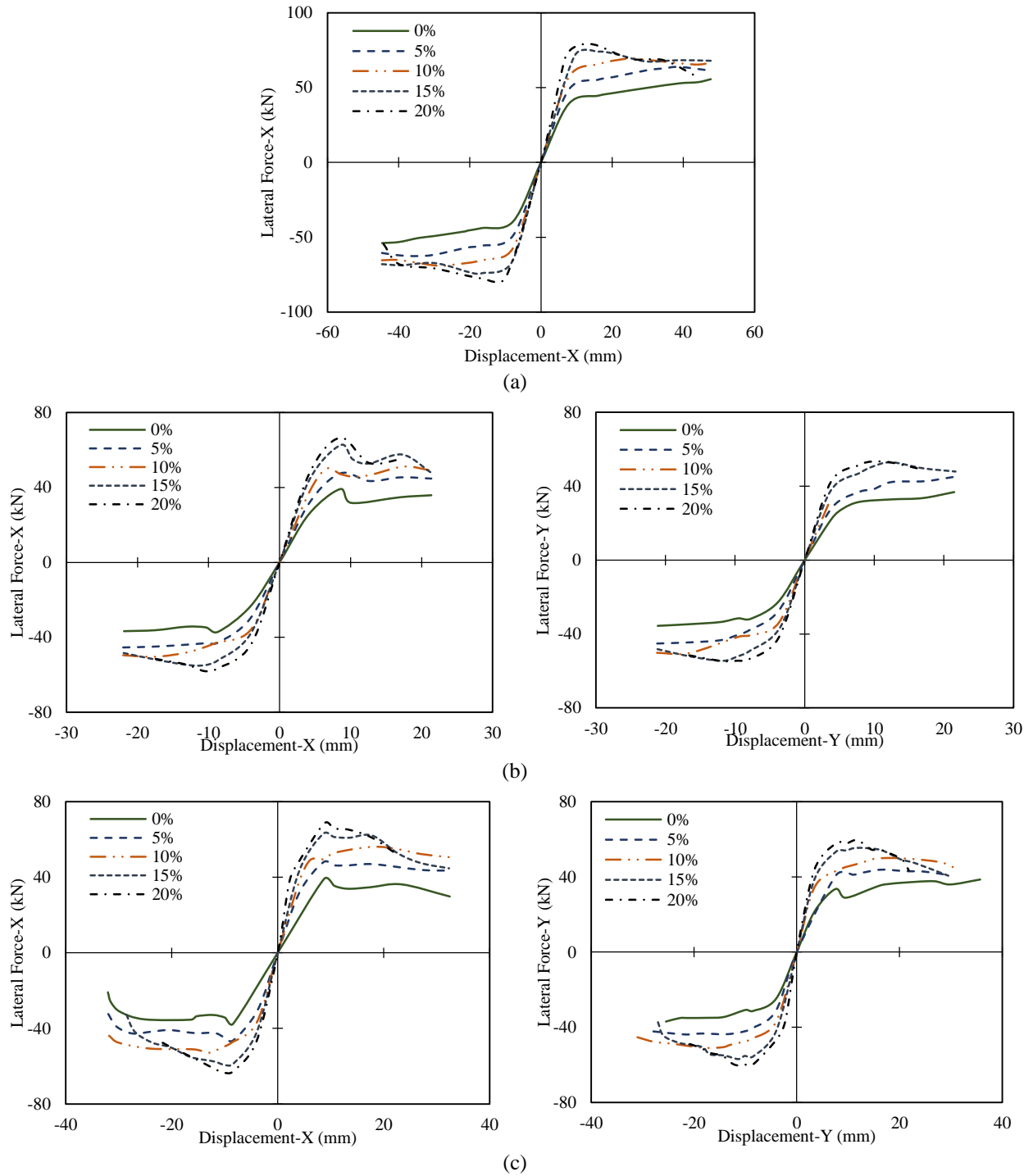


Figure 4-25 Force-deflection peak envelopes analysis of column PB12 under various levels of axial force and (a) uniaxial lateral displacement, (b) circular expanding lateral displacement path, and (c) square expanding lateral displacement path

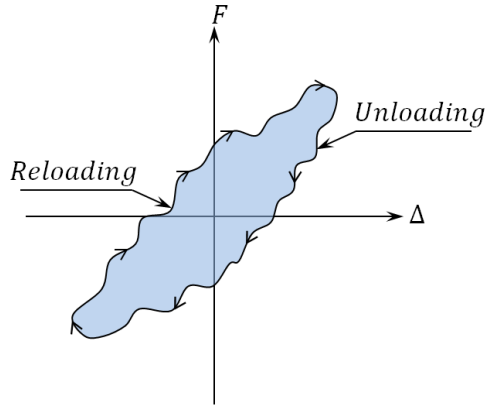


Figure 4-26 Dissipated energy in reversed cyclic loading

Although the coupling effect of the two transverse directions caused a reduction in strength and stiffness of columns in both transverse directions, it significantly increased hysteretic dissipated energy, as demonstrated in Figure 4-27 to Figure 4-29.

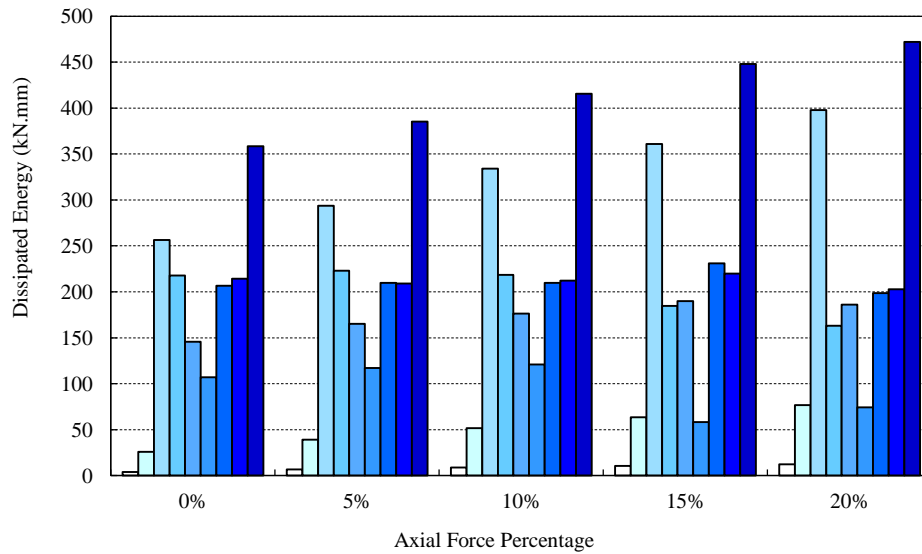


Figure 4-27 Individual cycle energy dissipation for PB01-N13 under uniaxial lateral displacement and various axial force levels

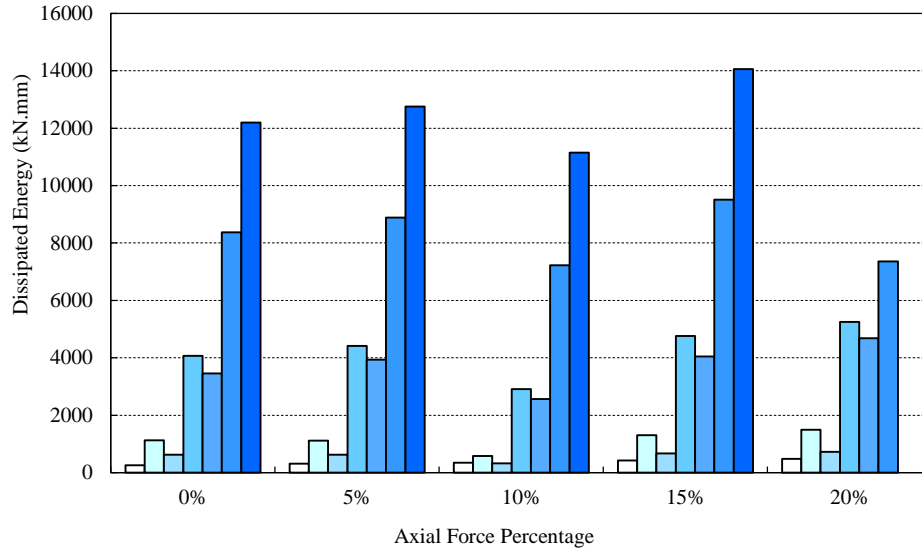


Figure 4-28 Individual cycle energy dissipation for PB12-N15 under expanding square displacement path and various axial force levels

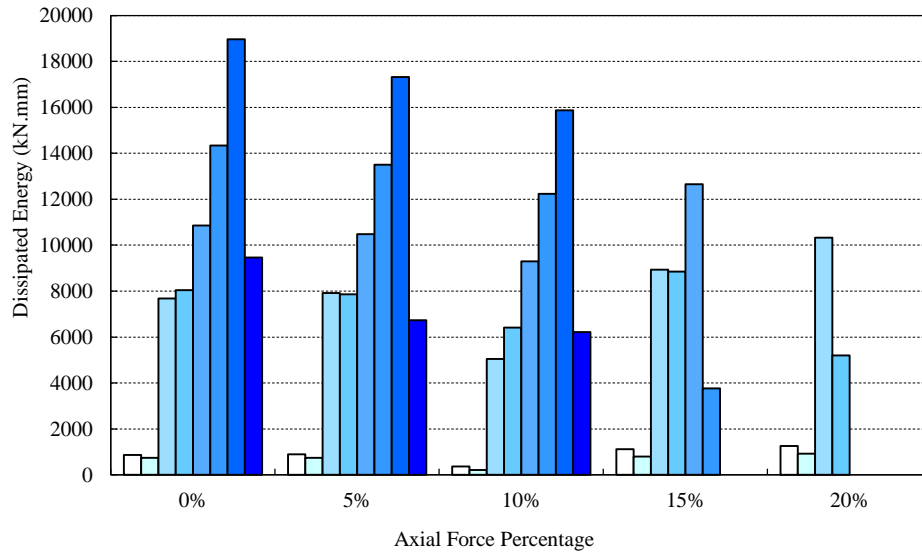


Figure 4-29 Individual cycle energy dissipation for PB12-N16 under expanding circular displacement path and various axial force levels

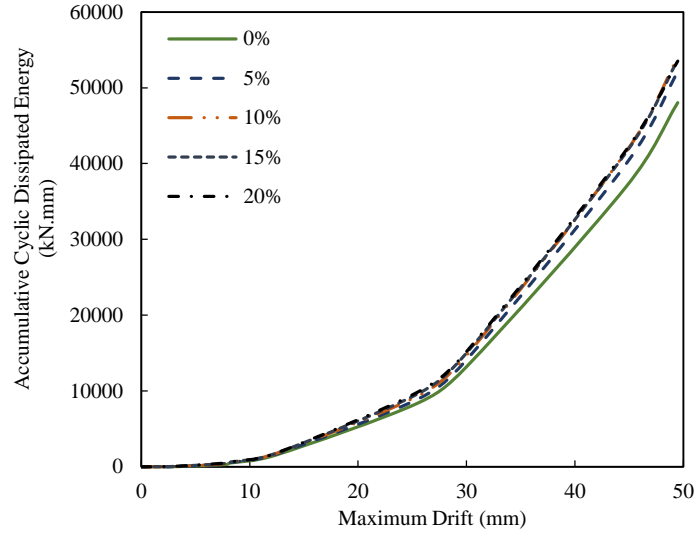


Figure 4-30 Comparison of cumulative dissipated energy for column PB01-N13 under uniaxial lateral displacement and various axial force levels

Cumulative dissipated energy versus maximum drift of the column for three lateral displacement paths is demonstrated in Figure 4-30 to Figure 4-32. As shown in Figure 4-30, the level of axial force only slight affected cumulative energy of the column under uniaxial lateral force. Columns under zero and 20% axial forces had the lowest and highest cumulative dissipated energy, respectively.

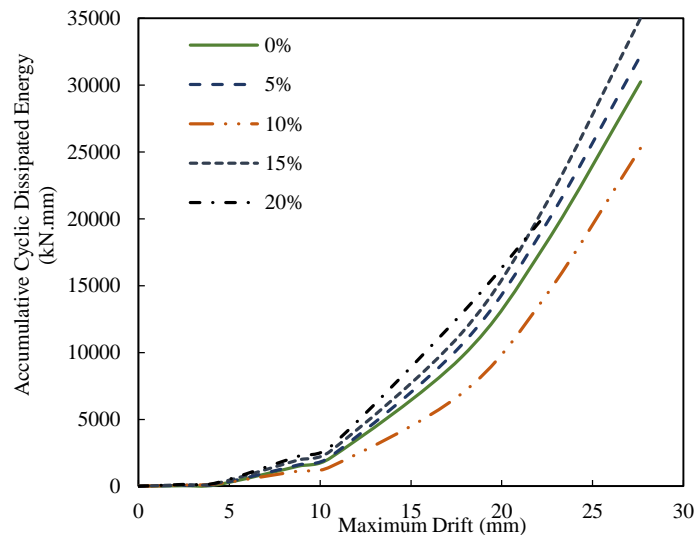


Figure 4-31 Comparison of cumulative dissipated energy for column PB12-N15 under expanding square displacement path and various axial force levels

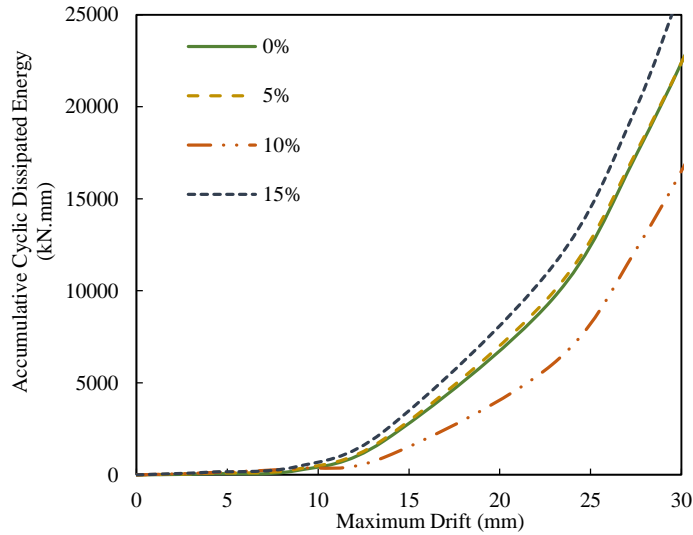


Figure 4-32 Comparison of cumulative dissipated energy for column PB12-N16 under expanding square displacement path and various axial force levels

For the column under biaxial displacement path, cumulative dissipated energy occurred when the axial force was equal to 10% of analytical axial force capacity of the section. Cumulative dissipated energy decreased when axial force level increased.

In summary, the coupling effect of the two transverse directions caused a reduction in strength and stiffness of the column in both transverse directions; however, the coupling effect increased accumulative hysteretic energy dissipation, as demonstrated in Figure 4-30 to Figure 4-32.

## **4-3 Effect of Axial Loading Pattern on Performance of RC Members**

### **4-3-1 Analytical Model**

### **4-3-2 Validation of Analytical Model**

Performance of the developed computer application for predicting behavior of RC columns under cyclic lateral force/displacements and variable axial load was assessed in comparison with experimental data of two RC columns (TP-31 and TP-33) originally tested by Kawashima et al. Both columns had a square cross section with dimensions of 400×400 mm and clear cover of 27 mm. They were reinforced longitudinally using 20 No. 13 evenly distributed bars, Grade SD295A (nominal yield strength of 374 MPa) and laterally using No. 6 tie with 50 mm spacing. Details of longitudinal and lateral reinforcement of these two columns are shown in Figure 4-33. Cylinder compressive strength of plain concrete was 22.9 MPa for both specimens. Column specimen TP-31 was tested under cyclic lateral forces/displacements and constant axial force of 470 kN; however, column specimen TP-33 was tested under cyclic lateral forces/displacements in addition to variable axial force. Maximum and minimum applied axial force in column specimen TP-33 were 310 kN and -10kN, respectively. Lateral displacements and axial forces for these two columns are shown in Figure 4-34 and Figure 4-35.

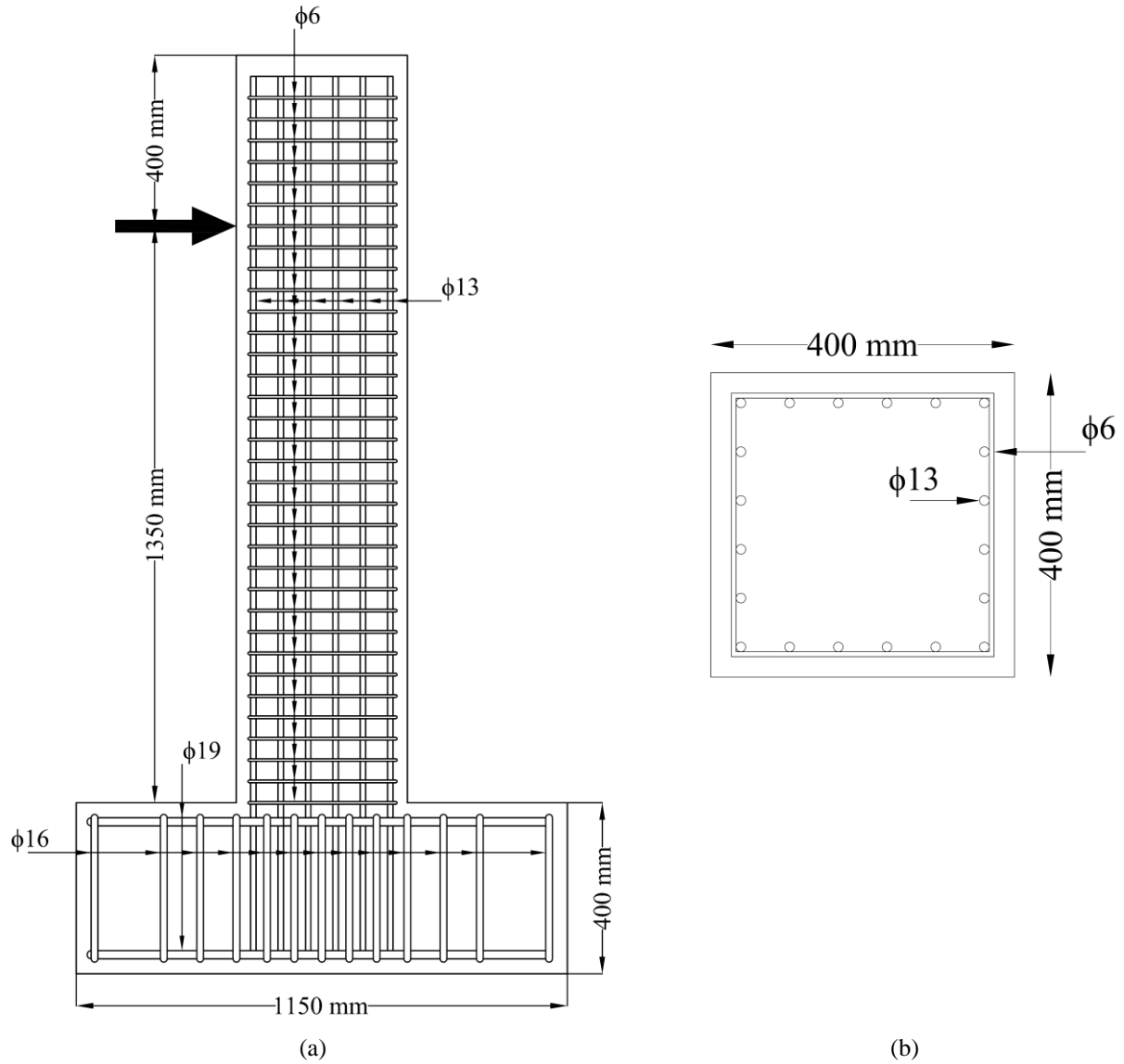
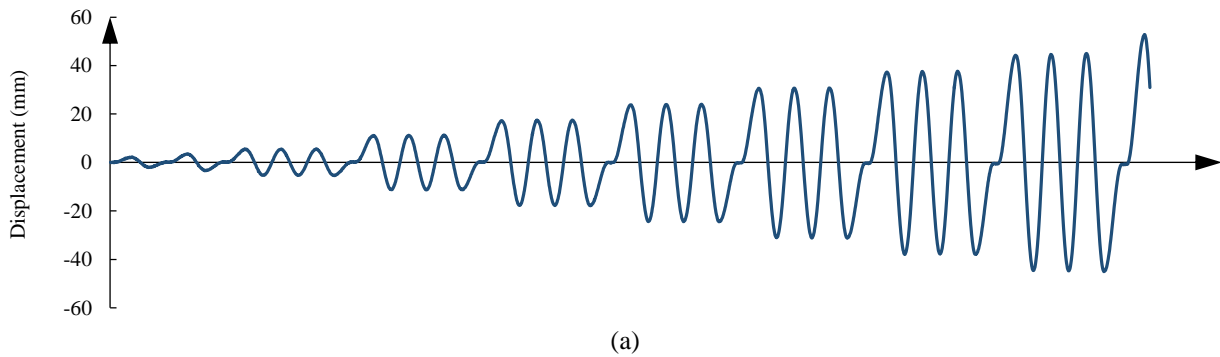


Figure 4-33 Geometry and reinforcement details of specimens TP-31 and TP-33: (a) elevation, (b) cross section





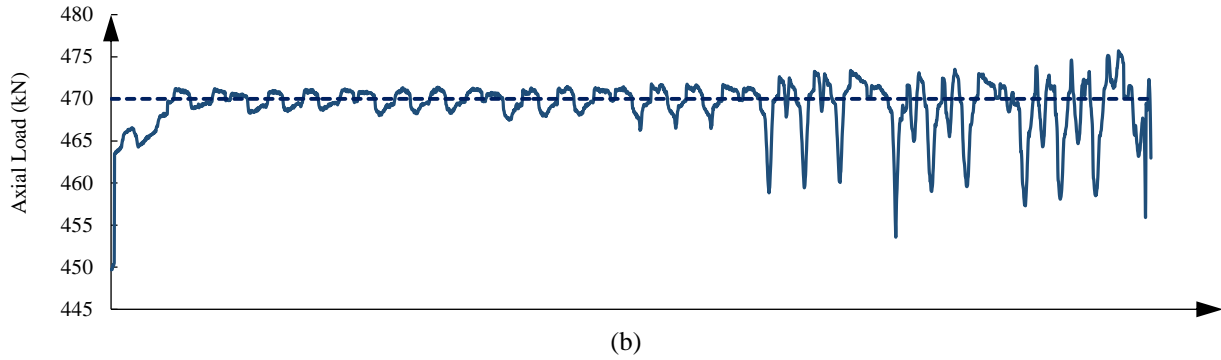


Figure 4-34 (a) Displacement and (b) axial load cycles for specimen TP-31

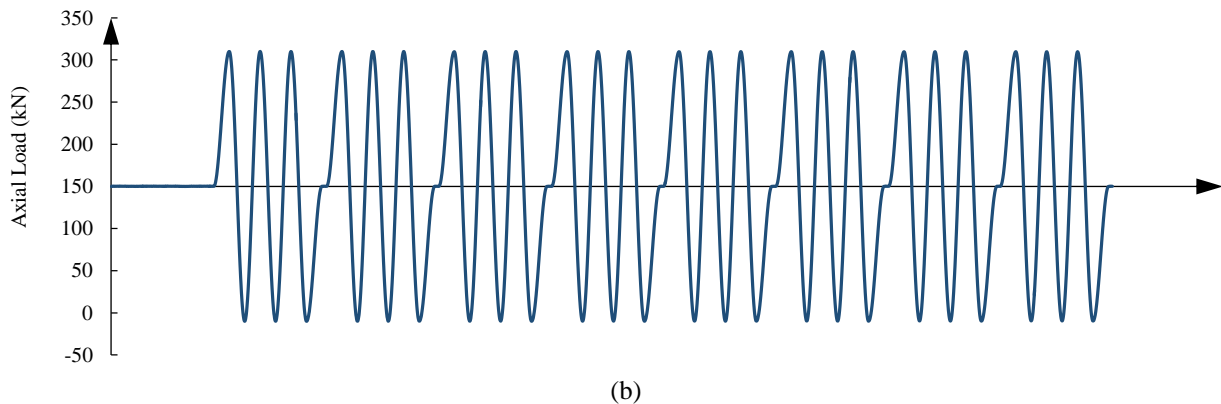
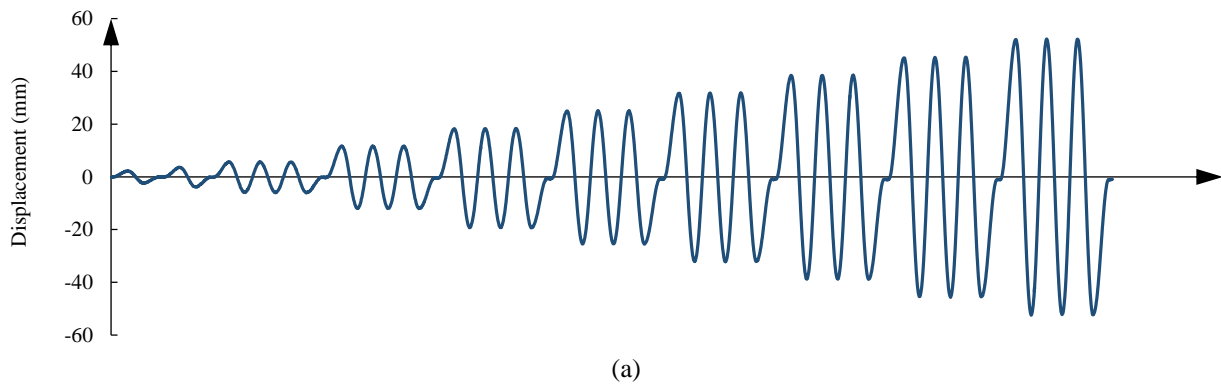


Figure 4-35 (a) Displacement and (b) axial load cycles for specimen TP-33

Monotonic and cyclic behavior of plain and confined concrete fibers was simulated using the model developed by Mander et al. (1988) in conjunction with the linear cyclic model. Longitudinal reinforcing steel behavior was modeled considering Menegotto-Pinto's (1973) cyclic and monotonic stress-strain relationships. The monotonic curve backbone coefficient ( $b$ ) in the Menegotto-Pinto model was set to 0.01, and cyclic parameters  $R_0$ ,  $a_1$ , and  $a_2$  were

considered 1.5, 2.0, and 0.18, respectively. The effect of lateral reinforcement was considered indirectly through uniaxial stress-strain relationship of the confined concrete core. The Esmaily-Xiao second plastic hinge model was used to evaluate the force-deflection response of both column specimens. As shown, this model is more effective than other models when column specimens are under uniaxial lateral force/displacements.

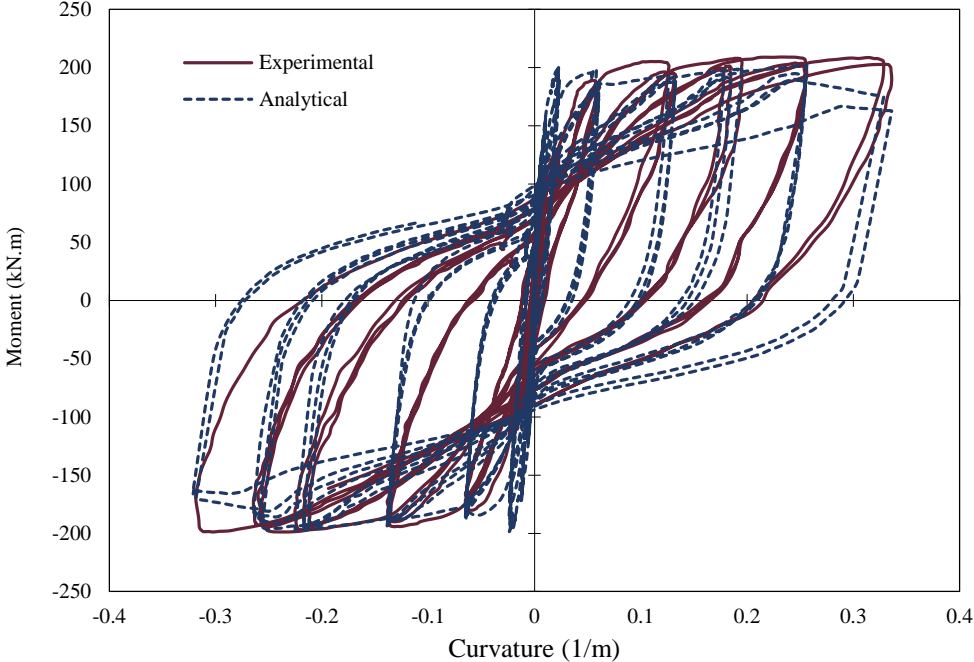


Figure 4-36 Moment-curvature analysis for specimen TP-31

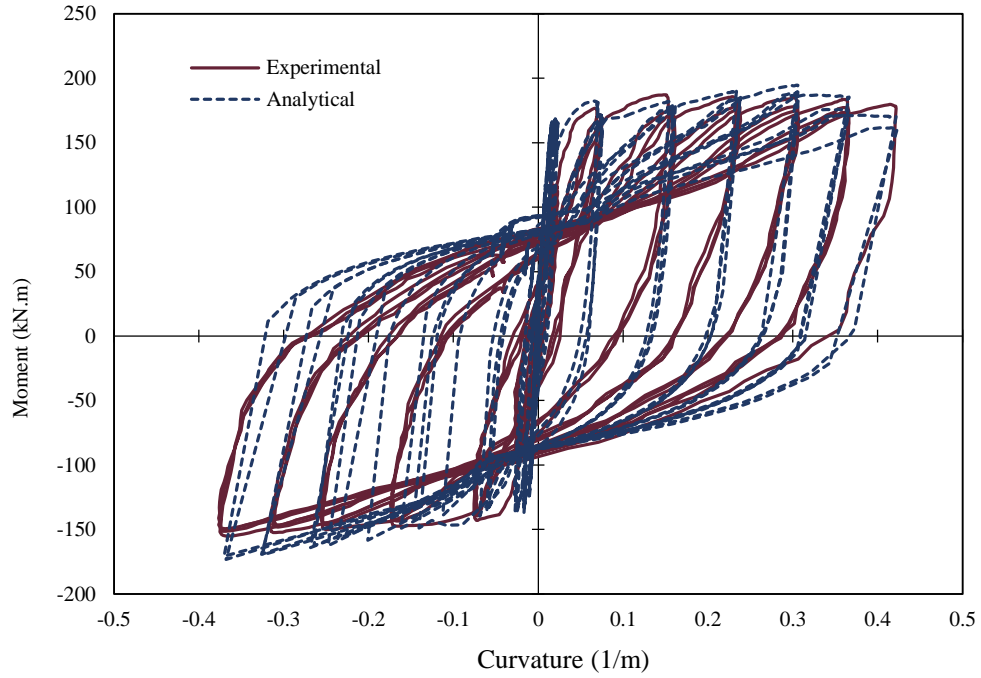


Figure 4-37 Moment-curvature analysis for specimen TP-33

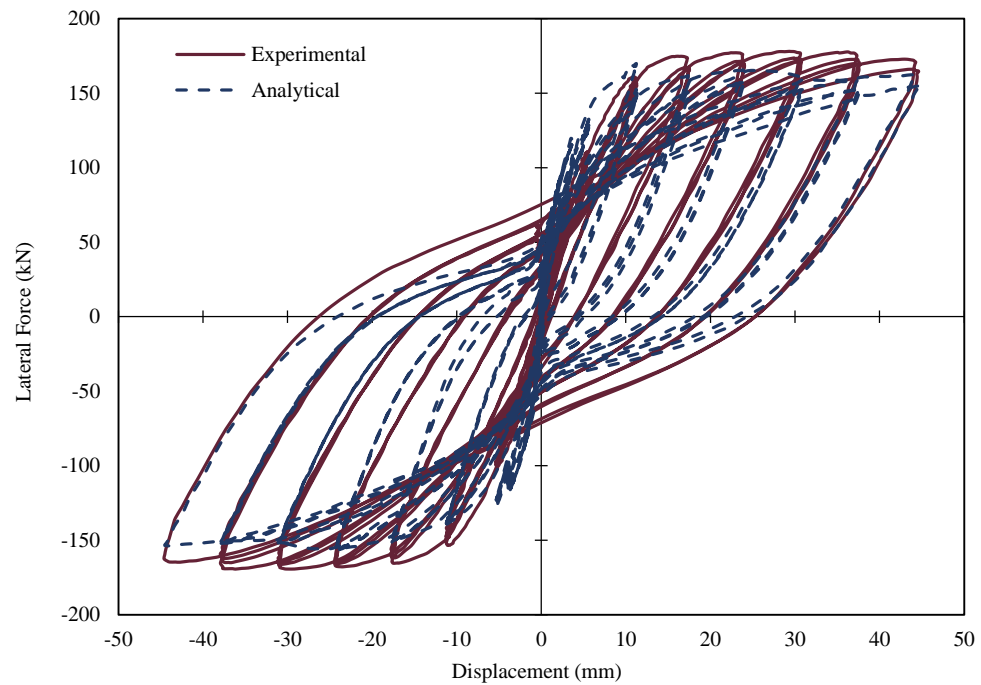


Figure 4-38 Force-deflection analysis for specimen TP-31

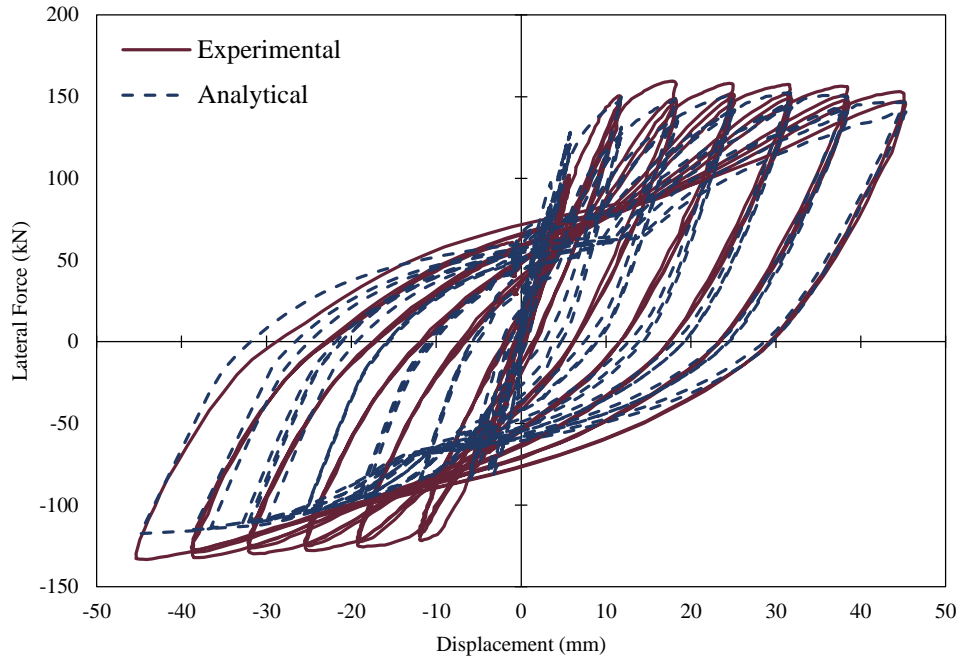


Figure 4-39 Force-deflection analysis for specimen TP-33

Figure 4-36 and Figure 4-37 show moment-curvature curves of specimens TP-31 and TP-33, respectively, analytically calculated using the fiber element method and measured experimentally by Kawashima et al. Analytical and experimental force-deflection curves for columns TP-31 and TP-33 are shown in Figure 4-38 and Figure 4-39, respectively.

### 4-3-3 Vital Consideration of Axial Force Variation

Many research studies have been conducted to investigate if variable axial load affects structure behavior, especially columns of structures located in near-fault regions. As a result of conducted studies in the literature, researchers have agreed that variable axial load affects performance of structures and special considerations must be taken into account for structures located in near-fault regions. The primary goal of this section is to determine the importance of axial force variability and its effect on flexural capacity of RC columns.

Columns are structural elements that are subjected to a combination of axial forces and bending moments. Engineers and researchers commonly utilize axial force-bending moment interaction curves as handy tools to design columns. Based on geometrical properties of a section, longitudinal reinforcement ratio, and arrangement and strength of concrete material, ACI provides axial force-bending moment interaction curves. These interaction curves were produced considering the equivalent stress-strain block proposed by Hognestad for simulating concrete behavior and elastic-perfectly plastic stress-strain relationship to simulate the behavior of reinforcing steel. However, lateral steel's confinement effect was not considered in ACI interaction curves. Therefore, engineers use ACI interaction curves as reliable, conservative tools to design RC sections under combined action of axial force and bending moment.

A new axial force-bending moment interaction curve was conducted to investigate the effect of variable axial load on RC section behavior. In this interaction curve for each level of axial force, a monotonic moment-curvature analysis was conducted considering variable axial force. The maximum moment in moment-curvature curve was selected as corresponding moment for the axial force.

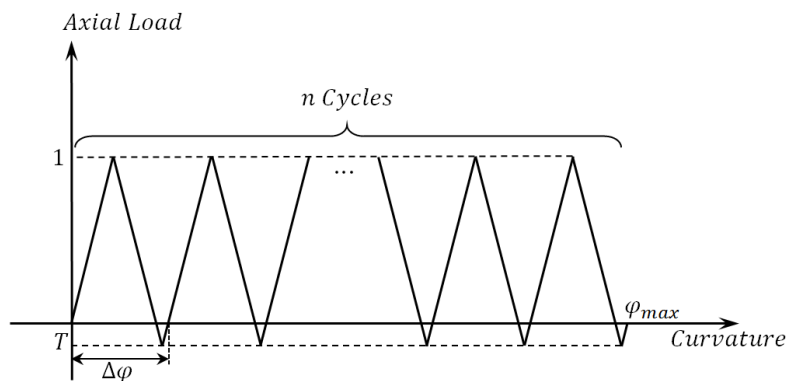
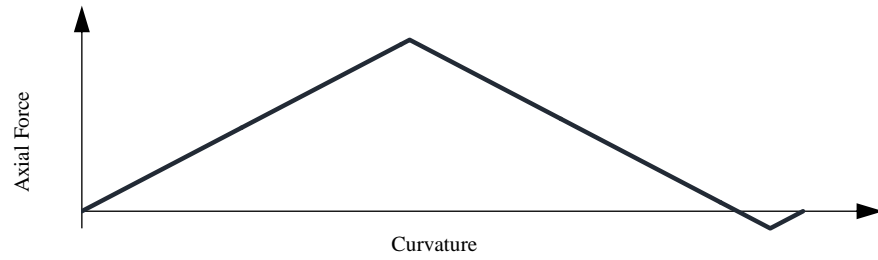
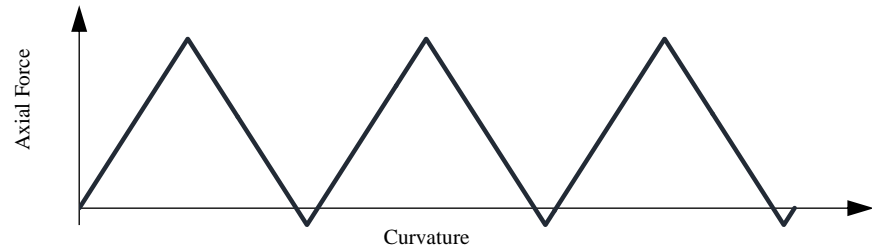


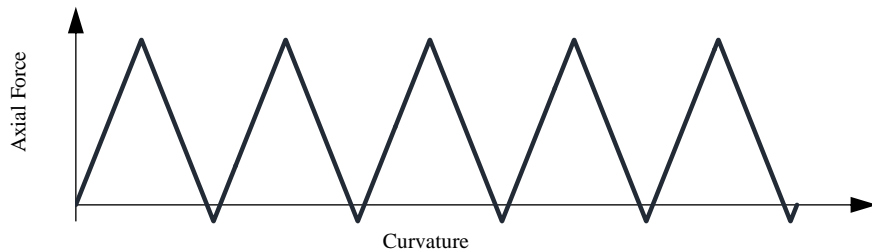
Figure 4-40 Axial loading pattern with  $n$  triangular cycles



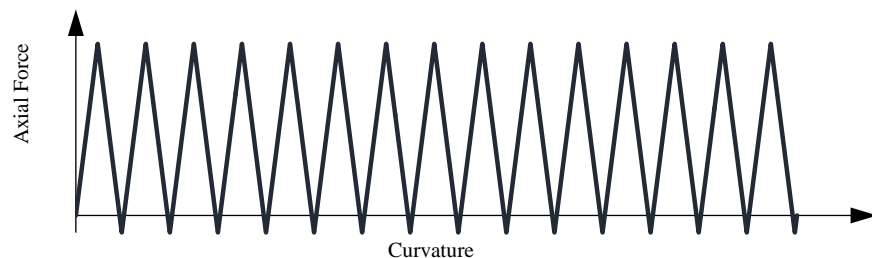
(a)



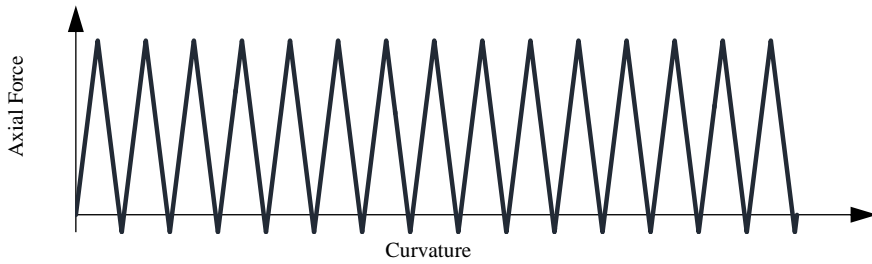
(b)



(c)



(d)



(e)

Figure 4-41 Axial loading pattern with (a) one cycle, (b) three cycles, (c) five cycles, (d) 10 cycles, and (e) 15 cycles

Axial force variation with respect to curvature along the x-axis considering  $n$  number of cycles is shown in Figure 4-40. In this figure,  $T$  is maximum tensile strength coefficient less than 1.0,  $\varphi_{\max}$  is maximum curvature, and  $\Delta\varphi$  is the curvature interval in which the axial load completes one cycle.

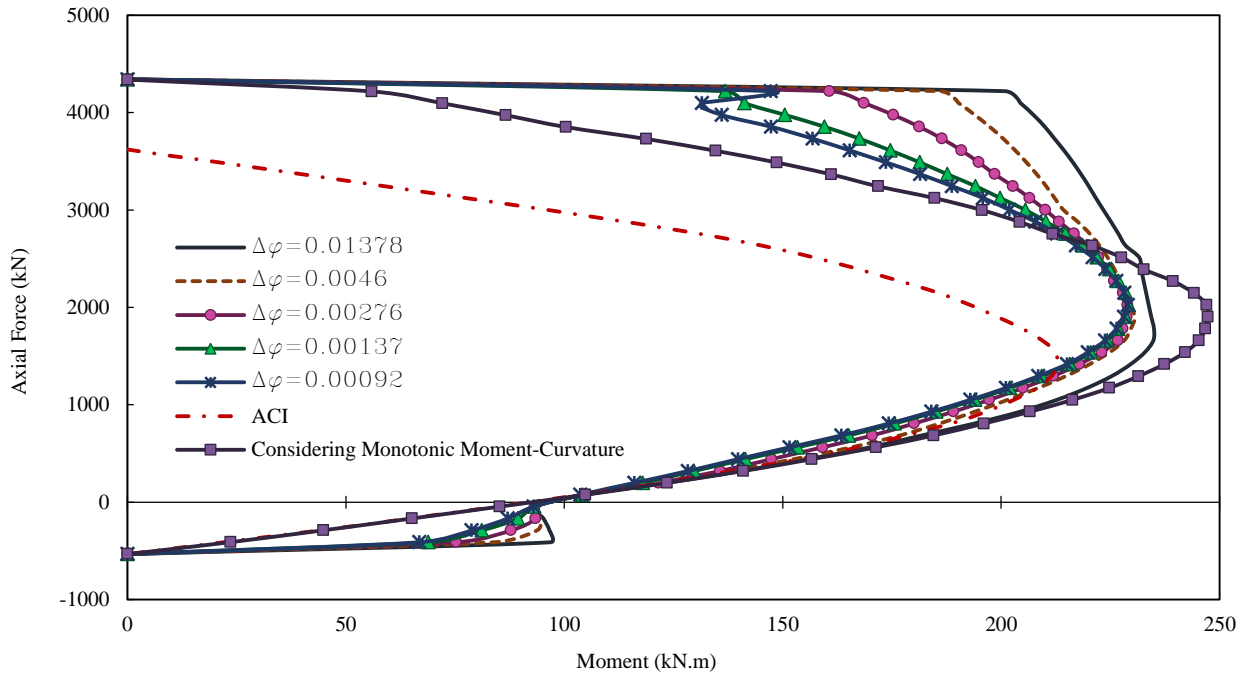


Figure 4-42 Axial force-bending moment interaction curves of the square section with  $\rho_s = 0.89\%$ , considering various axial loading patterns

#### 4-3-4 Results and Discussion

In order to investigate the effect of the number of cycles in variable axial load in specific curvature interval on axial force-bending moment interaction curve, axial force patterns with  $\Delta\varphi = 0.01378, 0.0046, 0.00276, 0.00137, 0.00092$ , and  $0.000921/m$  were considered to produce interaction curves. Figure 4-42 to Figure 4-48 show interaction curves of a square section with 0.89% to 8.05% longitudinal reinforcing steel ratio, respectively, considering various curvature intervals.

Interaction curves considering variable axial force were compared to the interaction curve predicted by the ACI and the interaction curve produced by considering monotonic moment-curvature analysis under constant axial force.

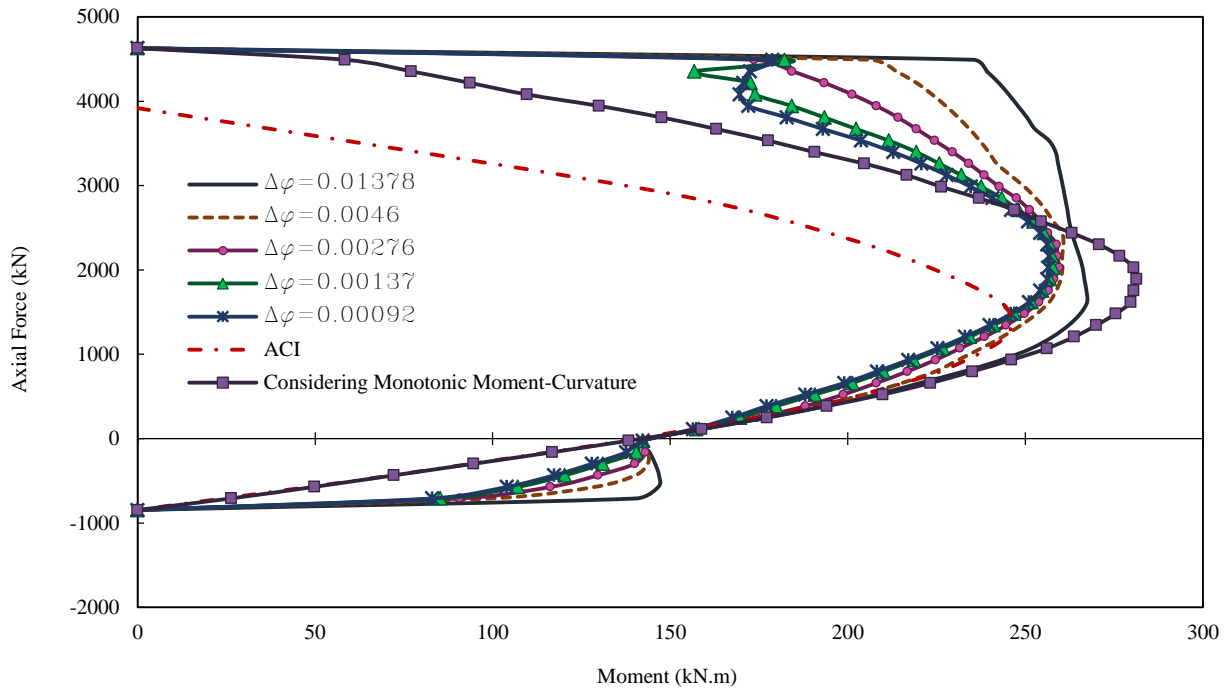


Figure 4-43 Axial force-bending moment interaction curves of the square section with  $\rho_s = 1.58\%$ , considering various axial loading patterns

Flexural capacity predicted by the ACI was less than flexural capacity calculated with consideration of fluctuating axial force for high levels of axial force. However, ACI flexural capacity was less than the predicted ultimate flexural capacity considering fluctuating axial force for middle to high levels of axial force. For all longitudinal steel ratios, flexural capacity of the column calculated using moment-curvature analysis and constant axial force was more than flexural capacity predicted by ACI and the flexural capacity calculated considering fluctuating axial force.



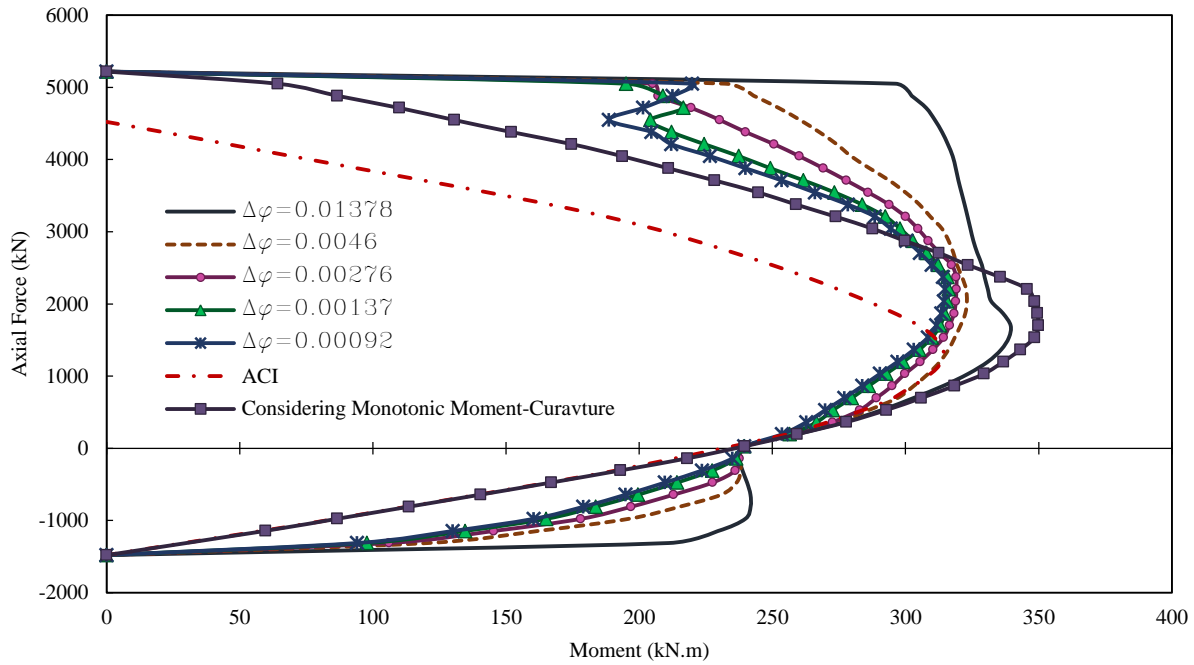


Figure 4-44 Axial force-bending moment interaction curves of the square section with  $\rho_s = 2.47\%$ , considering various axial loading patterns

Overestimation of flexural capacity, predicted by the ACI method as compared to ultimate flexural capacity calculated considering fluctuating axial force for the square section with longitudinal steel ratio of 0.89% to 8.05% are shown in Figure 4-49 to Figure 4-55, respectively. As shown in these figures, when the curvature interval decreased from  $\Delta\varphi = 0.01378$  to  $0.000921/m$ , the ACI overestimation capacity increased; when the steel ratio increased, the ACI overestimation decreased, as in the occurrence of no overestimation when the steel ratio of was 8.05%. Therefore, flexural capacity predicted by ACI is conservative for sections with high steel ratio longitudinal reinforcement.

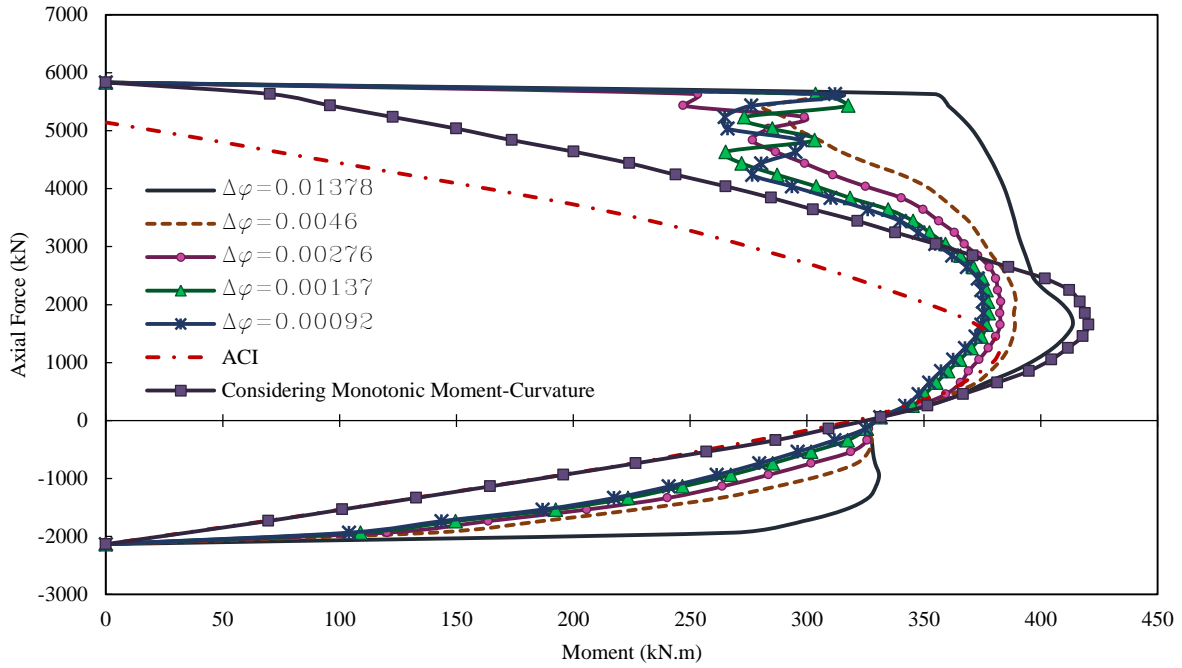


Figure 4-45 Axial force-bending moment interaction curves of the square section with  $\rho_s = 3.56\%$ , considering various axial loading patterns

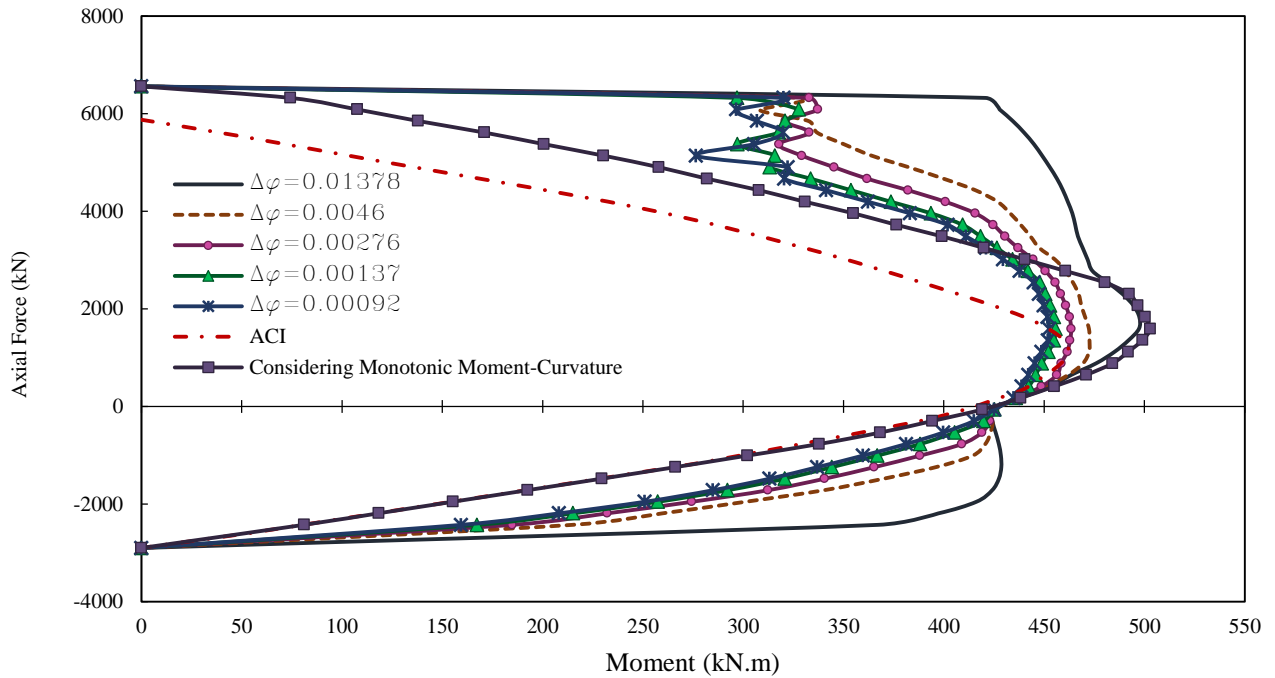


Figure 4-46 Axial force-bending moment interaction curves of the square section with  $\rho_s = 3.56\%$ , considering various axial loading patterns

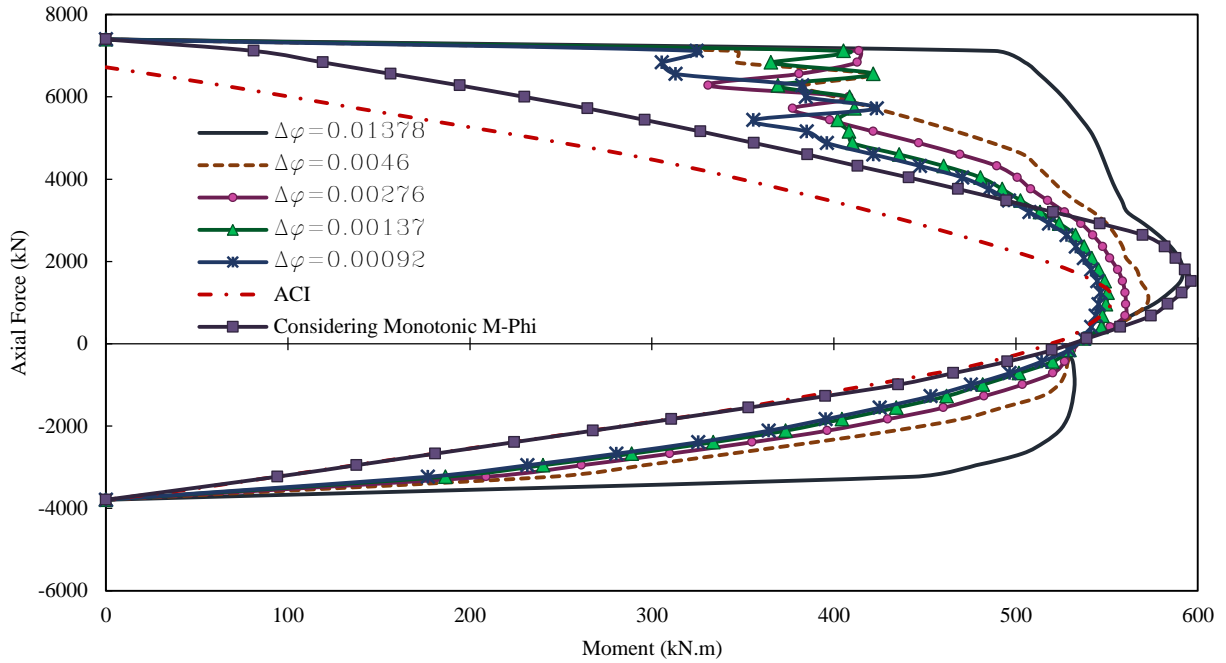


Figure 4-47 Axial force-bending moment interaction curves of the square section with  $\rho_s = 6.33\%$ , considering various axial loading patterns

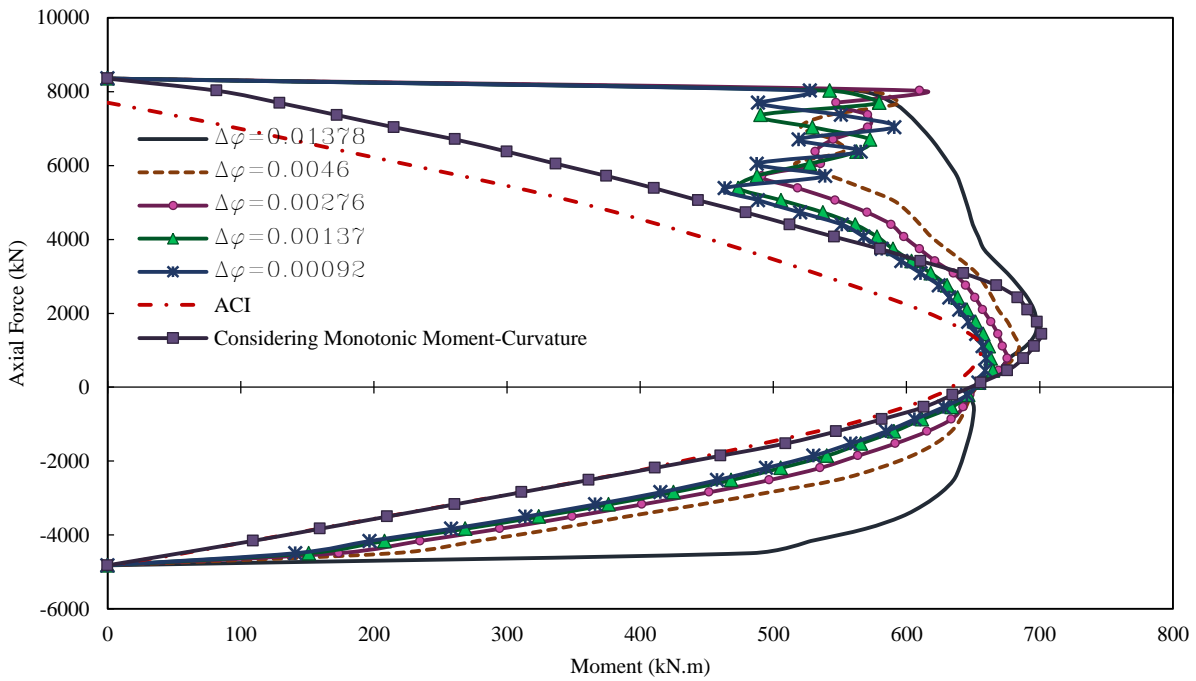


Figure 4-48 Axial force-bending moment interaction curves of the square section with  $\rho_s = 8.05\%$ , considering various axial loading patterns

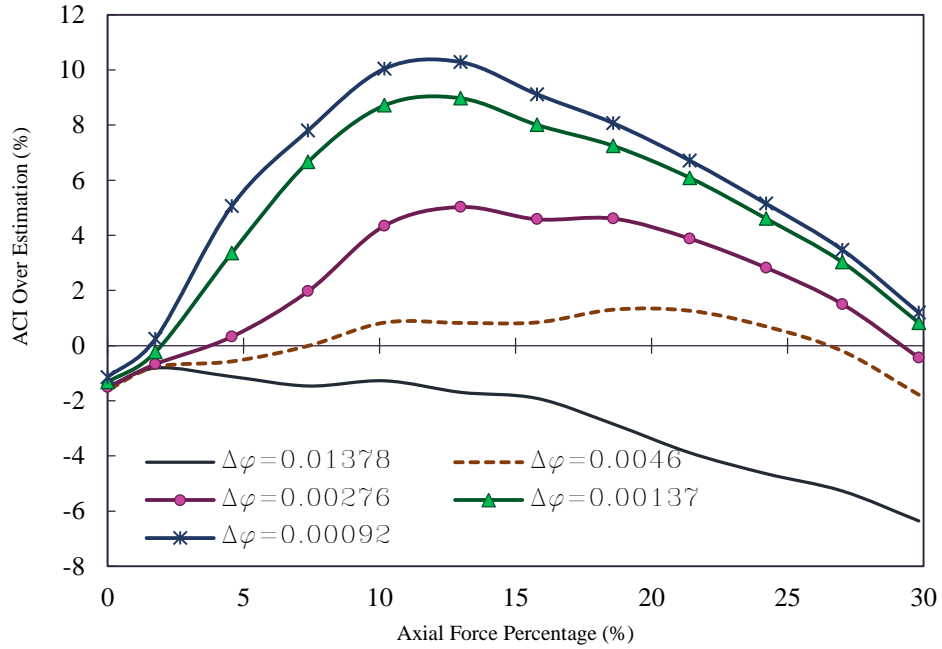


Figure 4-49 ACI bending moment overestimation of the square section with  $\rho_s = 0.89\%$

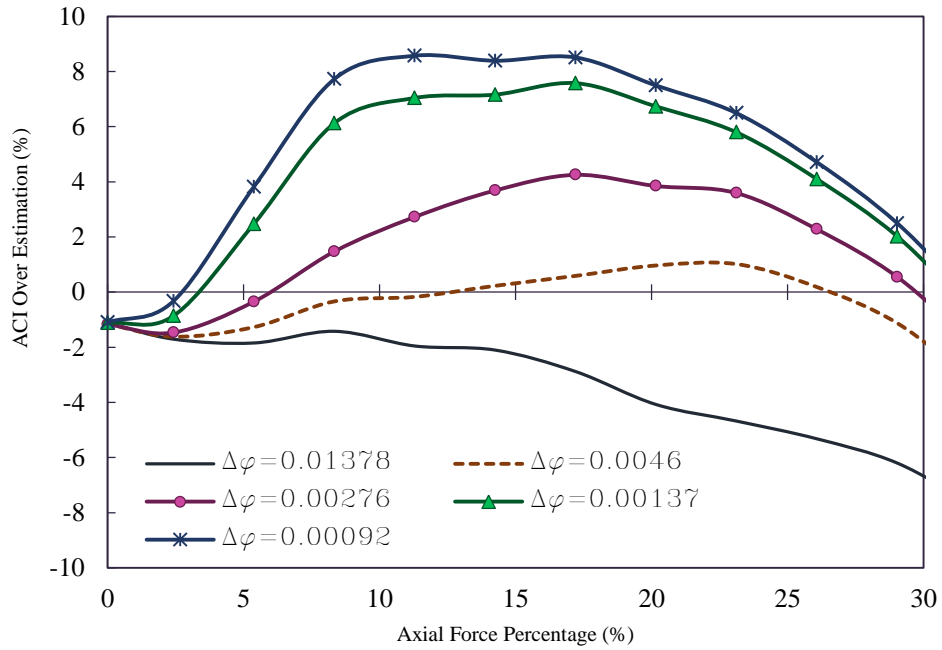


Figure 4-50 ACI bending moment overestimation of the square section with  $\rho_s = 1.58\%$

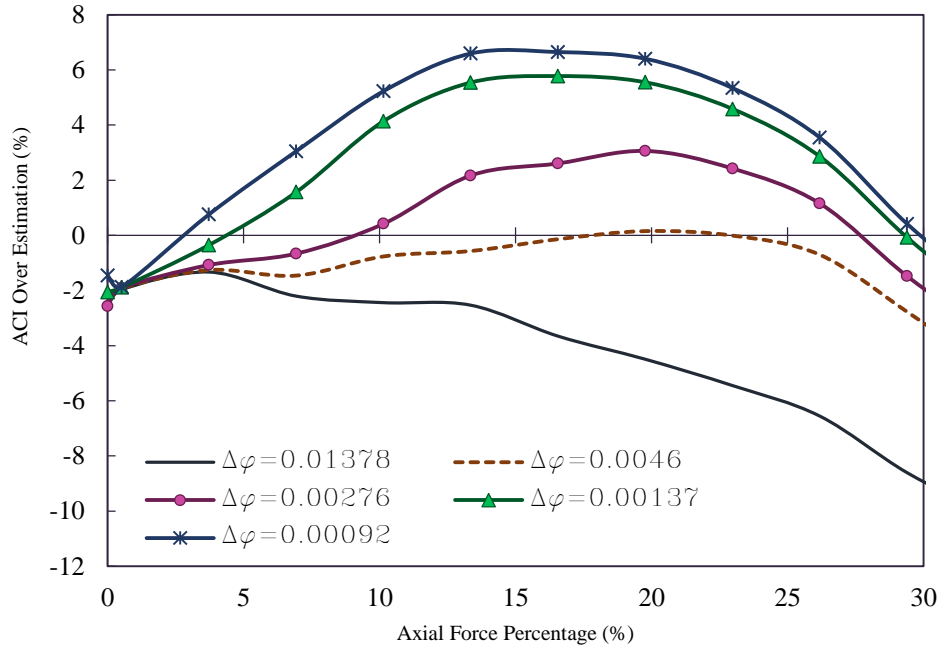


Figure 4-51 ACI bending moment overestimation of the square section with  $\rho_s = 2.47\%$

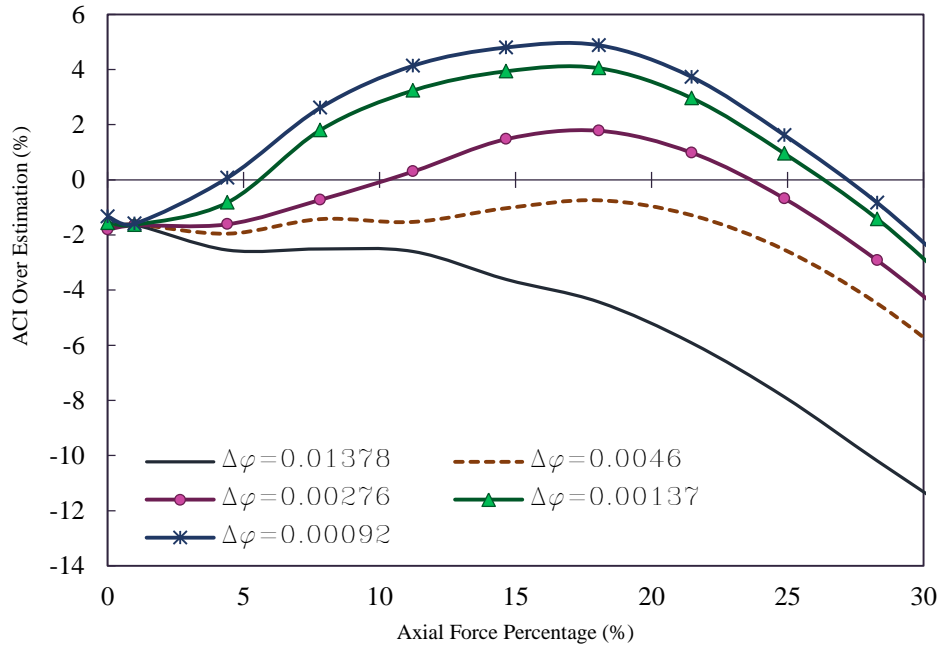


Figure 4-52 ACI bending moment overestimation of the square section with  $\rho_s = 3.56\%$

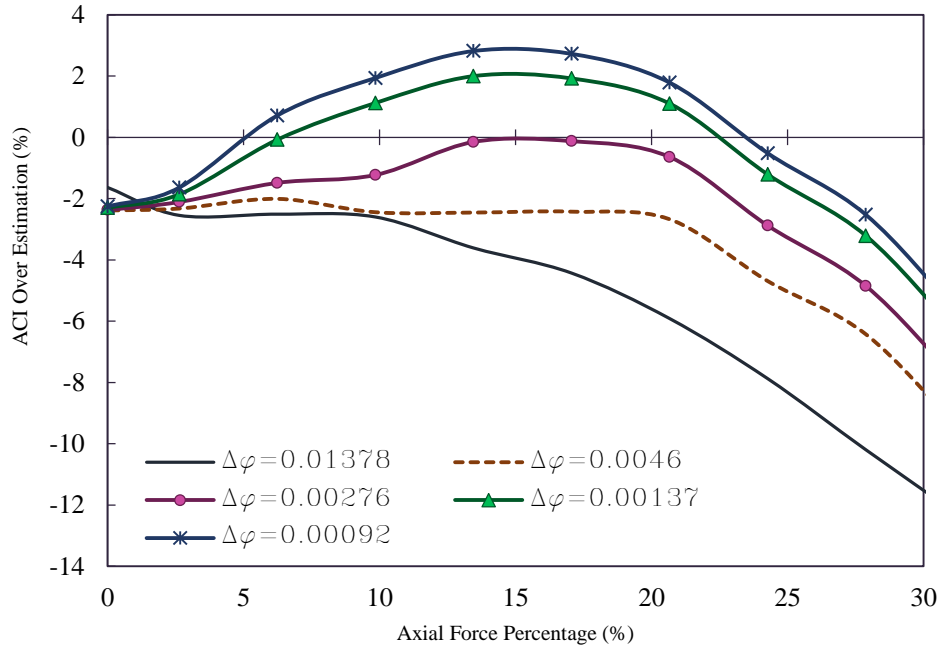


Figure 4-53 ACI bending moment overestimation of the square section with  $\rho_s = 4.85\%$

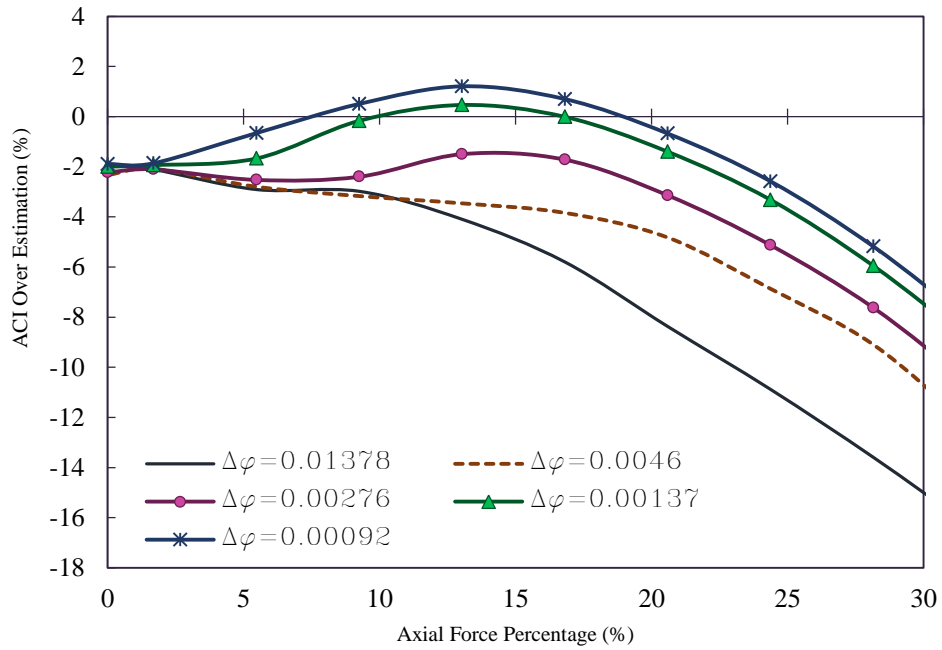


Figure 4-54 ACI bending moment overestimation of the square section with  $\rho_s = 6.33\%$

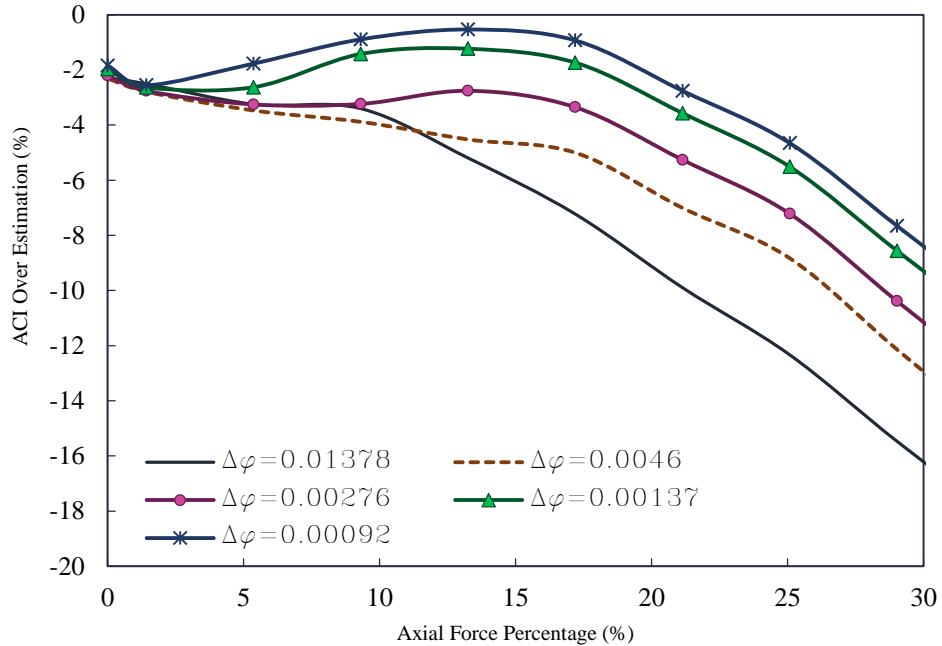


Figure 4-55 ACI bending moment overestimation of the square section with  $\rho_s = 8.05\%$

#### 4-4 Summary

Many finite and fiber element methods have been developed to predict cyclic behavior of RC columns. Most of these models have been used to investigate behavior of RC columns under uniaxial lateral force/displacement. The primary objective of this chapter was development, calibration, and validation of a nonlinear fiber-based model of RC columns to simulate the response of such columns under biaxial and uniaxial lateral forces/displacements and variable axial loading. The Mander et al. (1988) model was used as the envelope of the uniaxial stress-strain relationship of confined and unconfined concrete, and the cyclic response was considered linear. Monotonic and cyclic behavior of reinforcing steel bars were modeled using Menegotto-Pinto monotonic and cyclic models and an idealized bilinear monotonic model in conjunction with a linear cyclic model for columns under uniaxial and biaxial lateral force/displacements, respectively. The plastic hinge approach was applied to obtain force-deflection results of RC

columns. Force-deflection calculated results using Priestley and Park (1987) and Esmaily-Xiao (2002) plastic hinge models led to the closest agreement with experimental data for columns under biaxial and uniaxial lateral displacements, respectively. Accuracy of the analytical model was validated against experimental data through uniaxial moment-curvature, uniaxial force-deflection, and biaxial force-deflection analyses. Calculated results showed good agreement with experimental data.

The importance of biaxial analysis of RC columns was demonstrated through moment-curvature and force-deflection analyses using the developed analytical model. Monotonic-curvature analysis was performed for a circular column under five levels of axial force and seven curvature paths. Comparison of maximum calculated flexural strength of the circular column under various curvature paths and levels of axial force demonstrated that the flexural strength reduction ratio in x-direction increased when the axial force level increased. Force-deflection of an RC column was calculated considering five levels of axial force and three lateral displacement paths using the analytical model. The effect of axial force level was assessed on individual cycle and cumulative dissipated energy. Increased axial force level led to the increase of individual cycle and cumulative dissipated energy for the column under uniaxial lateral displacements. This trend was not demonstrated for the column under biaxial lateral displacements. The effect of axial force level on cumulative dissipated energy was more pronounced for the column under biaxial compared to uniaxial lateral displacements. In general, cumulative dissipated energy of a column under biaxial lateral displacements increases when the axial force level increases. However, cumulative dissipated energy of a column under 10% analytical axial force capacity did not follow this trend.



In order to investigate the effect of the variable axial force, a specific type of axial force-moment interaction curve was developed considering the moment-curvature analysis. The effect of number of cycles in variable axial load in specific curvature interval, and steel ratio was assessed on the realistic flexural capacity of the RC columns.

## Chapter 5 - Conclusions and Recommendations

### 5-1 Summary

The following objectives, related to the analysis, material modeling, and computer application development were achieved in this dissertation:

1. Monotonic material models, cyclic rule, and plastic hinge models were utilized in a fiber-based analytical procedure, validated against experimental data to simulate the behavior of RC columns under biaxial lateral forces/displacements and axial load.
2. The importance of considering biaxial analysis of the RC columns was demonstrated through moment-curvature and force-deflection analyses using the developed analytical model.
3. The effect of axial force level was assessed on individual cycle and cumulative dissipated energy.
4. A constitutive stress-strain model was proposed for concrete confined by FRP and conventional lateral steel reinforcement when they act simultaneously. Accuracy of the proposed model in predicting the monotonic stress-strain relationship of concrete confined by both FRP and conventional reinforcement was assessed compared to various experimental data from specimens tested under concentric monotonic load and several representative models.
5. Additionally, the moment-curvature response of two sections confined laterally by FRP and conventional lateral steel, using the proposed model in a fiber-based analysis, was compared and benchmarked against several independent experimental results.

6. A computer application was developed to analyze the nonlinear, cyclic flexural performance of RC structural members under various types of loading paths, including non-sequential variations in axial load and biaxial load or displacement.
7. Several monotonic material models and hysteresis rules were implemented in the computer application. In order to perform force-deflection analysis using proper assumptions on curvature distribution along the member, three plastic hinge models were also implemented into the program.
8. Program performance was verified against analytical results in the literature, and accuracy of the analytical process and implemented models were evaluated in comparison to experimental results.
9. The developed computer application can be used to predict the response of a member with arbitrary cross section and type of lateral and longitudinal reinforcement under various combinations of loading patterns in axial and biaxial directions. The application can also be used to examine analytical models and methods using proper experimental data.

## **5-2 Conclusion**

As discussed in the previous section, several objectives were accomplished in this dissertation. It may be concluded:

1. The material models and analytical methods have an important role in assessment of RC-sections and columns performance.

2. The load history experienced by an RC column has a significant effect on the flexural capacity. The flexural capacity of the column, assessed in Chapter 4, was decreased almost 17% when it was under 20% axial force.
3. The behavior of RC columns under biaxial loading cannot be predicted having the results of their uniaxial behavior.
4. For an RC column under uniaxial lateral loading, the individual cycle energy dissipations have an ascending trend when the level of applied axial force increases. However, for the same column under biaxial lateral displacements the same trend was not seen.
5. The realistic flexural capacity of RC-section is less than what is predicted by ACI when the column is under fluctuating axial force with the maximum less than 20% of its axial capacity. The effect of varying axial loading decreases when the section has higher steel ratio.
6. For RC-sections under high level of axial force (more than 20% of their axial capacities), fluctuating axial force was not important, since the realistic flexural capacity of the section under high level of axial force is more than the flexural capacity predicted by ACI.

### **5-3 Recommendations**

This work can be extended to address the following areas:

1. Perform dynamic analysis of columns of structures located in near fault regions to capture the effect of fluctuating axial force more accurately
2. Develop a new stress-strain model for concrete confined by both FRP and lateral conventional steel in rectangular sections

3. Develop a plastic hinge model for columns confined by FRP and both FRP and lateral conventional steel
4. Expand the software application to consider the curvature distribution along column height by considering multiple section along column height

## References

- Abrams, D. P. (1987). Influence of axial force variations on flexural behavior of reinforced concrete columns. *ACI Structural Journal*, 84 (3), 246-254.
- ACI Committee 318. Building code requirements for structural concrete (ACI 318-05) and commentary (318R-05). American Concrete Institute, 2005.
- ACI-ASCE Committee 428 (1968). Progress report on code clauses for limit design. *ACI Journal*, n.d.
- Ahmad, S. H., and Surendra P. Shah. (1982). Stress-strain curves of concrete confined by spiral reinforcement. *ACI Journal Proceedings*. 79(6). ACI.
- Alaghebandian, R., Otani, S., and Shiohara, H. (1998). Effect of distributed mass on earthquake response of reinforced concrete frames. University of Tokyo: Department of Architecture.
- Alemdar, Z. F. (2010). Plastic hinge behavior of reinforced concrete bridge columns. Ph.D. Thesis, University of Kasas.
- Attrad, M. M., Setunge, S. (1996). Stress-strain relationship of confined and unconfined concrete. *ACI Material Journal*, 93(5), 432-442.
- Bae, S., and Oguzhan B. (2008). Plastic hinge length of reinforced concrete columns. *ACI Structural Journal*, 105(3).
- Baker, A. L. L., and Amarakone, A. M. N. (1965). Inelastic hyperstatic frames analysis. *ACI Special Publication*, 12.
- Bayrak, O. S. (1998). Confinement reinforcement design consideration for ductile HSC columns. *Journal of Structural Engineering*, 124(9), 999-1010.
- Berry, M. P., Dawn E. L., and Laura N. L. (2008) Lumped-plasticity models for performance simulation of bridge columns. *ACI Structural Journal*, 105(3).
- Berthet, J. F., Ferrier, E., and Hamelin, P. (2005). Compressive behavior of concrete externally confined by composite jackets. Part A: experimental study. *Construction and Building Materials*, 19(3), 223-232.
- Benzaid, B, Mesbah H, and Nasr E. C. (2010) FRP-confined concrete cylinder: axial compression experiments and strength model. *Journal of Reinforced Plastic and Composites*, doi: 10.1177/0731684409355199.
- Binici, B. (2008) Design of FRPs in circular bridge column retrofits for ductility enhancement. *Engineering Structures*, 30(3), 766-776.

- Biskinis, D., and Fardis, M. N. (2010). Flexure- controlled ultimate deformations of members with continuous or lap- spliced bars. *Structural Concrete*, 11(2), 93-108.
- Blakeley, R. W. G., and Robert, P. (1971) Seismic resistance of prestressed concrete beam-column assemblies. *ACI Journal Proceedings*, 68(9).
- Balan, T. F. (1998). Hysteretic model of ordinary high-strength reinforcing steel. *Journal of Structural Engineering*, 124(3), 288-297.
- Berthet J. F., Ferrier, E., and Hamelin, P. (2006). Compressive behavior of concrete externally confined by composite jackets. *Construction and Building Materials*, 20, 338-347.
- Bonet, J. L., Barros, M. H. F. M., and Romero, M. L. (2006). Comparative study of analytical and numerical algorithms for designing reinforced concrete sections under biaxial bending. *Computers and Structures*, 84(31), 2184-2193.
- Candappa, D. P. (2000). The constitutive behavior of high strength concrete under lateral confinement. Monash University: Ph.D. Thesis.
- Chastre, C, Silva, M. A. G. (2010) Monotonic axial behavior and modeling of RC circular columns confined with CFRP. *Engineering Structures*, 32(8), 2268-2277.
- Chan, W. W. L. (1955). The ultimate strength and deformation of plastic hinges in reinforced concrete frame works. *Magazine of Concrete Research*, 7(21), 121-132.
- Chang, S. Y. (2010). Experimental studies of reinforced concrete bridge columns under axial load plus biaxial bending. *Journal of Structural Engineering*, 136(1), 12-25.
- Charalampakis, A. E., and Koumoussis, V. K. (2008). Ultimate strength analysis of composite sections under biaxial bending and axial load. *Advances in Engineering Software*, 39(11), 923-936.
- Cohn, M. Z., and Petcu. V. A. (1963). Moment redistribution and rotation capacity of plastic hinges in redundant reinforced concrete beams. *Indian concrete journal*, 37(8), 282-290.
- Corley, W. G. (1966) Rotational capacity of reinforced concrete beams. Portland Cement Association, Research and Development Laboratories.
- Cusson, D. and Paultre, P. (1995) Stress-strain model for confined high-strength concrete, *Journal of Structural Engineering*, 121(3), 468-477.
- Davey, B.E. (1975). Reinforced concrete bridge piers under seismic loading. Master of Engineering Report, University of Canterbury.
- Demers, M, and Neale K. W. (1999). Confinement of reinforced concrete columns with fiber-reinforced composite sheets-an experimental study. *Canadian Journal of Civil Engineering*, 26(2): 226-241.

- Dodd, L. L., and Cooke, N. (2000). Capacity of circular bridge columns subjected to base excitation. *ACI Structural Journal*, 97(2).
- Eid, R., and Paultre, P. (2008). Analytical model for FRP-confined circular reinforced concrete columns. *Journal of Composite for Costruction*, 12(5): 541-552.
- Esmaeily, A., and Xiao, Y. (2002). Seismic behavior of bridge columns subjected to various loading patterns. University of California, Berkeley, Peer Report 2002/15.
- Esmaeily, A, Xiao, Y. (2005). Behavior of reinforced concrete columns under variable axial loads: analysis. *ACI Structural Journal*, 102(5), 736-744.
- Esmaeily, A, Lucio, K. (2006). Analytical performance of reinforced concrete columns using various confinement models. *International Concrete Abstracts Portal (ACI)*, 95-110.
- Esmaeily, A, Peterman, R. J. (2007). Performance analysis tool for reinforced concrete members. *Computer and Concrete*, 4(5): 331-346.
- Esmaeily, A, and Shirmohammadi, F. (2014). Performance and capacity assessment of reinforced concrete bridge piers considering the current load and resistance factor design provisions and plastic hinge length in Kansas, No. K-TRAN: KSU-11-5.
- Fafitis, A., Shah, S. (1985). Lateral reinforcement for high strength concrete column. *ACI Special Publication*, SP 87, 213-232.
- Fossetti, M., and Papia, M. (2012). Dimensionless analysis of RC rectangular sections under axial load and biaxial bending. *Engineering Structures*, 44, 34-45.
- Ang, B. G. (1981). Ductility of reinforced concrete bridge piers under seismic loading. Master of Engineering Report, University of Canterbury.
- Ghobarah, A., and Elnashai, A. S. (1998). Contribution of vertical ground motion to the damage of RC Building. *Proceedings XI European Conference on Earthquake Engineering*.
- Gilbertsen, N. D., and Moehle, J. P. (1980). Experimental study of small-scale R/C columns subjected to axial and shear force reversals. Urbana-Champaign: University of Illinois Engineering Experiment Station. College of Engineering. University of Illinois at Urbana-Champaign.
- Gill, W. D., Park, L., and Priestley, M.J.N. (1979). Ductility of rectangular reinforced concrete columns with axial load. Research Report, Department of Civil Engineering, University of Canterbury.
- Gopinath, A., Nambiyanna, B., Nakul, R. and Prabhakara, R. (2014). Parametric study on rotation and plastic hinge formation in RC beams. *Journal of Civil Engineering Technology and Research*.



- Gu, D. S., Wu, Y. F., Wu, G., and Wu, Z. S. (2011) Plastic hinge analysis of FRP confined circular concrete columns. *Construction and Building Materials*, 27(1), 223-233.
- Hachem, M. M., Moehle, J. P., and Mahin, J. P. (2003) Performance of circular reinforced concrete bridge columns under bidirectional earthquake loading. Pacific Earthquake Research Center.
- Harajli, M. H., Hantouche, E., and Soudki, K. (2006). Stress-strain model for fiber reinforced polymer jacketed concrete columns. *ACI Structural Journal*, 103(5), 672-705.
- Heng, N. K. (1978). Seismic behaviour of circular reinforced concrete bridge piers. Master of Engineering Report, University of Canterbury.
- Ho, J. C. M., and Pam, H. J. (2003). Inelastic design of low-axially loaded high-strength reinforced concrete columns. *Engineering Structures*, 25(8), 1083-1096.
- Hognestad, E. (1951). A study of combined bending and axial load in reinforced concrete members. University of Illinois Engineering Experimental Station, Bulletin Series No. 399, 128 pp.
- Hoshikuma, K, Kawashima, K, Nagaya, K, and Taylor, A. W. (1997). Stress-strain model for confined reinforced concrete in bridge piers. *Journal of Structural Engineering (ASCE)*, 123(5), 624-633.
- Hostani, M., Kawashima, K., and Hoshikuma, J. (1988). A stress-strain model for concrete Cylinders confined by both carbon fiber sheets. *Journal of Concrete Engineering*, 39, 37-52 (In Japanese).
- Hsu, H. L., Jan, F. J., and Juang, J. K. (2009). Performance of composite members subjected to axial load and biaxial bending. *Journal of Constructional Steel Research*, 65(4), 869-878.
- Hu, H., and Seracino, R. (2013). Analytical model for FRP-and-steel-confined circular concrete columns in compression. *Journal of Composites for Construction (ASCE)*, ISSN 1090-0268/A4013012 (7).
- I.C.E. Research Committee (1962). Ultimate load design of concrete structures. Proc. I.C.E. (London), n.d.
- Imbsen, R. A. (2009). AASHTO guide specifications for LRFD seismic bridge design. AASHTO.
- Jaradat, O. A., Maclean, D. I., and Marsh, M. L. (1998). Performance of existing bridge Columns under cyclic loading-part 1: experimental results and observed behavior. *ACI Structural Journal*, 95-S63, 695-704.
- Jiang, Y., and Saiidi, M. (1990). Four spring Element for Cyclic Response of R/C Columns. *ASCE Journal of Structural Engineering*, 116(4), 1018-1029.

- Jiang, C., Wu, Y. F., and Wu, G. (2014). Plastic hinge length of FRP-confined square RC columns. *Journal of Composites for Construction*, 18(4).
- Kawashima, K., Hostani, M., and Yoneda, K. (2000). Carbon fiber sheet retrofit of reinforced concrete bridge piers. *Proceedings of the International Workshop on Annual Commemoration of Chi-Chi Earthquake, Vol. II-Technical Aspect*, National Center for Research on Earthquake Engineering, Taipei, Taiwan, 124-135.
- Kawashima, K., Hostani, M., and Yoneda, K. (2001). Carbon fiber sheet retrofit of reinforced concrete bridge piers. *Toward new generation seismic design methodology of bridges*, Tokyo Institute of Technology, Tokyo.
- Kent, D. C., and Park, R. (1971). Flexural members with confined concrete. *ASCE Journal of Structural Engineering*, 97 (ST7), 1969-1990.
- Kowalsky, M. J., Priestley, M. J. N., and Frieder, S. (1999). Shear and flexural behavior of lightweight concrete bridge columns in seismic regions. *ACI Structural Journal*, 96(1) 136-148.
- Kreger, M. E., and Linbeck, L. (1986). Behavior of reinforced concrete columns subjected to lateral and axial load reversals. *Proceeding of the Third U. S. National Conference on Earthquake Engineering*.
- Kuramoto, H. K., Kbeyasaswa, T. and Shen, F. H. (1995). Influence of axial deformation on ductility of high strength reinforced concrete columns under varying triaxial forces. *ACI Structural Journal*, 92(5), 610-618.
- Lam, L. and Teng, J. G. (2003). Design-oriented stress-strain model for FRP-confined concrete. *Construction and Building Materials*, 17(6-7), 471-489.
- Lee, D. H., Choi, E., and Zi, G. (2005). Evaluation of earthquake deformation and performance for RC bridge. *Engineering Structures*, 27(10), 1451-1464.
- Lee, J. Y., Yi, C. K., Jeong, H. S., Kim, S. W., and Kim, J. K. (2009). Compressive response of concrete confined with steel spirals and FRP composites. *Journal of Composite Materials*, 44(4): 1-24.
- Légeron, F., and Paultre, P. (2003). Uniaxial confinement model for normal- and high-strength concrete columns. *Journal of Structural Engineering*, 129(2), 241–252.
- Liang, Q. Q. (2008). Nonlinear analysis of short concrete-filled steel tubular beam–columns under axial load and biaxial bending. *Journal of Constructional Steel Research*, 64(3), 295-304.
- Liang Q. Q. (2009). Strength and ductility of high strength concrete-filled steel tubular beam-columns. *Journal of Constructional Steel Research*, 65(3), 687-698.

- Lokuge, W. P., Sanjayan, J. G. and Sujeeva S. (2005). Stress–strain model for laterally confined concrete. *Journal of Materials in Civil Engineering*, 17(6), 607-616.
- Lokuge, W. P., Setinge, S., Sanjayan, J. G. (2011). Stress-strain model for high strength concrete confined by FRP. *Incorporating Sustainable Practice in Mechanics of Structures and Materials* (pp. 481-486). London: Taylor and Francis Group.
- Mander, J. B., Priestley, M. J. N., and Park, R., (1984). Seismic design of bridge piers. Research Report No. 84-2, University of Canterbury, New Zealand.
- Mander, J. B., Priestley, M. J., and Park, R. (1988). Theoretical stress-strain model for confined concrete. *Journal of Structural Engineering*, 114(8), 1804-1826.
- Mattock, A. H. (1965). Rotational capacity of hinging regions in reinforced concrete beams. *Flexural Mechanics of Reinforced Concrete, Proceedings*.
- Mendis, P. A. (1986). Softening of reinforced concrete structures. Ph.D. Dissertation, Monash University.
- Mendis, P. (2001). Plastic hinge lengths of normal and high-strength concrete in flexure. *Advances in Structural Engineering*, 4(4), 189-195.
- Menegotto, M, and Pinto, P. (1973). Method of analysis for cyclically loaded reinforced concrete plane frames including changes in geometry and non-elastic behavior of elements under combined normal force and bending. *Proceedings of IABSE Symposium on Resistance and Ultimate Deformability of Structures Acted on by Well Defined Repeated Loads, International Association for Bridge and Structural Engineering, Zurich, Switzerland*, 12-15.
- Mortezaei, A., and Ronagh, H. R. (2012). Plastic hinge length of FRP strengthened reinforced concrete columns subjected to both far-fault and near-fault ground motions. *Scientia Iranica*, 19(6), 1365-1378.
- Mortezaei, A. (2014). Plastic hinge length of RC columns under the combined effect of near-fault vertical and horizontal ground motions. *Civil Engineering*, 58(3), 243-253.
- Munro, I. R. M. (1975). Seismic behaviour of reinforced concrete bridge piers. Master of Engineering Report, University of Canterbury.
- Ono, K., and Kasai, H., and Sasagawa, M. (1996). Up-down vibration effects on bridge piers. *Special Issue of Soil and Foundation, Japanese Geotechnical Society*, 211-218.
- Ottosen, N. S. (1979), Constitutive model for short-time loading of concrete, *Journal of the Engineering Mechanics Division ASCE*, 105(1): 127-141.
- Ozbakkaloglu, T., Lim, J. C., and Vicent, T. (2013). FRP-confined concrete in circular sections: review and assessment of stress-strain models. *Engineering Structures*, 49, 1068-1088.

- Papazoglou, A. J., and Elnashai, A. S. (1996). Analytical and field evidence of the damaging effect of vertical earthquake ground motion. *Earthquake Engineering and Structural Dynamics*, 25(10), 740-757.
- Pallarés, L., Senach, J. B. L., Sosa, P. F. M., and Prada, M. A. F. (2009). The influence of the weak axis on the behavior of high strength RC slender columns subjected to biaxial bending. *Engineering Structures*, 31(2), 487-497.
- Panagiotakos, T. B., and Fardis, M. N. (2001) Deformations of reinforced concrete members at yielding and ultimate. *ACI Structural Journal*, 98(2), 2001.
- Park R., and Paulay, T. (1975). *Reinforced Concrete Structures*. John Wiley and Sons, Inc.
- Park, R., and Kevin, J. T. (1977). Cyclic load tests on prestressed and partially prestressed beam-column joints. *Journal-Prestressed Concrete Institute*.
- Park, R., and Priestley, M. J. N. (1987). Strength and ductility of concrete bridge columns under seismic loading. *ACI Structural Journal*, 84(1), 61-76.
- Paulay, T., and Priestley, M J. N. (1992). *Seismic design of reinforced concrete and masonry buildings*. John Wiley and Sons Inc.
- Park, R., Kent, D. C., and Sampson, R. A. (1972). Reinforced concrete memebres with cyclic loading. *ASCE Journal of Structural Engineering*, 98 (ST7), 1341-1360.
- Pellegrino, C., and Modena, C. (2010). Analytical model for FRP confinement of concrete columns with and without internal steel reinforcement. *Journal of Composites for Construction*, 14(6), 693-705.
- Phan, V., Saiidi, M. S., Anderson, J., and Ghasemi, H. (2007). Near-fault ground motion effects on reinforced concrete bridge columns. *Journal of Structural Engineering*, 133(7), 982-989.
- Popovics, S. (1973). Numerical approach to the complete stress-strain relation for concrete. *cement and concrete research*, 3(5), 583-599.
- Potangaroa, R.T., Priestley, M. J. N. and Park, R. (1979). Ductility of spirally reinforced concrete columns under seismic loading. *Research Report*, Department of Civil Engineering, University of Canterbury.
- Press, W. H., Flannery, B. P., Teukolsky, S. A., and Vetterling, W. T. (1990). *Numerical recipes in C: the art of science computing*, Cambridge University Press, Cambridge, England.
- Priestley, N., Seible, F., and Calvi, G. (1996). *Seismic design and retrofit of bridges*. John Wiley and Sons Inc.
- Priestley, W. J. N., and Park, R. (1987). Strength and ductility of concrete bridge columns under seismic loading. *ACI Structural Journal*, 84(1).

- Progress report on code clauses for limit design. 428, ACE-ASCE Committee-ACI journal, 1968.
- Qinghua, A. I., Wang, D., LI H., and Zhiguo, S. (2008). Evaluation of the seismic performance of reinforced concrete bridge columns based on plastic hinge model. The 14th World Conference on Earthquake Engineering, Beijing, China, 2008.
- Qiu, F., Li, W., Pan, P., and Qian, J. (2002). Experimental tests on reinforced concrete columns under biaxial quasi-static loading. *Engineering Structures*, 24(4), 419-428.
- Ramberg, W., and Osgood, W. R. (1943). Description of stress-strain curves by three parameters. Technical Note No. 902, National Advisory Committee for Aeronautics. Washington D.C.
- Ranzo, G., Petrangely, M., and Pinto, P. E. (1999). Vertical oscillations due to axial-bending coupling during seismic response of RC bridge piers. *Journal of Earthquake Engineering and Structural Dynamics*, 28, 1685-1704.
- Richard, R. M. and Abbott, B. J. (1975). Versatile elastic-plastic stress-strain formula. *Journal of Engineering and Mechanics*, 101 (4), 511-515.
- Richart, F. E., Brandtzaeg, A., and Brown, R. L. (1928). A study of the failure of concrete under combined compressive stresses. University of Illinois Engineering Experimental Station, Bulletin No. 185, 104 pp.
- Riva, P., and Cohn, M. Z. (1990). Engineering approach to nonlinear analysis of concrete structures. *Journal of Structural Engineering*, 116(8), 2162-2186.
- Rodrigues, H., Romao, X., Andrade-Campos, A., Varum, H., Arede, A., and Costa, A. G. (2012). Simplified hysteretic model for the representation of the biaxial bending response of RC columns. *Engineering Structures*, 44, 146-158
- Rodrigues, H., Arede, A., Varum, H., and Costa, A. G. (2012). Experimental evaluation of rectangular reinforced concrete column behavior under biaxial cyclic loading. *Earthquake Engineering and Structural Dynamics*, 42(2), 239-259.
- Rodrigues, H., Varum, H., Arede, A., and Costa, A. (2012). A comparative analysis of energy dissipation and equivalent viscous damping of RC columns subjected to uniaxial and biaxial loading. *Engineering Structures*, 35, 149-164.
- Rodrigues, H., Varum, H., Arede, A., Costa, A. G. (2013). Behavior of reinforced concrete columns under biaxial cyclic loading-state of the art. *International Journal of Advanced Structural Engineering*, 5(4), doi: 10.1186/2008-6695-5-4.
- Rodrigues, H., Arede, A., Varum, H., and Costa, A. G. (2013). Experimental evaluation of rectangular concrete column behavior under biaxial cyclic loading. *Journal of Earthquake Engineering and Structural Dynamics*, 42(2), 239-259.

- Saadeghvaziri, M. A., and Foutch, D. A. (1991). Dynamic behavior of R/C highway bridges under the combined effect of vertical and horizontal earthquake motions. *Journal of Earthquake Engineering and Structural Dynamics*, 20, 535-549.
- Saadeghvaziri, M. A. (1996). Nonlinear response and modeling of RC columns subjected to varying axial load. New Jersey Institute of Technology: Department of Civil Engineering.
- Saatcioglu, M., Derecho A. T., and Corley W. G. (1983). Modelling hysteretic behavior of coupled wall for dynamic analysis. *Earthquake Engineering and Structural Dynamics*, 11(5) 711-726.
- Saatcioglu, M., and Razavi, S. (1992). Strength and ductility of confined Concrete, *ASCE Journal of Structural Engineering*, 118 (6), 1590-1607.
- Sakino, K., and Sun, Y. P. (1993). What do we know about confinement in reinforced concrete columns? a critical review of previous works and code provisions. *ACI Structural Journal*, 86 (2), 192-207.
- Samaan, M., Mirmiran, A. and Shahawy, M. (1998), Model of concrete confined by fiber composites, *Journal of Structural Engineering*, 124 (9), 1025-1031.
- Sargin, M. (1971). Stress-strain relationship for concrete and the analysis of structural concrete section. Ph.D. Dissertation, University of Waterloo, Waterloo, Ont., Canada.
- Sawyer, H. A. (1964). Design of concrete frames for two failure states. *Proceeding Symposium on the Flexural Mechanics of Reinforced Concrete*. ASCE- ACI.
- Sfakianakis, M. G. (2002). Biaxial bending with axial force of reinforced, composite and repaired concrete section of arbitrary shape by fiber model and computer graphics. *Advances in Engineering Software*, 33(4) , 227-242.
- Shao, Y., Zhu, Z., and Mirmiran, A. (2006). Cyclic modeling of FRP-confined concrete with improved ductility. *Cement and Concrete Composites*, 28(10), 959-968.
- Shao, Y., Aval, S., and Mirmiran, A. (2005). Fiber-element model for cyclic analysis of concrete-filled fiber reinforced polymer tubes. *Journal of Structural Engineering*, 131(2), 292-303.
- Sheikh, S. A., and Shafik S. K. (1993). Confined concrete columns with stubs. *ACI Structural Journal*, 90(4).
- Sheikh, S. A., and Uzumeri, S. M. (1982). Analytical model for concrete confinement in tied columns. *Journal of the Structural Division*, 108(12), 2703-2722.
- Shirmohammadi, F., Esmaily, A., and Kiaeipour, Z. (2015). Stress-strain model for circular concrete columns confined by FRP and conventional lateral steel. *Engineering Structures*, 84, 395-405.

- Shirmohammadi, F., and Esmaeily, A. (2015). Performance of reinforced concrete columns under bi-axial lateral force/displacement and axial load. *Engineering Structures*, 99, 63-77.
- Tamuzs, V., Tepfers, R., Zile, E., and Ladnova, O. (2006). Behavior of concrete cylinders confined by a carbon composite III: deformability and ultimate axial strain. *Mechanics of Composite Materials*, 42(4), 303-314.
- Tanaka, H. (1990). Effect of lateral confining reinforcement on the ductile behaviour of reinforced concrete columns. University of Canterbury.
- Thompson, K. J., and Park, R. (1980). Ductility of prestressed and partially prestressed concrete beam sections. *PCI Journal*, 25(2), 47-69.
- Thorenfeldt, E., Tomaszewicz, A., and Jensen, J. J. (1987). Mechanical properties of high-strength concrete and application in design. *Proceedings of the Symposium on Utilization of High Strength Concrete*, Tapir, Trondheim, Norway, 149-159.
- Teng, J. G., Jiang, T., Lam, L., and Luo, Y. Z. (2009). Refinement of a design-oriented stress-strain model for FRP-confined concrete. *Journal of Composites for Construction*, 13(4), 269-278.
- Teng, J. G. (2009). Refinement of a design-oriented stress-strain model for FRP confined concrete. *Journal of Composites for Construction ASCE*, 13(4), 269-278.
- Varma, R. K., Barros, J. J., and Sena-Cruz, J. M. (2009). Numerical model for CFRP confined concrete elements subject to monotonic and cyclic loadings. *Composites: Part B*, 40, 766-775.
- Wang, D., Li, H. N., and Li, G. (2013). Experimental tests on reinforced concrete columns under multi-dimensional dynamic loadings. *Construction and Building Materials*, 47, 1167-1181.
- Wei, Y. Y., and Wu, Y. F. (2012). Unified stress-strain model of concrete for FRP-confined columns. *Construction and Building Materials*, 26(1), 381-392.
- Wu, Y. F., and Wei, Y. Y. (2010). Effect of cross-sectional aspect ratio on the strength of CFRP-confined rectangular concrete columns. *Engineering Structures*, 32(1), 32-45.
- Xiao, Y., and Wu, H. (2003). Compressive behavior of concrete confined by various types of FRP composite jackets. *Journal of Reinforced Plastics and Composites*, 22(13), 1187-1201.
- Youssef, M. N., Feng, M. Q. and Mosallam, A. S. (2007). Stress-strain model for concrete confined by FRP composites. *Composites: Part B*, 38(5-6), 614-628.
- Zahn, F. A. (1985). Design of reinforced concrete bridge columns for strength and ductility. University of Canterbury.

Zhao, X., Wu, Y. F., Leung, A. Y., and Lam, H. F. (2011). Plastic hinge length in reinforced concrete flexural members. *Procedia Engineering*, 14, 1266-1274.



## **Appendix A - Developed Computer Application Help File**

### **Introduction**

As mentioned in Chapter 3, the computer program described in this study is the next generation of the KSU-RC program with additional functionality and options. This appendix provides an instruction to use the computer program.

### **Description of Buttons**

#### ***File Dropdown Button***

##### **Open**

User can open a saved project using this option. The project which was saved in binary format is retrieved clicking on “Open”.

##### **Save**

Using “Save”, the project is saved in the existing project address that user entered when the project was saved for the first time. If user has not “Save As” the project, “Save” does the same as “Save As”.


##### **Save As**

Using “Save As”, the defined project can be saved in binary format. When the RC-Section, monotonic and cyclic material models and Material properties are defined this button is activated. In binary file, first RC-Section properties, then material properties, then monotonic

models and at the end cyclic models are serialized. The address of project will be saved in the program. In case that user uses “Save” button, the whole project is saved in the existing address.

### ***RC-Section Button***

#### **RC-Section Type**

The geometrical properties of a section can be specified in RC-Section window. This window can be called by clicking on RC-Section button . Seven options are currently available for cross-sectional geometry of an RC section:

- Rectangular Section
- Hollow Rectangular Section
- Circular Section
- Hollow Circular Section
- Caltrans Section (Oval Section)
- T-Shape Section
- I-Shape Section

#### **Transverse Reinforcement Type**

Based on the cross section’s shape, the type of lateral reinforcement can be selected using the Transverse reinforcement drop down button. For example for circular and hollow circular sections, the type of lateral reinforcement can be one of the following types:

- Tie
- Spiral


- FRP
- FRP and Tie
- FRP and Spiral

Selecting the transverse reinforcement type, the steel reinforcement or FRP reinforcement or both of them are activated. In FRP reinforcement group box user can specify the thickness of FRP and specify if the FRP works in “Only Transverse Direction” which means it has stiffness in hoop direction and FRP is used only for confining the concrete or “In Transverse and Longitudinal Direction” which means FRP has the confinement effect for concrete as well as stiffness in longitudinal direction same as steel longitudinal bars.


### **Longitudinal Reinforcement**

The steel bars numbers and size are defined in this group box. If the “Evenly Distributed” option is selected in Bar Arrangement dropdown button, the program will arrange the location of bars automatically. Otherwise, the user should specify the size and location of bars individually by clicking on the cross section on the main window.

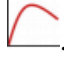
### ***Delete RC-Section***

Using the Delete Section button  the defined RC-Section and generated mesh are deleted.

## ***Material Properties***

Mechanical properties of materials, including concrete, steel in longitudinal and lateral directions, FRP wraps, and FRP longitudinal bars, are provided in the computer application. Concrete strength, as measured in the lab or desired for analysis, must be provided. For steel material, yield strength and modulus of elasticity are provided as basic mechanical properties, assuming symmetric behavior for steel in tension and compression. Because behavior of FRP wraps in tension and compressive directions may not be similar in general, tensile and compressive strength and modulus of elasticity of FRP wraps must be individually provided. The material properties window can be called by clicking the Material Properties button .


## ***Monotonic Models***

A number of widely-used existing material models were implemented in the computer application in order to model uniaxial monotonic behavior of fibers with various materials. These models can be accessed using the Monotonic Models button . Here are the monotonic material models implemented in the software for each material:

- Plain concrete: Mander et al. model (1988) for normal strength concrete, and Cussan and Paultre model (1995) for high strength concrete
- Concrete confined by lateral steel (tie/spiral): Mander et al. model (1988) for normal strength concrete, and Cussan and Paultre model (1995) for high strength concrete,
- Concrete confined by FRP: Youssef et al. model (2007) and Samaan et al. model (1998),
- Concrete confined by FRP and lateral steel: Shirmohammadi et al. model (2015), Lee et al. model (2009) and Kawashima et al. model (2000),

- Reinforcing steel: elastic-perfectly plastic model, Esmaeily and Xiao model (2005), Menegotto-Pinto model (1973), bilinear model, three-linear model, quadric-linear model, and Mander et al. model (1984),
- Reinforcing FRP: bilinear model

### ***Cyclic Models***

Various cyclic models were implemented in the computer application to model cyclic behavior of materials in a composite section. These models can be accessed by clicking on Cyclic Models button . Here are the cyclic rules implemented in the software for each material:

- Plain and confined concrete: linear model and Esmaeily and Xiao model (2005)
- Reinforcing steel: linear model, Menegotto-Pinto model (1973), and Esmaeily-Xiao model (1983)
- Reinforcing FRP: linear model

### ***Test Cyclic Models***

To test if the cyclic and monotonic material models work well, the user can use “Test Cyclic Models” dropdown button. Moving the mouse to the right and left, the strain is calculated based on the location of the mouse. Using the selected cyclic and material models and having strain calculated from the location of mouse, the stress is calculated. In each strain the stress is shown in the textbox below left of the window. To restart the form, user may use the “Restart”

button. In that case, the form will be cleaned and user can test the models again by moving the mouse to the left and right. To save the drawn cyclic path, user may use the “Save” button.

### ***Interaction analysis***

Four types of axial force-bending moment interaction curves can be conducted by the software: (1) ACI interaction curve, (2) Actual interaction curve considering strain at extreme fiber, (3) actual interaction curve considering moment-curvature analysis and constant axial force, and (4) actual interaction curve considering moment-curvature analysis and axial loading pattern. All four types of analysis are explained in detail in Chapter 4. In the last type of interaction curve, the axial loading pattern should be interred as a text file. To avoid any error while reading data from the text file, the following format should be followed. The loading patch should include three columns of data. First column is axial force coefficient which is between 0 and 1. Second column is curvature along x-axis and third column in curvature along y-axis. The axial force coefficient ( $ac$ ) for any combination of x- and y- curvature cannot exceed 1.0, meaning that the maximum compressive axial force ( $ac \times P$ ) in that pattern is equal to the specified level of axial force ( $P$ ). The axial force coefficient may consider more than -0.1, meaning that the maximum tensile axial force capacity of the section should not be considered more than  $0.1 \times P$ . We recommend creating those columns in Excel and copy-past data in a text file. Please do note copy any empty cell from Excel. Here is an example of text file arrangement:

$ac_1 \ \varphi_{x,1} \ \varphi_{y,1}$

$ac_2 \ \varphi_{x,2} \ \varphi_{y,2}$

⋮

$ac_n \ \varphi_{x,n} \ \varphi_{y,n}$




### ***Moment-curvature analysis***

Two types of moment-curvature analyses can be conducted: (1) moment-curvature analysis based on ACI, and (2) moment-curvature analysis considering material models. The second type can be conducted having the curvature path.

### ***Force-deflection analysis***

As explained in Chapter 3, in fiber-based method, the plastic hinge models are used to predict the curvature distribution along column height. Three plastic hinge models have been implemented in the software: (1) Esmaily and Xiao first model, (2) Esmaily and Xiao second model, and (3) Park and Priestley model.

### ***Mesh***

Before any analysis, the section should be divided to a number of fibers. The new version of our software uses triangular cross section fibers. To do the mesh the first button of meshing  can be used. To refine the mesh and create a finer mesh, use may use the second button in the mesh section buttons (Refine Mesh) . To delete the mesh for any reason, the third button (Delete Mesh)  can be used. The mesh setting may control in Option window.

### ***Option***

The general setting of the software can be defined in Options window. The Options window has four tabs: Units, Data Points, Analysis Setting, and Mesh Setting. In Units tab, the

unit system of the project can be defined. If a section is defined, the unit system of a project cannot be changed. To change the unit system, the defined RC-section should be deleted and then the Units tab will be activated. The Options window with the Units tab as the active tab is shown in Figure A-1.

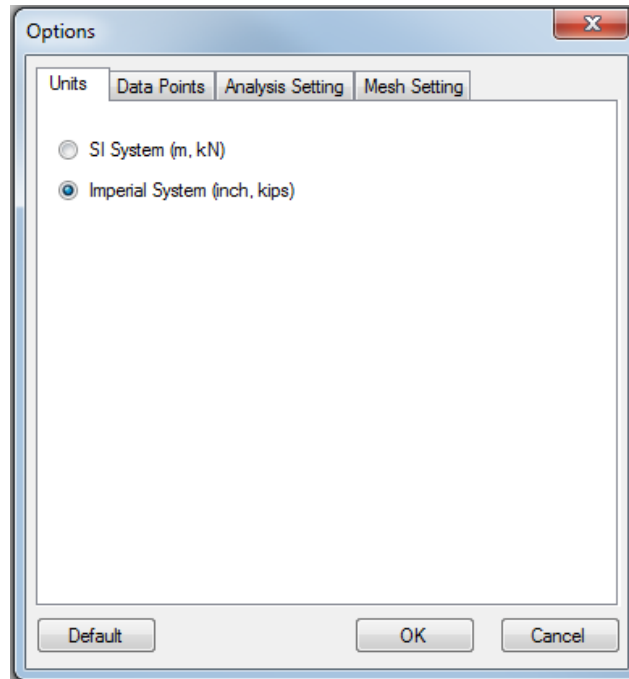


Figure A-1 Units tab in Options widow

The number of data points in each analysis can be defined using the “number of points” in the second tab of Options window. The number of points is the number of pair points in each analysis graph. Increasing the “number of points” increases the analysis time since larger number of pair points should be calculated for each type of analysis.

The analysis setting may define in “Analysis Setting” tab, the third tab of Options window. Three types of end conditions are defined in the software. The first end condition is when the moment falls below the specific percentage of the maximum moment. The second one



is when the strain at one of the concrete fibers reaches a specific value or the ultimate compressive strain. The third condition is when the steel strain reaches a specific value of the ultimate tensile/compressive strain.

At the fourth and last tab of Options window, the mesh setting can be defined. There are two parameters to control the seed setting and three parameters to control triangular mesh setting. In Sees Setting group box, the first parameter is the number of seeds around each longitudinal reinforcement bar.

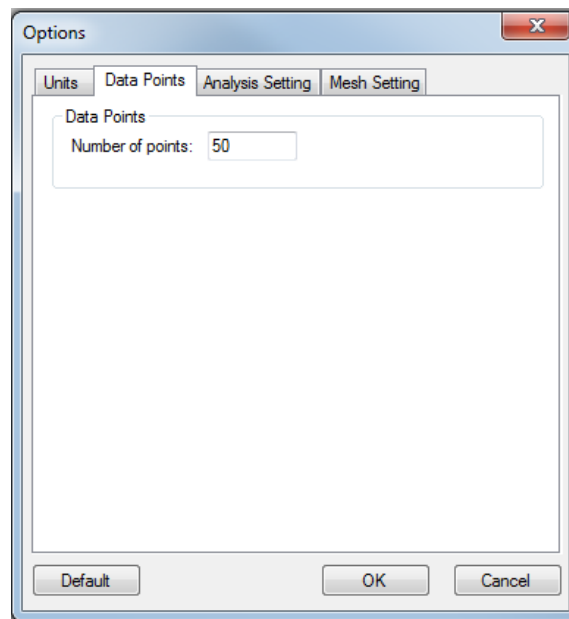


Figure A-2 Data Points tab in Options window

To avoid any inaccuracy, the number of seeds around the longitudinal bars should be more than 4. The number of seeds in each length may vary based on the geometrical properties of the section.

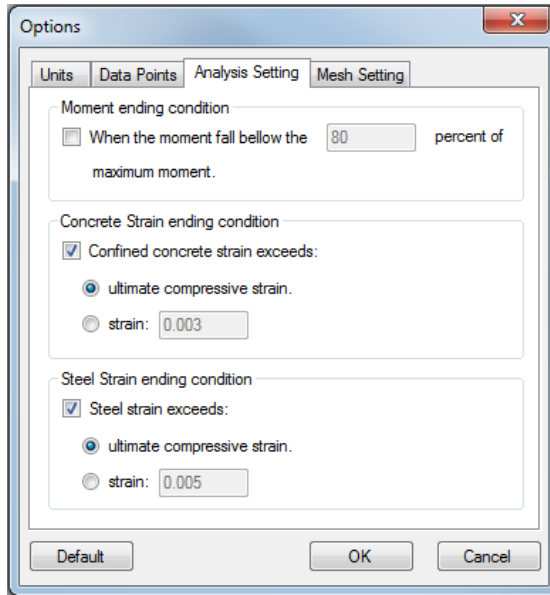


Figure A-3 Analysis setting tab in Options window

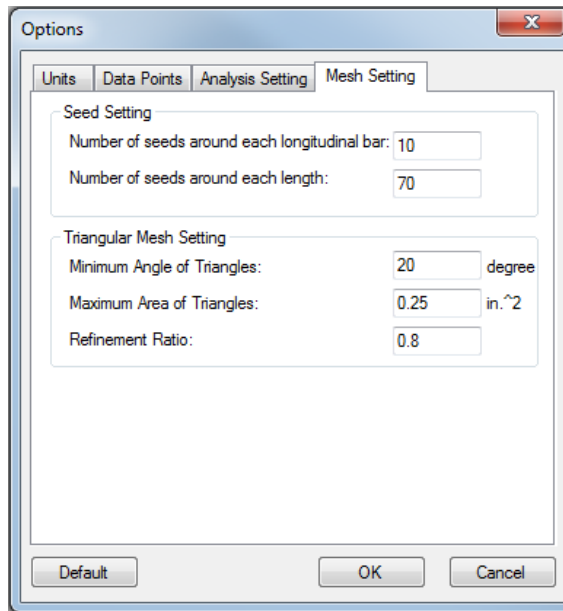


Figure A-4 Mesh setting tab in Options window

To set the triangular meshing, there are three parameters. The first parameter specifies the minimum angle of triangles. The second parameter is the maximum area of each triangle. And

the last one is the refinement ratio. When user clicks on “Refine Mesh” buttons, the Maximum are of triangles will decreases with the refinement ratio.

## Examples

### *Axial force-bending moment interaction analysis*

To conduct an axial force-bending moment interaction analysis following steps should be followed:

1. Defining RC-section geometrical and reinforcement properties: the section-type, geometrical properties, longitudinal reinforcement and lateral reinforcement should be defined as the first step. A sample window of RC-section properties is shown in Figure A-5

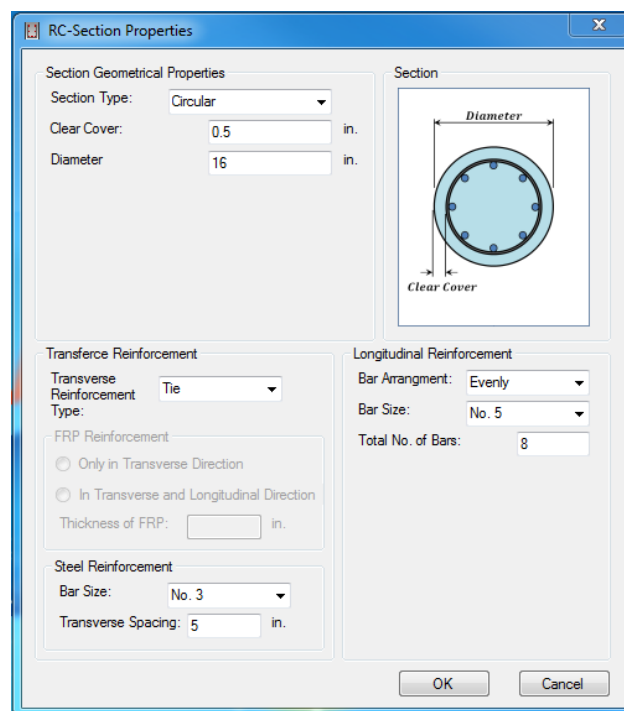


Figure A-5 A sample window of RC-Section

2. Defining mechanical properties of material: the basic mechanical properties of concrete, steel and FRP (if section is wrapped with FRP) should be defined as the second step. A sample window of basic material properties is shown in Figure A-6.

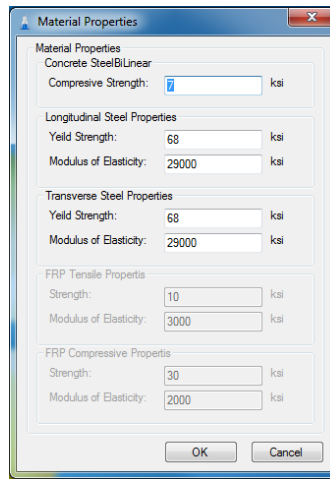


Figure A-6 A sample window of material properties

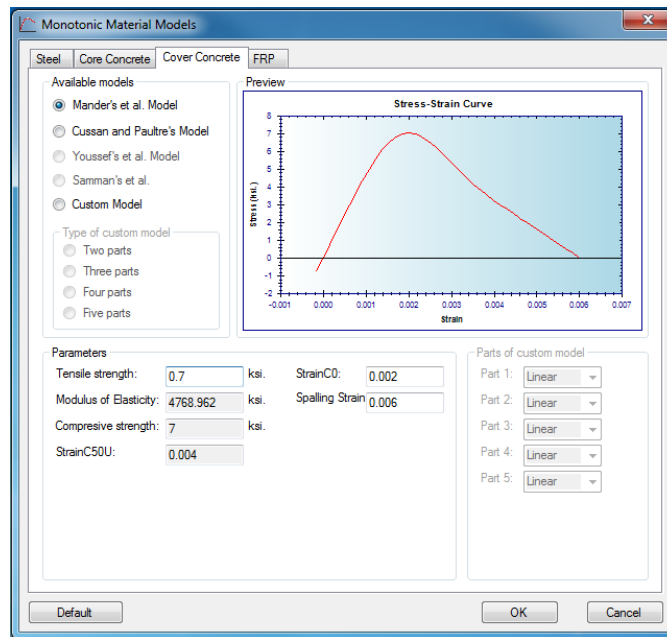


Figure A-7 A sample window of monotonic material models

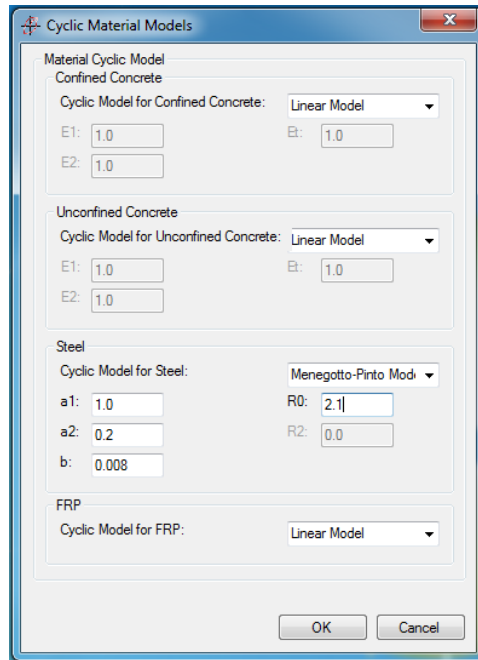


Figure A-8 A sample window of cyclic material models

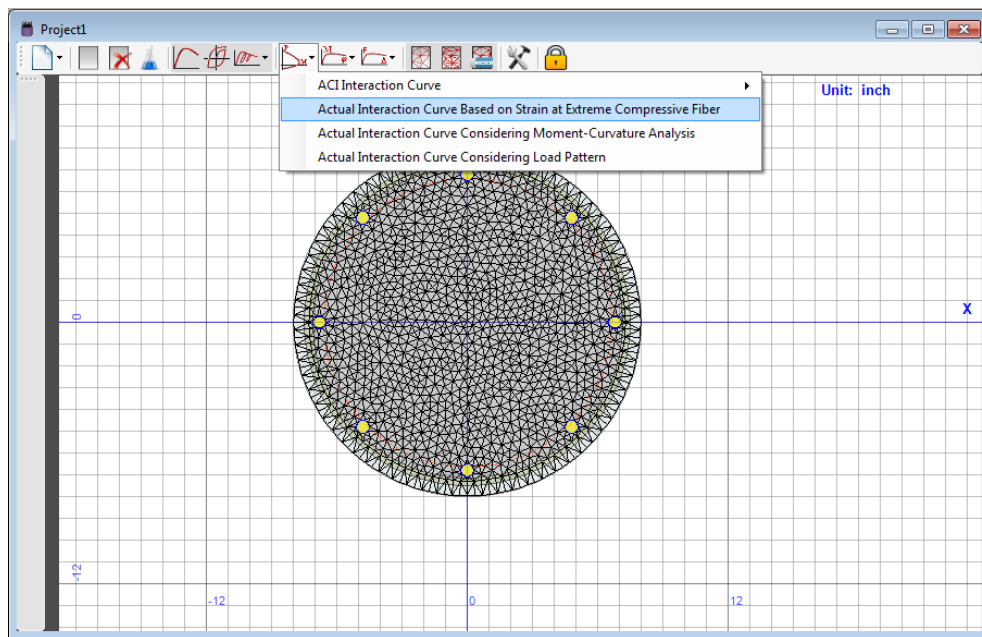


Figure A-9 A sample window of project choosing axial force-bending moment interaction

3. Defining monotonic behavior of materials: as the third step, the monotonic behavior of plain concrete, confined concrete, steel and FRP should. Figure A-7 shows a sample window of monotonic material models.
4. Defining cyclic behavior of materials: the cyclic behavior of materials is defined in step 4. A sample window of cyclic material models is shown in Figure A-8.
5. Meshing the RC-section: by clicking on the mesh button the RC-section is meshed. User may refine the mesh using the “Refine Mesh” button.
6. Conducting axial force-bending moment interaction analysis: defining RC-section, material mechanical properties, monotonic and cyclic behavior of materials and meshing the section, the program is ready to do any main three types of analyses. Here, the second type of axial force-bending moment interaction analysis was chosen to conduct. Clicking on “Interaction Analysis”; dropdown button and choosing “Actual Interaction Curve Based on Strain at Extreme Compressive Fiber”, axial force-bending moment interaction analysis window shown in, pops up. The strain at extreme fiber and analysis axis are needed to be defined by user. Clicking on “OK” button, the analysis is done and the window of results will come up.

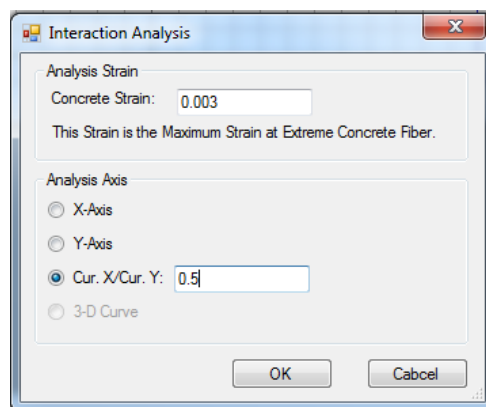


Figure A-10 A sample window of axial force-bending moment interaction analysis

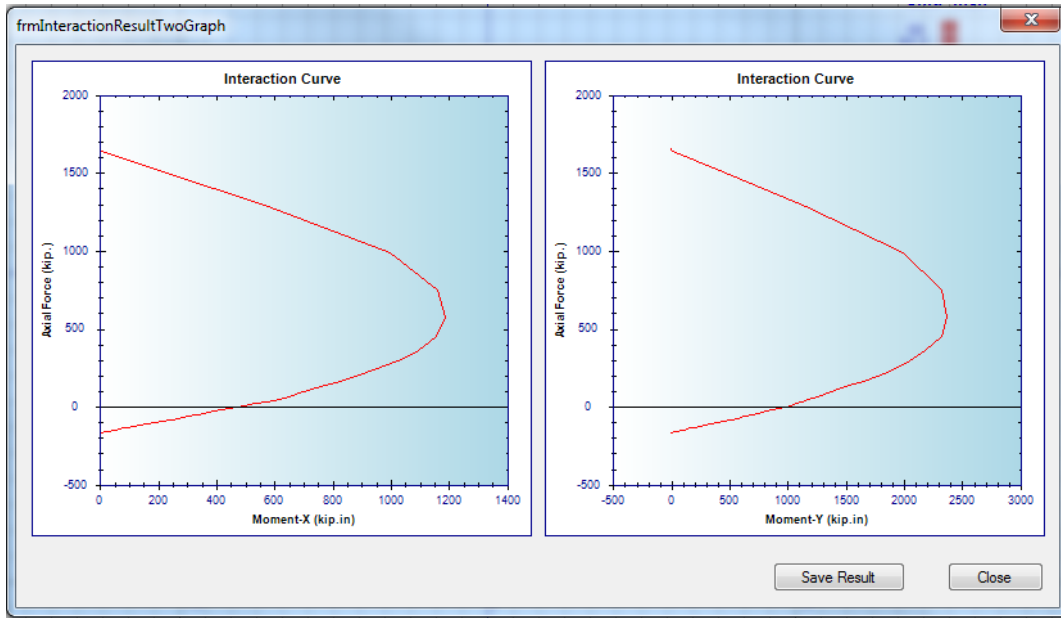


Figure A-11 A sample window of axial force-bending moment interaction analysis results

To save the data in a text file, user may click on “Save Result” button on axial force-bending moment interaction analysis result shown in Figure A-11.

### ***Moment-curvature analysis***

Since the RC-section, material mechanical properties, monotonic and cyclic behavior of materials have been defined and meshing the section has been done, the program is ready to do any main three types of analyses. To conduct a moment-curvature analysis, the user may click on “Moment-Curvature” dropdown button. In this example, the second type of moment-curvature analysis is conducted which considered the monotonic and cyclic behavior of the materials as shown in Figure A-12. By clicking on “Actual Moment-Curvature Analysis” a window will come up which is shown in Figure A-13. The axial force value and axis of analysis are entered by the user. In this example, axial force level is 100 kips and the analysis axis is Y-axis.

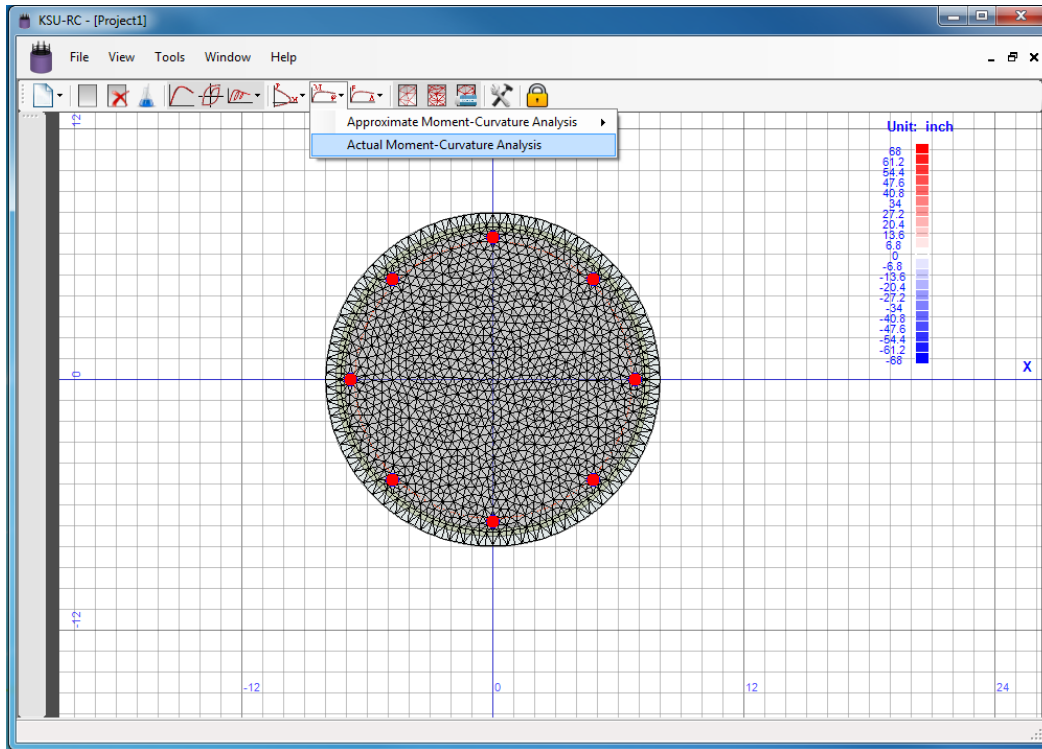


Figure A-12 A sample window of project choosing the second type of moment-curvature analysis

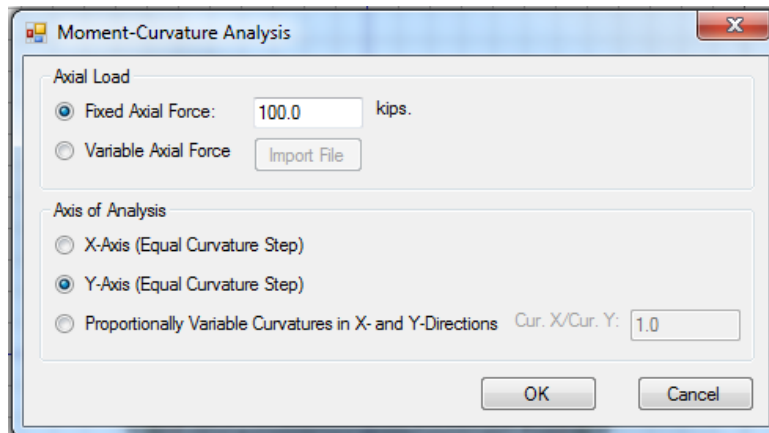


Figure A-13 A sample window of moment-curvature analysis



Clicking on “OK” button, the moment-curvature analysis will be performed and a window will come up containing the moment-curvature graph (Figure A-14). The results of moment-curvature analysis can be saved clicking on “Save” button on the results window.

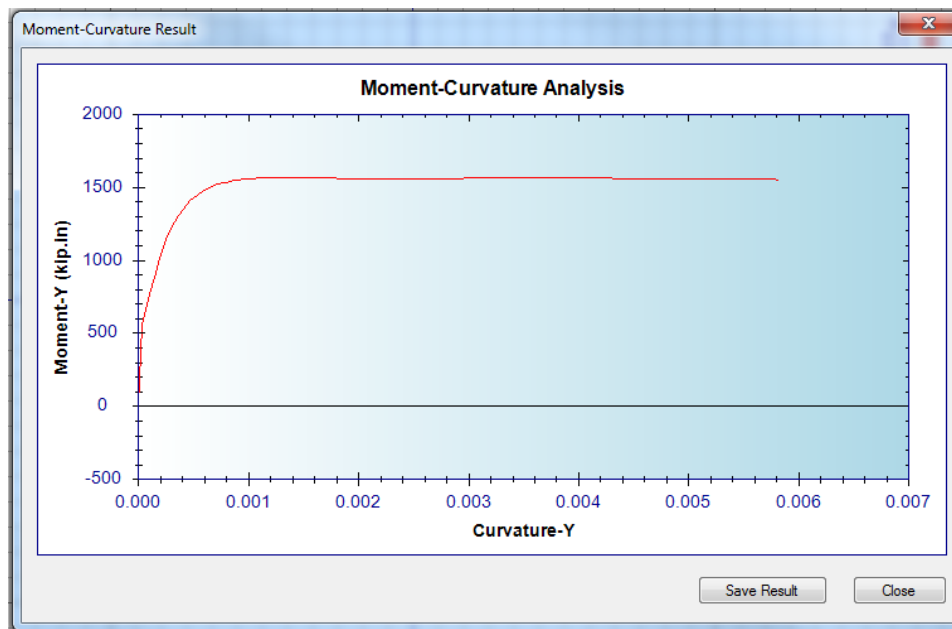


Figure A-14 A sample window of moment-curvature analysis results

### ***Force-deflection analysis***

To conduct a force-deflection analysis, one of the three implemented plastic hinge models is chosen. In this example, Priestly and Park plastic hinge has been used. Clicking on “Priestly and Park’s Method”, a window comes up (Figure A-15) and the user can enter the column height, the axial force (constant or variable) and define the analysis axis. In this example, the cyclic force-deflection of the RC-section along X-axis under constant axial force was conducted.

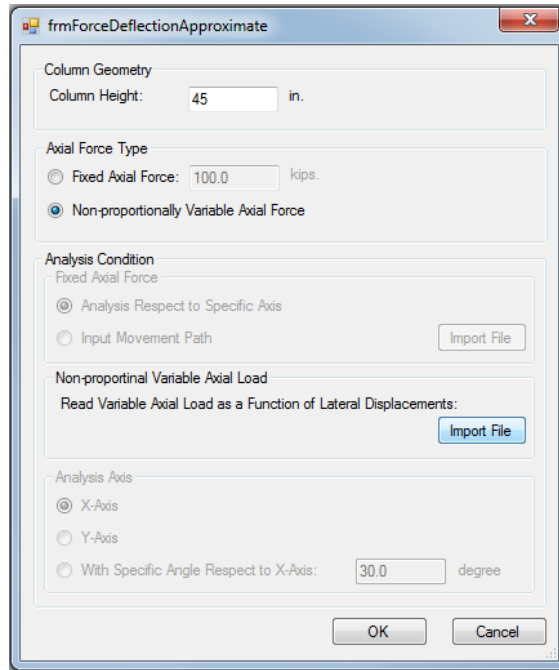


Figure A-15 A sample window of force-deflection analysis

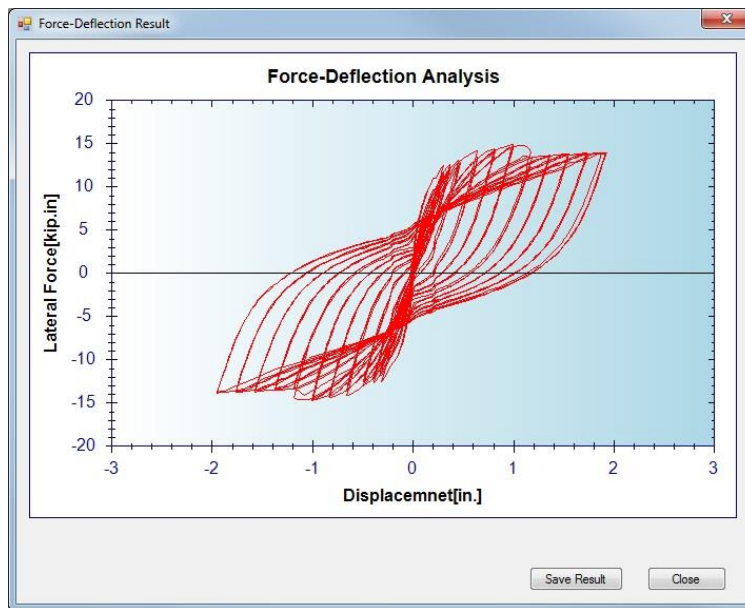


Figure A-16 A sample window of force-deflection analysis

The axial force and displacement along x- and y-axis were given as an input to the program. The column height is 45 in this example. The force-deflection curve is shown in Figure A-16.